NOVEL SPECTROSCOPIC IMAGING METHODS FOR ^{19}F MRI

by

Muhammed Yıldırım

B.S., in Physics, Boğaziçi University, 1999
M.S., in Nanoscale Science and Technology, Chalmers University of Technology, 2005

Submitted to the Institute of Biomedical Engineering
in partial fulfillment of the requirements
for the degree of
Doctor
of
Philosophy

Boğaziçi University
2025

NOVEL SPECTROSCOPIC IMAGING METHODS FOR ^{19}F MRI

APPROVED BY:

Prof. Dr. Esin Öztürk Işık (Thesis Advisor)	.....
Prof. Dr. Holger Grüll	.....
Prof. Dr. Mehmed Özkan	.....
Prof. Dr. Cengizhan Öztürk	.....
Assoc. Prof. Dr. Otar Akanyeti	.....

DATE OF APPROVAL: 01 July 2025

ACADEMIC ETHICS AND INTEGRITY STATEMENT

I, Muhammed Yıldırım, hereby certify that I am aware of the Academic Ethics and Integrity Policy issued by the Council of Higher Education (YÖK) and I fully acknowledge all the consequences due to its violation by plagiarism or any other way.

Name :

Signature:

Date:

ACKNOWLEDGMENTS

"It takes a village to raise a child," they say.

This child has passed through several villages, each of which deserves a sincere note of gratitude.

The village of Eindhoven

It all began with the invitation of Dr. Holger Grüll, my mentor and big brother, to join his molecular imaging research group at Philips Research Eindhoven. For that, I remain deeply grateful. Thank you, Herr Professor!

In Eindhoven, I had the chance to collaborate with Dr. Rolf Lamerichs. When we didn't have our own scanner, our trips to Hamburg to use the famously unique setup at Philips Research Hamburg became both a necessity and an adventure. There, we collaborated—and *competed*—with our dear colleague Dr. Jochen Keupp, the father of 3D UTE bSSFP. With Dr. Lamerichs, we "fought" valiantly to defend the honor of ^{19}F MRSI. Rolf, your companionship was a gift—thank you for being such a fun partner in crime. And to Jochen—appreciation for the friendly collaboration and rivalry!

The MR squad wouldn't have been complete without Frits DeBruijn, Roland van de Molengraaf, and Dr. Edwin Heijman. Working alongside you was a pleasure—my sincere thanks to each of you.

Despite my long-standing aversion to chemistry, I somehow kept falling into it. Fortunately, I had help: Anke de Vries showed me how to prepare emulsified nanoparticles, and Dr. Raquel Díaz-López provided the PLGA microbubbles. On the animal side, Caren van Kammen and Carlijn van Helvert made sure I didn't fumble the live subjects, while Monique Berben guided me through postmortem procedures. Your support in the lab made all the difference—I'm incredibly grateful.

During this time, I also had the joy of contributing to the graduation of Desiree Abdurrachim and Markus Glitzner, two promising researchers now charting their own paths in academia and R&D. Wishing you both continued success!

And finally, to Prof. Dr. Klaas Nicolay: thank you for your mentorship and your patience with the "eigenwijs" young man that I was. I only can seek consolation in considering myself your student for eternity. *May you rest in peace, sir.*

The village of Cologne

"Hey. Muhammed. Interested in reviving the fluorine research?"

These words from Dr. Holger Grüll reignited a familiar journey—this time in the "cold basement of a German hospital". Holger, your ongoing mentorship, friendship, and encouragement have meant the world. *Danke schön*, once again.

Knowing my limitations as a chemist, I stuck to the safe side: 3D printing, saline solutions, and micro-pipetting. For everything else, the Experimental Imaging Group at University Clinics had my back.

I owe special thanks to Dr. Juan Castillo Gómez and Dr. Markus Schütz for keeping my radiosafety and access credentials intact, and to Dr. Sin Yuin Yeo, whose weekend company and support I won't forget.

For the constant flow of emulsions, microbubbles, and yes, even *dead bodies*, I tip my hat to Lukas Sebbeke, Patrick Scholtz, and again Markus Schütz. The *mouse-wraps* in the freezer kept this project alive before and during the pandemic.

Toward the end, I was fortunate to collaborate with Xenia Kovalyk and Dr. Johannes Lindemeyer, who became my eyes, ears, and hands during remote imaging sessions. We didn't get to wrap it up the way we hoped, but our work isn't over. Thank you both—I'll see you soon!

The village of Istanbul

Becoming a PhD student at my *alma mater*—in my *forties*, while juggling a full-time job and a full-time family—was probably not the most sensible decision. But it happened, thanks to a few extraordinary people.

Gökçe Hale Hatay, the founding student of the Computational Imaging Laboratory; we've walked this path together since your ^{31}P project and my days at Philips. I couldn't have asked for a better comrade—thank you for always being there.

I was also fortunate to have two sisters, Sevim Cengiz and Dilek Betül Arslan, and a big brother, Asım Samli. Together, indulged the needs of the remote PhD student I was. Much love and appreciation to all of you.

My academic path was anything but conventional. I'm grateful to my professors, Dr. Burçin Ünlü and Dr. Bora Garipcan, for their continued support during this long-distance journey. Dr. Özgür Kocatürk, my old classmate and now professor of medical devices—thank you for your guidance and for serving on my thesis committee.

Prof. Dr. Cengizhan Öztürk, your energy and sharp insight remain as inspiring today as they were when we first met over 25 years ago. Thank you, sir.

My deepest gratitude goes to Prof. Dr. Esin Öztürk Işık. From your initial invitation to join your new lab, to your steadfast support through every phase—you've been the reason this journey began, and the reason it could continue. There are no words, but if I must try: thank you for believing in me when I doubted myself, for anchoring me when I lost momentum, and for leading with unwavering kindness and clarity. Your mentorship transformed what began as a lighthearted idea into one of the most meaningful chapters of my life.
A heartfelt thank you *hocam*.

The Family

The journey through all these villages—spanning nearly two decades—would not have been possible without the understanding and unwavering support of my partner in life, my best friend, and greatest supporter, Münibe. Thank you for letting me tilt at windmills, fight my fights, and slay my dragons. I promise: after this, my *professional* student days are over.
To my daughter Azra and my son Ahmed Eren—thank you for being my joy, my inspiration, and my constant source of motivation throughout this unusual journey. I can only hope that the example of persistence I tried to set will make up for the weekends I missed.
And to my parents—thank you for everything. For your sacrifices, for believing in me long before I believed in myself, and for being the quiet strength behind every chapter of my life. This achievement is yours as much as it is mine.

ABSTRACT

NOVEL SPECTROSCOPIC IMAGING METHODS FOR ^{19}F MRI

Fluorine-19 (^{19}F) magnetic resonance imaging (MRI) provides high specificity and no background signal, making it ideal for molecular imaging of disease markers and therapeutic carriers. This work was driven by the need to monitor targeted drug delivery in peritoneal carcinoma, requiring sensitive and quantifiable detection of fluorinated nanocarriers in vivo. To meet this need, two novel Magnetic Resonance Spectroscopic Imaging (MRSI) sequences were developed: Fluorine ultrafast Turbo Spectroscopic Imaging (F-uTSI) and Balanced Spiral Spectroscopic Imaging (BaSSI). These methods addressed the challenges of low ^{19}F sensitivity and spectral complexity in perfluorocarbon (PFC) agents through optimized RF pulses, k-space sampling, and artifact-suppressing reconstructions. Both sequences were validated through *in silico* simulations and *in vitro* experiments, and evaluated using imaging efficiency and a Rose-criterion-based detection framework. Compared to 3D ultra-short echo time balanced steady-state free precession (UTE bSSFP), BaSSI achieved superior performance in detecting sub-microliter PFC phantoms. Postmortem imaging with BaSSI further confirmed accurate anatomical localization using PFC-labeled polymer capsules. While both F-uTSI and BaSSI enabled robust ^{19}F imaging, BaSSI emerged as a strong candidate for targeted therapy monitoring in oncology.

Keywords: Fluorine-19 (^{19}F) Magnetic Resonance Imaging (MRI), Magnetic Resonance Spectroscopic Imaging (MRSI), Fluorine ultrafast Turbo Spectroscopic Imaging (F-uTSI), Balanced Spiral Spectroscopic Imaging (BaSSI), Perfluorocarbons (PFCs), Molecular imaging, Spectroscopic detection, Hot-spot imaging, Contrast agents, Ghosting artifacts, Chemical shift, Sensitivity benchmarking, Imaging efficiency, Rose criterion

ÖZET

^{19}F MRI İÇİN YENİ SPEKTROSKOPİK GÖRÜNTÜLEME YÖNTEMLERİ

Florin-19 (^{19}F) manyetik rezonans görüntüleme (MRG), yüksek özgüllüğü ve biyolojik dokularda sıfır arka plan sinyali sayesinde moleküler görüntüleme için güçlü bir platform sunar. Bu tez, peritoneal karsinom tedavisinde hedeflenmiş ilaç iletimini izlemek amacıyla, florlu nano-taşıyıcıların *in vivo* olarak hassas ve nicel tespiti ihtiyacından doğmuştur. Bu doğrultuda, iki yeni Manyetik Rezonans Spektroskopik Görüntüleme (MRSG) sekansı geliştirilmiştir: Florin ultrahızlı Turbo Spektroskopik Görüntüleme (F-uTSI) ve Dengelenmiş Spiral Spektroskopik Görüntüleme (BaSSI). Bu yöntemler, düşük ^{19}F duyarlılığı ve birçok perflorokarbon (PFC) ajanının spektral karmaşıklığına çözüm getirecek şekilde, optimize RF eksitasyonu, k-uzayı örnekleme ve yapaylık azaltıcı yeniden yapılandırma teknikleriyle tasarlanmıştır. Her iki sekans, *in silico* simülasyonlar ve *in vitro* deneylerle test edilerek, görüntüleme verimliliği ve bu tezde geliştirilen Rose kriterine dayalı tespit çerçevesiyle değerlendirildi. F-uTSI ve BaSSI, yüksek performanslı bir görüntüleme yöntemi olan 3D UTE bSSFP ile karşılaştırılmıştır. Mikrolitre altı PFC fantomlarla yapılan deneylerde, BaSSI her iki yöntemi de geride bırakmıştır. BaSSI ile elde edilen ^{19}F sıcak-nokta görüntüleri, florlu polimer mikrokapsüllerle yapılan postmortem deneylerle anatomik olarak doğrulanmıştır. Her iki yöntem güvenilir bulunmuş; ancak sonuçlar, BaSSI'nin onkolojik uygulamalarda hedefe yönelik tedavi takibi için güçlü bir aday olduğunu ortaya koymuştur.

Anahtar Kelimeler: Manyetik Rezonans Spectroskopik Gorunteleme, Florin-19 (^{19}F) Manyetik Rezonans Görüntüleme, Florin Ultra-Hızlı Turbo Spektroskopik Görüntüleme (F-uTSI), Dengelenmiş Spiral Spektroskopik Görüntüleme (BaSSI), Perflorokarbonlar, Moleküler görüntüleme, Sıcak-nokta görüntüleme, Hayalet artefaktlar, Kimyasal kayma, Duyarlılık karşılaştırması, Görüntüleme verimliliği, Rose kriteri

TABLE OF CONTENTS

ACADEMIC ETHICS AND INTEGRITY STATEMENT . . . iii
ACKNOWLEDGMENTS . . . iv
ABSTRACT . . . vii
ÖZET . . . viii
LIST OF FIGURES . . . xiii
LIST OF TABLES . . . xvi
LIST OF SYMBOLS . . . xvii
LIST OF ABBREVIATIONS . . . xviii
1. INTRODUCTION . . . 1
1.1 Research Origins . . . 1
1.2 Background and Motivation . . . 2
2. PRINCIPLES, APPLICATIONS AND CHALLENGES OF ^{19}F MRI . . . 6
2.1 Historical Background and Development . . . 7
2.2 Technical and Physical Challenges . . . 12
2.3 Chemical Shift Artifacts in ^{19}F MRI . . . 13
2.4 Summary . . . 17
3. MAGNETIC RESONANCE SPECTROSCOPIC IMAGING . . . 18
3.1 Principles of Magnetic Resonance Spectroscopic Imaging . . . 19
3.1.1 2D Spectroscopic Imaging . . . 20
3.1.2 3D Spectroscopic imaging . . . 21
3.1.3 Projection Imaging . . . 23
3.1.4 3D Backprojection Imaging . . . 24
3.2 Spectral Integration and Image Reconstruction . . . 27
3.3 Summary . . . 29
4. PERFORMANCE METRICS FOR ^{19}F MRI . . . 30
4.1 Rose Criterion and Object Visibility . . . 32
4.2 Denoising Using the Rose Criterion . . . 34
4.3 Image Resolution and the Point Spread Function . . . 36
4.4 Summary . . . 37
5. PULSE SEQUENCE ENGINEERING FOR ^{19}F MRSI . . . 38
5.1 In Silico Methods for ^{19}F Spectroscopic Imaging . . . 39
5.1.1 Simulating an RF Pulse . . . 39
5.1.2 Gradients and Phase Encoding . . . 43
5.1.3 Acquisition Window . . . 46
5.2 RF Pulse Selection for ^{19}F Spectroscopic Imaging . . . 47
5.2.1 Amplitude-Modulated RF Pulses . . . 48

5.2.2 Multi-band Pulses . . . 50
5.3 Engineering F-uTSI . . . 53
5.3.1 Core Sequence Structure and Timing Parameters . . . 53
5.3.2 Timing Constraints and Optimization . . . 54
5.3.3 Spectral Complexity and Signal Dynamics . . . 55
5.3.4 Echo Train Length and Relaxation . . . 57
5.3.5 In-silico Assessment of Magnetization . . . 58
5.3.6 Acquisition Strategies and PSF . . . 59
5.3.7 Reversed Echo Train Acquisition . . . 62
5.4 Engineering BaSSI . . . 63
5.4.1 Core Sequence Structure and Timing Parameters . . . 63
5.4.2 Exploring the Parameter Space . . . 65
5.4.3 In-silico Assessment of Magnetization . . . 68
5.4.4 Acquisition Strategy and PSF Analysis . . . 69
5.5 Implementation of Sequences in MR System Software . . . 72
5.6 Summary . . . 76
6. EXPERIMENTAL VALIDATION OF F-uTSI AND BaSSI . . . 77
6.1 Methods . . . 78
6.1.1 Contrast Media and Phantom Materials . . . 78
6.1.1.1 Bulk Material-Based Phantoms . . . 79
6.1.1.2 Emulsions . . . 80
6.1.1.3 Polymer Microbubbles . . . 82
6.1.2 Animal Studies . . . 84
6.1.3 Measurement Setup . . . 85
6.1.4 Thermal Effects on SNR and Pre-Acquisition Stabilization . . . 86
6.1.5 Experimental Methodology . . . 87
6.2 Optimization of F-uTSI and BaSSI . . . 89
6.2.1 Optimized Hardware Settings . . . 89
6.2.2 Sampling Bandwidth and Spectral Resolution . . . 90
6.2.3 Optimization of F-uTSI . . . 91
6.2.4 Optimization of BaSSI . . . 93
6.3 Summary . . . 96
7. BENCHMARKING OF F-uTSI AND BaSSI . . . 97
7.1 Benchmarking BaSSI against 3D UTE bSSFP . . . 100
7.1.1 Benchmark Sequence: 3D UTE bSSFP . . . 100
7.1.1.1 Sequence Design and Key Features . . . 101
7.1.1.2 Acquisition Parameters . . . 102
7.1.1.3 Performance and Conclusions . . . 102

7.1.2 In-House Implementation and Optimization of 3D UTE-bSSFP 102
7.1.3 Benchmarking Results . . . 105
7.2 Summary . . . 111
8. APPLICATIONS OF ^{19}F SPECTROSCOPIC IMAGING . . . 112
8.1 *Post-Mortem* Imaging of PFOB Microcapsules Using BaSSI . . . 112
8.2 *In Vivo* 3D Backprojection ^{19}F Spectroscopic Imaging . . . 115
8.3 *In Vivo* Multicolor Imaging of PFC Emulsions . . . 118
8.4 *In Vivo* Imaging of Vx-2 tumors in Rabbit Models . . . 120
8.5 *In Vivo* Imaging of Angiogenesis in Murine Models . . . 122
8.6 Summary . . . 124
9. SUMMARY OF INNOVATIONS AND CONTRIBUTIONS . . . 125
10. DISCUSSION AND CONCLUDING REMARKS . . . 127
APPENDIX A. PRINCIPLES OF NMR AND MRI . . . 132
A.1 Nuclear Magnetic Resonance . . . 132
A.2 RF Excitation and Signal Generation . . . 134
A.2.1 Free Induction Decay (FID) . . . 135
A.2.2 The RF Echo . . . 138
A.2.3 The Gradient Echo . . . 141
A.2.4 The RF Echo Train . . . 143
A.2.5 The Gradient Echo Train . . . 145
A.3 The Bloch Equation . . . 146
A.3.1 Magnetization Dynamics . . . 146
A.3.2 Simplified Cases and Analytical Solutions . . . 147
A.4 Rotating Frame of Reference . . . 147
A.5 RF Pulses and Rotating Frame Dynamics . . . 149
A.5.1 On-Resonance Excitation . . . 150
A.5.2 Off-Resonance Excitation . . . 151
A.6 Spatial Localization . . . 153
A.6.1 Selective Excitation (Slice Selection) . . . 153
A.6.1.1 Mathematical Formulation . . . 154
A.6.1.2 Simplified Solution for Hard Pulses . . . 155
A.6.1.3 RF Pulse Design and Slice Profile . . . 156
A.7 Spatial Encoding . . . 157
A.7.1 Frequency Encoding . . . 158
A.7.2 Phase Encoding . . . 159
A.7.3 Multi-slice 2D Acquisition . . . 160
A.7.4 Volumetric 3D Acquisition . . . 161
A.8 The k-space and Fourier Imaging . . . 162

A.8.1 k-Space as the Domain of Fourier Encoding 163
A.8.2 Trajectories and Sampling in k-Space 163
A.8.3 k-Space and Phase Encoding 164
A.8.4 2D and 3D k-Space Sampling 164
A.8.5 Sampling Theorem and Resolution Limits 165
A.8.6 Implications for Reconstruction 165
A.9 Image Reconstruction 166
A.9.1 From k-Space to Image Space 166
A.9.2 Practical Considerations in DFT Reconstruction 167
A.9.2.1 DFT Definitions 167
A.9.2.2 Interpolation and Zero Filling 168
A.9.2.3 Aliasing 168
A.9.2.4 Gibbs Ringing 168
A.9.2.5 Reconstruction from Non-Cartesian Trajectories 169
A.10 Noise and SNR 170
APPENDIX B. THE GENERALIZED BLOCH EQUATION 176
B.1 Overview 176
B.2 Bloch Equation in the Rotating Frame 176
B.3 Effective Field Components 176
B.4 Effective Field with Gradients and Off-Resonance 177
B.5 Scalar Form of the Bloch Equation 177
B.6 Generalized Form with Gradient and Detuning Terms 178
B.7 Conclusion 178
REFERENCES 179

LIST OF FIGURES

Figure 1.1	Schematic illustration of HIPEC setup.	2
Figure 1.2	Schematic and SEM image of microsphere DDS.	3
Figure 1.3	Fluorinated DDS core design for ^{19}F MRI.	4
Figure 2.1	Chemical shift artifact in a fluorine-19 image.	15
Figure 2.2	Selective excitation	16
Figure 3.1	2D Slice selective MRSI sequences.	20
Figure 3.2	2D spectroscopic data.	21
Figure 3.3	3D Spectroscopic imaging with slice selection.	21
Figure 3.4	All-phase encoded 3D Spectroscopic imaging.	22
Figure 3.5	2D Projection imaging.	23
Figure 3.6	Projection imaging.	24
Figure 3.7	Sinogram of a complex object.	25
Figure 3.8	Image generation by spectral integration.	27
Figure 3.9	SNR vs spectral integration bandwidth.	28
Figure 4.1	Object visibility with varying object size and background noise.	32
Figure 4.2	Rose criterion for small objects.	33
Figure 4.3	Rose criterion as a denoising tool for hot-spot images.	35
Figure 4.4	PSF and image resolution.	37
Figure 5.1	Block pulse and sinc pulse.	40
Figure 5.2	Discretization of RF pulse.	40
Figure 5.3	Runge-Kutta stepwise integration.	42
Figure 5.4	Trapezoidal gradient waveforms for phase encoding.	45
Figure 5.5	Amplitude modulated RF pulses.	49
Figure 5.6	Multi-band pulse spectrum formation.	51
Figure 5.7	Simulation of multi-band RF excitation.	52
Figure 5.8	F-uTSI:The core sequence.	53
Figure 5.9	F-uTSI: Simulation of a single peak spin system.	55
Figure 5.10	F-uTSI: Simulation of a complex peak spin system.	55
Figure 5.11	F-uTSI: Impact of carrier frequency on echos.	56
Figure 5.12	F-uTSI: Signal vs offset frequency.	56
Figure 5.13	F-uTSI: Signal vs varying TR.	57
Figure 5.14	F-uTSI: Magnetization of a 32x32 scan.	58
Figure 5.15	F-uTSI: Magnetization of a 64×64 scan.	59
Figure 5.16	F-uTSI: Cartesian k-space acquisition strategies.	60
Figure 5.17	F-uTSI: *Psuedo*-radial k-space acquisition strategy.	61
Figure 5.18	F-uTSI: Pseudo-radial reconstruction.	61

Figure 5.19	F-uTSI: Reversed echo train acquisition.	62
Figure 5.20	F-uTSI: Improved image quality with reversed averaging.	62
Figure 5.21	BaSSI: Balanced Spiral Spectroscopic Imaging Sequence.	64
Figure 5.22	BaSSI simulation of single peak NMR spectrum.	65
Figure 5.23	BaSSI: Simulation results of pulse shapes vs flip angle.	65
Figure 5.24	BaSSI: Simulation results for different offset frequencies.	66
Figure 5.25	BaSSI: Signal level vs offset frequency.	67
Figure 5.26	BaSSI: SNR landscape as a function of flip angle and TR.	68
Figure 5.27	BaSSI: Simulated magnetization for a 64×64 acquisition.	69
Figure 5.28	BaSSI: Spiral k-space trajectory.	70
Figure 5.29	BaSSI: PSF analysis with dummy scans.	71
Figure 5.30	Impact of dummy scans on imaging efficiency.	71
Figure 5.31	UI Parameters of implementation.	73
Figure 5.32	Timing parameters of BaSSI.	74
Figure 5.33	Phase encoding sequence diagram of BaSSI.	74
Figure 5.34	Example of implemented code.	75
Figure 6.1	Molecular structures and NMR spectra of PFOB and PFCE.	78
Figure 6.2	Sample height of bulk phantoms.	80
Figure 6.3	Emulsified PFC nanoparticle.	80
Figure 6.4	Cryo-TEM images of PFC emulsions.	82
Figure 6.5	PLGA microbubbles filled with PFCs.	82
Figure 6.6	PLGA microbubbles filled with PFOB.	83
Figure 6.7	Setup for precise phantom measurements.	85
Figure 6.8	SNR variation due to thermal drift.	86
Figure 6.9	Tuning/matching of RF transmission.	87
Figure 6.10	Flip angle series for power optimization.	88
Figure 6.11	ROIs used for signal and noise analysis.	88
Figure 6.12	Hardware parameter sweep.	89
Figure 6.13	Acquisition bandwidth and spectral resolution.	90
Figure 6.14	F-uTSI: NSA vs TR.	92
Figure 6.15	F-uTSI: Imaging Efficiency.	92
Figure 6.16	Frequency sweep to identify peaks of PFOB.	93
Figure 6.17	BaSSI: SNR vs. T_{acq}.	94
Figure 6.18	BaSSI: SNR vs. TR.	94
Figure 6.19	BaSSI: TR and flip angle optimization.	95
Figure 7.1	2D F-uTSI Sensitivity assessment.	97
Figure 7.2	2D F-uTSI comparison with MCSS-RARE.	98
Figure 7.3	2D F-uTSI comparison with 3D UTE bSSFP.	99

Figure 7.4	Simultaneous 3D $^{19}F/^{1}H$ UTE bSSFP sequence.	100
Figure 7.5	Optimization of 3D UTE bSSFP: SNR vs Long TR.	103
Figure 7.6	Optimization of 3D UTE bSSFP: SNR vs TE.	103
Figure 7.7	Optimization of 3D UTE bSSFP: Flip Angle vs TR.	104
Figure 7.8	Benchmarking BaSSI against 3D UTE bSSFP.	106
Figure 7.9	Benchmarking with 0.10 µL PFOB sample.	107
Figure 7.10	Estimating detection threshold for 0.05 μL PFOB.	108
Figure 7.11	BaSSI: Detection of 0.05 µL PFOB sample.	109
Figure 7.12	BaSSI: Spectra of 0.10 µL and 0.05 µL PFOB samples.	110
Figure 8.1	BaSSI sequence and spiral k-space sampling.	112
Figure 8.2	Rose criterion based filtering of hot-spots.	113
Figure 8.3	Anatomic localization of hot-spots.	114
Figure 8.4	3D Backprojection imaging textintin vivo.	115
Figure 8.5	3D Backprojection Reconstruction.	116
Figure 8.6	Anatomical localization of ^{19}F backprojection images.	117
Figure 8.7	SNR vs angular resolution.	117
Figure 8.8	Multicolor spectroscopic imaging.	118
Figure 8.9	In vivo multicolor ^{19}F spectroscopic imaging.	119
Figure 8.10	3D stack of stars spectrocopic imaging.	121
Figure 8.11	In vivo ^{19}F MRSI of Vx2 tumors.	121
Figure 8.12	In vivo ^{19}F MRSI of angiogenesis in murine models.	123
Figure 8.13	^{19}F spectroscopy of excised organs.	123
Figure A.1	Lorentzian distribution of spin densities.	137
Figure A.2	MR Sequence for FID and T_2^*.	138
Figure A.3	MR sequence that generates an RF echo.	139
Figure A.4	MR sequence that generates gradient echo.	142
Figure A.5	Five echoes generated by a 3-pulse sequence.	143
Figure A.6	Spin-echo train.	144
Figure A.7	Gradient echo train.	145
Figure A.8	Magnetization in rotating frame of reference.	149
Figure A.9	On-resonance flipping of magnetization in rotating frame.	151
Figure A.10	Off-resonance flipping of magnetization in rotating frame.	152
Figure A.11	Slice selection in three orthogonal directions.	153
Figure A.12	Slice profile of a bandwidth-limited sinc pulse.	157
Figure A.13	Multi-slice acquisition with slice selection.	161
Figure A.14	Volumteric 3D acquisition.	162
Figure A.15	Gradient waveforms.	164
Figure A.16	Noise complex magnitude images.	174

LIST OF TABLES

Table 2.1	NMR properties of common nuclei	6
Table 5.1	SLR: Time step size vs accuracy and computation time.	41
Table 5.2	Bandwidth and duration of RF pulse shapes	49
Table 6.1	Physical properties of selected perfluorocarbons	79
Table 6.2	Volume and weights of bulk PFOB phantoms	79
Table 6.3	SNR values for different acquisition settings.	91
Table 7.1	Imaging efficiencies of BaSSI and 3D UTE bSSFP	106

LIST OF SYMBOLS

$^{1}\mathrm{H}$	Proton, reference nucleus in conventional MRI
$^{19}\mathrm{F}$	Fluorine-19, the nucleus used for MRI in this thesis
B_0	Static magnetic field strength
$B_1(t)$	RF magnetic field
$G(t)$	Gradient waveform as a function of time
G_x, G_y, G_z	Gradient amplitudes along x, y, z axes
$\vec{G}(t)$	Gradient field vector as a function of time
$\langle I \rangle$, μ	Mean signal intensity
$\vec{k}$	k-space vector
k_x, k_y, k_z	k-space coordinates
M_0	Equilibrium magnetization
$\vec{M}$	Magnetization vector
M_x, M_y, M_z	Magnetization components along x, y, z axes
N_x, N_y, N_z	Number of phase-encoding steps in x, y, z
R_c	Rose criterion
$S(k)$	Signal in k-space
T_1	Longitudinal relaxation time
T_2	Transverse relaxation time
T_2^*	Effective transverse relaxation time
T_{acq}	Acquisition time or time after excitation
χ	Magnetic susceptibility
δ	Chemical shift (in ppm)
$\delta(t)$	Dirac delta function
ΔB_0	Main magnetic field inhomogeneity
$\Delta\omega$	Off-resonance frequency
$\Delta\omega_c$	Frequency offset due to chemical shift
$\Delta x, \Delta y, \Delta z$	Voxel size or spatial resolution in x, y, z
γ	Gyromagnetic ratio
μ_{noise}	Mean intensity in a noise-only region
ω_0	Larmor angular frequency
ω_{RF}	Applied RF frequency
ρ	Proton or spin density
σ	Standard deviation (noise level)
$\vec{r}$	Spatial position vector
$\mathcal{F}$, $\mathcal{F}^{-1}$	Fourier transform and Inverse Fourier transform

LIST OF ABBREVIATIONS

BaSSI	Balanced Spiral Spectroscopic Imaging
(b)SSFP	(Balanced) Steady-State Free Precession
CE-FAST	Chemical Shift Encoded Fast Acquisition with Steady State
CNR	Contrast-to-Noise Ratio
DDS	Drug Delivery System
ES	Echo spacing between successive echoes
ETL	Echo Train Length
FA	Flip Angle
FFT	Fast Fourier Transform
FID	Free Induction Decay
FOV	Field of View
F-uTSI	Fluorine Ultrafast Turbo Spectroscopic Imaging
GRE	Gradient Recalled Echo
IEC	International Electrotechnical Commission
KMA	Ketamine–Medetomidine–Atropine anesthesia mixture
MP-RAGE	Magnetization Prepared Rapid Acquisition Gradient Echo
(N)MR	(Nuclear) Magnetic Resonance
NSA	Number of Signal Averages
PFCE	Perfluoro-15-crown-5-ether
PFOB	Perfluorooctylbromide
PFPE	Perfluoropolyether
PLGA	Poly(lactic-co-glycolic acid)
PSF	Point Spread Function
PTBCH	Perfluoro-tert-butylcyclohexane
RARE	Rapid Acquisition with Relaxation Enhancement
RF	Radiofrequency
RGD	Arg-Gly-Asp (Integrin-binding peptide)
ROI	Region of Interest
SAR	Specific Absorption Rate
SLR	Shinnar-Le Roux
SNR	Signal-to-Noise Ratio
TE	Echo Time
TR	Repetition Time
TSI	Turbo Spectroscopic Imaging
UTE	Ultrashort Echo Time

1. INTRODUCTION

1.1 Research Origins

This thesis presents the author's research on ^{19}F MR spectroscopic imaging, which began in late 2005 as part of the molecular imaging program at Philips Research Laboratories in Eindhoven, and later resumed, after a long hiatus, within the framework of a PhD program at Boğaziçi University.

During the early stages of the research, the author collaborated with Dr. Rolf Lamerichs, Dr. Jochen Keupp, Prof. Dr. Holger Grüll, and the late Prof. Dr. Klaas Nicolay on the development of the Fluorine ultrafast Turbo Spectroscopic Imaging (F-uTSI) sequence, aimed at overcoming challenges such as low sensitivity and complex spectral characteristics [1–13]. Upon moving to the MR business unit at Philips Healthcare in 2009, the author continued contributing informally. Though sporadic, this phase yielded several conference publications [14], [15].

The research resumed thanks to a series of fortunate developments. In 2014, Dr. Esin Öztürk Işık joined Boğaziçi University and founded the Computational Imaging Laboratory. Having previously collaborated on ^{31}P MRSI, she invited the author to join her lab as a PhD researcher. Around the same time, Prof. Dr. Grüll proposed reviving ^{19}F imaging research as part of a new project on drug delivery systems for peritoneal carcinoma. This was made possible by infrastructure originally developed at Philips Research and later transferred to University Clinics Cologne.

The PhD work began with reimplementation and optimization of F-uTSI on a clinical Philips 3.0 T scanner with a dual-tuned ^{1}H/^{19}F coil. While effective for detecting low concentrations of fluorinated agents, the sequence lacked the sensitivity required for imaging therapeutic microcapsules in vivo. This motivated the development of the Balanced Spiral Spectroscopic Imaging (BaSSI) sequence—a fast and efficient method combining free induction decay acquisition with pseudo-spiral k-space sampling to improve both sensitivity and speed.

Despite disruptions from the COVID-19 pandemic and limitations of an aging scanner, the sequence was successfully developed, rigorously benchmarked, and presented at the ISMRM annual meeting [16]. This effort culminated in a peer-reviewed article, "Fast ^{19}F spectroscopic imaging with pseudo-spiral k-space sampling", published in NMR in Biomedicine [17].

1.2 Background and Motivation

The work presented in this dissertation was carried out as part of a broader research project aimed at developing novel drug delivery systems (DDS) for the treatment of peritoneal carcinoma (PC). Peritoneal carcinoma is a term used to describe both primary malignancies originating in the peritoneal lining and secondary complications arising from metastatic dissemination of tumors into the peritoneal cavity. While primary peritoneal carcinoma is relatively rare, secondary peritoneal involvement due to peritoneal metastases and malignant ascites is a common and serious complication in advanced gastrointestinal, gynecological, and hepatopancreatobiliary cancers. It is estimated to affect between 700,000 and 900,000 patients worldwide each year [18–21]. Peritoneal dissemination typically presents as diffuse nodular infiltration of the peritoneum, leading to complications such as bowel obstruction, malignant ascites, and a marked reduction in quality of life. Prognosis remains poor, with median survival often limited to a few months in the absence of treatment [22–24].

Cytoreductive surgery followed by hyperthermic intraperitoneal chemotherapy (HIPEC) has emerged as a standard treatment approach for selected patients with peritoneal metastases (Figure 1.1) [25], [26]. This two-step protocol combines the physical removal of macroscopic tumor deposits with the localized delivery of heated chemotherapeutic agents to eradicate microscopic residuals. The therapeutic efficacy of HIPEC arises from both the pharmacologic compartmentalization of the peritoneal cavity and the synergistic cytotoxic effects of hyperthermia [21], [27]. Despite its proven clinical benefits, however, broader adoption remains limited. Access to HIPEC is restricted by the requirement for dedicated perfusion systems and highly trained teams, which hampers its scalability and availability across treatment centers [28], [29].

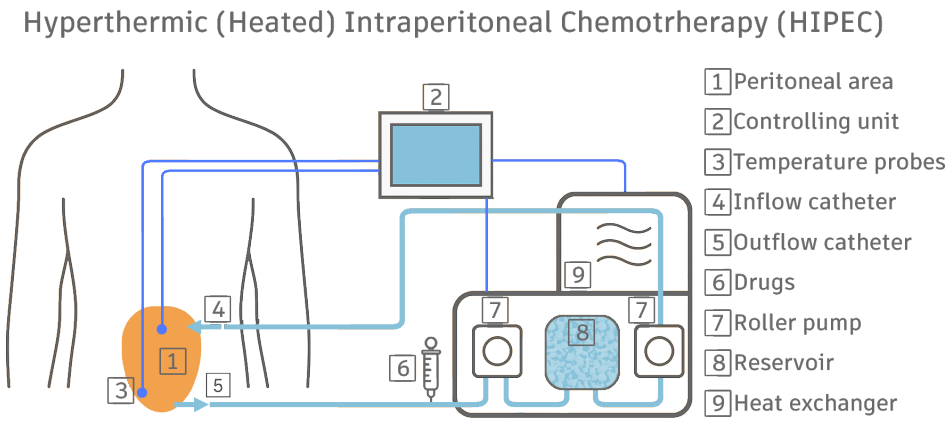

Figure 1.1 Schematic illustration of a HIPEC system.

These limitations have spurred the development of DDS capable of achieving localized, controlled chemotherapeutic delivery with minimal invasiveness. A recent review identified only 17 preclinical studies focused on novel DDS for PC, most of which employed murine models and carrier systems such as liposomes, hydrogels, microspheres, or nanoparticles to deliver agents including paclitaxel, doxorubicin, cisplatin, and 5-fluorouracil [30]. This limited body of work underscores the need for continued exploration and optimization of carrier platforms. Among these approaches, biodegradable microsphere-based DDS are particularly promising due to their structural versatility, drug-loading capacity, and favorable biocompatibility.

Several preclinical studies have demonstrated improved tumor suppression as a result of increasing exposure to therapeutic agents, prolonged survival, and reduced systemic toxicity using such microsphere platforms [31–35]. These systems enable sustained, passive release of chemotherapeutic agents in close proximity to the target site, thereby maintaining high local drug concentrations while minimizing systemic exposure. Notably, porous and polymeric microspheres loaded with docetaxel, camptothecin, or cisplatin have shown significant inhibition of angiogenesis, metastatic progression, and increased apoptosis [32–35]. Additionally, micro- and nanoparticle carriers have been co-loaded with multiple agents, such as paclitaxel and 5-FU in hydrogel composites, which demonstrated synergistic tumor inhibition and increased survival in preclinical PC models [36].

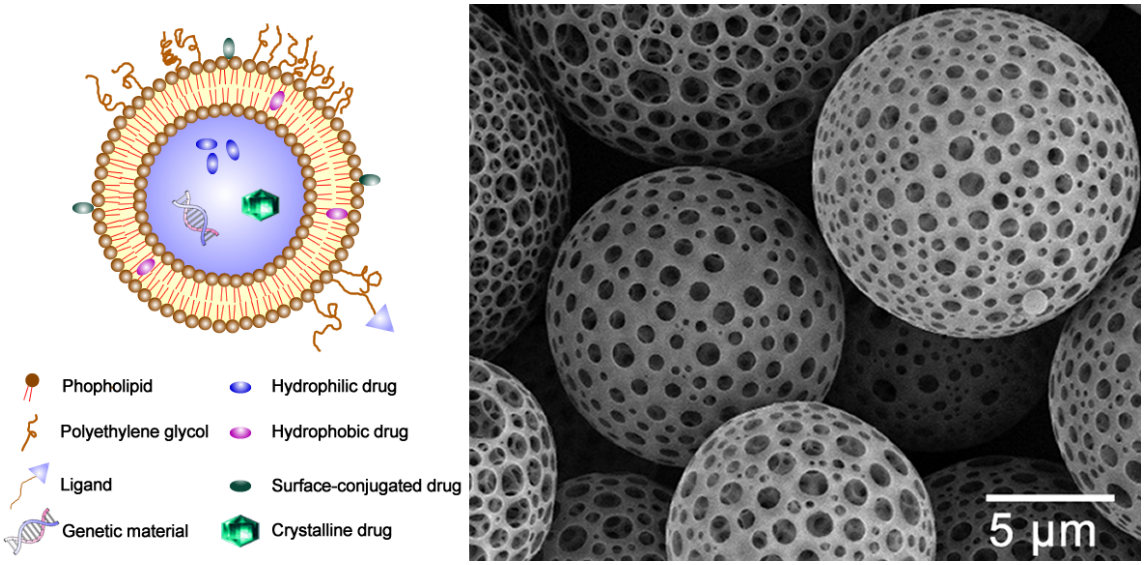

Figure 1.2 Schematic representation of a multifunctional liposomal DDS (left), which can carry therapeutic agents and is functionalized to bind to target lesions, alongside an SEM image of biodegradable porous polymer microspheres (right). (The SEM image is adapted from [37].)

Despite their therapeutic potential, the clinical translation of DDS is significantly hindered by the lack of imaging tools that can quantitatively and noninvasively assess in vivo carrier behavior. Conventional imaging modalities lack the specificity and sensitivity to visualize the small amounts of material delivered to complex anatomical environments. In this context, fluorine-19 (^{19}F) magnetic resonance imaging (MRI) offers a compelling solution. Fluorinated compounds such as perfluorooctyl bromide (PFOB) or perfluoropolyether (PFPE) can be encapsulated within DDS carriers (Figure 1.3), enabling real-time tracking of biodistribution, retention, and clearance. Since ^{19}F is virtually absent in biological tissues, it generates no endogenous signal, allowing for highly specific and quantitative detection with zero background.

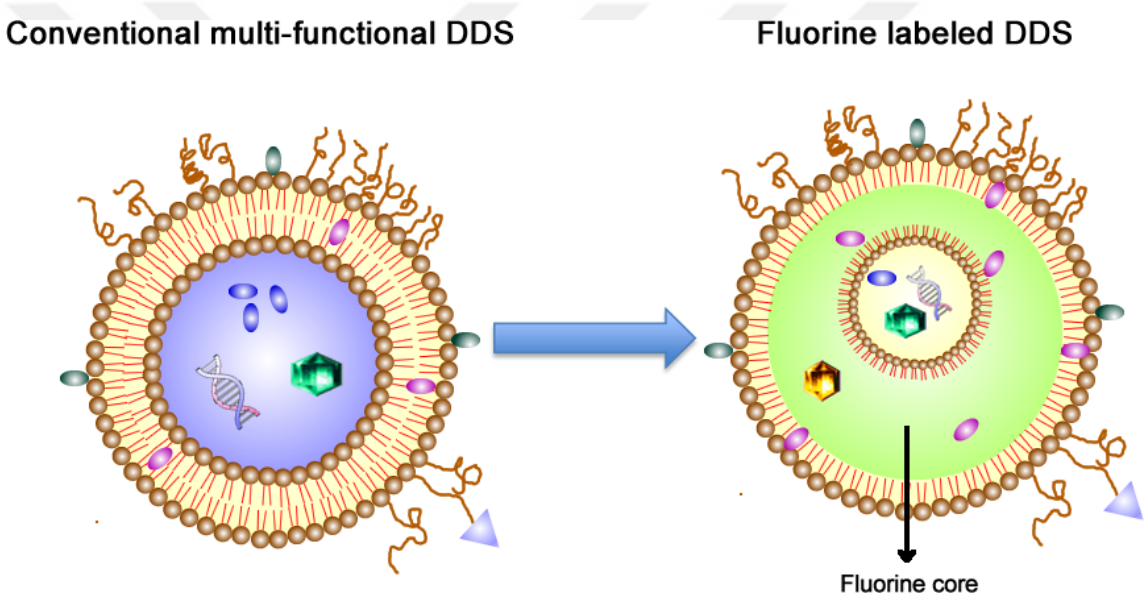

Figure 1.3 Conceptual transition from a conventional multifunctional liposomal carrier to a fluorinated core system compatible with ^{19}F MRI. Encapsulation of perfluorocarbon compounds enables noninvasive signal detection and quantitative pharmacokinetic assessment via ^{19}F MRI.

^{19}F MRI is further enabled by favorable NMR properties: a high gyromagnetic ratio, 100% natural abundance, and a resonance frequency close to that of ^{1}H, which allows imaging on conventional MRI hardware. These factors make ^{19}F MRI well suited for molecular imaging and theranostic applications. However, its broader adoption is hindered by several technical limitations. Low signal intensity at the dilute concentrations typically present in vivo, combined with spectral complexity and chemical shift artifacts, presents major challenges for conventional acquisition methods. These issues are further compounded when multiple fluorinated species or compounds with broad spectra are involved. These limitations have motivated the development of novel acquisition strategies with improved spectral robustness, spatial resolution, and efficiency.

The goal of the dissertation research was to develop, optimize, and experimentally validate novel spectroscopic imaging methods for ^{19}F MRI that enable artifact-free detection of fluorinated contrast agents under conditions of low concentration, broad spectral dispersion, and limited scan time. To this end, two advanced pulse sequences, F-uTSI and BaSSI, were engineered to achieve chemically agnostic spatial encoding, robust spectral resolution, and high imaging efficiency. These methods were evaluated using a combination of in silico simulation, scanner-side implementation, and phantom-based benchmarking, with particular emphasis on quantitative performance metrics and spatial fidelity. The work was motivated by the imaging requirements of targeted drug delivery studies and is intended to support preclinical assessment of fluorinated nanocarriers in models of peritoneal carcinoma, with the goal of facilitating future integration into clinically translatable molecular imaging workflows.

This thesis begins with a historical and technical overview of ^{19}F MRI, tracing its early applications, reviewing its chemical and physical constraints, and motivating its adoption in spectroscopic imaging. It then introduces the principles of MR signal encoding, the challenges associated with imaging chemically heterogeneous agents, and the rationale for employing magnetic resonance spectroscopic imaging (MRSI) in lieu of frequency-selective methods.

Subsequent chapters detail the design and implementation of the F-uTSI and BaSSI sequences, the latter of which constitutes an original contribution of this dissertation. Sequence development is supported by *in silico* simulations and validated through phantom experiments and comparative benchmarking against gold-standard imaging techniques, using performance metrics developed during the project.

Experimental results demonstrate the capacity of spectroscopic imaging techniques, particularly BaSSI, to detect microliter- and sub-microliter volumes of perfluorocarbon (PFC) agents with high fidelity and to localize signal anatomically under conditions compatible with clinical MRI systems.

Finally, the thesis presents several preclinical applications, including hot-spot imaging, multicolor detection, and targeted angiogenesis imaging in murine and rabbit models. These studies highlight the translational potential of spectroscopic ^{19}F MRI for the noninvasive monitoring of therapeutic payloads and molecular targets.

2. PRINCIPLES, APPLICATIONS AND CHALLENGES OF ^{19}F MRI

The ^{19}F nucleus, with 100% natural abundance, resonates at a frequency 94% that of proton (^{1}H) and has an NMR sensitivity 83% relative to ^{1}H (Table 2.1), contributing to a signal-to-noise ratio (SNR) approximately 89% per nucleus [38–41]. The negligible endogenous ^{19}F signal in the body, due to low physiological concentrations of mobile fluorine (typically less than 10^{-3} mmol/g wet tissue weight), combined with its high resonance in immobilized forms like bone, offers high specificity and contrast-to-noise ratio (CNR), especially when enhanced with perfluorinated compounds. These compounds, known as perfluorocarbons (PFCs), replace hydrogen with fluorine, modifying electronic and structural properties advantageous for medical imaging [38–41]. Leveraging these attributes, ^{19}F MRI provides a noninvasive, high-sensitivity tool for *in vivo* applications, outperforming other MR-visible nuclei in many respects [39–41]. Despite ongoing challenges in sensitivity and acquisition speed, improvements in scanner hardware and molecular contrast agent design continue to elevate its promise as a dual-modality imaging platform alongside ^{1}H MRI [42].

Table 2.1
Natural abundance and gyromagnetic ratio of selected NMR-active nuclei.

Material	Natural Abundance (%)	γ (MHz/T)
^{1}H	**99.985**	**42.5759**
^{2}H	0.015	6.53566
^{10}B	19.58	4.5754
^{11}B	80.42	13.66
^{13}C	1.108	10.7054
^{14}N	99.63	3.0774
^{15}N	0.37	4.3142
^{17}O	0.037	5.772
^{19}F	**100**	**40.0541**
^{23}Na	100	11.262
^{29}Si	4.7	8.4578
^{31}P	100	17.235
^{33}S	0.76	3.2654
^{35}Cl	75.53	4.1717
^{37}Cl	24.47	3.472

2.1 Historical Background and Development

The initial feasibility studies of ^{19}F MRI can be traced back to the early years of MRI, notably in 1977 when Holland et al. demonstrated the technique by imaging NaF, a water-soluble salt, as well as a more complex PFC, namely perfluorotributylamine (PTFA) *in vitro* [43]. Before the emergence of MRI applications, fluorinated compounds were developed as oxygen carriers [44] and anticancer drugs in the 1950s [45]. In the 1980s, PFCs were found to be chemically inert and resistant to metabolization in organisms. This discovery positioned PFCs as ideal for medical imaging, despite challenges like their hydrophobic nature, which led to the development of water-soluble PFC emulsions. These provide a versatile platform to investigate biological function applications [38], [46–49].

Liquid perfluorocarbons (PFCs) exhibit extremely low solubility in water, which contributes to their prolonged retention and limited diffusion at target sites. Although PFCs are lipophobic, their pronounced hydrophobicity often enables partial incorporation into the lipid components of cellular membranes. This interaction can modulate cellular responses to specific stimuli or stressors, facilitating functional studies at both the cellular and systemic levels. The depth and rate of tissue penetration by PFCs can be further controlled by tuning particle size and by engineering their lipid solubility—for example, through the synthesis of compounds with different chain lengths and molecular structures [41], [50–60].

In Magnetic Resonance Imaging (MRI), the use of perfluorocarbons (PFCs) predominantly revolves around utilizing the distinctive NMR response of fluorine as a tracer signal to generate what are referred to as 'hot-spot' images [61] depicting the accumulation sites of the contrast material, and quantify changes in physical properties of the hot-spots, such as signal intensity, which is proportional to amount of contrast material, and relaxation rates that are indicative of interaction with the surrounding tissue [62–67].

PFCs can be utilized for indirect observation of molecular-level changes in critical biological molecules or environmental factors, facilitated by the presence of PFCs and changes in the ^{19}F NMR response. Fluorinated compounds, for instance, are sensitive to changes in pH, Na^+, Ca^{2+} and Mg^{2+} concentrations, as well as oxygen, and respond to their micro-environment either by changes in spin-lattice (R_1) relaxation, or chemical shift of the NMR spectrum [62–64, 66–72]. The interplay of PFCs with their surroundings has been exploited in early applications of ^{19}F MRI, where the oxygen dissolving capability of perfluorocarbon allowed quantification of oxygen partial

pressure (pO_2) in a non-invasive manner and map different areas of the tumorous tissue [39], [70–73]. Alongside mapping pO_2, the very presence of PFC were observed to induce hypoxia, and therefore inhibit tumor growth significantly, ultimately contributing to the success of treatment [62–78].

In the emerging fields of molecular imaging and theranostics, PFCs are used for the direct detection and quantification of ^{19}F NMR signal in a broad spectrum of applications, including functional lung imaging employing gases and liquid PFCs, the surveillance of fluorinated pharmaceuticals, the tracking of cells and therapeutic agents using PFC emulsions, and the imaging of lesions via targeted PFC emulsions. Among these, ligand-targeted tumor imaging dates back to the late 1980s when Shimizu et al. [79] used FTBA (perfluorotributylamine) emulsion conjugated with anticarcinoembryonic antigen (anti-CEA) antibody to target tumors in small mice and image at a field strength of 2 T using ^{19}F spectroscopy both *in vivo* and in excised tumors.

The use of PFC emulsion nanoparticles as targeted contrast agent started to gain traction in early 2000s in research, where targeted PFC nanoparticles were used as ^{1}H contrast media rather than fluorine-19 tracers [80–83]. The inherent physico-chemical characteristics of PFCs are rendered exceptionally suitable for the synthesis of nanoparticles in the form of water-soluble emulsions, enveloped within a lipid shell. This lipid membrane provided an optimal scaffold for the functionalization of the nanoparticles. It facilitated the incorporation of specific ligands targeting pathological lesions, tumors, and other anomalies, as well as the integration of paramagnetic ion complexes. These complexes were instrumental in modifying the T_1 and T_2 relaxation properties of ^{1}H, thereby enhancing the contrast and improving the visualization of the targeted areas during MRI [55], [81–83].

This line of work led to more specialized studies using functionalized PFC emulsions. In 2000, Yu et al. [84] synthesized emulsions of perfluorodichlorooctane (PFDCO), by integrating gadolinium-diethylenetriamine pentaacetic acid-bis(oleate) (Gd-DTPA-BOA) within the lipid bilayer. The emulsions were further modified by attaching biotinylated anti-fibrin monoclonal antibodies to target fibrin present on human thrombi. The work presented results of ^{1}H MRI at 4.7 T *in vitro* using fibrin-rich cloths. In these, the areas of the cloths treated with the emulsions showed clear variations in T_1 and T_2 relaxation times. Following this study, Flacke et al. [85] used similar PFCs to target canine fibrin. The results, obtained at 1.5 T, yielded an elevated CNR between the clot and the surrounding blood in the treated clots, indicating the potential clinical utility of this approach.

To enhance the specificity and sensitivity of fibrin targeting, Winter et al. [86] investigated the relaxivity of thrombi treated with two different types of emulsion nanoparticles, each characterized by distinct gadolinium chelates: Gd-DTPA-BOA and Gd-DTPA-PE. The work identified a significant increase in R1 relaxation at the clot's surface when utilizing Gd-DTPA-PE, indicating improved detection sensitivity. In a subsequent study, Winter et al. [87] targeted atherosclerosis in rabbits by employing perfluorooctylbromide (PFOB) emulsion nanoparticles carrying Gd-DTPA-BOA and an Arg-Gly-Asp mimetic targeting $\alpha_v\beta_3$-integrin, a protein associated with angiogenesis in early-stage atherosclerosis. In their findings, a pronounced increase in CNR during ^{1}H MRI at 1.5 T was observed in areas of angiogenesis in the abdominal aortic wall among rabbits administered the targeted emulsion. This work was followed by another study where PFCs functionalized to target $\alpha_v\beta_3$-integrin were used to image angiogenesis in early-stage atherosclerosis [88], incorporating fumagillin in the lipid layer of PFC nanoparticles. These were observed to inhibit angiogenesis, resulting in a decreased CNR in rabbits treated with these nanoparticles, showcasing the potential of such innovations in targeted therapeutic interventions [89].

Building on prior work with functionalized PFC emulsions, Lanza et al. [90] combined ^{1}H MRI and ^{19}F spectroscopy to investigate emulsified perfluorooctylbromide (PFOB) nanoparticles targeted to vascular smooth muscle cells (VSMCs) using a biotinylated tissue factor antibody. Since VSMC proliferation and migration contribute to restenosis after coronary angioplasty, the nanoparticles were loaded with doxorubicin or paclitaxel to inhibit these processes. T_1-weighted ^{1}H imaging at 4.7 T visualized the emulsion-induced contrast, while ^{19}F spectroscopy confirmed nanoparticle attachment to VSMC surfaces. This dual-modality approach enabled precise assessment of both localization and therapeutic potential.

Morawski et al. [91] extended the study on VSMCs imaging using ^{19}F spectroscopy to quantify nanoparticles that were bound to target surface. In this, human plasma clots were treated with emulsions containing a mixture of perfluoro-15-crown-5-ether (PFCE) and safflower oil. The clots were then visualized using ^{1}H and ^{19}F imaging at 4.7 T, and the ^{19}F signal was quantified by comparing the ^{19}F signal to a calibration curve that was obtained on a series of dilution samples of the PFCE emulsion nanoparticles. The work demonstrated that the ^{19}F signal was linearly correlated to the amount of Gd^{3+}, hence, the number of nanoparticles.

In parallel with these developments, Ahrens et al. utilized ^{19}F hot-spot imaging to monitor dendritic cells (DCs) labeled with perfluoropolyether (PFPE) emulsions [92]. DCs can be used as immunotherapeutics for cancer and autoimmune diseases and

tracking of their migration within the body is crucial for evaluating the effectiveness of treatments. This study successfully visualized DCs injected intravenously into the quadriceps of mice and traced their migration to draining lymph nodes using ^{19}F MRI at a high field strength of 11.7 T, while simultaneously using ^{1} H MRI to anatomically locate cells.

Building on this approach, Srinivas et al. [93] applied similar PFPE nanoparticles to label and track T-cells in non-obese diabetic mice. Their work involved acquiring ^{19}F MRI at 11.7 T, which provided insights into the early homing behavior of the T-cells within the pancreas. Furthermore, Srinivas and his team developed a method to quantify migrating T cells directly from the MR images ^{19} F. They established that the number of cells had a linear correlation with the intensity of the ^{19}F MRI signal. This innovative approach to quantification marks a significant stride in the field, offering a robust method for tracking and quantifying immune cells, thereby enhancing the understanding and potential treatment strategies for various immunological conditions.

The scope of ^{19}F MRI in cell tracking has expanded to include noninvasive labeling and monitoring of immune cells both *ex vivo* and *in vivo*. This technique has been effectively utilized to understand the dynamics of various conditions such as myocardial infarction and myocarditis [94], atherosclerosis [95], pneumonia [96], arthritis [97], and tumors infiltrated by macrophages [98] across different animal models.

The key advantage of ^{19}F MRI is the complete absence of background signals, enabling highly precise localization and quantification of cell numbers—crucial for devising treatment strategies and tracking disease progression. Leveraging this, Constantinides et al. [99] used ^{19}F MRI at 9.4 T to monitor intra-cardiac injections of cardiac progenitor cells (CPCs) labeled with perfluoro-crown-ether nanoparticles (PFCE-NP), and quantified label uptake facilitated by DNA transfection [100]. Similarly, Gaudet et al. [101] demonstrated the *in vivo* tracking of PFPE-emulsion-labeled human mesenchymal stem cells (hMSCs) and showed a strong linear correlation between implanted and detected cell numbers based on 3D ^{19}F MRI.

Along the same line as cell tracking, the high specificity of the ^{19}F signal generated by PFCs has also been utilized in noninvasive quantification of tissue drug concentrations during targeted therapies. This advancement has facilitated the development of engineered nanoparticles designed to transport highly potent drugs directly to specific cell populations marked by distinct disease biosignatures. Among the first of such work, Rapoport et al. have developed drug-loaded PFC emulsions stabilized by biodegradable amphiphilic block copolymers and used these to deliver lipophilic ther-

apeutic agents to solid tumors while simultaneously enabling the monitoring of their biodistribution *in vivo* by means of ^{19}F MRI [60], [102–104].

Beyond the traditional use of perfluorocarbons (PFCs), a variety of alternative compounds have been effectively employed for quantitative ^{19}F MRI to address specific challenges and expand its diagnostic capabilities. For instance, in functional lung imaging where ^{1}H MRI faces limitations due to low proton density, respiratory motion, and susceptibility artifacts from air-tissue interfaces, fluorinated gases like SF_6, C_2F_6, CF_4, and C_3F_8 have emerged as valuable agents [105–111]. Their utilization overcomes these inherent obstacles, providing clearer and more reliable imaging of lung structures and functions.

Higuchi et al. [112] demonstrated the use of fluorinated amyloidophilic probes for detecting amyloid β plaques in a mouse model of Alzheimer's disease. This application became particularly relevant where traditional T_1 and T_2 weighted ^{1}H MRI proved less reliable, offering a more targeted and effective approach for imaging the plaques. Porcari demonstrated the efficacy of ^{19}F MRI in tracing the biodistribution and pharmacokinetics of ^{19}F-labeled boronophenylalanine, a compound used in Boron Neutron Capture Therapy (BNCT) for treating rat glioma tumors [113], [114]. The findings suggested that the dynamic assessment of boronophenylalanine concentration within tumors could significantly improve BNCT outcomes. By providing estimations of the optimal timing for neutron irradiation, this technique promises to enhance the precision and effectiveness of cancer treatments [115].

An early and compelling application of non-PFC compounds in the field of oncology was the *in vivo* monitoring of 5-fluorouracil (5-FU), a widely used fluorine-containing chemotherapeutic agent, using ^{19}F NMR and MRS techniques [116–120]. These studies utilized advanced NMR and data analysis techniques to extract the NMR response from the low tissue concentration of 5-FU, a necessity given the limitations imposed by clinical doses. Through these investigations, it was quantitatively established that the sensitivity of ^{19}F MRS and MRI is primarily dependent on the number of fluorine atoms present in the compound and the administered dose in addition to the conventional factors that determine the SNR, such as magnetic field strength and detector design. These studies laid the groundwork for applications where combination of 5-FU with PFC nanoemulsions was used to image and quantify biodistribution of the therapeutic payload *in vivo* using MRS and MRI more effectively [121].

2.2 Technical and Physical Challenges

Despite its significant potential in molecular imaging and targeted diagnostics, ^{19}F MRI presents several technical and physical challenges that have limited its widespread clinical adoption. One of the most fundamental limitations is the intrinsically low signal intensity in ^{19}F MRI, resulting from both biological and physical constraints. Specifically, the amount of fluorinated tracer that can be safely administered *in vivo* is tightly regulated by toxicity thresholds and pharmacokinetics, leading to relatively low concentrations of ^{19}F nuclei in the body [122], [123]. In contrast to ^{1}H MRI, which benefits from the ubiquitous presence of hydrogen in water and fat, ^{19}F MRI must contend with sparse spin populations and reduced spin density in target tissues.

While ultra-high-field MRI systems with field strengths typically higher than 6.0 T can partially address these limitations by boosting nuclear polarization and thereby enhancing the signal level of fluorinated probes, such systems remain largely confined to pre-clinical research. Most clinical imaging is performed at 1.5 T or 3.0 T, where SNR is significantly lower. As a result, signal detectability often becomes a limiting factor for ^{19}F MRI in routine clinical settings, particularly in quantitative imaging or in detecting small or deeply located fluorinated targets [124]. This limitation is further exacerbated in longitudinal or multi-parametric studies, where repeated acquisitions must remain within clinically acceptable scan durations.

Additionally, commonly used PFCs, such as perfluorooctylbromide (PFOB) and perfluoro-15-crown-5-ether (PFCE), exhibit long longitudinal relaxation times (T_1), approximately 1200–1500 ms for PFOB and about 1000 ms for PFCE at 3.0 T [125–127]. These prolonged T_1 values necessitate longer repetition times (TR) for sufficient magnetization recovery, which in turn lengthens scan durations and reduces imaging throughput [60], [125], [128], [129]. In time-constrained imaging protocols, incomplete longitudinal recovery results in saturation and loss of signal fidelity, particularly for compounds with multiple fluorine resonances.

Maintaining adequate SNR under these constraints often requires extended acquisitions, which may not be clinically practical. Moreover, saturation effects resulting from insufficient TR can further degrade SNR and compromise image quality. In response, efforts have focused on developing novel PFC compounds with intrinsically shorter T_1 values [130]. A complementary strategy involves incorporating paramagnetic additives, particularly Gd^{3+} chelates, into the lipid shell of emulsion nanoparticles to accelerate longitudinal relaxation and improve imaging efficiency [125, 131, 132]. How-

ever, such modifications introduce new concerns regarding toxicity, biodistribution, and regulatory approval, which limit their current clinical applicability.

Short apparent T_2 values and homonuclear J-coupling interactions among fluorine nuclei present additional obstacles. These phenomena broaden spectral lines, degrade temporal signal coherence, and reduce the effectiveness of signal averaging [122], [130], [133]. The impact of these relaxation dynamics is particularly pronounced in multi-peak agents like PFOB, where different fluorine environments exhibit distinct relaxation behavior, complicating both pulse sequence optimization and post-processing strategies. Even when ^{19}F signal levels are adequate, these factors can impair spectral resolution and reduce the accuracy of quantification and localization—especially in acquisition schemes that rely on coherent time-domain signals such as free induction decay (FID)-based or echo-train methods.

Adding to these challenges is the spectral complexity of many fluorinated probes, which often exhibit multiple, widely spaced resonances. This characteristic gives rise to chemical shift artifacts that undermine accurate spatial encoding in frequency-based acquisitions. Such artifacts can manifest as signal displacement, blurring, or ghosting, particularly in conventional gradient echo sequences with limited bandwidth. The following section explores the physical basis of this artifact and reviews methods for its mitigation in the context of broadband and spectrally inclusive imaging sequences.

2.3 Chemical Shift Artifacts in ^{19}F MRI

The broad chemical shift dispersion characteristic of many fluorinated compounds poses one of the most fundamental obstacles in ^{19}F MRI. Unlike ^{1}H nuclei, which typically resonate within a narrow frequency range due to relatively uniform chemical environments, PFCs often contain multiple chemically distinct fluorine atoms. This results in complex NMR spectra with widely spaced resonance peaks [41], complicating both spatial encoding and image reconstruction.

Chemical shift in MRI arises from variations in Larmor frequency that reflect differences in the local magnetic environment of nuclei. Based on the frequency encoding principles discussed in Appendix A.7.1, the frequency offset for a nucleus at chemical shift δ is given by:

$$\Delta\omega_c = \gamma\delta B_0 \tag{2.1}$$

where γ is the gyromagnetic ratio and B_0 is the static magnetic field strength. When a frequency-encoding gradient G_x is applied, the frequency range per pixel becomes:

$$\Delta\omega_x = \gamma G_x \Delta x \tag{2.2}$$

and the resulting spatial displacement of signals due to chemical shift is:

$$\Delta x_c = \frac{\delta B_0}{G_x} \tag{2.3}$$

In conventional ^{1}H MRI, the fat–water shift of about 3.5 ppm using a readout gradient strength of 10 mT/m at 3.0 T corresponds to a displacement of:

$$\Delta x_c = \frac{3.5 \times 10^{-6} \times 3.0}{10 \times 10^{-3}} = 1.05 \text{ mm} \tag{2.4}$$

At a resolution of 1 mm, such displacement is generally tolerable. However, in high-resolution imaging with sub-millimeter voxel sizes—such as a 256 mm $\times$ 256 mm field of view (FOV) sampled on a 512$\times$512 matrix. This shift equates to approximately two pixels.

One effective method for reducing chemical shift displacement is to increase the pixel bandwidth by applying a stronger readout gradient. This reduces the spatial misregistration caused by frequency offsets. For instance, using a readout gradient strength of 40 mT/m, the displacement corresponding to a 3.5 ppm shift at 3.0 T becomes:

$$\Delta x_c = \frac{3.5 \times 10^{-6} \cdot 3.0}{40 \times 10^{-3}} = 0.26 \text{ mm} \tag{2.5}$$

Being smaller than the pixel size, this displacement effectively mitigates chemical shift artifacts in ^{1}H imaging.

In ^{19}F MRI, however, the chemical shift separation between resonances can range from 5 to 100 ppm. For example, in perfluorooctyl bromide (PFOB), the chemical shift between CF_2 and CF_3 groups is approximately 60 ppm. For a 3.0 T field and a readout gradient of 40 mT/m the chemical shift displacement would become:

$$\Delta x_c = \frac{60 \times 10^{-6} \cdot 3.0}{40 \times 10^{-3}} = 4.5 \text{ mm} \tag{2.6}$$

Such a large displacement can cause severe spatial misregistration and ghosting artifacts when the spectral width of a compound exceeds the pixel bandwidth [41], [60],

[134–139]. Pixel bandwidth, defined as the frequency range encoded per voxel along the frequency-encoded axis, sets a hard limit on the amount of spectral content that can be spatially resolved during image reconstruction. When the intrinsic frequency spread of a fluorinated compound surpasses this bandwidth, signals from distinct resonances are projected onto incorrect spatial locations, resulting in ghosting or blurring. These artifacts degrade anatomical fidelity, hinder accurate quantification, and often give rise to displaced or ghosted images of the original signal source. An example of this spatial distortion is shown in Figure 2.1, where multiple peaks of a compound exceed the encoding bandwidth and become mislocalized across the image domain.

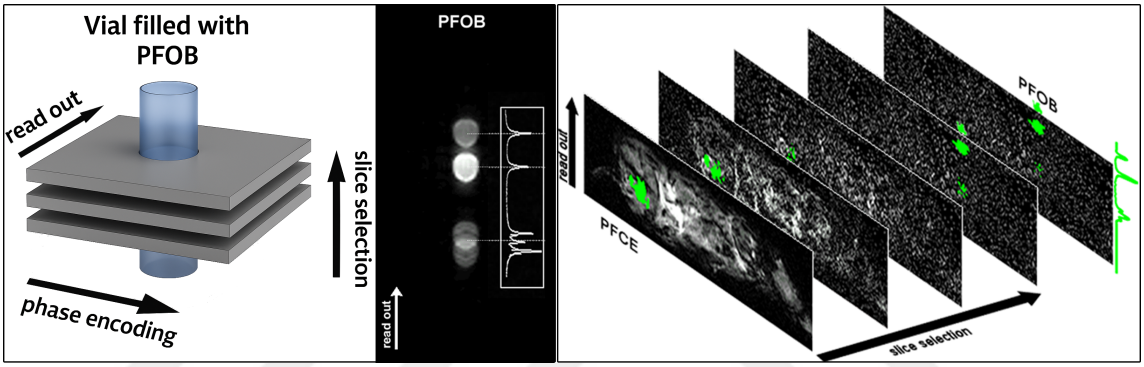

Figure 2.1 The complex NMR spectrum of PFOB results in ghosting artifacts in a frequency encoded ^{19}F image (left), which may lead to incorrect localization of the source *in vivo* (right).

One strategy for minimizing such artifacts is the use of fluorinated probes with spectrally simple signatures—such as perfluoro-15-crown-5-ether (PFCE), perfluoro polyether (PFPE), or their derivatives—which exhibit a single narrow resonance or tightly grouped multiplet [41], [140]. These agents suppress intra-molecular chemical shift dispersion and reduce ghosting in frequency-encoded acquisitions, making them particularly suited for hot-spot imaging and semi-quantitative tracking. However, their simple spectra often come at the cost of limited biocompatibility, poor metabolic clearance, or suboptimal formulation. Many cannot be readily emulsified or encapsulated, exhibit limited biodegradability, or accumulate in the reticuloendothelial system—factors that hinder clinical translation [65], [141–144].

Alternatively, acquisition strategies can be tailored to isolate individual resonances. Spectrally selective RF pulses can confine excitation to a single peak [145], as depicted in Figure 2.2. Additionally, contrast-weighting schemes exploiting T_1 differences may preferentially emphasize a specific resonance [146]. These strategies are particularly useful in applications where accurate localization of a single fluorinated species is critical, such as targeted drug delivery or immune cell tracking.

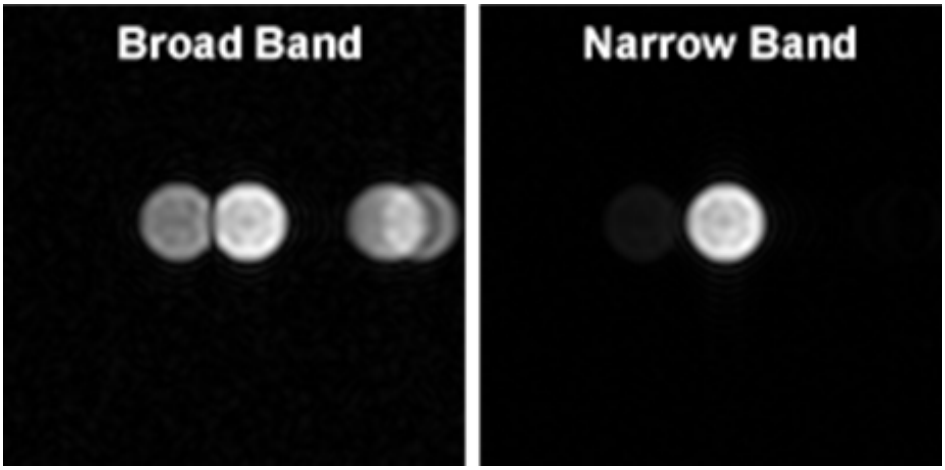

Figure 2.2 Broadband excitation versus Narrowband (*spectrally selective*) excitation.

Other approaches include simultaneous multi-slice excitation [135], chemical shift encoded multi-echo imaging [147], and post-processing approaches such as Dixon-type separation or deconvolution [134], [136], [138], [148].

Collectively, these methods offer partial solutions for managing spectral complexity in ^{19}F imaging, but they are often limited to specific compounds or experimental conditions. Spectrally selective pulses require precise frequency calibration. Relaxation-based methods depend on favorable T_1 dispersion. Post-processing methods are computationally intensive and sensitive to noise, and may yield inaccurate results in the presence of motion, field inhomogeneities, or signal overlap. Moreover, all these strategies remain inherently limited by the spectral resolution and bandwidth of the acquisition system [41], [143–145].

An alternative and more generalizable solution is magnetic resonance spectroscopic imaging (MRSI), which directly resolves the full NMR spectrum at each voxel through an additional spectral encoding dimension. By treating chemical shift as an independent axis, which is orthogonal to the spatial axes, MRSI separates resonances explicitly in the reconstructed spectrum, thereby eliminating spatial misregistration, chemical shift displacement, and ghosting artifacts at their root. This makes MRSI an inherently chemically agnostic framework: it imposes no restriction on the number, spacing, or relative intensity of resonance peaks, and does not require frequency-selective excitation, relaxation weighting, or prior knowledge of the agent's spectral profile. As a result, MRSI provides a robust platform for accurate, artifact-free ^{19}F imaging, particularly in applications involving spectrally complex contrast agents.

2.4 Summary

Fluorine-19 MRI presents a powerful and highly specific imaging modality, owing to the unique NMR properties of the ^{19}F nucleus and the absence of endogenous signal in biological tissues. The development and functionalization of PFC emulsions have enabled a wide range of applications, from tumor imaging and vascular targeting to immune cell tracking and functional lung imaging. The historical trajectory of ^{19}F MRI underscores its transition from a technical curiosity to a robust platform for molecular imaging and theranostics.

Despite these advancements, ^{19}F MRI remains challenged by physical and technical limitations, including low signal intensity, long relaxation times, and complex spectral signatures that give rise to chemical shift artifacts. These challenges constrain both sensitivity and spatial accuracy, especially in low-concentration or multi-resonant fluorinated agents. Solutions such as paramagnetic relaxation enhancement, probe selection, and spectral filtering offer partial relief, but often at the cost of generalizability, clinical feasibility, or robustness in complex imaging environments.

Among these strategies, MRSI stands out as a chemically agnostic framework that fully resolves chemical shift dimensions and eliminates spatial misregistration. As the next chapter will explore in detail, MRSI provides a robust foundation for developing advanced ^{19}F imaging sequences optimized for detectability, accuracy, and clinical translatability.

3. MAGNETIC RESONANCE SPECTROSCOPIC IMAGING

MRSI, also known as Chemical Shift Imaging (CSI), is an advanced MRI technique that combines spatial and spectral encoding to produce localized NMR spectra across an imaging volume. While conventional MRI generates contrast based on relaxation properties (T_1, T_2) or proton density, MRSI resolves the full NMR spectrum at each voxel, enabling identification and quantification of distinct chemical species based on their resonance frequencies [148], [149]. MRSI can be viewed as a natural extension of single-voxel magnetic resonance spectroscopy (MRS), providing spatially resolved spectra across an entire field of view rather than a single anatomical location. This makes it especially well-suited for probing heterogeneous tissues or mapping distributions of metabolic or exogenous compounds, where localized chemical information is essential.

The technique is applicable to a range of NMR-sensitive nuclei, including ^{1}H, phosphorus (^{31}P), carbon-13 (^{13}C), and ^{19}F. Each nucleus offers unique insights: ^{31}P spectroscopy is used to monitor endogenous energy metabolites such as ATP, phosphocreatine (PCr), and inorganic phosphate, providing valuable information on cellular energetics [150]. ^{13}C-labeled substrates trace metabolic pathways, especially when hyperpolarization is used to enhance sensitivity. In contrast, ^{19}F is absent from biological tissue and therefore must be introduced via fluorinated drugs or perfluorocarbon-based contrast agents, enabling highly specific, background-free imaging.

A major challenge in ^{19}F MRI is its susceptibility to chemical shift artifacts. Fluorinated compounds, especially PFCs, often exhibit broad spectral dispersion that exceeds the acquisition bandwidth of conventional frequency-encoded imaging. This leads to spatial misregistration and ghosting artifacts along both the readout and slice-select directions [41], [60], [134–139]. These artifacts can severely degrade spatial fidelity, particularly in high-resolution or quantitative applications.

MRSI resolves these limitations by encoding chemical shift along an independent spectral dimension. This eliminates the misregistration seen in conventional imaging and allows accurate representation of even complex fluorinated compounds with multiple, widely spaced resonances. As a result, MRSI preserves both spatial and spectral fidelity, enabling robust and artifact-free ^{19}F imaging [3], [14].

3.1 Principles of Magnetic Resonance Spectroscopic Imaging

The core principle of spectroscopic imaging lies in its ability to encode both spatial and spectral information simultaneously, resulting in multidimensional datasets that reflect the distribution and chemical environment of NMR-active species. This is achieved by applying phase-encoding gradients along two or three orthogonal spatial axes while recording the time-domain signal, which is typically as a FID or a spin echo (A detailed explanation of FID, echo formation, and spatial encoding is provided in Appendix A). The acquired signal captures both spatial localization and spectral evolution, enabling voxel-wise reconstruction of resonance frequencies associated with distinct chemical species.

This dual encoding is especially powerful in applications involving exogenous tracers or metabolites with well-separated resonance frequencies. In ^{19}F MRI, for instance, fluorinated compounds often exhibit broad spectral dispersion due to multiple chemically distinct fluorine environments. Spectroscopic imaging separates these components without inducing the spatial misregistration artifacts, which are commonly referred to as chemical shift artifacts or ghosting, that frequently affect conventional frequency-encoded techniques.

The spectroscopic imaging signal can be expressed mathematically as:

$$S(\vec{k}, t) = \int_{\text{object}} \int_{\delta} \rho(\vec{r}, \delta)\, e^{-i2\pi\vec{k}\cdot\vec{r}}\, e^{i\delta\omega_0 t}\, d\delta\, d\vec{r} \tag{3.1}$$

where $\rho(\vec{r}, \delta)$ is the spin density as a function of spatial location $\vec{r}$ and chemical shift δ, and ω_0 is the Larmor frequency. The spatial term $2\pi\vec{k} \cdot \vec{r}$ corresponds to phase encoding, while $\delta\omega_0 t$ captures chemical shift evolution. The spatial-spectral image is reconstructed using an inverse Fourier transform in both domains:

$$\rho(\vec{r}, \delta) = \int_{\vec{k}} \int_{t} S(\vec{k}, t)\, e^{i2\pi\vec{k}\cdot\vec{r}}\, e^{-i\delta\omega_0 t}\, dt\, d\vec{k} \tag{3.2}$$

This yields a complete NMR spectrum at each voxel, enabling localized chemical analysis. Such multidimensional representations support diverse applications in diagnostic imaging, pharmacokinetics, and metabolic profiling.

MRSI can be implemented in two-dimensional (2D) or three-dimensional (3D) configurations, depending on spatial coverage and time constraints.

3.1.1 2D Spectroscopic Imaging

Two-dimensional Chemical Shift Imaging (2D CSI) acquires spatially resolved spectra over a single slice by combining in-plane phase encoding with time-domain spectral encoding. The temporal signal can be acquired using either an FID or spin echo sequence, as illustrated in Figure 3.1.

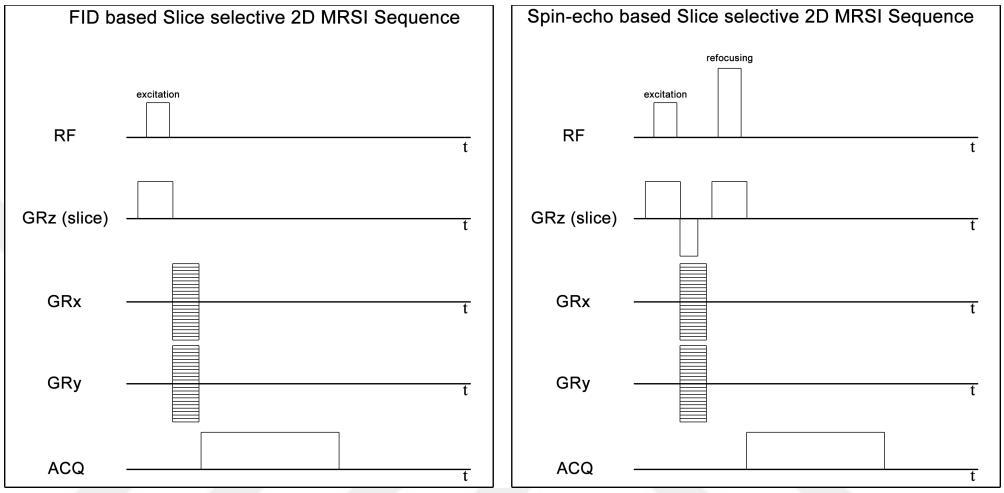

Figure 3.1 Commonly used 2D MRSI sequences with slice selection. 2D FID sequence (left) consists of an excitation pulse accompanied by a slice selection gradient, phase encoding and an acquisition window. 2D Spin-echo sequence (right) consists of an excitation pulse and refocusing pulse that are paired with slice selective gradients, phase encoding and an acquisition window.

The acquired signal reflects the joint spatial encoding along the x and y directions and spectral encoding via time evolution:

$$S(k_x, k_y, t) = \iint_{\text{FOV}} \int_{\delta} \rho(x, y, \delta)\, e^{-i2\pi(k_x x + k_y y)}\, e^{i\delta\omega_0 t}\, d\delta\, dx\, dy \tag{3.3}$$

The spatial-spectral distribution $\rho(x, y, \delta)$ is reconstructed by applying a multi-dimensional inverse Fourier transform:

$$\rho(x, y, \delta) = \iint_{k_x, k_y} \int_{t} S(k_x, k_y, t)\, e^{i2\pi(k_x x + k_y y)}\, e^{-i\delta\omega_0 t}\, dt\, dk_x\, dk_y \tag{3.4}$$

This reconstruction yields a full NMR spectrum at each voxel within the selected slice, allowing spatially resolved analysis of the chemical composition. 2D MRSI is particularly useful in applications where the chemical information is localized to a thin slab of tissue, as illustrated in Figure 3.2.

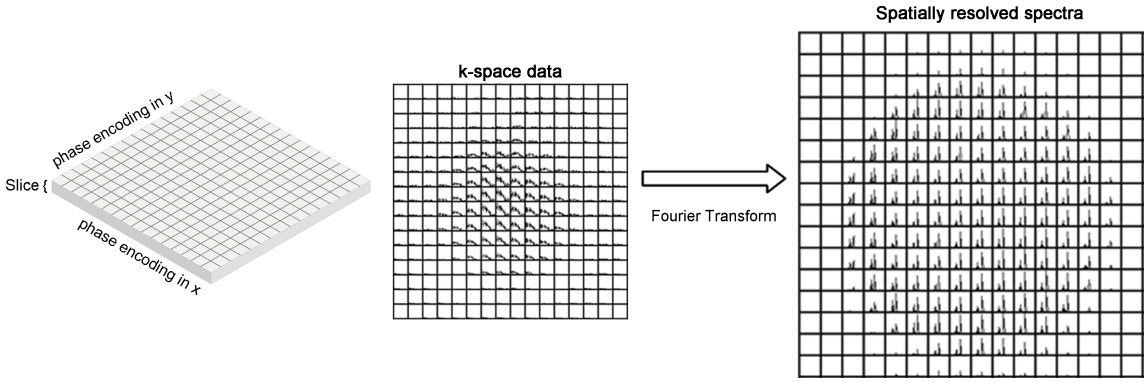

Figure 3.2 MRSI encodes k-space with 2D phase encoding, and Fourier transformation over spatial and temporal axes produces voxel-wise spectra reflecting local chemical composition.

3.1.2 3D Spectroscopic imaging

A three-dimensional spectroscopic dataset can be acquired using a slice-by-slice method as shown in Figure 3.3. In this approach, the imaging volume is segmented into slices through frequency encoding, and each slice is subsequently encoded via two-dimensional phase encoding. The 3D imaging process through slice selection can be executed using either a single RF pulse FID sequence or a multi-pulse spin-echo sequence. This process yields a dataset that essentially consists of a stack of two-dimensional spatially resolved spectra, which is then converted into slices of a three-dimensional object using Fourier transformation along the phase encoding directions and spectral integration along the chemical shift axis.

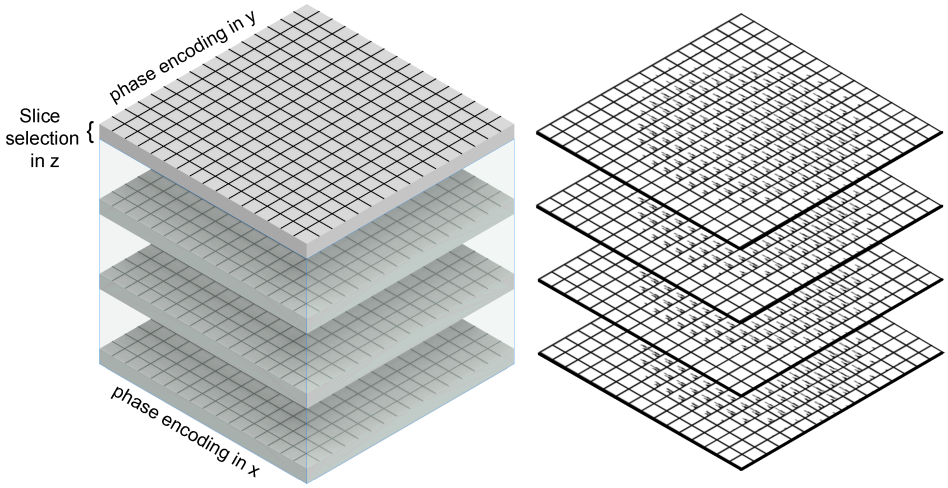

Figure 3.3 A 3D MRSI acquisition can be realized by slice selection and 2D phase encoding (left). This scheme generates a set of slices comprising spatially resolved spectra (right).

In ^{19}F imaging, slice selection using a frequency encoding gradient poses challenges in spatial localization due to the significant chemical shift dispersion of NMR peaks in perfluorinated contrast materials, which translates into the ghosting artifact as discussed in Section 2.3.

To avoid complications imposed by the slice selection gradient, it is preferable that ^{19}F 3D spectroscopic imaging utilizes an all-phase encoded acquisition scheme, where 2D Cartesian phase encoding is extended into the third dimension and thus is also applied along the *slice* axis. In this approach, k-space along the longitudinal axis is divided into equidistant discrete encoding steps, similar to the in-plane encoding method used with 2D encoding steps (Figure 3.4). Data is obtained by populating the 3D k-space grid through uniquely encoding and acquiring an FID or echo signal for each point on the 3D grid.

For 3D MRSI with phase encoding expanded in the z dimension the corresponding signal equation becomes:

$$S(k_x, k_y, k_z, t) = \iiint_{\text{FOV}} \int_{\delta} \rho(x, y, z, \delta)\, e^{-i2\pi(k_x x + k_y y + k_z z)}\, e^{i\delta\omega_0 t}\, d\delta\, dx\, dy\, dz \tag{3.5}$$

with the spatial-spectral image recovered via:

$$\rho(x, y, z, \delta) = \iiint_{k_x, k_y, k_z} \int_{t} S(k_x, k_y, k_z, t)\, e^{i2\pi(k_x x + k_y y + k_z z)}\, e^{-i\delta\omega_0 t}\, dt\, dk_x\, dk_y\, dk_z \tag{3.6}$$

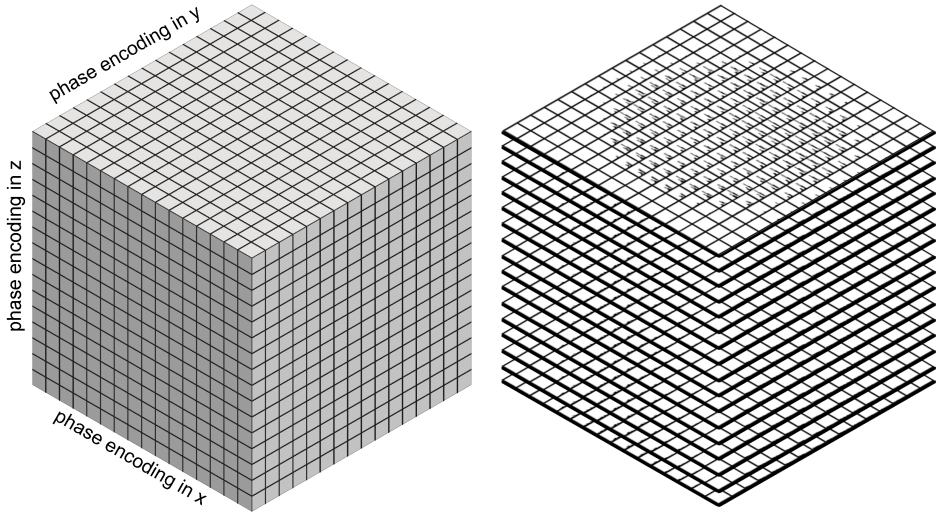

Figure 3.4 All-phase-encoded 3D acquisition encodes all axes (left) and yields a 3D spectroscopic dataset that can be converted into a set of 2D spectra by slicing along any axis (right).

3.1.3 Projection Imaging

Projection imaging is a simplified form of two-dimensional MRSI in which slice selection is omitted. Instead of encoding signal within a specific slice, the excitation pulse is applied uniformly across the entire volume, and spatial encoding is performed only in two dimensions. The resulting data represent a projection of the spin system along the unencoded (typically longitudinal) axis.

This method is illustrated in Figure 3.5, where a FID based sequence is applied without the use of a slice-selective gradient. Instead of restricting excitation to a single anatomical plane, the RF pulse is applied uniformly across the entire imaging volume, ensuring that all spins within the object contribute to the measured signal. As a result, spins along the full extent of the longitudinal axis are excited and encoded collectively, producing a volumetric response to the excitation pulse.

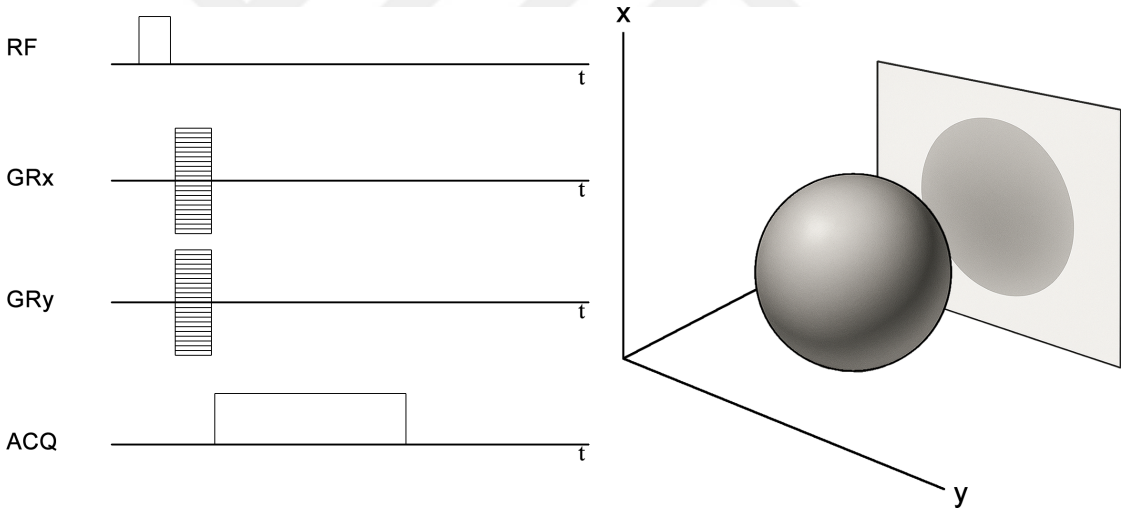

Figure 3.5 A 2D sequence without slice selection applies in-plane phase encoding only (left). Absence of slice selection generates a projection image along the non-encoded axis (right).

Spatial encoding is performed in two orthogonal in-plane directions using phase encoding gradients, typically applied along the x and y axes. The third spatial dimension, usually corresponding to the z-axis, remains unencoded, resulting in a projection of the signal along this axis. Consequently, the acquired dataset consists of FID signals that are spatially encoded in two dimensions. Following Fourier transformation, this yields a set of spatially resolved spectra, where each voxel contains a spectrum reflecting the integrated contribution of spins along the projection axis, which is the unencoded depth of the sample.

The signal equation for projection imaging is similar to that of 2D MRSI, with the distinction that $\rho(x, y, \delta)$ now represents the projection-integrated spin density:

$$S(k_x, k_y, t) = \iint_{\text{FOV}} \int_{\delta} \bar{\rho}(x, y, \delta)\, e^{-i2\pi(k_x x + k_y y)}\, e^{i\delta\omega_0 t}\, d\delta\, dx\, dy \tag{3.7}$$

where

$$\bar{\rho}(x, y, \delta) = \int \rho(x, y, z, \delta)\, dz \tag{3.8}$$

represents the projection of the 3D spin density along the z-axis.

Projection imaging is particularly useful for rapid surveying, as it enables short acquisition times and can guide subsequent high-resolution scans by identifying regions of interest based on integrated signal intensity and spectral content.

3.1.4 3D Backprojection Imaging

As an alternative to the Cartesian phase-encoded imaging schemes described in the previous sections, three-dimensional spectroscopic images can also be generated using backprojection imaging. This approach, which originally was developed for X-ray computed tomography—constructs a volumetric representation of the object by acquiring projection images at multiple orientations, as illustrated in Figure 3.6 and reconstructing the 3D spin density via the inverse Radon transform [151], [152].

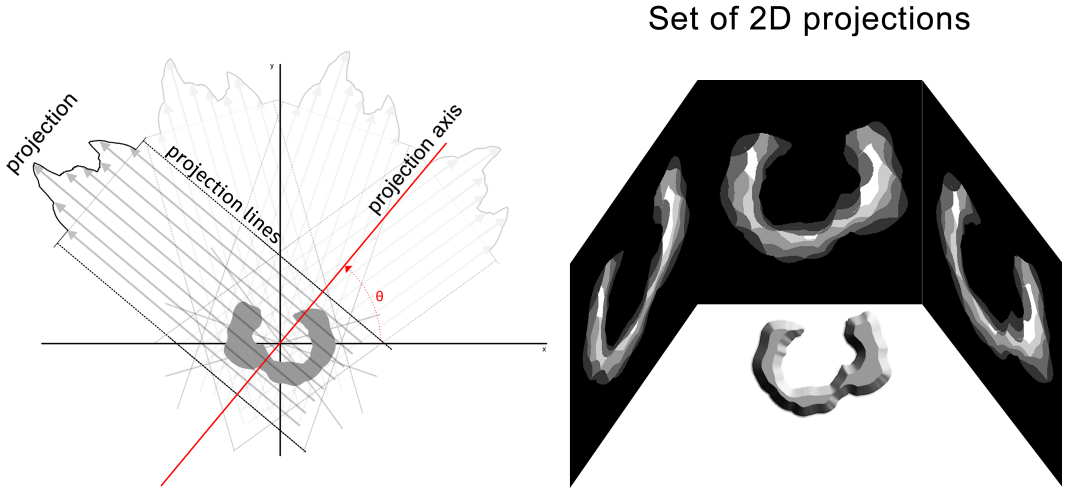

Figure 3.6 Projection imaging acquires projection lines at multiple projection angles (left), producing projection images that represent different angular views of the object (right).

The mathematical foundation of backprojection imaging lies in the Radon transform, which maps a two-dimensional spatial function $\rho(x, y)$ to a set of its line integrals taken at different angles. These integrals, represent the total signal collected along specific lines in space. For a given angle θ, the projection $P(p, \theta)$ is defined as:

$$P(p, \theta) = \mathcal{R}\{\rho(x, y)\} = \int_L \rho(x, y)\, ds \tag{3.9}$$

where p is the perpendicular distance from the origin to the line L, and the integral is taken along that line.

To illustrate the transform, consider a point source represented by a Dirac delta function $\delta(\vec{r} - \vec{r}_0)$, located at $\vec{r}_0 = (x_0, y_0)$. Its Radon transform yields:

$$\mathcal{R}\{\delta(\vec{r} - \vec{r}_0)\} = \delta(p - \vec{\mu} \cdot \vec{r}_0) \tag{3.10}$$

where $\vec{\mu} = (\cos\theta, \sin\theta)$ is a unit vector in the projection direction. This expression traces a sinusoid in (p, θ) space:

$$p = x_0 \cos\theta + y_0 \sin\theta \tag{3.11}$$

which can be recast in polar form as:

$$p = r_0 \cos(\theta - \theta_0), \quad \text{where } r_0 = \sqrt{x_0^2 + y_0^2}, \quad \theta_0 = \tan^{-1}\left(\frac{y_0}{x_0}\right) \tag{3.12}$$

For complex objects, shown in Figure 3.7, the Radon transform becomes a sum of such sinusoids, weighted by local spin density. The full set of angular projections forms a *sinogram*, which encodes all spatial information needed for reconstruction.

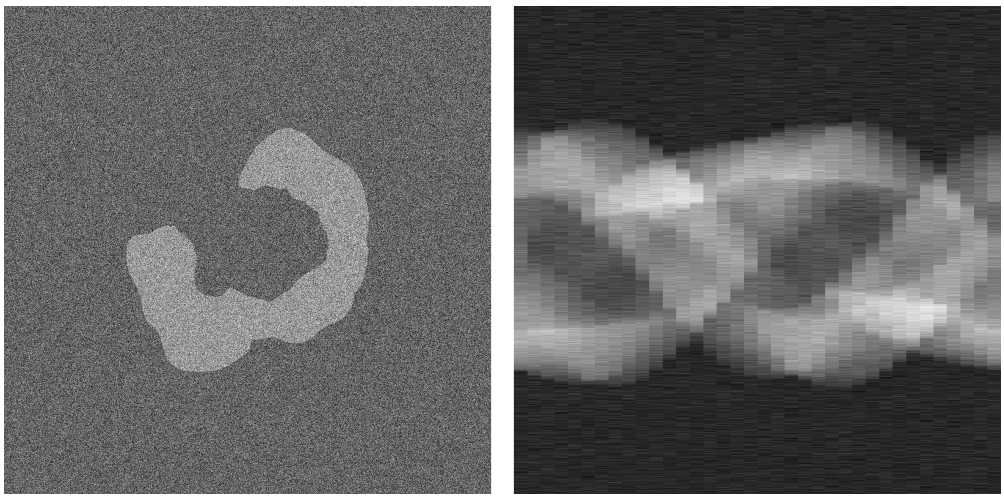

Figure 3.7 Projection imaging of a complex object (left) produces a sinogram (right), which encodes line-integral data along angular axis, for image reconstruction via the Radon transform.

Image reconstruction from the sinogram constitutes an inverse problem that can be solved using the inverse Radon transform. Among various numerical solutions, *filtered backprojection* has emerged as the standard method due to its efficiency, computational simplicity, and robust performance in practical imaging applications. This approach reconstructs the original spatial distribution by reversing the projection process, converting line integrals back into spatial intensity values.

To improve image fidelity, filtered backprojection applies a frequency-domain correction step prior to the backprojection operation. This involves convolving the projection data with a low-pass filter, typically a Shepp-Logan, Hamming, or cosine filter—which suppresses high-frequency noise that would otherwise degrade image quality.

In filtered backprojection, the reconstructed image $I(\vec{r})$ is expressed as:

$$I(\vec{r}) = \int B\{\bar{P}(p, \vec{\mu})\}\, d\vec{\mu} \tag{3.13}$$

where $B\{\cdot\}$ denotes the backprojection operator:

$$B\{P(p, \vec{\mu})\} = P(\vec{\mu} \cdot \vec{r}, \vec{\mu}) \tag{3.14}$$

and $\bar{P}(p, \vec{\mu})$ is the filtered projection obtained by:

$$\bar{P}(p, \vec{\mu}) = \int_{-\infty}^{\infty} S_p(k\vec{\mu})\, H(k)\, k^{n-1}\, u(k)\, e^{i2\pi kp}\, dk \tag{3.15}$$

here, $S_p(k\vec{\mu})$ is the Fourier transform of the projection data, $H(k)$ is the filter kernel, $u(k)$ is the Heaviside step function, and n denotes the spatial dimensionality of the image (typically 2 or 3).

In the 3D case, where volumetric reconstruction is desired, the full filtered backprojection formula becomes:

$$I(x, y, z) = \int_0^{\pi} \int_0^{\pi} \int_{-\infty}^{\infty} S_p(k, \theta, \phi)\, H(k)\, k^2\, e^{i2\pi kp}\, \sin\theta\, dk\, d\theta\, d\phi \tag{3.16}$$

Backprojection imaging is a viable and efficient strategy for ^{19}F MRSI, especially when data are acquired using 2D projection imaging without slice selection. With sufficient angular sampling, it can reconstruct high-resolution volumetric images from a reduced number of acquisitions, offering a practical alternative to time-intensive 3D Cartesian phase encoding.

3.2 Spectral Integration and Image Reconstruction

As established thus far, MRSI provides spatially resolved spectra that map the distribution of molecular targets within an imaging volume. These spectra offer insight into the chemical and physiological environment of the signal source. By integrating spectral peaks corresponding to specific resonances, MRSI enables the generation of images—often referred to as metabolite maps—that visually represent the spatial localization of molecular species of interest.

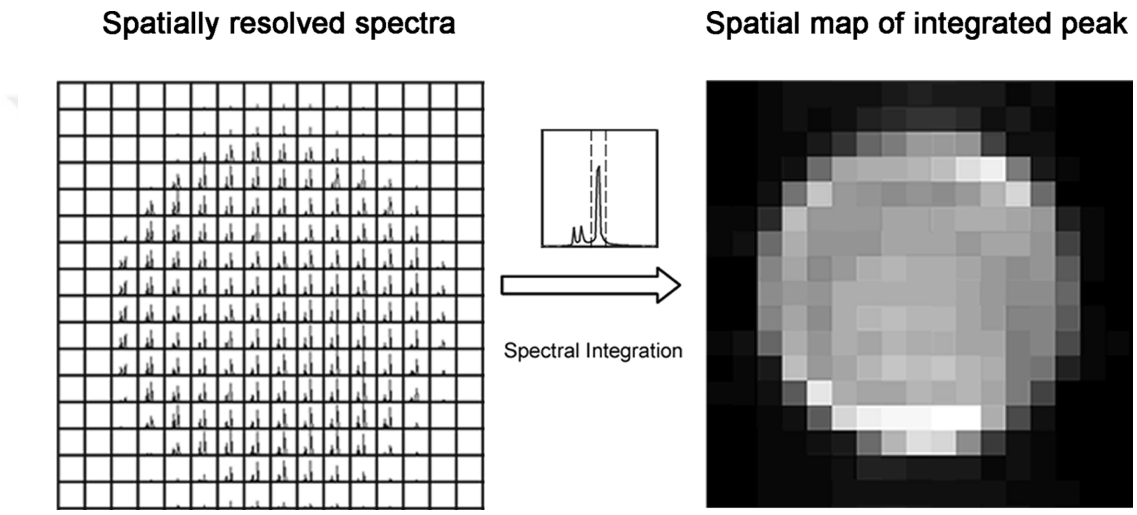

Figure 3.8 2D spectroscopic data (left) is converted into a 2D image representing the spatial distribution of spin density (right) by integrating each spectrum over a selected interval.

This image reconstruction method, known as spectral integration, involves summing the signal intensity across a defined spectral bandwidth centered on a peak of interest. The resulting integral is then assigned to the corresponding voxel in the image, as shown in Figure 3.8. Crucially, since classical MRSI relies solely on phase encoding without the use of frequency encoding gradients, the reconstructed images are inherently free of ghosting artifacts caused by chemical shift.

In ^{19}F MRSI, the SNR is often limited by the low *in vivo* concentration of fluorinated contrast agents. Therefore, optimizing the spectral integration bandwidth is essential to maximize SNR and improve signal detectability.

The NMR spectrum in MRSI typically comprises signal and noise components. The signal is modeled as a Lorentzian peak with full width at half maximum (FWHM), denoted as 2Γ, while the noise is assumed to be Gaussian white noise and accumulates

proportionally to the square root of the integrated bandwidth:

$$N \propto \sqrt{\mathrm{BW}} \tag{3.17}$$

For a Lorentzian peak centered at frequency f_0, the signal integrated symmetrically around f_0 over a total bandwidth BW is given by:

$$S = \int_{\mathrm{BW}} \frac{A\Gamma^2}{\Gamma^2 + (f - f_0)^2}\, df \propto A \tan^{-1}\left(\frac{\mathrm{BW}}{2\Gamma}\right) \tag{3.18}$$

Here, A is the amplitude of the peak. Combining the signal and noise models, the resulting SNR as a function of integration bandwidth becomes:

$$\mathrm{SNR} \propto \frac{A \tan^{-1}\left(\frac{\mathrm{BW}}{2\Gamma}\right)}{\sqrt{\mathrm{BW}}} \tag{3.19}$$

As illustrated in Figure 3.9, this relationship demonstrates that SNR increases with integration bandwidth up to a certain point, after which it begins to decline due to accumulating noise. An empirical analysis of curves calculated for various linewidths yields the following relationship for the bandwidth that maximizes SNR:

$$\mathrm{BW}_{\mathrm{optimal}} = 1.4 \times \mathrm{FWHM} \tag{3.20}$$

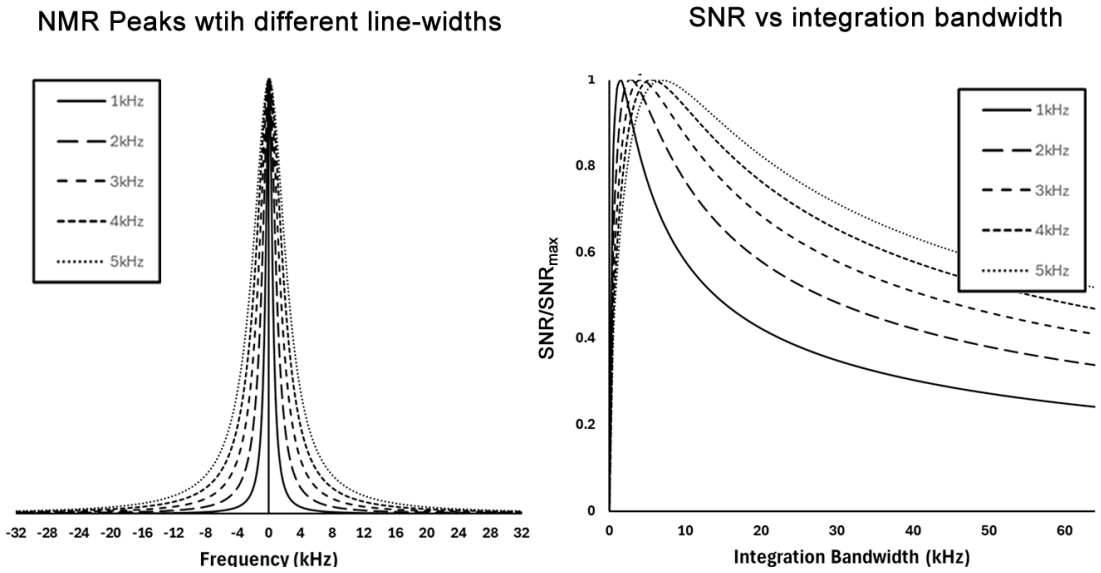

Figure 3.9 When peaks with different line-widths (left) are integrated, SNR reaches a maximum when the integration bandwidth is approximately 1.4 times the FWHM of the spectral peak (right).

3.3 Summary

MRSI extends conventional MRI by enabling simultaneous spatial and spectral encoding, allowing the acquisition of localized NMR spectra across an imaging volume. Unlike traditional methods that rely on relaxation-based contrast, MRSI provides chemically specific information at each voxel by resolving distinct resonance frequencies. This is particularly advantageous for ^{19}F MRI, where broad chemical shift dispersion often renders conventional frequency-encoded techniques prone to severe artifacts.

This chapter introduced the fundamental principles, mathematical formulation, and implementation strategies of MRSI, with particular emphasis on artifact-free acquisition schemes such as all-phase encoding, projection imaging, and backprojection reconstruction. These approaches are essential for preserving spatial fidelity in the presence of multiple ^{19}F resonances.

Spectral integration was presented as a critical step in image formation, converting multidimensional spectral data into spatial maps of molecular species. The discussion highlighted the importance of optimizing integration bandwidth to enhance signal detection while minimizing noise contributions—an essential consideration in low-SNR environments.

Taken together, these insights establish MRSI as a powerful framework for robust, chemically specific imaging of sparse or spectrally complex targets, particularly in the challenging context of ^{19}F molecular imaging.

4. PERFORMANCE METRICS FOR ^{19}F MRI

Assessing the performance of an MRI experiment requires a careful balance between image quality and scan duration. To evaluate image quality, the most fundamental metrics are the SNR and CNR, which determine the clarity and distinguishability of anatomical or molecular features within the image. High SNR ensures that acquired signals can be reliably distinguished from background noise. High CNR, on the other hand, allows for accurate differentiation between tissues or signal sources with varying intensities—critical for detecting subtle physiological differences or identifying pathological changes.

SNR is typically defined as the ratio of the mean signal magnitude to the standard deviation of background noise:

$$\mathrm{SNR} = \frac{\langle I \rangle}{\sigma} \tag{4.1}$$

CNR, similarly, quantifies the contrast between two regions A and B as the difference in their mean signal intensities normalized by the noise:

$$\mathrm{CNR}_{AB} = \left| \frac{S_A - S_B}{\sigma} \right| \tag{4.2}$$

These expressions assume that noise follows a Gaussian distribution in the complex domain—an assumption that holds true for the raw MR signal, which consists of quadrature-detected real and imaginary components. In practice, however, most MRI systems reconstruct images as magnitude images, transforming the noise distribution from Gaussian to Rayleigh. This shift introduces a non-zero mean and reduced standard deviation, which must be accounted for to ensure accurate estimation of SNR and CNR.

For a signal-free region in a magnitude image, the noise standard deviation σ can be estimated from the mean intensity μ_{noise} of the background using:

$$\sigma \approx \frac{\mu_{\mathrm{noise}}}{1.25} \tag{4.3}$$

where μ_{noise} is the average pixel value measured in the region (A detailed discussion of complex and magnitude noise statistics is provided in).

In addition to image quality, MRI protocols must also operate within practical time constraints. Patient comfort, animal welfare, and sample stability all demand

that scan durations be minimized without compromising diagnostic utility. This leads to the concept of *imaging efficiency*, which expresses the amount of usable information acquired per unit time. A compact and widely used formulation relates imaging efficiency to the signal-to-noise ratio and total scan duration:

$$\text{Imaging Efficiency} \propto \frac{\text{SNR}}{\sqrt{T_{\text{scan}}}} \tag{4.4}$$

where T_{scan} denotes the total acquisition time. For a typical 3D Cartesian scan, this is given by:

$$T_{\text{scan}} = TR \cdot N_y \cdot N_z \cdot NSA \tag{4.5}$$

Here, TR is the repetition time, N_y and N_z are the number of phase-encoding steps, and NSA is the number of signal averages. Since SNR itself depends on voxel volume, acquisition bandwidth, and signal averaging, imaging efficiency provides a normalized metric for comparing protocols across clinical or preclinical settings(Please see Appendix A.10 for a more detailed formulation of imaging efficiency.).

Although SNR, CNR, and imaging efficiency are indispensable for characterizing image quality and scan productivity, they are not always sufficient, particularly in ^{19}F MRI applications that rely on the detection of sparse signal sources such as isolated hot-spots of fluorinated contrast agents. In these scenarios, conventional metrics fail to capture the true performance of the imaging task: the ability to *visually detect* small regions of signal embedded in a noisy background.

This visual detectability is better described by the notion of *object visibility*, which quantifies the likelihood that an object can be distinguished from surrounding noise. The framework most commonly used to assess visibility is the *Rose criterion*, which specifies the minimum contrast-to-noise ratio required for an object to be reliably perceived in an image.

The remainder of this chapter explores object visibility and the Rose criterion as performance metrics tailored to ^{19}F hot-spot imaging. It also introduces a practical denoising strategy based on the Rose threshold and concludes with a discussion of image resolution and the point spread function (PSF), which influences the visual appearance and separability of small objects.

4.1 Rose Criterion and Object Visibility

For any medical imaging modality, the primary objective is to visualize a physiological region or function of interest. In MRI, this goal translates into distinguishing anatomical structures or molecular targets from background signals. While the SNR quantifies how clearly a signal stands out from random noise, and the CNR measures the intensity difference between two regions, these metrics alone may not fully capture an observer's ability to perceive a target in the image. A more suitable measure in many practical cases, particularly in low-SNR scenarios such as ^{19}F MRI,is *object visibility*.

Object visibility builds on the concept of CNR and postulates that two regions can be reliably distinguished if their contrast difference is several times greater than the standard deviation of noise. The formal basis for this visibility metric was established by Albert Rose, who developed a model to describe human visual detection performance in noisy environments [153]. The Rose criterion formalizes this idea by setting a minimum CNR for reliable detection:

$$R_c = \frac{\langle I_{\text{obj}} \rangle - \langle \text{background} \rangle}{\sigma} > 3 \tag{4.6}$$

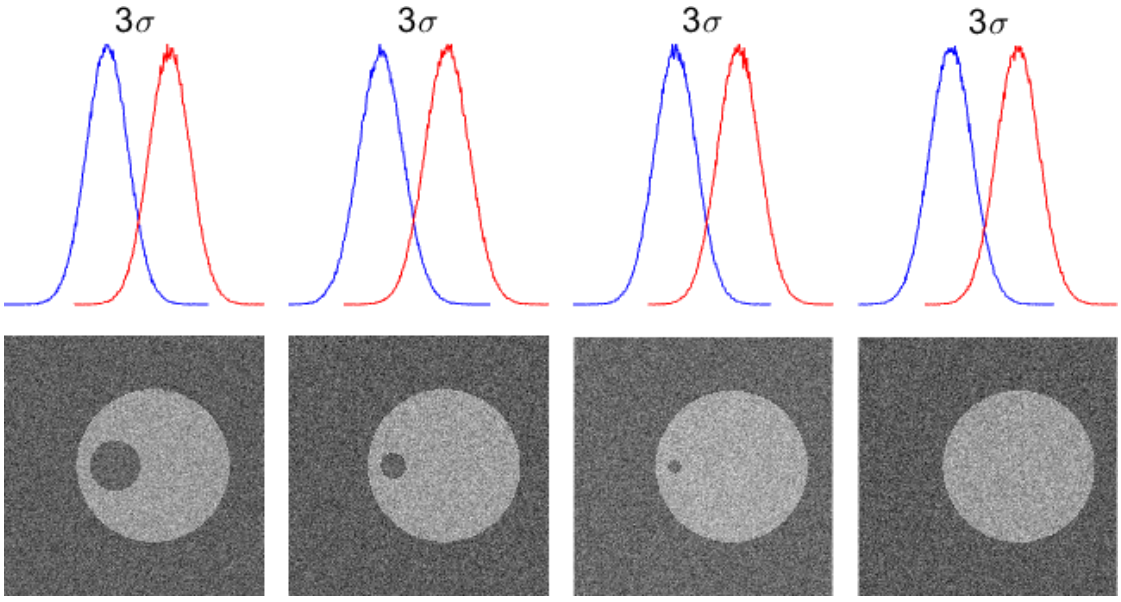

Figure 4.1 Small objects are difficult to detect even if they satisfy the Rose criterion of 3σ.

For complex-valued images corrupted by Gaussian white noise, the background signal has zero mean. However, as discussed earlier, MR images are typically reconstructed as magnitude images, which transform the noise distribution from Gaussian to Rayleigh. This results in a non-zero mean and a reduced standard deviation. In such cases, the Rose criterion must be adjusted to reflect Rayleigh-distributed noise:

$$R_c = \frac{\langle I_{\text{obj}} \rangle - \langle \text{noise} \rangle}{0.8 \cdot \langle \text{noise} \rangle} > 3 \tag{4.7}$$

While a 3σ threshold is generally accepted for visibility, actual detectability also depends on the object's spatial extent. As shown in Figure 4.1, small objects become increasingly difficult to distinguish from background noise as their size decreases—even if their signal intensity satisfies the nominal Rose criterion. This size-dependent degradation in visibility is especially relevant in ^{19}F MRI, where contrast-agent accumulation sites may span only a few voxels. Such small regions fall within the regime of small-object imaging and often require a Rose threshold higher than 3σ, as demonstrated in Figure 4.2.

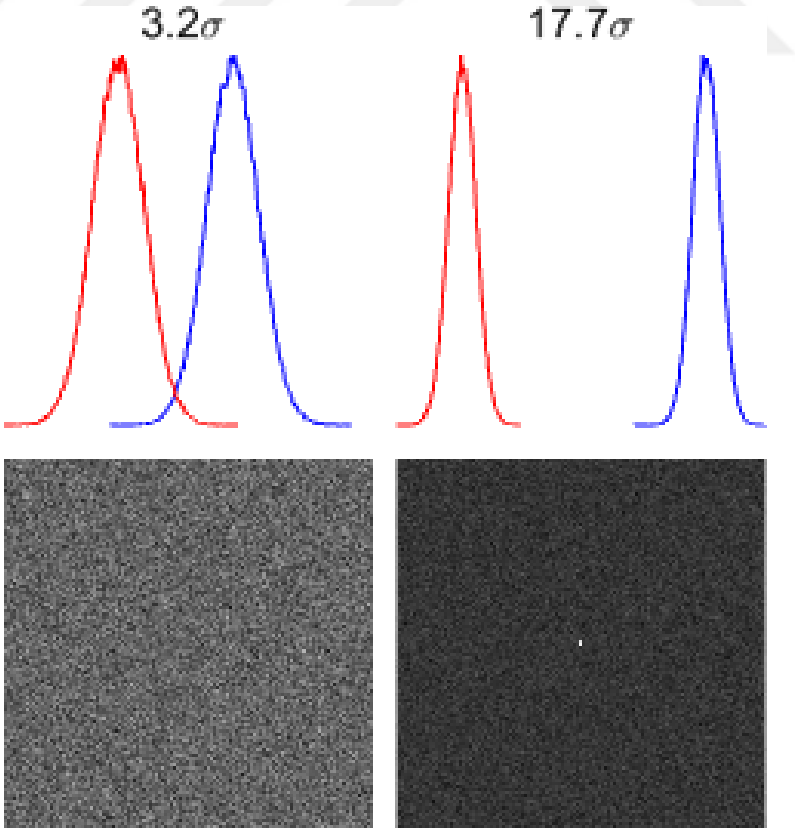

Figure 4.2 The Rose criterion of 3σ needed for object visibility is often not valid for small objects.

4.2 Denoising Using the Rose Criterion

Although the Rose criterion offers a useful benchmark for visual detectability, there is no universally applicable threshold that can be set *a priori*—particularly in ^{19}F MRI. Hot-spot signal intensities and spatial extents vary widely depending on factors such as contrast agent pharmacokinetics, molecular target density, binding efficiency, and imaging sequence parameters. In some cases, contrast accumulation is localized to a small number of voxels with low overall intensity; in others, a more diffuse but higher-intensity distribution may be present. As such, applying a fixed Rose threshold across all datasets may lead either to false positives, where background noise fluctuations are misinterpreted as signal, or to the omission of weak but biologically meaningful signals.

Despite this limitation, the Rose criterion can be effectively repurposed as a local denoising filter. Rather than acting as a strict visibility requirement, it serves as a statistical gatekeeper, used to suppress voxels whose intensity does not exceed a user-defined multiple of the estimated background noise level. This approach retains only those image regions that meet or exceed the expected visibility threshold, thereby reducing visual clutter and enhancing contrast between candidate hot-spots and noise.

Operationally, the denoising procedure involves estimating the standard deviation of noise, σ_N, from a signal-free region of the image, and applying a threshold operation on each voxel according to:

$$I(x,y) = \begin{cases} I(x,y) & \text{if } \frac{I(x,y)}{\sigma_N} \geq R_c \\ 0 & \text{otherwise} \end{cases} \tag{4.8}$$

where R_c is the selected Rose threshold.

This filtering step functions as a spatial denoising mask, eliminating background regions dominated by Rayleigh-distributed noise while preserving candidate hot-spots. The value of R_c must be carefully selected based on the expected SNR and the anticipated size of the objects of interest. Lower thresholds (e.g., $R_c = 1$) allow the preservation of weaker signal features in relatively low-noise datasets, but may risk retaining noise artifacts. Higher thresholds (e.g., $R_c = 4$) enforce more conservative filtering, reducing false positives but potentially discarding subtle hot-spots, especially those that span only one or two voxels.

As demonstrated in Figure 4.3, Rose-based denoising can substantially improve image interpretability, particularly when used as a post-processing step in low-SNR ^{19}F datasets, where traditional filtering techniques (e.g., Gaussian smoothing) risk blurring

sparse features or altering their shape. However, care must be taken not to discard diagnostically relevant signals that fall just below the threshold.

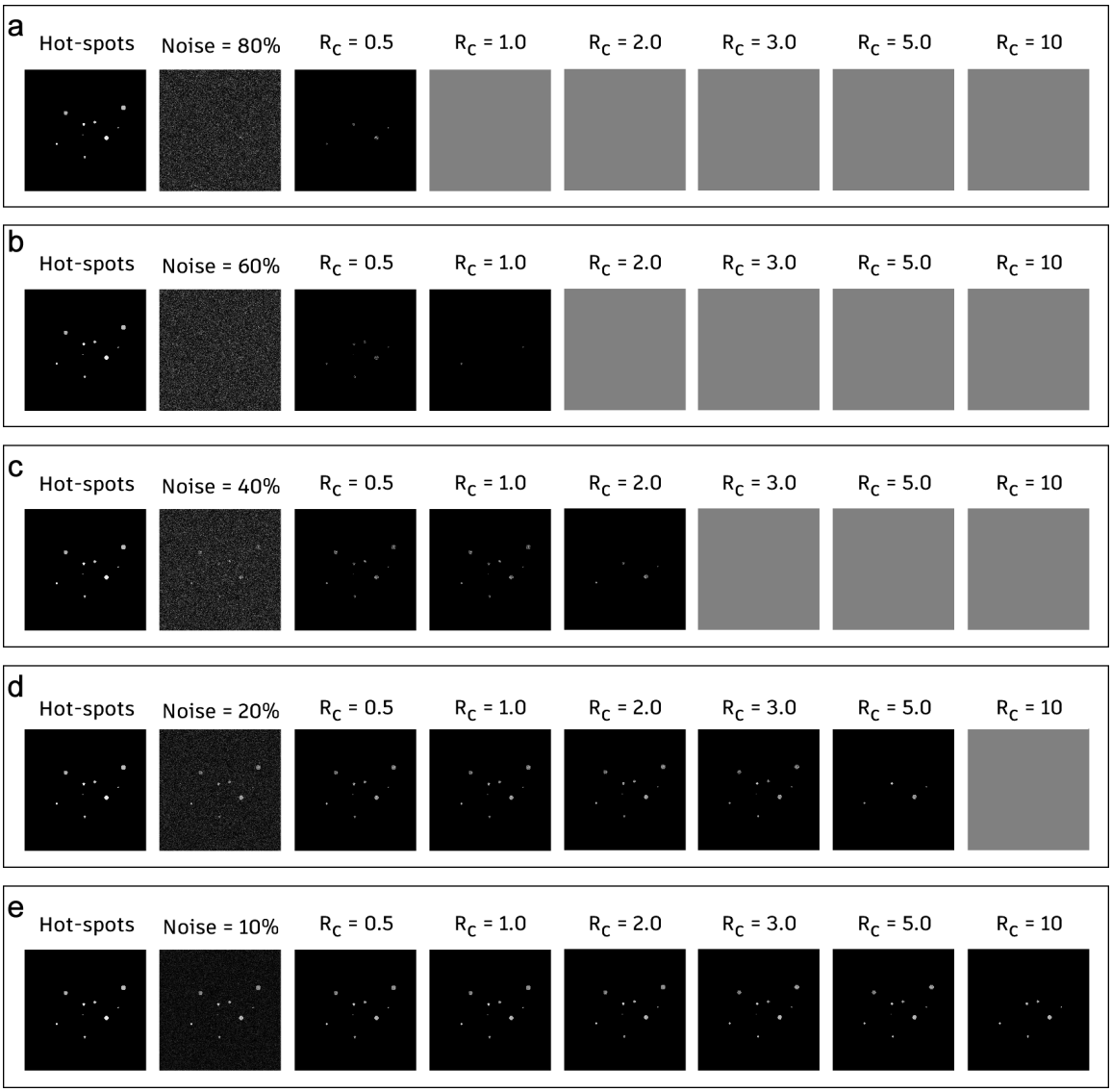

Figure 4.3 The Rose criterion can be used to denoise hot-spot images by eliminating pixels below a certain value of R_c. Hot-spot images with very high noise level (**a**) are difficult to denoise as pixels with meaningful information are removed even with the lowest values of R_c. As noise level decreases Rose criterion based denoising becomes more effective, while preserving the hot-spots (**b** to **e**) .

In practice, interactive or semi-automated tuning of R_c may be employed, optionally guided by anatomical priors, co-registered proton images, or prior expectations about contrast agent behavior. The Rose criterion thus provides a principled yet flexible approach to denoising, tailored to the unique challenges of sparse-signal detection in molecular imaging.

4.3 Image Resolution and the Point Spread Function

Image resolution refers to the ability to distinguish between adjacent spatial features and is fundamentally governed by the PSF, which is the reconstructed image of an ideal point source. In ^{19}F hot-spot imaging, the PSF plays a critical role in determining whether small objects are sharply depicted or blurred into the background.

In ideal Fourier imaging with uniform Cartesian sampling, the PSF takes the form of a sinc function whose main lobe width is inversely proportional to the extent of sampled k-space:

$$\mathrm{PSF}(x) = \sum_{n=-N/2}^{N/2-1} e^{i2\pi n \Delta k_x x} \tag{4.9}$$

where Δk_x is the spacing in k-space and N is the number of acquired samples.

However, real acquisitions are subject to signal decay during readout—most notably due to T_2 relaxation—which introduces amplitude modulation across successive k-space samples. This results in a non-uniform weighting of k-space, ultimately distorting the PSF in image space. In many sequences, particularly those based on echo trains, k-space lines are acquired at different echo times. As the MR signal decays over time, later-acquired lines—typically encoding higher spatial frequencies—are attenuated more strongly. This effect can be modeled as an exponential decay envelope applied across k-space:

$$\mathrm{PSF}(x) \propto \sum_{n=-N/2}^{N/2-1} e^{-n \cdot ES/T_2} \cdot e^{i2\pi n \Delta k_x x} \tag{4.10}$$

where ES is the echo spacing and T_2 is the transverse relaxation time.

The exponential term $e^{-n \cdot ES/T_2}$ compresses the dynamic range of k-space and reduces high-frequency content. In image space, this leads to Lorentzian-like broadening of the PSF, characterized by heavier tails and diminished resolution. Fine structures become smeared, and closely spaced hot-spots may merge or blend into the background. The severity of this effect increases with longer echo spacings and shorter T_2 values, which are conditions commonly encountered in ^{19}F imaging due to low signal lifetimes and sparse labeling. Figure 4.4 illustrates the impact of PSF broadening for an object consisting of two point sources.

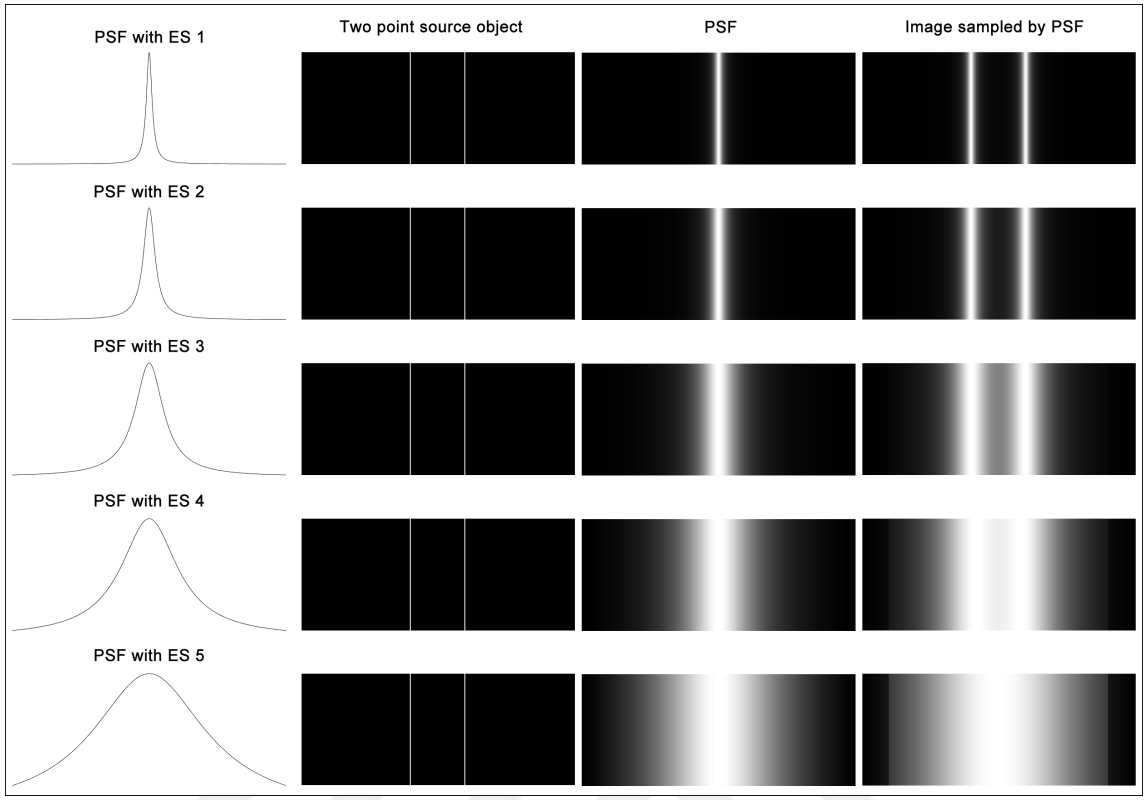

Figure 4.4 Two point sources acquired with different echo spacings (ES). A longer ES broadens the PSF reducing resolution. For very long ES two objects become visually indistinguishable.

Understanding and minimizing PSF broadening is essential when designing ^{19}F MRI sequences aimed at detecting small, sparse signals. The interplay between object size, Rose detectability, and resolution ultimately defines the practical limits of visibility in low-SNR imaging. Even when the Rose criterion is satisfied, degraded resolution may render a hot-spot indistinguishable due to signal spillover and contrast loss.

4.4 Summary

In ^{19}F MRI, conventional metrics such as SNR, CNR, and imaging efficiency offer valuable but incomplete insight into image performance. Detecting sparse, low-intensity hot-spots requires a deeper understanding of object visibility, which is effectively captured by the Rose criterion. This chapter introduced Rose-based visibility and its application as a denoising filter, enabling selective enhancement of hot-spot images. It also examined how transient signal behavior during data acquisition, such as relaxation effects or timing-related modulation, can distort the PSF, reducing resolution and contributing to signal blurring. Together, these tools provide a practical framework for optimizing ^{19}F MRSI under low-SNR conditions.

5. PULSE SEQUENCE ENGINEERING FOR ^{19}F MRSI

Pulse sequence design refers to the deliberate orchestration of radiofrequency (RF) pulses and magnetic field gradient events to control nuclear spin dynamics and elicit measurable MR signals. The goal is to encode spatial and spectral information into these signals while optimizing performance parameters such as acquisition time, resolution, SNR, and artifact sensitivity.

A pulse sequence is defined by the precise temporal arrangement of RF excitations, gradient pulses for spatial encoding, and acquisition windows during which signal readout occurs. Each component shapes contrast, spectral and spatial fidelity, and sensitivity to relaxation. For example, the envelope and bandwidth of an RF pulse govern the uniformity and selectivity of excitation across the frequency spectrum, while gradient timing and echo spacing modulate phase coherence and relaxation sensitivity during acquisition.

In ^{19}F MRI, pulse sequence engineering must address two principal challenges that are less prominent in conventional ^{1}H imaging:

- **Broad chemical shift dispersion:** Perfluorinated compounds typically contain multiple chemically distinct fluorine atoms, each giving rise to a separate resonance. These resonances can span several kilohertz, necessitating wideband excitation schemes and encoding strategies that preserve spatial registration across the full spectral range.
- **Low *in vivo* signal concentration:** Targeted ^{19}F agents are generally present at micromolar concentrations, resulting in intrinsically low signal amplitudes. Pulse sequences must therefore be optimized for maximal sensitivity and minimal signal loss due to relaxation or suboptimal flip angle profiles.

To address this, *in silico* simulations are employed to model spin dynamics under candidate pulse sequences. These simulations provide a flexible, accurate, and efficient framework for evaluating excitation uniformity, timing feasibility, signal evolution, and artifact behavior prior to physical implementation.

This chapter presents the simulation strategy and modeling tools used to guide sequence development, followed by the detailed design and evaluation of two spectroscopic imaging sequences tailored to ^{19}F MRI: Fluorine ultrafast Turbo Spectroscopic Imaging (F-uTSI) and Balanced Spiral Spectroscopic Imaging (BaSSI).

5.1 In Silico Methods for ^{19}F Spectroscopic Imaging

MRI sequences consist of timed components. RF pulses, magnetic field gradients, and acquisition windows are all executed in a precise temporal order. Each element has a finite duration and evolves over time, making the sequence discretizable.

In *in silico* experiments, the physical object is replaced with a digital phantom: a spatial grid of isochromats with defined resonance frequencies and spin densities. Signal evolution is modeled using time-domain integration of the Bloch equations. The approach resembles a finite element method, where temporal, spatial, and spectral resolutions can be adjusted to trade accuracy for computation time.

To ensure tractability, the simulations in this work were designed with two simplifying assumptions:

1. **No frequency-encoded spatial selection is simulated:** Since both F-uTSI and BaSSI use full phase encoding, their RF excitation profiles can be simulated independently of spatial gradients.
2. **Phase encoding is assumed ideal:** Spatial encoding is modeled as analytical phase labels. Imperfections in encoding are not simulated, focusing instead on magnetization dynamics.

Next sections describe RF pulse simulation, numerical integration of the Bloch equations, and evaluation of sequence behavior under representative ^{19}F conditions.

5.1.1 Simulating an RF Pulse

An RF pulse represents the time-varying B_1 field used to excite spin systems. When its frequency matches the Larmor frequency, energy transfer is most efficient. The RF field is typically applied over durations ranging from microseconds to milliseconds and lies within ± 10 kHz of the Larmor frequency.

Each RF pulse is defined by three parameters: frequency, duration, and envelope shape. Under small flip angle and near-resonance conditions, the spectral profile of the pulse can be approximated by the Fourier transform of its time-domain envelope [154]. This determines how flip angle and phase are distributed across frequency.

A simple case is the *block* or *hard* pulse, with a rectangular envelope. It is spectrally broad but yields a sinc-shaped frequency response, which causes flip-angle nonuniformity. Alternatively, a time-domain *sinc* pulse yields a rectangular spectral profile, improving uniformity across frequency (Figure 5.1).

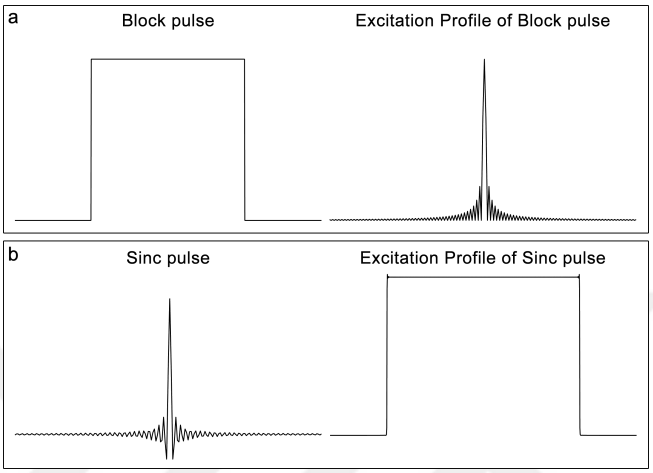

Figure 5.1 **a)** A rectangular shaped (hard) RF pulse has a sinc-shaped profile in the frequency domain. **b)** A Sinc-shaped RF pulse results in a rectangular shaped profile in the frequency domain.

The Fourier approximation breaks down for large flip angles or off-resonance excitation. In such cases, numerical integration of the Bloch equations is required. A standard method is to discretize the RF pulse into short-duration sub-pulses (Figure 5.2) and apply them in sequence to simulate magnetization evolution.

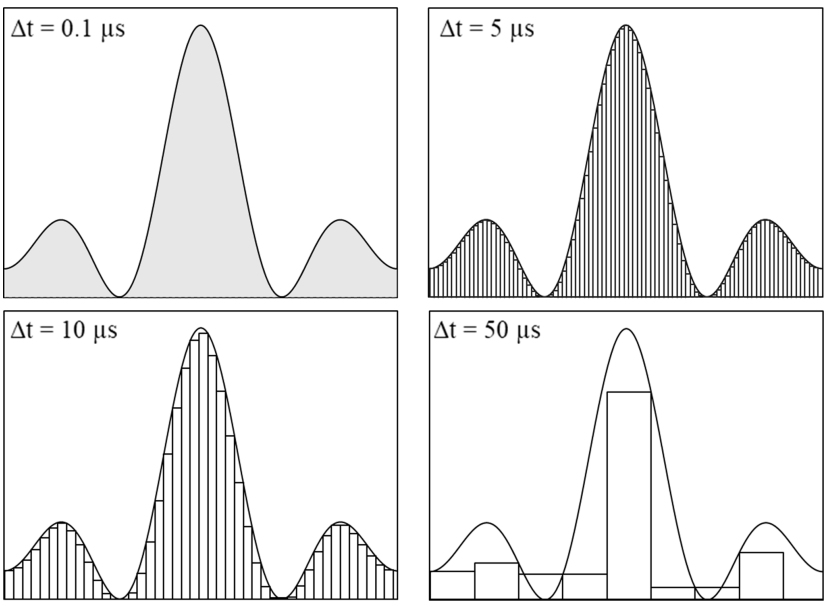

Figure 5.2 Discretizing a continuous RF pulse into short hard pulses for stepwise simulation.

This forms the basis of the Shinnar-Le Roux (SLR) algorithm [155–158], where each sub-pulse is modeled as a rotation. Under on-resonance conditions, for an RF pulse along x', the Bloch equations simplify to:

$$\frac{dM_{x'}}{dt} = 0, \quad \frac{dM_{y'}}{dt} = \gamma B_1^e(t) M_{z'}, \quad \frac{dM_{z'}}{dt} = -\gamma B_1^e(t) M_{y'} \tag{5.1}$$

which corresponds to a rotation around the x'-axis by angle θ_i:

$$R_{\theta_i} = \begin{bmatrix} 1 & 0 & 0 \\ 0 & \cos\theta_i & \sin\theta_i \\ 0 & -\sin\theta_i & \cos\theta_i \end{bmatrix} \tag{5.2}$$

with cumulative magnetization:

$$\vec{M} = R_{\theta_N} \cdots R_{\theta_1} \vec{M}_0 \tag{5.3}$$

In numerical implementations of the SLR algorithm, the choice of step duration directly affects both the accuracy and computational efficiency of the simulation. Smaller step sizes yield finer temporal resolution, allowing more accurate modeling of spin dynamics, particularly in the presence of rapidly varying RF amplitudes. The refined step size is essential for preserving spectral fidelity and ensuring that the simulated excitation profile matches the intended design. However, this improved accuracy comes at a cost: reducing the step duration increases the total number of time steps required for the same pulse duration, thereby increasing computational load and runtime. In time-critical applications or iterative design processes, this trade-off must be carefully managed. Table 5.1 shows the quantitative relationship between step duration, flip angle accuracy, and computation time.

Table 5.1
Effect of time-step duration on flip angle accuracy and computation time in the SLR hard-pulse approximation. Coarser steps improve speed but reduce accuracy.

Step duration (μs)	**Flip Angle (°)**	**Computation time (ms)**
0.1	90.0	283.84
1	89.9	27.51
5	89.7*	7.02
10	89.7*	2.90
50	85.3*	0.77
100	85.3*	0.62

*Identical results arise from numerical truncation.

Under off-resonance conditions, the Bloch equations become coupled and non-linear:

$$\begin{aligned}\frac{dM_{x'}}{dt} &= \Delta\omega_0 M_{y'} \\ \frac{dM_{y'}}{dt} &= -\Delta\omega_0 M_{x'} + \gamma B_1^e(t) M_{z'} \\ \frac{dM_{z'}}{dt} &= -\gamma B_1^e(t) M_{y'}\end{aligned} \tag{5.4}$$

where $\Delta\omega_0$ is the offset from the carrier frequency. These equations describe simultaneous nutation and precession, and their solution requires numerical integration.

To solve this, a fourth-order Runge-Kutta (RK4) numerical integration method is used [159], [160]. RK4 estimates the magnetization at each step based on four derivative evaluations, which are depicted in Figure 5.3, and described as below:

$$\begin{aligned}k_1 &= f(t_n, \vec{M}_n) \\ k_2 &= f\left(t_n + \tfrac{h}{2}, \vec{M}_n + \tfrac{h}{2}k_1\right) \\ k_3 &= f\left(t_n + \tfrac{h}{2}, \vec{M}_n + \tfrac{h}{2}k_2\right) \\ k_4 &= f\left(t_n + h, \vec{M}_n + hk_3\right)\end{aligned} \tag{5.5}$$

where h is the step size, and $f(t, \vec{M})$ is the right-hand side of the Bloch equation in the rotating frame.

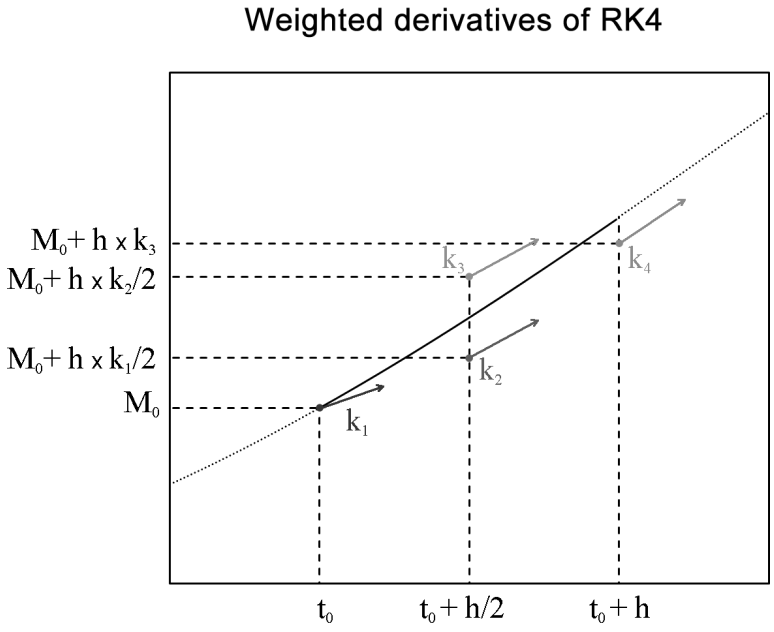

Figure 5.3 Graphical representation of the classical fourth-order Runge–Kutta method (RK4), illustrating the weighted intermediate derivatives used to advance the solution from t_0 to $t_0 + h$.

Based on the computed derivative, the RK4 algorithm calculates the value of magnetization in for the next discrete time step as:

$$\vec{M}_{n+1} = \vec{M}_n + \frac{h}{6}(k_1 + 2k_2 + 2k_3 + k_4) \tag{5.6}$$

In this work, the RK4 solver was implemented in *Matlab*^{TM} [161] using the `ode45` and `ode23` functions. These solvers were selected for their accuracy and adaptive step size control. They enabled precise simulation of excitation behavior, especially under wideband and off-resonance conditions as encountered in ^{19}F imaging.

The Bloch equations in the rotating frame, with gradients and arbitrary RF phases, were solved using the generalized form:

$$\begin{aligned}
\frac{dM_{x,\mathrm{rot}}}{dt} &= \gamma_s M_{y,\mathrm{rot}}(\vec{G}(t)\cdot\vec{r}) + (\gamma_s B_0 - \omega_{\mathrm{rot}})M_{y,\mathrm{rot}} \\
&\quad + \gamma_s M_{z,\mathrm{rot}} B_1^e(t)\sin(\omega_{\mathrm{RF}}t + \phi_{\mathrm{RF}} - \omega_{\mathrm{rot}}t) - \frac{M_{x,\mathrm{rot}}}{T_2} \\
\frac{dM_{y,\mathrm{rot}}}{dt} &= -\gamma_s M_{x,\mathrm{rot}}(\vec{G}(t)\cdot\vec{r}) - (\gamma_s B_0 - \omega_{\mathrm{rot}})M_{x,\mathrm{rot}} \\
&\quad + \gamma_s M_{z,\mathrm{rot}} B_1^e(t)\cos(\omega_{\mathrm{RF}}t + \phi_{\mathrm{RF}} - \omega_{\mathrm{rot}}t) - \frac{M_{y,\mathrm{rot}}}{T_2} \\
\frac{dM_{z,\mathrm{rot}}}{dt} &= -\gamma_s M_{x,\mathrm{rot}} B_1^e(t)\sin(\omega_{\mathrm{RF}}t + \phi_{\mathrm{RF}} - \omega_{\mathrm{rot}}t) \\
&\quad - \gamma_s M_{y,\mathrm{rot}} B_1^e(t)\cos(\omega_{\mathrm{RF}}t + \phi_{\mathrm{RF}} - \omega_{\mathrm{rot}}t) - \frac{M_{z,\mathrm{rot}} - M_z^0}{T_1}
\end{aligned} \tag{5.7}$$

This general form of the Bloch equation accommodates all relevant effects encountered in MRI, including off-resonance precession, gradient encoding, relaxation, as well as arbitrary pulse shapes or phase modulation. A detailed derivation is of the generalized Bloch equation provided in Appendix B.

5.1.2 Gradients and Phase Encoding

Phase encoding is the primary spatial localization mechanism used in both F-uTSI and BaSSI, forming the foundation of how spatial information is embedded into the acquired signal. It introduces position-dependent phase shifts by applying brief, controlled magnetic field gradients prior to acquisition, thereby mapping the physical location of spins into the phase of their precession. This approach avoids frequency encoding entirely and is particularly well-suited for spectroscopic imaging applications, where maintaining minimizing chemical shift artifacts are paramount.

In contrast to frequency encoding, which maps spatial position onto signal frequency and may introduce spectral blurring in the presence of multi-resonant signals, phase encoding preserves the full spectral content by confining spatial localization to the signal phase. This method avoids distortion of the frequency axis, allowing complete and accurate spectral acquisition. Such precision is especially critical for imaging agents like PFOB, whose complex spectral profile requires faithful representation of multiple well-separated resonances for accurate quantification and interpretation.

The spatially dependent phase shift introduced by a phase-encoding gradient is given by:

$$\phi(x) = -\gamma \int_0^{T_{\mathrm{PE}}} G(t)\, dt \cdot x = -\gamma\, \mathrm{GA} \cdot x, \tag{5.8}$$

where γ is the gyromagnetic ratio, $G(t)$ is the time-dependent gradient amplitude, T_{PE} is the duration of the gradient, and GA denotes the total gradient area.

In practice, this gradient is realized using trapezoidal waveforms, constrained by hardware limits on maximum gradient amplitude and slew rate. The area of a trapezoidal gradient waveform is determined by its flat-top duration and the ramp times:

$$\mathrm{GA} = G_{\max} \left(T_{\mathrm{plat}} + \frac{G_{\max}}{S} \right), \tag{5.9}$$

where $G_{\max}$ is the maximum gradient amplitude, and S is the slew rate—the maximum rate of change of the gradient field.

For a typical 64×64 Cartesian acquisition at 1 mm in-plane resolution, 64 unique phase-encoding steps are applied along each encoding axis to fully sample k-space. To ensure symmetric k-space coverage from $-k_{\max}$ to $+k_{\max}$, the required maximum phase-encoding gradient is calculated as:

$$G_{\max} = \frac{1}{\gamma \cdot \mathrm{FOV}} \cdot \frac{N}{2}, \tag{5.10}$$

where FOV is the field of view, and N is the number of phase-encoding steps. Achieving this gradient amplitude within a short encoding time demands a sufficiently high slew rate, compatible with scanner limitations. Hence, the duration of every phase encoding step id dictated by the hardware specifications of the system.

On the Philips Achieva 3.0 T system used in this study, the maximum gradient strength was 33 mT/m and the maximum slew rate was 225 T/m/s. Within these

constraints, a phase-encoding step duration of 0.87 ms was sufficient to reach the required gradient area for 1 mm resolution.

Each phase-encoding waveform was defined by its index in the encoding table and comprised symmetric ramp-up and ramp-down intervals surrounding a central flat plateau. The plateau amplitude was scaled linearly with the encoding index, thereby generating the appropriate phase shift for each corresponding line in k-space (Figure 5.4).

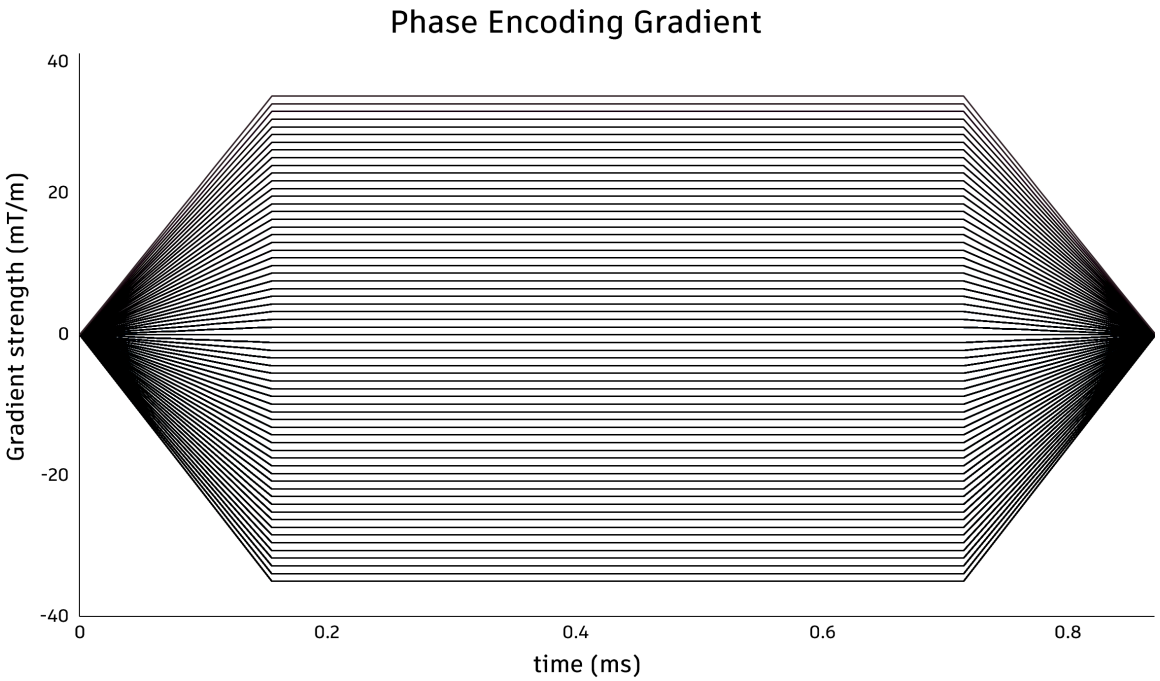

Figure 5.4 Gradient waveforms for 64 encoding steps with 1 mm resolution have a duration of 0.87 ms. Waveforms scale linearly with the encoding index to achieve the required gradient area.

Although these waveforms are essential for practical sequence implementation, they are not explicitly simulated in the Bloch equation framework. As discussed in Section 5.1, the simulation assumes *ideal phase encoding*: signal evolution during gradient application is neglected, and the cumulative phase imparted to each voxel is calculated analytically and applied as a complex phase label.

Nonetheless, the timing of the phase-encoding gradients is included in the total sequence design to maintain accurate synchronization between RF excitation, gradient switching, and acquisition windows. This ensures that echo spacing, repetition time, and spectral acquisition intervals remain physically realistic and compatible with the constraints of clinical MRI hardware.

5.1.3 Acquisition Window

The acquisition window is the temporal interval during which the MR signal is recorded following RF excitation and spatial encoding. This signal, which is typically an FID or spin echo, encodes spectral information as a function of time and is sampled at uniform intervals to enable spectral reconstruction via Fourier transformation. The quality of the resulting spectrum directly depends on how this window is configured.

The two key parameters defining the acquisition window are the dwell time Δt and the number of sampling points N. These determine the spectral bandwidth and resolution, respectively:

$$\text{Bandwidth} = \frac{1}{\Delta t}, \qquad \Delta f = \frac{1}{N\Delta t}. \tag{5.11}$$

The dwell time Δt is the inverse of the sampling rate and sets the spectral bandwidth: shorter dwell times allow acquisition of broader spectra, while longer dwell times reduce bandwidth but improve resolution for a fixed number of points. This introduces a critical trade-off between capturing a wide frequency range and achieving fine spectral discrimination, which must be balanced according to the application.

In ^{19}F spectroscopic imaging, compounds such as PFOB may exhibit spectra with a total width exceeding 10 kHz. To avoid spectral aliasing, the acquisition must satisfy the Nyquist criterion: Bandwidth $\geq 2 \cdot f_{\max}$, where $f_{\max}$ is the highest frequency component of interest in the spectrum.

For an 8 kHz-wide spectrum, this implies a minimum bandwidth of 16 kHz and a maximum dwell time of 62.5 µs. Violating this condition leads to aliasing, in which spectral content folds back into the observable range, producing spurious peaks and rendering chemical identification unreliable.

To resolve resonances separated by Δf, the number of points must satisfy:

$$N \geq \frac{1}{\Delta t \cdot \Delta f}. \tag{5.12}$$

For instance, resolving peaks 500 Hz apart with a dwell time of 50 µs requires at least $N = 40$ samples. Higher spectral resolution facilitates unambiguous assignment of overlapping peaks, which is essential for identifying the contributions of different chemical environments.

In practice, the MR system enforce a minimum number of points (typically 64) and offer discrete sampling rates (e.g., 32 kHz, 64 kHz). For example, a dwell time of 15.6 µs (64 kHz sampling rate) over 64 points yields a total acquisition duration of 1.0 ms and a spectral resolution of 1 kHz.

This configuration ensures faithful capture of all relevant spectral features, particularly the multiple resonance peaks of complex agents such as PFOB, without aliasing or overlap, while keeping the acquisition window short enough to minimize signal loss due to T_2 and T_2^* relaxation.

In simulation, this process is modeled by sampling the time-domain NMR signal at intervals of Δt, using a discrete convolution with a Dirac comb (train of Kronecker delta functions). This approach mimics the behavior of an ideal analog-to-digital converter, preserving the time-frequency structure of the signal without introducing windowing artifacts.

Accurate modeling of the acquisition window is essential for optimizing spectral resolution, detecting narrow peaks, and ensuring fidelity in frequency-domain reconstruction—especially in sequences like F-uTSI and BaSSI, where echo spacing and TR are tightly constrained. Improper configuration may lead to either under-sampling of the spectral content or unnecessary extension of scan time without appreciable gain in resolution.

5.2 RF Pulse Selection for ^{19}F Spectroscopic Imaging

Effective excitation is essential for ^{19}F MRSI, particularly when targeting compounds such as PFOB that exhibit broad chemical shift dispersions. Unlike conventional ^{1}H imaging, fluorinated tracers generate multiple resonance peaks distributed over several kilohertz. This spectral complexity imposes two principal constraints on RF pulse design: (1) adequate flip-angle uniformity across the relevant frequency range, and (2) short pulse duration to satisfy sequence timing and reduce RF power deposition. These requirements demand a careful trade-off between spectral bandwidth, energy efficiency, and the achievable excitation profile.

This section evaluates RF excitation strategies within the timing and performance constraints of the F-uTSI and BaSSI sequences. After introducing the amplitude- and frequency-modulated pulses available on the Philips R5 platform, we assessed their suitability for exciting broad, multi-peak spectra such as that of PFOB.

5.2.1 Amplitude-Modulated RF Pulses

Amplitude-modulated RF pulses operate by applying a fixed carrier frequency with a shaped amplitude envelope. Under the assumptions of small-tip-angle excitation and near-resonance conditions, their spectral profile can be approximated by the Fourier transform of the time-domain waveform. However, for large flip angles or significant off-resonance excitation, the linear approximation breaks down, and accurate performance prediction necessitates full numerical integration of the Bloch equations.

This challenge becomes especially relevant in spectroscopic imaging applications involving perfluorocarbon compounds, where the ^{19}F spectrum often spans several kilohertz. In such cases, RF pulses must maintain consistent excitation or refocusing across a broad spectral range without exceeding the duration limits imposed by timing constraints or exceeding SAR thresholds. Achieving both wide bandwidth and short pulse duration requires optimized pulse designs that provide efficient spectral coverage.

To evaluate the suitability of available RF pulse shapes for such applications, 64 amplitude-modulated designs provided by the Philips R5 platform were assessed using a simple but practical figure of merit: the ratio of spectral bandwidth to pulse duration, denoted BW/dur. This metric favors pulses that deliver wide spectral coverage with minimal time investment. Bloch equation simulations were conducted using a Runge-Kutta solver across a range of flip angles (5° to 90°, in 5° increments), as well as at 180°, which is critical for the refocusing pulses employed in F-uTSI.

For each simulated flip angle, the effective bandwidth was defined as the frequency range over which the simulated flip angle remained above 90% of the target value. Based on this criterion, 12 pulse shapes emerged as promising candidates. These exhibited favorable bandwidth-to-duration tradeoffs and appeared well-suited for both excitation and refocusing. The selected pulse shapes are illustrated in Figure 5.5; most are variants of the sinc-Gauss family, known for their compact time-domain support and sharp frequency profiles, although one block pulse (Pulse 1) was also retained based on performance.

The performance of these 12 pulses was further characterized by recording the bandwidth and duration required to achieve flip angles of 90° and 180°. These two cases are of particular interest for the CPMG echo train used in the F-uTSI sequence, which relies on consistent excitation and refocusing across the frequency range of interest. Table 5.2 summarizes the quantitative assessment.

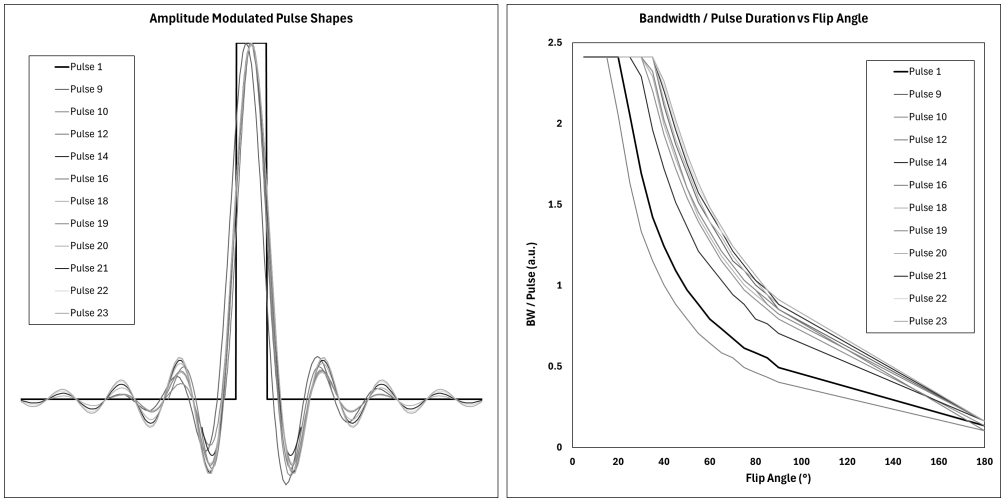

Figure 5.5 Amplitude-modulated RF pulses selected from the scanner's pulse library (left). The selection primarily consists of shapes of the sinc-Gauss types, and includes one block pulse (Pulse 1). Smooth bandwidth-to-duration ratio curves indicate linear scalability of the pulse shapes (right).

Table 5.2
Bandwidth and duration of the selected pulse shapes, for 90° and 180° excitation.

	Flip Angle	**Pulse 1**	**Pulse 9**	**Pulse 10**	**Pulse 12**	**Pulse 14**	**Pulse 16**	**Pulse 18**	**Pulse 19**	**Pulse 20**	**Pulse 21**	**Pulse 22**	**Pulse 23**
BW (kHz)	90°	4.0	6.8	6.4	3.2	5.6	6.8	6.6	6.6	7.1	7.1	7.3	7.3
	180°	1.1	1.3	1.1	0.8	1.3	0.8	1.3	1.3	1.3	1.3	1.3	1.3
Dur (ms)	90°	0.11	1.18	0.70	0.21	0.39	0.66	1.08	1.13	1.62	2.02	2.43	2.84
	180°	0.23	2.39	1.41	0.42	0.82	1.32	2.16	2.27	3.24	4.05	4.87	5.69

The results show that the 90° pulses offered wide bandwidths, ranging from 3.2 kHz to over 7 kHz, allowing effective excitation across large spectral windows. In contrast, the 180° pulses exhibited significantly narrower bandwidths, limited to about 1.3 kHz or less. This reduction arises from the full inversion requirement and the inherent tradeoff between pulse duration and bandwidth. Crucially, none of the tested 180° pulses were able to refocus the entire ^{19}F spectrum of PFOB, which spans approximately 8 kHz. These bandwidth limitations restrict their effectiveness to a single isochromat, thereby precluding their direct use in wideband spectroscopic imaging of multi-resonant compounds.

The findings are revisited for sequence-specific requirements in subsequent sections, where their implications for F-uTSI and BaSSI are further discussed.

5.2.2 Multi-band Pulses

Multi-band RF pulses enable the simultaneous excitation of multiple spectral regions by modulating a conventional amplitude-shaped pulse with a sinusoidal function. This amplitude modulation introduces additional frequency components into the RF waveform, resulting in a replicated spectral profile composed of discrete excitation bands symmetrically arranged around the carrier frequency. The resulting excitation spectrum consists of multiple lobes, each mimicking the shape of the original pulse spectrum, but shifted in frequency by fixed intervals set by the modulation frequency.

This method is particularly advantageous in ^{19}F MRSI of multi-resonant compounds such as perfluorooctylbromide (PFOB), where the most relevant resonances, namely CF_2, CF_2Br, and CF_3, are spaced several kilohertz apart. In such cases, a single narrowband excitation is insufficient to encompass all peaks of interest. While broadband excitation could, in principle, achieve uniform coverage, it typically comes at the cost of increased pulse duration or higher RF energy deposition. These trade-offs can violate SAR limits or exceed the RF amplifier capabilities, and may not be compatible with the tight timing constraints of fast imaging sequences.

Multi-band pulses address this challenge by simultaneously targeting separate frequency regions, thereby avoiding the need to extend pulse duration or increase RF power. Their spectral efficiency allows for selective excitation without wasting energy on intermediate spectral regions that contain no signal. In this way, they offer a highly efficient solution to a common limitation in ^{19}F MRSI, where spectral complexity and timing constraints often compete.

Unlike frequency-swept pulses, such as adiabatic pulses, which continuously vary their instantaneous frequency over time, multi-band pulses maintain a constant carrier frequency throughout the RF duration. Spectral broadening is achieved instead by amplitude modulation, which introduces symmetric frequency sidebands. This design strategy maintains phase coherence and simplifies hardware implementation, while still allowing wide spectral coverage and sharp selectivity. The ability to define excitation only at selected frequencies makes multi-band pulses especially appealing in systems where the desired spectral targets are known a priori and sparsely distributed.

Mathematically, multi-band excitation is implemented by modulating a base RF pulse $p(t)$ with a cosine function at a chosen modulation frequency f_M:

$$p_{\mathrm{MB}}(t) = p(t) \cdot \cos(2\pi f_M t). \tag{5.13}$$

This time-domain multiplication corresponds to convolution in the frequency domain with two delta functions located at $\pm f_M$, resulting in two shifted and scaled copies of the original spectrum:

$$\mathcal{F}\{p(t) \cdot \cos(2\pi f_M t)\} = \frac{1}{2}P(f - f_M) + \frac{1}{2}P(f + f_M), \tag{5.14}$$

where $P(f)$ denotes the Fourier transform of the original pulse $p(t)$.

This result is a direct consequence of the Fourier shift theorem, which states that modulation in the time domain corresponds to spectral translation. The generated excitation profile consists of dual or multiple spectral lobes, each retaining the shape of the base spectrum but scaled by a factor of one-half. By carefully selecting the modulation frequency f_M, the spectral lobes can be aligned with desired resonance frequencies, allowing a single RF waveform to simultaneously excite multiple spectral bands.

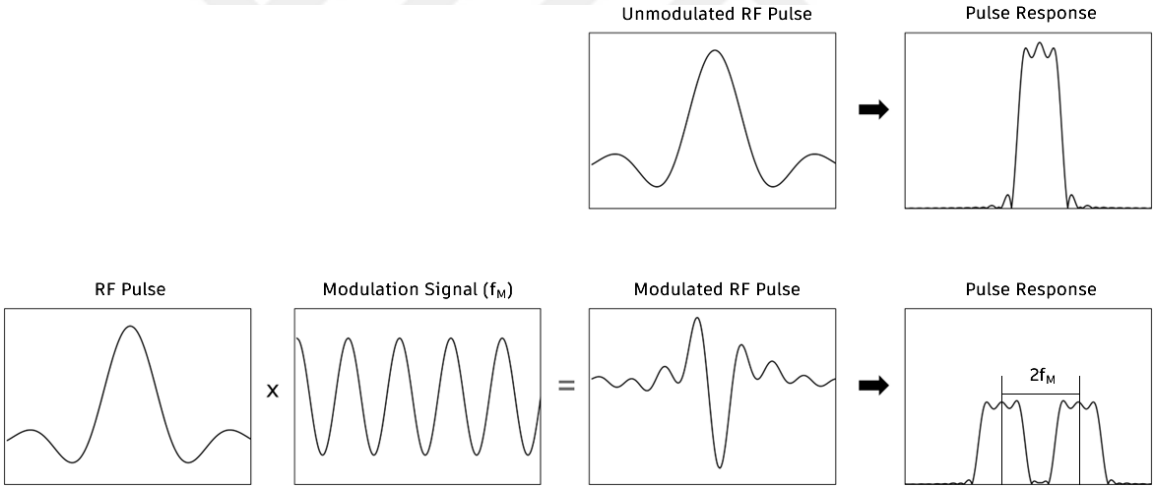

Figure 5.6 Modulating an RF pulse with a sinusoidal signal generates a multi-band excitation profile with distinct lobes at frequency offsets determined by the modulation frequency (f_M).

Applied to PFOB, this approach allows a narrowband pulse targeting the CF_2 peak to also excite CF_2Br and CF_3 by selecting $f_M \approx 2.5$–3 kHz, resulting in total spectral separations of 5–6 kHz. Simulations confirmed that multi-band pulses achieved uniform excitation across these peaks at a 90° flip angle (Figure 5.7).

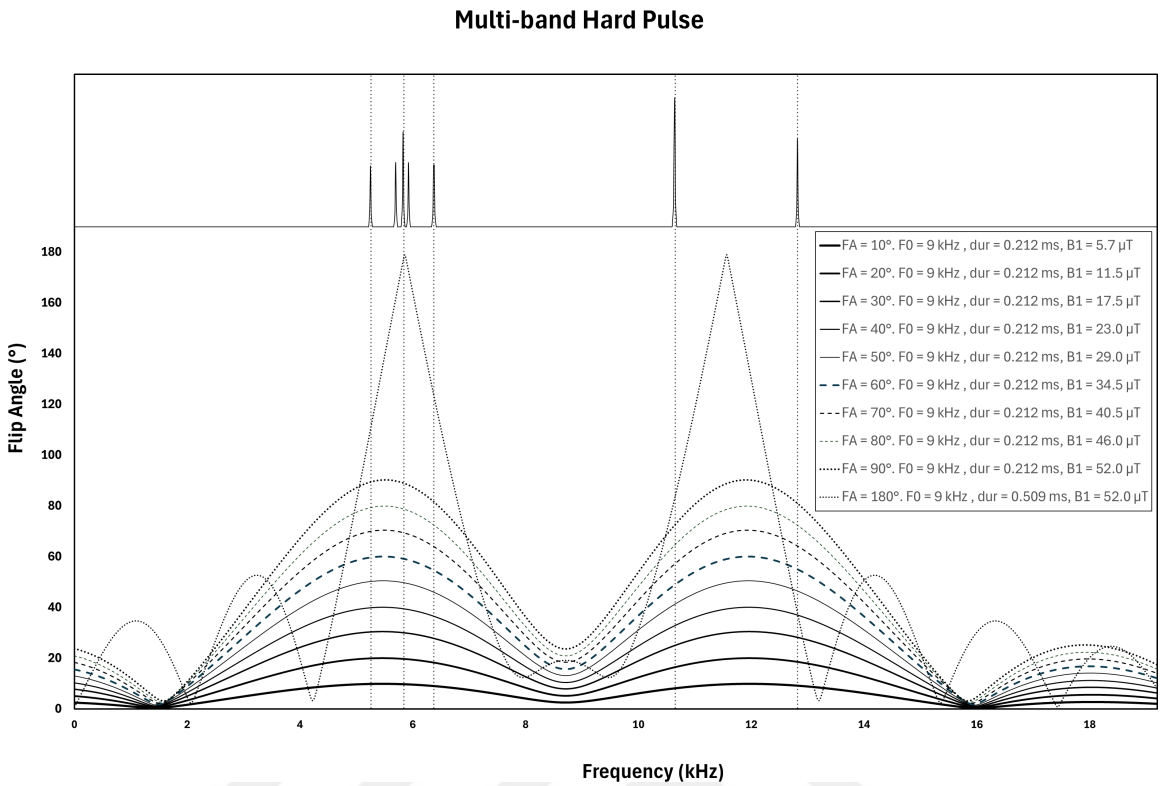

Figure 5.7 Simulation of flip-angle profiles for a multi-band RF pulse exciting CF_2, CF_2Br, and CF_3. Modulation enables uniform excitation across bands with minimal loss at the center frequency.

At higher flip angles, particularly at 180°, the performance of multi-band pulses was more constrained. While the central CF_2 region could be effectively inverted, the side bands of CF_2, and the CF_2Br and CF_3 peaks did not reach full inversion. Nevertheless, the flip angles achieved at these secondary peaks increased significantly compared to those obtained with conventional single-band pulses, improving from roughly 20° to over 80°. This enhancement translates to a stronger signal from minor components and improves the reliability of spectral quantification in MRSI reconstructions.

Despite the strong theoretical and numerical support for multi-band excitation, the method was not integrated into the final implementation of F-uTSI or BaSSI. Limitations in the scanner software and RF transmission chain, particularly regarding waveform generation and phase coherence, prevented robust, repeatable deployment of multi-band pulses.

However, the concept remains technically valid and was protected in a patent application [2].

5.3 Engineering F-uTSI

The F-uTSI sequence acquires spectroscopic imaging data using a CPMG-style echo train combined with full phase encoding across all spatial dimensions. It draws conceptual inspiration from the work of Duyn et al. [162], [163], who applied a similar method to ^{1}H spectroscopic imaging of the human brain.

Unlike Duyn's implementation, which employed volume selection, F-uTSI omits spatial selection entirely. As discussed in Section 3.1.1, this design avoids chemical shift-induced distortions arising from the broad NMR spectra of ^{19}F-based contrast agents.

F-uTSI supports both 2D and 3D spatial encoding, allowing for projection imaging or full volumetric reconstruction. The sequence consists of repeated execution of the core sequence, with phase encoding gradients incrementally adjusted to traverse k-space.

5.3.1 Core Sequence Structure and Timing Parameters

As illustrated in Figure 5.8, the F-uTSI sequence comprises three main components: (1) an RF pulse train generating a CPMG echo sequence, (2) phase encoding and rewinding gradients, and (3) a train of acquisition windows sampling echo signals.

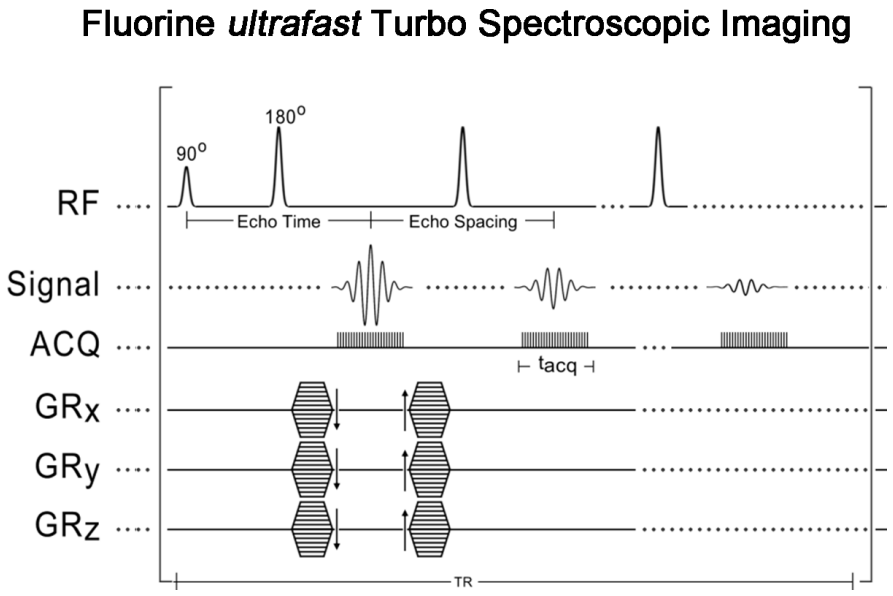

Figure 5.8 Core structure of the F-uTSI sequence. An excitation pulse initiates an echo train generated by refocusing pulses. Spatial encoding is performed by incremental phase gradients.

To meet the CPMG condition, the excitation pulse is set to 90° and the refocusing pulses to 180°, with alternating phase.

The timing of F-uTSI is governed by three key parameters:

- **Echo Time (TE)** — delay between excitation and the first echo.
- **Echo Spacing (ES)** — interval between successive echoes.
- **Repetition Time (TR)** — time between successive excitation cycles.

The terms *ultrafast* and *turbo* reflect the sequence's ability to achieve short echo spacing and repetition times, enabling faster acquisition than conventional ^{1}H or ^{31}P MRSI.

5.3.2 Timing Constraints and Optimization

The total duration of the echo train is determined by the echo spacing (ES) and the turbo factor (TF), i.e., the number of echoes per train. A higher TF increases acquisition efficiency but also prolongs the train, amplifying T_2-related decay. Minimizing ES is therefore essential.

ES is composed of RF pulse duration, gradient switching, and the acquisition window. Gradient timing is constrained by hardware limits: on a system with 33 mT/m amplitude and 233 T/m/s slew rate, each step takes 0.870 ms (Section 5.1.2). The acquisition window depended on desired spectral resolution and was 2.0 ms for 500 Hz, 1.0 ms for 1 kHz (Section 5.1.3).

RF duration depends on shape, flip angle, and available B_1. As detailed in Section 5.2.1, all candidate refocusing pulses provided similar bandwidths (0.8–1.3 kHz). Excitation pulses varied more (3.2–7.3 kHz), but under CPMG conditions, refocusing bandwidth was the limiting factor. Thus, duration was the primary criterion for pulse selection.

Based on Table 5.2, the block pulse (Pulse 1) offered the shortest durations with —0.11 ms for excitation and 0.23 ms for refocusing, while providing adequate bandwidth (4.0 kHz for excitation, 1.1 kHz for refocusing) for PFOB.

With block pulses, the minimum achievable ES became:

$$\text{For 500 Hz resolution:} \quad \text{ES} = 0.23 + 2 \times 0.87 + 2.0 = 3.97\,\text{ms} \approx 4\,\text{ms}$$
$$\text{For 1 kHz resolution:} \quad \text{ES} = 0.23 + 2 \times 0.87 + 1.0 = 2.97\,\text{ms} \approx 3\,\text{ms}$$

TE was bound similarly. With hard pulses, a minimum TE of 0.35 ms was possible. In practice, TE is often set equal to ES for temporal symmetry and robustness.

5.3.3 Spectral Complexity and Signal Dynamics

Each excitation was followed by a full echo train. Signal evolution depends not only on sequence timing, but also on the spectral characteristics of the spin system. In simple cases with a single resonance, the echoes decay exponentially according to T_2 relaxation (Figure 5.9).

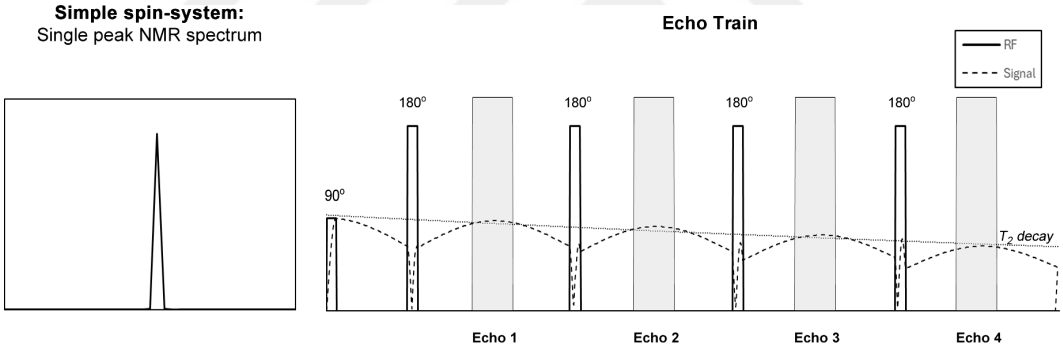

Figure 5.9 For simple spin systems, echo signals decay exponentially according to T_2.

In more complex spectra, such as PFOB, interference among multiple resonances disrupts this ideal behavior (Figure 5.10).

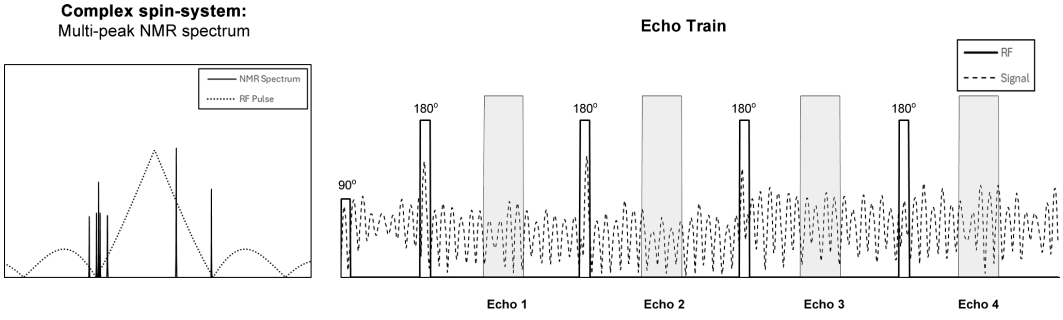

Figure 5.10 In complex spin systems, echo signals exhibit interference from multiple resonances.

Excitation bandwidth and carrier frequency played a critical role in shaping the echo profile. As shown in Figure 5.11, signal intensity and stability variedstrongly with RF offset frequency.

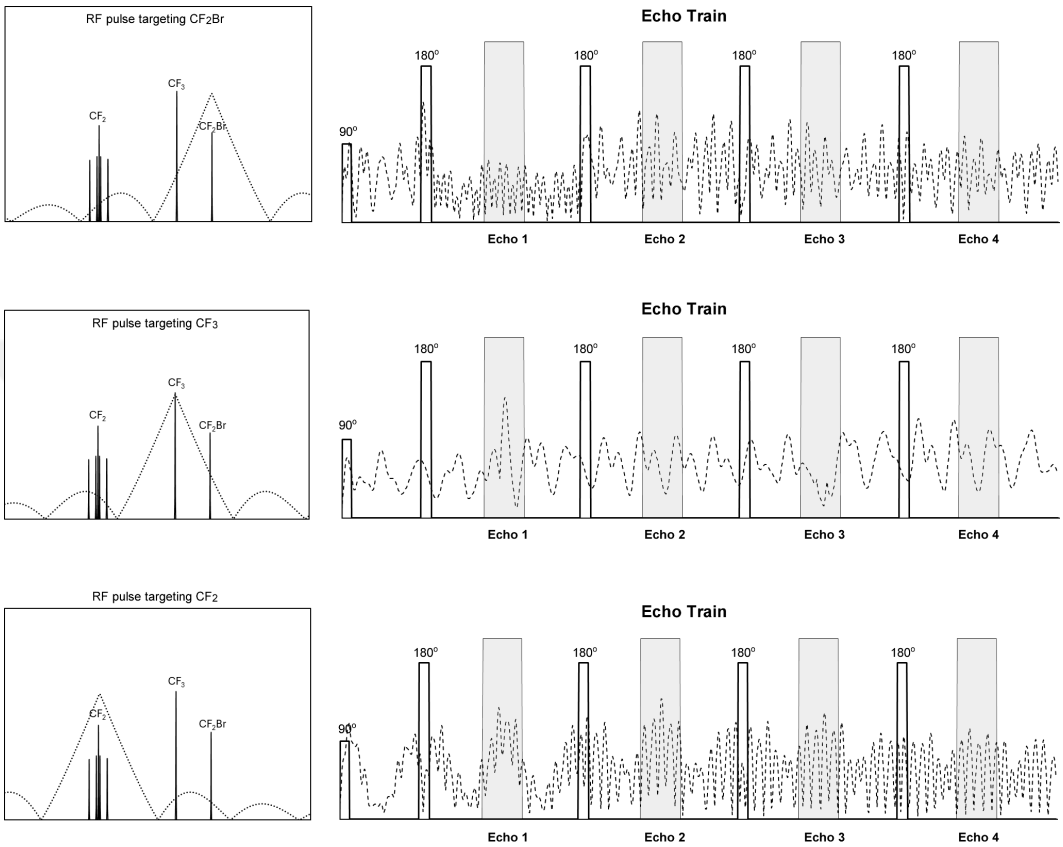

Figure 5.11 Echo signal characteristics varied with the offset frequency of the RF pulses.

Simulation results indicated that centering the excitation pulse on the CF_2 resonance yields the most stable and intense echo signals (Figure 5.12).

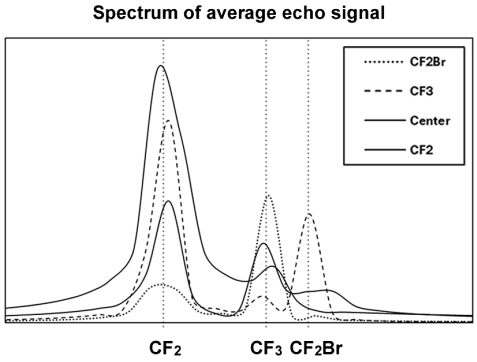

Figure 5.12 Average echo signal vs. excitation offset, with CF_2 showing the strongest response.

5.3.4 Echo Train Length and Relaxation

The echo train length (ETL) is defined as:

$$\mathrm{ETL} = \mathrm{TE} + \frac{\mathrm{ES}}{2} + (\mathrm{TF} - 1) \cdot \mathrm{ES}, \tag{5.15}$$

where TE is the echo time, ES is the echo spacing, and TF is the turbo factor. The total repetition time (TR), including any recovery delay ΔT_R, is:

$$\mathrm{TR} = \mathrm{ETL} + \Delta T_R. \tag{5.16}$$

Longer recovery periods allow the longitudinal magnetization to fully restore, ensuring maximum signal intensity. Figure 5.13 shows normalized peak signal as a function of ΔT_R, where signal strength generally increased with T_1 recovery but exhibited fluctuations at short intervals, likely due to spectral interference effects between overlapping peaks.

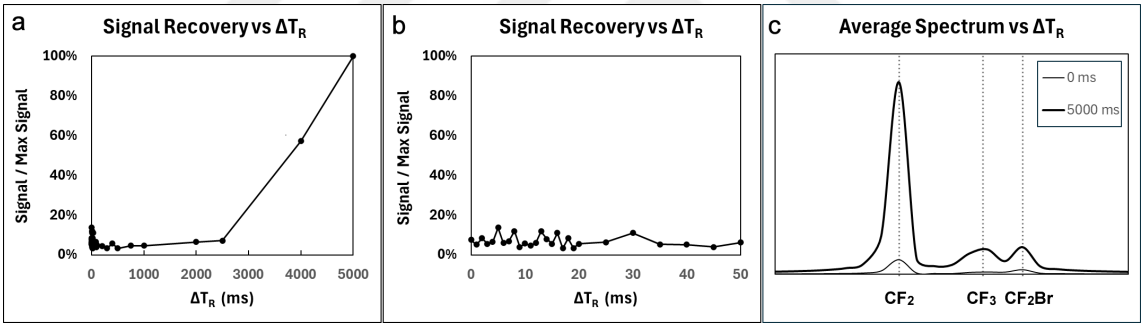

Figure 5.13 **a)** Long TR allows full signal recovery and high SNR. **b)** Short TR can produce comparable or higher peaks. **c)** Average spectra show stronger CF_2 signal under both TR conditions.

Interestingly, signals measured at $\Delta T_R = 0$–5 ms could match or even exceed those observed at longer TR values, suggesting efficient signal formation even under rapid repetition conditions.

Consistent with previous observations, the CF_2 peak remains the dominant resonance line for both short and long TR settings, reflecting its favorable relaxation characteristics.

These results suggest that TR can be reduced to just above the echo train length with minimal signal loss. For instance, a 64×64 acquisition at 1 mm resolution using a 32-echo train (TE = ES = 4 ms) and TR = 130 ms completes in approximately 17 s.

5.3.5 In-silico Assessment of Magnetization

In a typical implementation, F-uTSI acquires a 32×32 k-space grid by executing one echo train per phase-encoding line. Each echo train consists of 32 echoes, with an echo spacing of ES = 4 ms, beginning at an initial echo time TE = 4 ms. This results in a total echo train duration of approximately 130 ms. Because only one line of k-space is filled per echo train, a complete acquisition of the 2D grid requires 32 repetition times (TRs). Under the assumption of continuous acquisition with no inter-TR delay (i.e., $\Delta T_R = 0$), the total scan time is approximately 4.16 s.

This timing structure is compatible with the relaxation characteristics of common perfluorocarbon agents such as PFCE and PFOB, whose transverse relaxation times T_2 typically range from 200 to 800 ms depending on formulation and environment. Although the echo train length is non-negligible relative to T_2, the majority of signal decay occurs in the early echoes, and a substantial portion of the magnetization remains available across the train. Importantly, the timing parameters of F-uTSI, including the number of echoes per train, the echo spacing, and the absence of recovery delay, are well matched to these relaxation limits. This enables efficient k-space sampling within a compact temporal footprint, while minimizing artifacts due to relaxation-induced signal variation across the dataset.

This behavior is illustrated in Figure 5.14, which shows simulated spectra acquired over 32 TRs. The signal amplitude decreases notably during the first few excitations but quickly stabilizes, converging to a steady-state value of approximately 9% of the initial fully relaxed signal. This stable plateau is advantageous as it allows consistent and reproducible sampling the k-space lines.

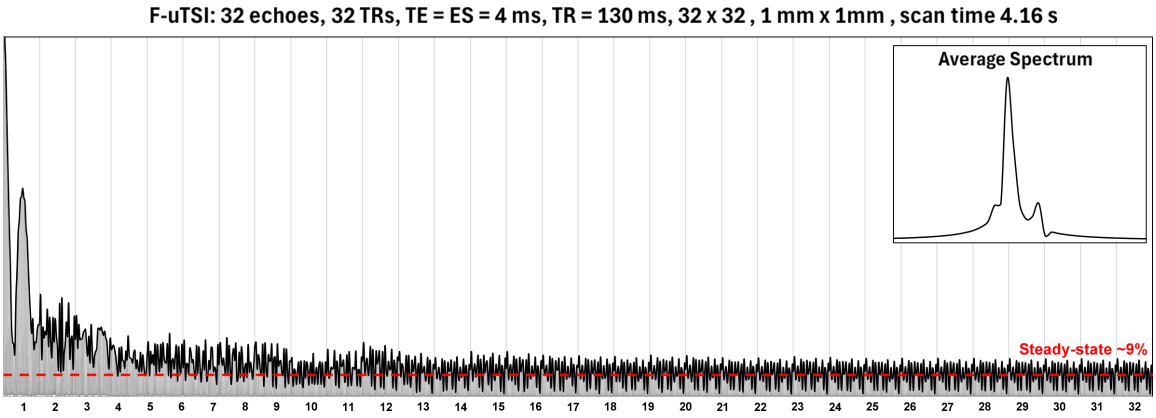

Figure 5.14 Simulated 32×32 F-uTSI. Signal stabilizes at 9% of the initial value.

For a 64×64 grid, each k-space line is sampled over two TRs, requiring 128 TRs in total. With TR = 130 ms, the full scan takes 16.64 s. Figure 5.15 shows that the residual signal again stabilizes at 9%, but the average level is 25% lower than in the 32×32 case. While the larger grid expands the field of view without reducing resolution, it lowers signal intensity, potentially affecting sensitivity.

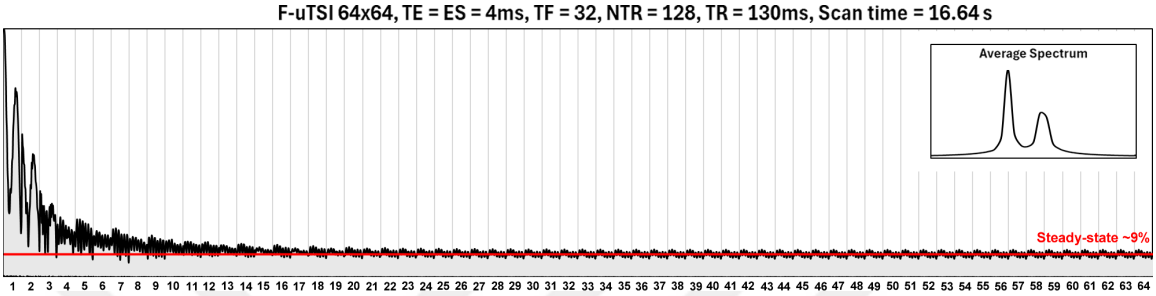

Figure 5.15 Simulated 64×64 F-uTSI acquisition with TF = 32. The signal reaches a steady state at approximately 9% similar to the 32×32 case, while the average amplitude is about 25% lower.

5.3.6 Acquisition Strategies and PSF

As discussed in Section 4.3, the PSF describes the image of an ideal point source and serves as the system's transformation kernel. Because Fourier imaging is linear, any object is imaged as a superposition of point responses. Simulations of full F-uTSI sequences revealed transient magnetization behavior caused by interference among heterogeneous isochromats, relaxation effects (T_1, T_2), and interactions between spin and stimulated echoes. These transients were projected into k-space according to the sampling order, meaning acquisition sequence affected image quality.

F-uTSI uses a Cartesian scheme, where each k-space line is acquired by an echo train. While adhering to the linear structure of the scheme, the sequence can sample k-psace in various ways. Figure 5.16 shows five such strategies and their corresponding PSFs. While core profiles were similar, artifact patterns varied. These differences were quantified by the mean squared error (MSE):

$$\mathrm{MSE} = \frac{1}{N^2} \sum_{i,j} \left(I_{ij} - \hat{I}_{ij} \right)^2 \tag{5.17}$$

where I is the ideal image, $\hat{I}$ is the reconstructed image, and N^2 is the number of pixels.

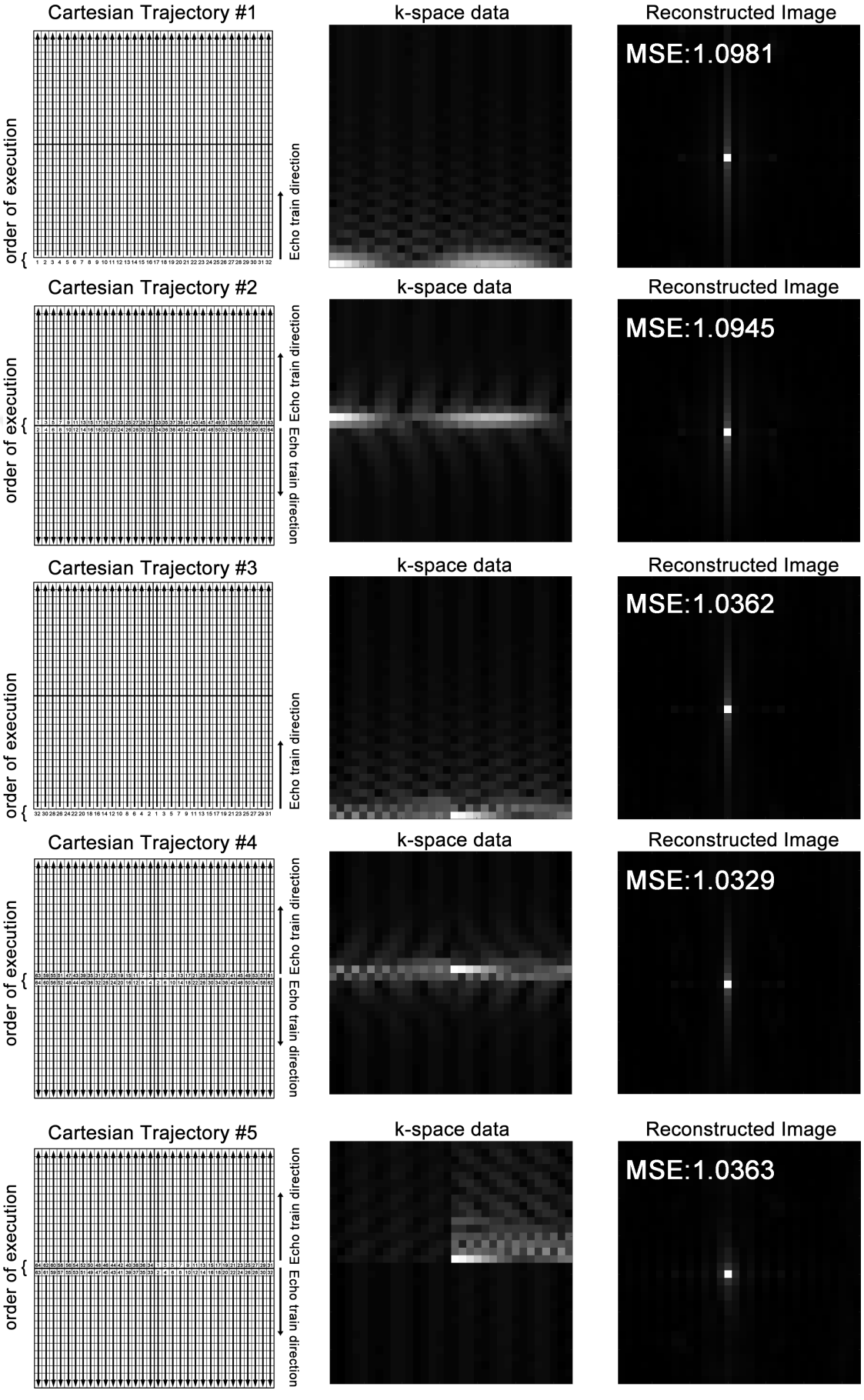

Figure 5.16 Comparison of Cartesian sampling strategies and their PSFs.

Strategies that began near the center of k-space yielded lower MSE than edge-to-edge methods. Alternating line directions (scenario #4) further reduced MSE but required rapid gradient switching, which increased electro-mechanical stress and acoustic noise. Balancing fidelity and hardware demands, the four-quadrant scheme (scenario #5) offered the best tradeoff, making it the preferred approach for F-uTSI.

An alternative is radial sampling, in which k-space lines extend outward from the center at incrementally varying angles. Since echoes correspond to discrete points, radial trajectories must be mapped to the nearest grid locations—yielding a "pseudo-radial" pattern (Figure 5.17).

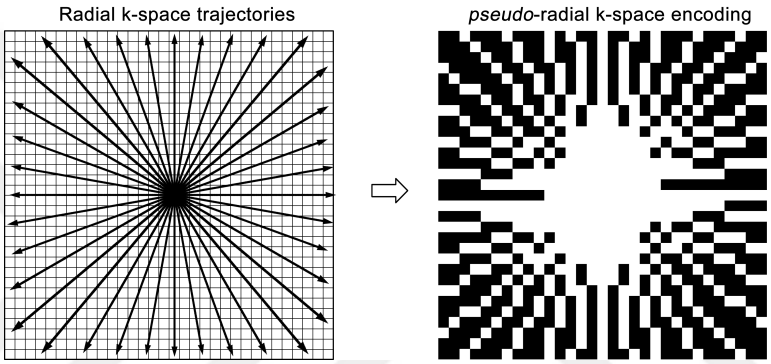

Figure 5.17 *Pseudo*-radial trajectories mapped onto discrete k-space grid points.

As shown in Figure 5.18, pseudo-radial F-uTSI resulted in slightly higher MSE than Cartesian sampling. However, it reduced the visibility of strike artifacts by spreading the echo-train decay across k-space. This radial dispersion smeared artifact energy, increasing background noise but improving overall image appearance.

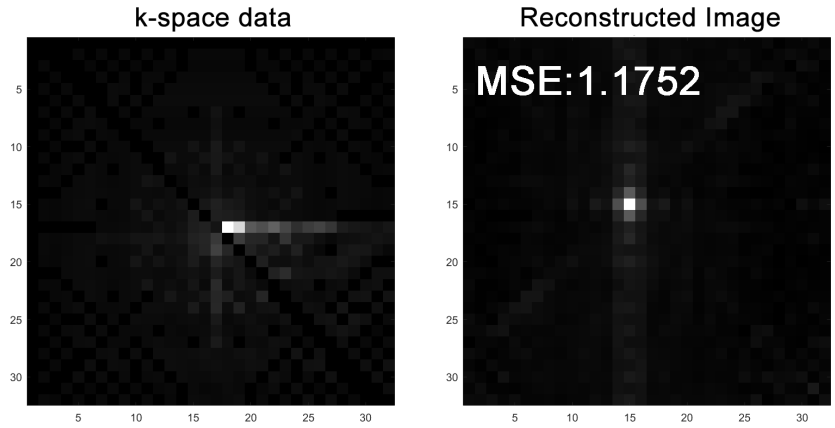

Figure 5.18 Pseudo-radial sampling mitigates the streak artifact by distributing signal decay across k-space. This improves PSF, whilst elevating image noise and impacting MSE negatively.

5.3.7 Reversed Echo Train Acquisition

In practice—especially when imaging low-concentration contrast agents, multiple signal averages (NSA > 1) are often required to boost SNR. Repeated acquisitions also offer a practical means to suppress strike artifacts, which arise from signal decay along the echo train. Since this decay produces directionally biased artifacts in the reconstructed image, reversing the readout direction in alternate averages can effectively mitigate this effect by averaging out the asymmetry (Figure 5.19).

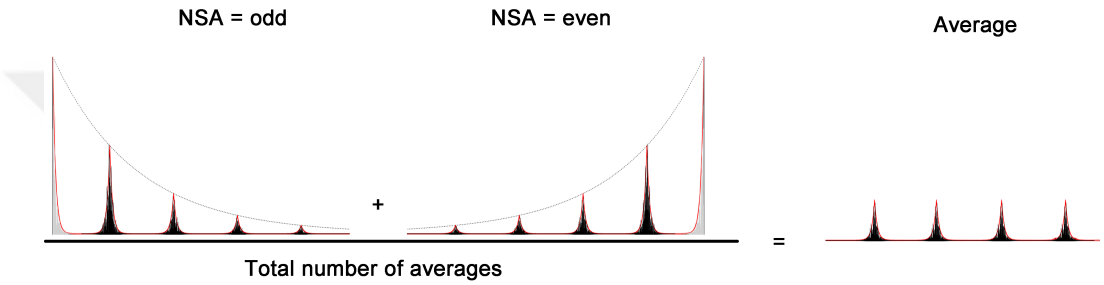

Figure 5.19 Alternating line directions in subsequent averages cancels directional strike artifacts.

Figure 5.20 illustrates this strategy in a Cartesian acquisition with NSA $= 2$, where the second average uses reversed echo trains. The resulting image shows a marked reduction in directional artifacts compared to single-average acquisition, highlighting the benefit of directional averaging for improving image fidelity.

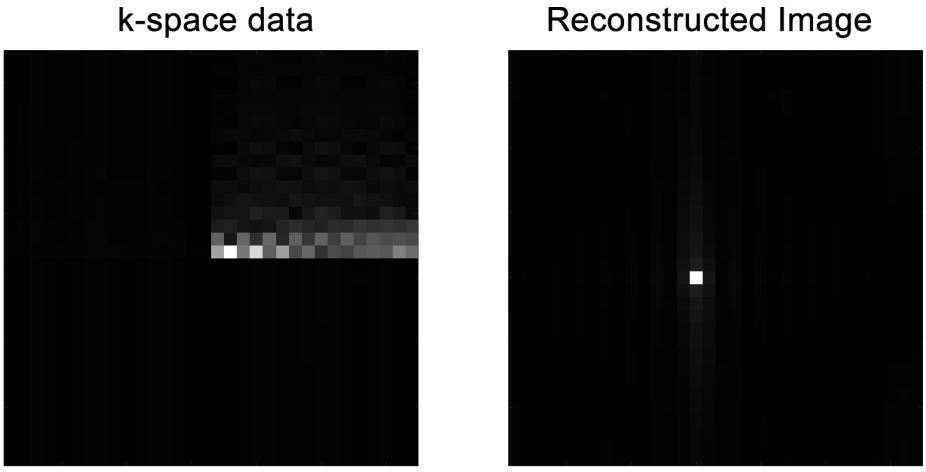

Figure 5.20 Reversed acquisition directions improve image quality by averaging out artifacts.

5.4 Engineering BaSSI

Balanced Spectroscopic Steady-State Imaging (BaSSI) was developed to enhance both detection sensitivity and imaging efficiency in ^{19}F MRSI. As discussed in the experimental section of this thesis, F-uTSI proved to be a robust ^{19}F imaging technique, competitive with contemporary methods such as spectrally selective multi-gradient-echo imaging. Over time, however, F-uTSI was surpassed by more advanced approaches, most notably by 3D ultrashort echo-time balanced steady-state free precession imaging (3D UTE bSSFP) [145].

Despite its complex name, 3D UTE bSSFP is a relatively simple gradient echo-based technique. It combines spectrally selective excitation with 3D radial k-space trajectories and achieves extremely short echo (TE) and repetition (TR) times to enhance sensitivity and reduce scan durations (See Section 7.1.1 for details of 3D UTE bSSFP).

The development of BaSSI builds directly on insights gained from F-uTSI, while drawing inspiration from the minimalist, high-efficiency design of 3D UTE bSSFP. By combining ultrashort TE/TR timing with spectral acquisition, BaSSI introduces a streamlined sequence architecture that preserves spectral fidelity while maximizing imaging speed. This offers a viable and competitive alternative to 3D UTE bSSFP.

5.4.1 Core Sequence Structure and Timing Parameters

The BaSSI sequence is an FID-based method that acquires MR signal using a fully phase-encoded sampling scheme. It operates without spatial or spectral selection and does not employ gradient spoilers, making it inherently compatible with balanced steady-state imaging. Conceptually, BaSSI can be regarded as a simplified, non-selective derivative of the CE-FAST sequence [164], preserving its steady-state and FID-readout features while omitting spatial selection modules. Compared to F-uTSI, BaSSI offers a more compact and efficient design.

As illustrated in Figure 5.21, each repetition of the sequence consists of a single non-selective broadband excitation pulse, followed by phase-encoding and rewinding gradients, and concludes with an acquisition window to capture the FID signal. A complete k-space dataset is acquired by repeating this sequence with a fixed repetition time (TR), incrementally adjusting the phase-encoding gradients to traverse k-space.

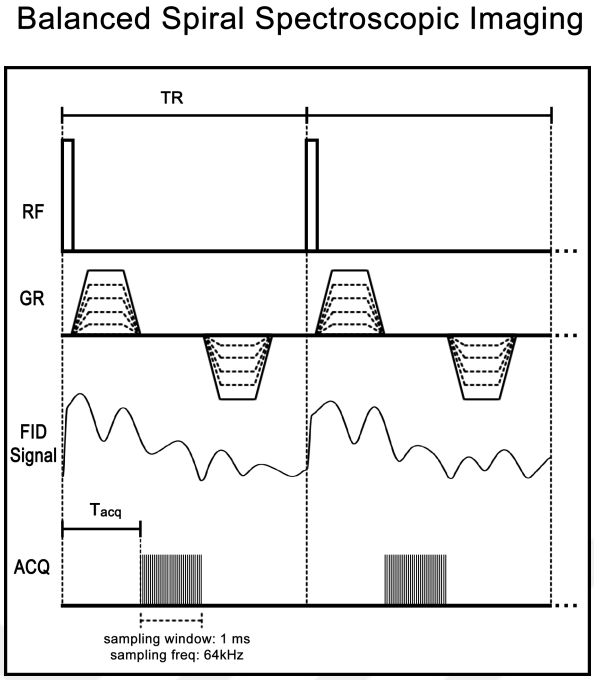

Figure 5.21 BaSSI: An FID-based, all-phase-encoded spectroscopic imaging sequence.

Unlike F-uTSI, which uses 90° and 180° pulses to satisfy CPMG conditions, BaSSI does not impose such constraints and allows flexible flip-angle selection. This flexibility enables the use of shorter RF pulses and facilitates rapid cycling.

The duration of the acquisition window is determined by the desired spectral resolution. As calculated in Section A.8.5, a sampling bandwidth of 64 kHz and 1 kHz resolution yields an acquisition duration of 1.0 ms. The start of this window (T_{acq}) is defined by the sum of the RF pulse and phase-encoding gradient durations.

According to Section 5.1.2, the encoding gradient duration for a 64×64 acquisition at 1 mm resolution using 33 mT/m gradient strength and a 225 T/m/s slew rate is 0.870 ms. With a 5° block pulse lasting 6.7 µs, the minimum T_{acq} becomes approximately 0.877 ms. For a 90° block pulse (110 µs; Table 5.2), T_{acq} is 0.980 ms.

Assuming $T_{\text{acq}} = 1.1$ ms (sufficient for flip angles up to 90°), the minimum TR becomes 2.97 ms. At this TR, a full 64×64 acquisition at 1 mm resolution—where each k-space point is sampled by a single FID takes approximately 12 seconds. In comparison, the same acquisition using F-uTSI takes 17 seconds (Section 5.3.4).

Thus, with its reduced TR and streamlined structure, BaSSI has emerged as *the fastest ^{19}F spectroscopic imaging sequence in the west.*

5.4.2 Exploring the Parameter Space

Given the novelty of the BaSSI sequence, it was essential to systematically explore its largely uncharted parameter space. Although empirical studies on a clinical scanner would provide definitive insight, preliminary *in silico* simulations were used to enhance efficiency and reduce scanner time. These computational experiments were instrumental in defining meaningful parameter ranges and guiding subsequent *in vivo* investigations.

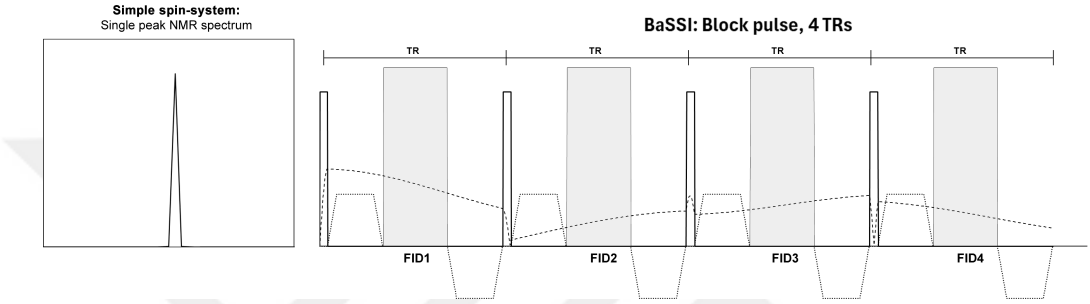

Figure 5.22 Parameter space of BaSSI explored via 4-TR simulation of a single-peak spin system.

To evaluate how flip angle and pulse shape influence signal behavior in BaSSI, a minimal 4-TR acquisition on a single-peak spin system was simulated (Figure 5.22), with relaxation times representative of bulk fluorinated compounds (T_1 = 1420 ms, T_2 = 450 ms) [125–127].

Five short-duration RF pulses consisting of one hard pulse (Pulse 1) and four sinc-Gauss (Pulses 10, 12, 14, and 16), were tested over flip angles from 10° to 90°, at a fixed TR of 2.87 ms. Peak signal amplitudes were extracted using the RK4 solver (Section 5.1.1), normalized to the global maximum, and averaged across the four acquisitions.

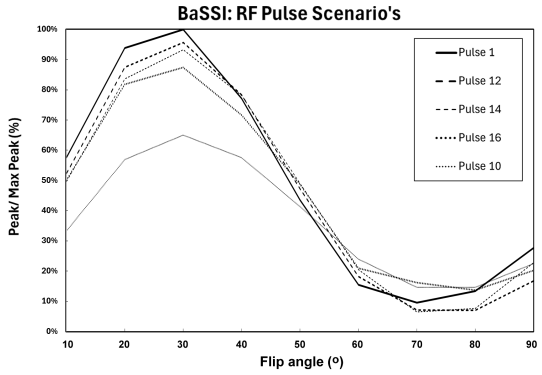

Figure 5.23 Simulation results with pulse shapes vs. flip angle. The hard pulse (Pulse 1) produced the highest signal level, with 30° identified as the optimal flip angle across all tested pulse shapes.

As shown in Figure 5.23, the highest signal was consistently obtained at a flip angle of approximately 30°, regardless of pulse shape. The block pulse (Pulse 1) produced the strongest signal across the entire flip angle range, likely due to its short duration and broadband excitation profile, which minimized signal decay during excitation and permitted earlier acquisition. In contrast, sinc-Gauss pulses (e.g., Pulse 10) exhibited reduced performance at higher flip angles, attributable to longer duration and narrower spectral bandwidth.

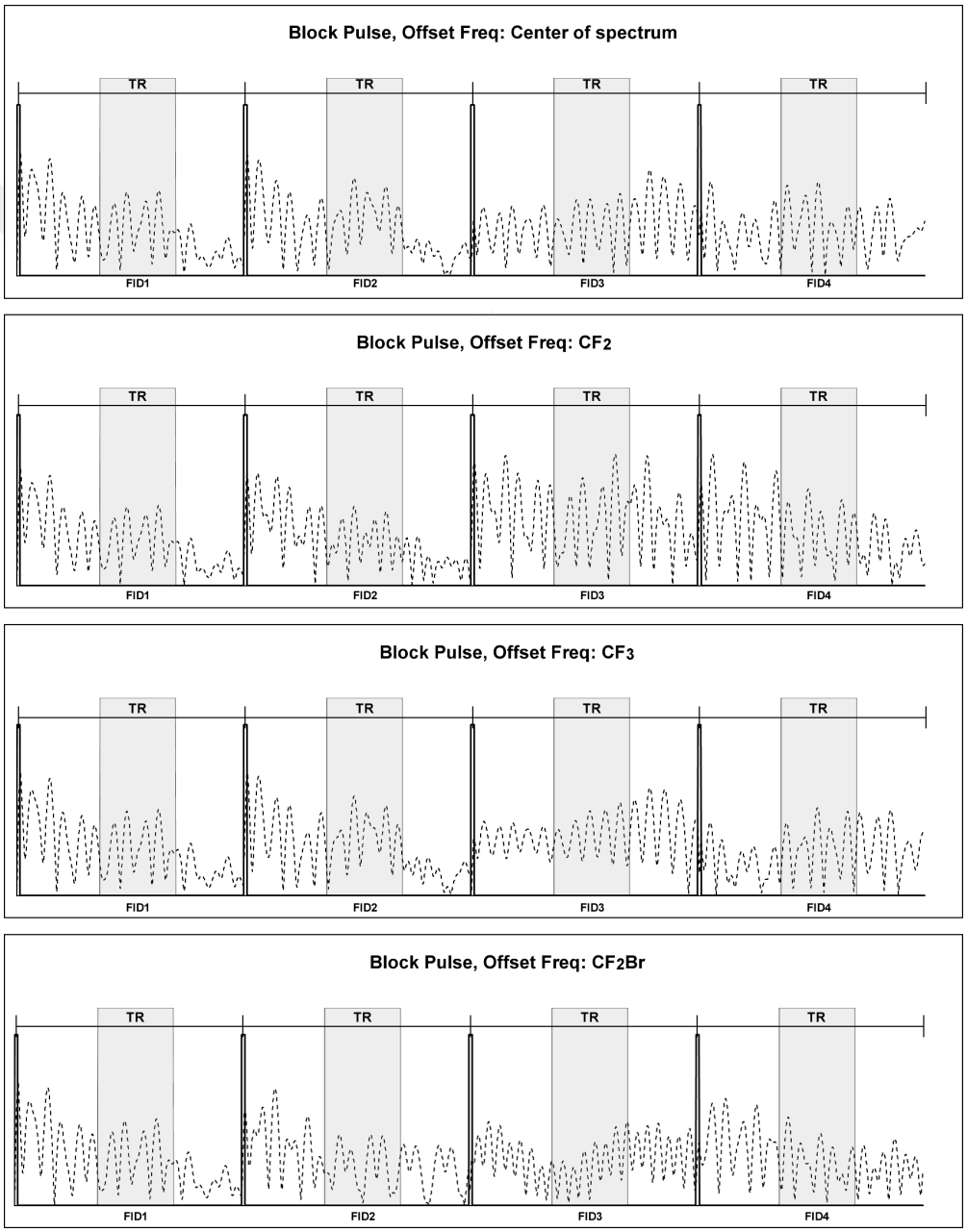

Figure 5.24 Simulated signals of four TRs of BaSSI obtained with offset frequencies corresponding to the center of the NMR spectrum, and the three resonance lines of PFOB (CF_2, CF_3 and CF_2Br).

To assess the impact of RF offset under realistic conditions, simulations were extended to a multi-peak spin system mimicking the full ^{19}F NMR spectrum of perfluorooctyl bromide (PFOB). A 30° non-selective hard pulse was applied, with T_{acq} and TR set to their shortest feasible values. The excitation frequency (carrier offset) was varied systematically, centering either on the midpoint of the spectrum or on specific resonance frequencies of individual spin groups (Figure 5.24).

Spectral analysis revealed that while CF_2 and CF_3 peaks consistently yielded the highest amplitudes due to favorable relaxation and concentration, centering the RF pulse on the CF_2 resonance improved spectral resolution across the spectrum. Both CF_3 and CF_2Br were more clearly resolved and less distorted when CF_2 was targeted (Figure 5.25).

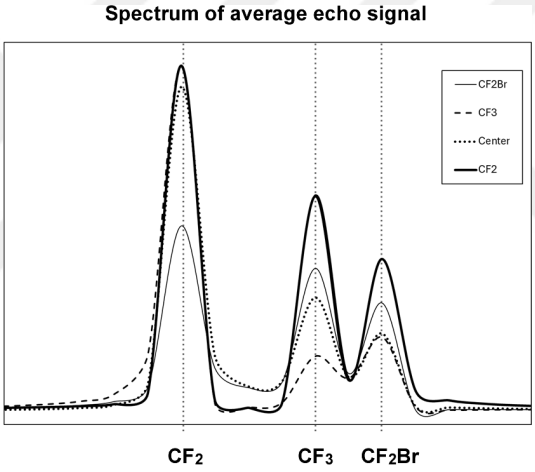

Figure 5.25 Average echo signal as a function of excitation offset obtained with BaSSI simulations. While all of the resonance lines are clearly resolvable, the CF_2 peak provided the strongest response.

To further optimize BaSSI parameters, flip angle and TR were jointly varied. Flip angles ranged from 5° to 55° in 5° increments. TR was divided into two regimes: short TR (1–5 ms), sampled every 0.1 ms; and long TR (6–10 ms), sampled every 1 ms. This dual-resolution strategy enabled a comprehensive scan of the TR–FA space, capturing both fine-scale optima and broader trends.

Figure 5.26 shows that TR = 3.4 ms and FA = 30° consistently yielded the highest SNR in the short-TR regime. Although TR = 8 ms offered a slight increase in SNR, it incurred a 2.35× longer scan time with only 2% gain. Based on this trade-off, TR = 3.4 ms and FA = 30° were selected as optimal for subsequent simulations and sequence implementation.

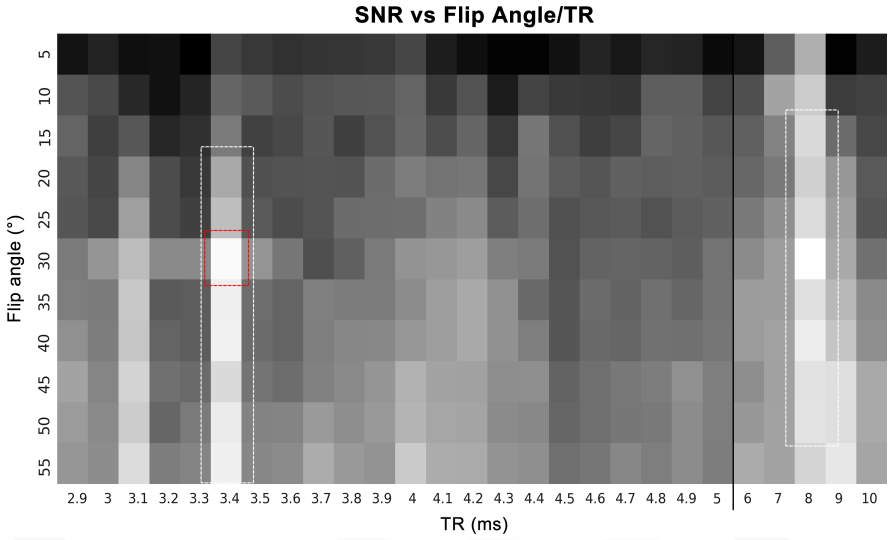

Figure 5.26 Simulated SNR landscape as a function of flip angle and repetition time for BaSSI. Two regimes of optimal SNR can be distinguished: a short-TR regime (< 5 ms), and a long-TR regime (5–10 ms). The short-TR regime exhibits a local maximum at TR = 3.4 ms and FA = 30°, which provides the highest SNR for rapid acquisitions. The global maximum is found at TR = 8 ms and FA = 30°, but offers only a marginal (2%) improvement at the cost of a 2.35× longer scan time.

5.4.3 In-silico Assessment of Magnetization

BaSSI is designed for high-resolution spectroscopic imaging applications where detecting very small amounts of contrast agent is critical. Typical experiments involve acquisition of a 64×64 k-space matrix, corresponding to 1 mm or 2 mm in-plane resolution depending on the FOV. To fully sample k-space, the core BaSSI sequence was repeated once per encoding step, resulting in 4096 TRs for a 64×64 acquisition. With a TR of 3.0 ms, the total acquisition time was approximately 12 seconds.

Because this sequence operates with a short, fixed TR and no inter-repetition recovery, the magnetization evolves under transient conditions. The net magnetization may decrease significantly in the early TRs before stabilizing into a steady state. This non-equilibrium evolution alters signal strength across k-space and introduces asymmetries that affect image reconstruction.

To characterize this behavior, BaSSI was simulated with PFOB as the spin system. The Runge-Kutta integration framework (Section 5.1) was used to compute signal evolution over 512 TRs. Figure 5.27 shows the normalized peak signal for each repetition.

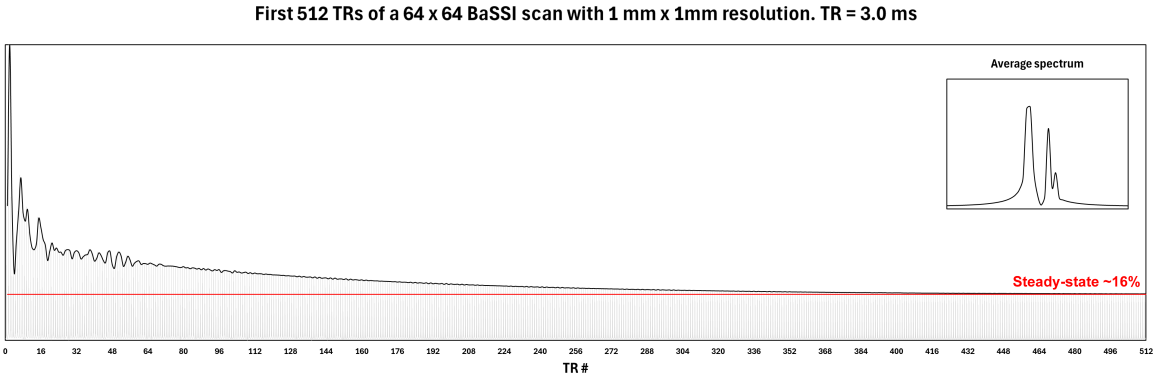

Figure 5.27 The first 512 repetitions of a full simulation of a 64×64 BaSSI acquisition of PFOB with in-plane resolution set to 1 mm $\times$ 1 mm and TR set to 3 ms. After a few hundred iterations magnetization of BaSSI approaches to steady-state conditions and maintains a signal level of 16%.

The simulation shows a steep decline in signal amplitude during the first 100 TRs, falling to roughly 30% of the initial value. After this initial decay, magnetization continues to decline slowly and stabilizes around 16% by iteration 500. This transient phase affects k-space weighting and must be considered when selecting acquisition order and reconstruction methods.

5.4.4 Acquisition Strategy and PSF Analysis

The magnetization dynamics simulated in the previous section revealed significant transient decay in the early phase of the BaSSI acquisition. If left unaddressed, this transient behavior can introduce uneven signal weighting in k-space, degrading the spatial resolution and introducing artifacts. In conventional Cartesian acquisitions, such effects are often seen as strike artifacts, which are streaks or directional blurring that stem from uneven signal contributions along different phase-encoding lines. These artifacts were a known limitation of F-uTSI and motivated a redesign of the k-space trajectory for BaSSI.

To mitigate the effects of early transient decay observed in BaSSI, the sequence was designed to employ a pseudo-spiral phase encoding strategy. Instead of sampling k-space in linear or symmetric Cartesian order, BaSSI acquired lines in a spiral pattern that originated at the center of k-space and gradually expanded outwards. This design ensured that the high-SNR, low-frequency components, which are most critical for image contrast, were acquired early, while outer high-frequency encodes, which are more susceptible to decay and noise, were acquired later. By frontloading the acquisition with contrast-dominant signal content, BaSSI effectively reduced the visual impact of transient signal fluctuations on image quality.

The specific trajectory followed a discretized Fibonacci spiral, which incrementally increased radial distance while rotating by the golden angle ($\approx 137.5°$). Although inspired by continuous spiral geometry, the trajectory consisted of discrete Cartesian k-space coordinates and was therefore more accurately described as a *pseudo-spiral* (Figure 5.28). The result was a quasi-isotropic, space-filling sampling pattern that integrated seamlessly with Cartesian reconstruction methods while retaining the radial symmetry and encoding efficiency of true spiral designs.

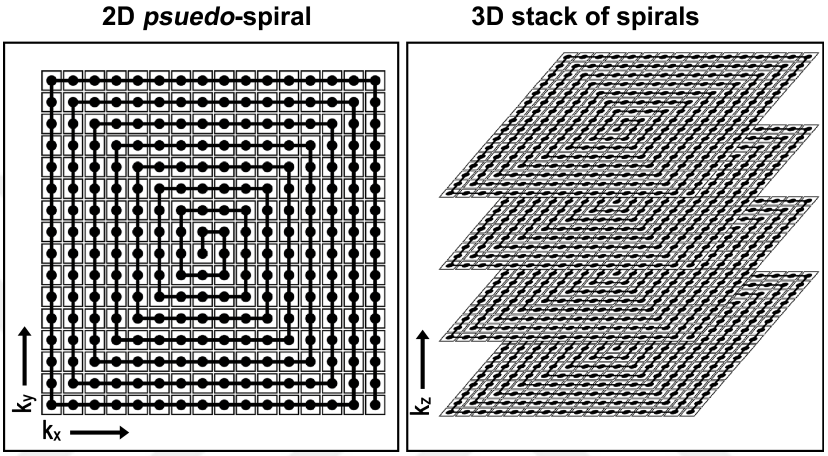

Figure 5.28 BaSSI employs a 2D *pseudo*-spiral k-space trajectory that samples discrete k-space points. For 3D, a stack of spirals is used by adding phase encoding along the longitudinal axis.

Simulations confirmed that the spiral trajectory substantially reduced structured artifacts caused by transient magnetization decay. Because k-space lines were sampled in an isotropic pattern, temporal variations in signal were spread uniformly across all directions, avoiding directional streaking. Furthermore, spiral encoding enabled 3D acquisitions by stacking multiple spiral planes, using phase encoding along the slice axis.

To quantify the benefits of signal stabilization, we evaluated the PSF under two scenarios: (1) acquisition without dummy scans, and (2) acquisition after 500 dummy iterations. Dummy scans are repeated TR cycles at the start of the sequence that are not used for signal acquisition. These allow the magnetization to reach steady state before sampling k-space.

As seen in Figure 5.29, dummy scanning significantly improved the sharpness of the PSF. Without dummy scans, central PSF values exhibited 4% signal spillover due to early transient signal decay. After 100 dummy scans, this error dropped below 1%. With 500 dummy scans, PSF broadening became negligible ($<0.025\%$), indicating near-ideal spatial resolution.

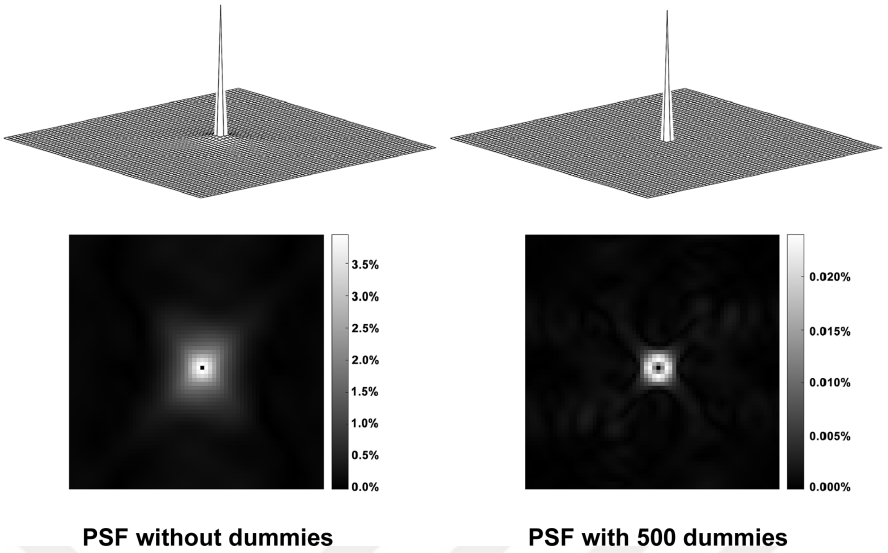

Figure 5.29 PSF after 500 dummy iterations was notably sharper than PSF obtained without dummy iterations. *Note: central points with the highest intensity are excluded from the scaling.*

However, dummy scans come at a cost. Each 100 iterations added approximately 0.35 s to the scan time. For 500 dummy scans, the overhead was 1.75 s, which is about 12% of the total scan time for a 64×64 acquisition. Moreover, initial TRs yielded the highest signal amplitudes; discarding them reduced total integrated signal and resulted in a 3.5% decrease in effective sensitivity. To assess this tradeoff, we computed the imaging efficiency, defined as $\mathrm{SNR}/\sqrt{T_{scan}}$. The result, plotted in Figure 5.30, showed that dummy scans offered diminishing returns: while PSF sharpness improved significantly, the overall imaging efficiency decreased due to time and signal losses.

Ultimately, BaSSI was implemented without dummy scans. While this decision introduced minor PSF broadening, it preserved sensitivity and scan speed, which are critical factors in low-SNR ^{19}F imaging. The pseudo-spiral strategy of BaSSI thus balanced signal preservation, artifact suppression, and practical feasibility.

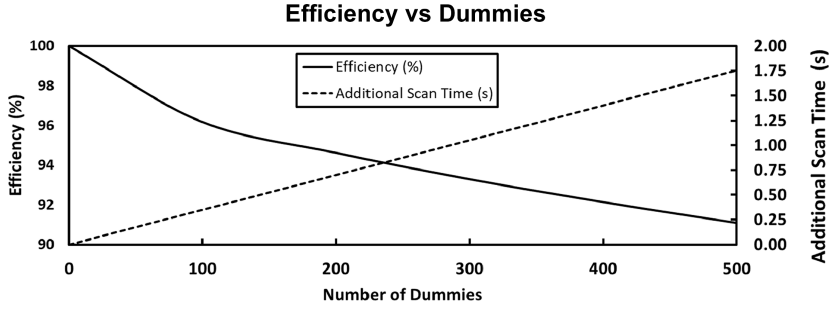

Figure 5.30 Imaging efficiency of BaSSI decreases with an increasing number of dummy scans.

5.5 Implementation of Sequences in MR System Software

F-uTSI and BaSSI were implemented on a Philips Achieva 3.0T clinical MR scanner using the proprietary PARADISE framework (Philips Application Research And Development Integrated Sequence Environment), which is provided to academic collaborators under a research agreement with Philips Healthcare. PARADISE is a virtualized development and simulation environment that faithfully replicates the architecture of commercial Philips MR systems, offering a complete toolchain, including compilers, simulators, instruction sets, and diagnostic utilities, for prototyping, testing, and deploying custom sequences in a controlled, safety-compliant setting.

The implementation followed a modular two-layer model:

- The **pdf** (parameter definition file) layer specifies sequence parameters, GUI components, default values, and input validation routines.
- The **mpf** (machine programming file) layer translates validated parameters into hardware-level instructions defining RF, gradients, readout timing, and reconstruction.

Over 120 source files were modified to implement F-uTSI and BaSSI, enabling:

- Custom GUI controls for enabling F-uTSI and BaSSI modes
- Input validation for new sequence parameters
- k-space trajectories for spectroscopic and sparse encoding
- Echo-train reversal logic to suppress strike artifacts
- Extended spectral bandwidth, resolution, and offset frequency support
- Spectral integration-based reconstruction
- Reconstruction domains with optional time-/spatial-domain filtering
- Data export for up to 256 slice-select encoding points
- Support for a custom-built $^{1}H/^{19}F$ RF coil

An example user interface is shown in Figure 5.31, illustrating the configurable parameters for sequence and reconstruction.

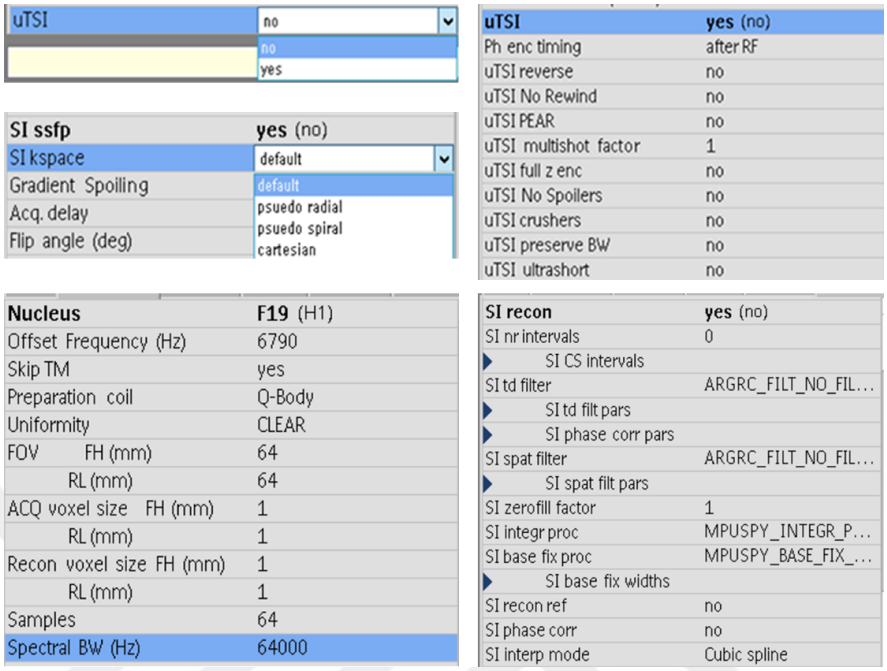

Figure 5.31 User interface to enable and control F-uTSI and BaSSI.

After source modification, the updated sequences were compiled into platform-compatible binaries using the PARADISE toolchain and deployed to both test and clinical systems via the Philips patching mechanism. This deployment process ensured seamless integration with the scanner software stack, retaining full compatibility with clinical workflows and maintaining compliance with hardware safety constraints and regulatory standards.

All timing-critical sequence elements—including RF excitation, gradient ramping, and acquisition windows—were initially calculated analytically based on system specifications and design targets. These values were then validated empirically using internal scanner diagnostics and waveform monitoring tools. In general, system behavior closely matched simulation results and analytical estimates. However, one notable discrepancy was observed in the timing of the phase-encoding gradients: for a 64×64 scan at 1 mm resolution, the predicted step time of 0.87 ms—derived from gradient amplitude and slew rate limits—was reduced to 0.6 ms in practice. This deviation resulted from a proprietary waveform optimization routine embedded in the Philips gradient controller firmware, which dynamically compresses trapezoidal shapes based on trajectory symmetry and hardware duty cycle thresholds.

Finalized timing parameters calculated for a standard BaSSI scan are summarized in Figure 5.32. The excitation employed a 3.8 μs rectangular hard pulse at a nominal flip angle of 30°, delivering a broadband excitation profile spanning 26 kHz. The acquisition window opened at 0.608 ms post-RF, leaving sufficient margin to avoid contamination from residual eddy currents. The minimum achievable repetition time (TR) was 2.9 ms, consistent with the timing constraints described in Section 5.4.1. For a standard 64×64 acquisition with 1 kHz spectral resolution and no dummy scans, the total scan time was 11.9 s, closely matching theoretical predictions and confirming the accuracy of the simulation-guided implementation process.

Total scan duration	00:11.9
Act. TR/TE (ms)	2.900 / 0.608
ACQ matrix M x P	64 x 64
ACQ voxel MPS (mm)	1.00 / 1.00 / 300.0
REC voxel MPS (mm)	1.00 / 1.00 / 300.0
Scan percentage (%)	100
Min. TR/TE (ms)	2.900 / 0.608
Spectral resolution (Hz/p...	1000
Readout duration (ms)	1
RF BW Ex/Refo (Hz)	26041.000 / 4772.000
RF Dur Ex/Refo (ms)	0.038

Figure 5.32 Timing parameters for a 64×64 BaSSI acquisition using a 30° hard pulse.

Correctness of k-space logic and sequence timing was further verified using system-generated visualizations. Figure 5.33 shows an 8×8 phase encoding diagram, where gradient amplitude and slew rate increase incrementally to span k-space linearly. The readout axis is k_y, and k_x is phase-encoded. Sampling follows Scenario #5 (Section 5.3.6), with symmetric, progressively shifted lines. These diagrams confirmed agreement between theoretical design and executed waveforms.

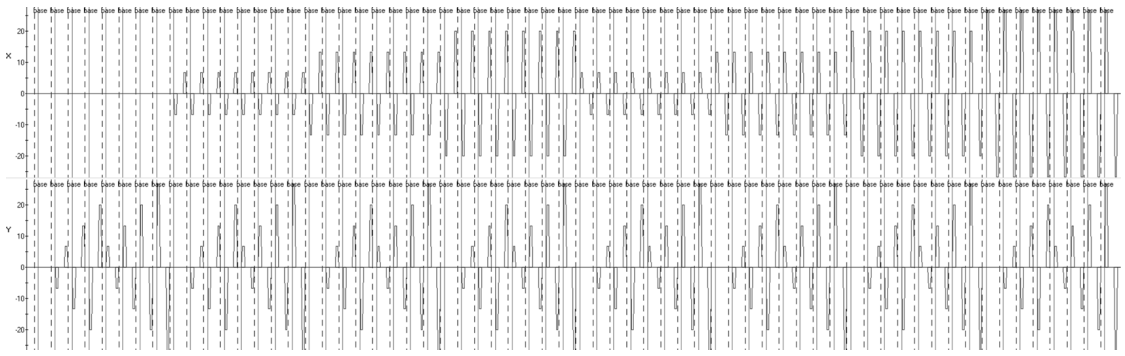

Figure 5.33 Validation using the phase encoding diagram generated by the system software.

All project-specific logic was isolated from proprietary source files to preserve modularity and ease of debugging. This also facilitates sharing of non-confidential components. For example, the routine that calculates pseudo-radial encoding steps (Figure 5.34) was developed independently and can be distributed without violating IP agreements.

```
if (MPF_SPY->kspace == MGUSPY_SI_KSPACE_PSEUDO_RADIAL)
{

    double delta_theta = 360.0 / (nroflines - 1);
    double errmarg = 0.0001;

    for (int line = 0; line < nroflines; line++)                    //`UGN1_uTSI_nr_of_lines // loop over number of radial lines
    {
        double theta = line * delta_theta + errmarg;                // angle of radial line
        theta = theta - 360.0 * floor(theta / 360.0);               // calculate modulo
        double thetarad = theta * PI / 180.0;
        double tantheta = tan(thetarad);

        double y_int = floor(max_x * tantheta);                     //intersection point of radial line and y axis
                                                                    //int y_int_i=(int) y_int;
        int qux = qspy_quadr(theta, 0);                             // quadrant coefficients of x and y
        int quy = qspy_quadr(theta, 1);

        std::vector<int> k_line_x_buff;
        std::vector<int> k_line_y_buff;

        k_line_x_buff.clear();
        k_line_y_buff.clear();

        for (int point = 0; point < nr_line_points; point++)
        {
            double x_value = point;
            double y_value = fabs(x_value * tantheta);

            if (fabs(y_int) <= max_y)
            {
                x_value = point;
                y_value = fabs(x_value * tantheta);
            }
            else
            {
                y_value = point;
                x_value = fabs(y_value / tantheta);
            }

            k_line_x_buff.push_back(qux * floor(x_value));
            k_line_y_buff.push_back(quy * floor(y_value));
        }

        for (int msf = 0; msf < mshotfactor; msf++)
        {
            for (int tf = 0; tf < turbofactor; tf++)
            {
                int index = msf + mshotfactor * tf;
                int reverse_index = mshotfactor * (turbofactor - tf - 1) + msf;

                k_line_x_even.push_back(k_line_x_buff[index]);
                k_line_y_even.push_back(k_line_y_buff[index]);

                if (MPF_TSI->uTSI_reverse == YES)
                {
                    k_line_x_odd.push_back(k_line_x_buff[reverse_index]);
                    k_line_y_odd.push_back(k_line_y_buff[reverse_index]);

                }
                else
                {
                    k_line_x_odd.push_back(k_line_x_buff[index]);
                    k_line_y_odd.push_back(k_line_y_buff[index]);
                }
            }
        }
        k_line_x_buff.clear();
        k_line_y_buff.clear();
    }
}
```

Figure 5.34 Custom routine for calculating *pseudo*-radial encode steps.

5.6 Summary

This chapter detailed the design and implementation of two pulse sequences—F-uTSI and BaSSI. Both sequences were developed to address the unique challenges of ^{19}F imaging, including broad spectral dispersion, low tracer concentrations, and relaxation-induced signal loss.

The chapter began by introducing the simulation framework used to evaluate excitation uniformity, magnetization dynamics, and timing feasibility under realistic conditions. Bloch equation solvers based on Runge-Kutta integration were implemented to simulate RF pulse behavior across broad frequency ranges and varying relaxation parameters. This allowed systematic testing of amplitude- and frequency-modulated pulses, including multi-band excitation strategies designed to efficiently cover the complex spectral signatures of compounds like PFOB.

F-uTSI was designed as a CPMG-style echo-train sequence with full 2D and 3D phase encoding. Its performance was evaluated *in silico* through detailed timing analysis and PSF modeling. Particular attention was given to acquisition strategies, including reversed averaging and pseudo-radial k-space trajectories to suppress structured artifacts. F-uTSI demonstrated robust spectral fidelity and moderate scan times.

BaSSI was developed as a minimalist, high-efficiency alternative. Leveraging ultrashort TR and non-selective excitation, BaSSI replaced echo trains with FID readouts and used a pseudo-spiral k-space trajectory to prioritize early acquisition of high-SNR data. Parameter space exploration revealed that a flip angle of 30° and TR = 3.4 ms offered an optimal balance between SNR and acquisition time, outperforming longer-TR configurations with only marginal signal gains but significantly greater time penalties.

Both sequences were fully implemented on a 3.0 T clinical Philips MR system using the PARADISE development platform. Custom user interface controls, parameter validation routines, and reconstruction pathways were integrated, and system timing behavior was empirically verified. The resulting sequence binaries maintained full compliance with clinical safety and operational standards, enabling routine use in phantom, postmortem, and animal experiments.

Together, F-uTSI and BaSSI form an effective toolset for ^{19}F spectroscopic imaging. The next chapter presents experimental results validating these sequences across a range of imaging scenarios.

6. EXPERIMENTAL VALIDATION OF F-uTSI AND BaSSI

This chapter presents the experimental validation of the spectroscopic imaging sequences developed in this work. Specifically, the performance of F-uTSI and BaSSI was evaluated under controlled phantom and preclinical conditions designed to replicate key challenges of ^{19}F MRI, namely, low SNR, large chemical shift dispersion, and spatial–spectral trade-offs inherent to non-proton imaging.

F-uTSI and BaSSI represent distinct yet complementary approaches to spectroscopic imaging. F-uTSI employs a rapid spin-echo train combined with pseudo-Cartesian or pseudo-radial phase encoding strategies. In contrast, BaSSI is a free induction decay (FID)-based method that uses pseudo-spiral sampling to efficiently encode both spatial and spectral dimensions in a discretized readout.

These sequences were developed to overcome limitations of conventional ^{19}F MRI, particularly the chemical shift artifacts associated with fluorinated compounds and the difficulty of detecting low-concentration signals under time constraints. Through careful sequence timing, excitation modeling, and encoding strategy, both F-uTSI and BaSSI aim to enable artifact-free, high-fidelity spectroscopic imaging with clinically feasible scan times.

To evaluate the efficacy of the developed sequences, a series of phantom experiments were conducted to quantify key performance metrics, including SNR, spatial fidelity, and sensitivity to small quantities of contrast material.

The phantom configurations used for sequence optimization and benchmarking were based on undiluted bulk samples of PFOB. Multiple acquisition parameters — particularly timing variables, flip angle, number of signal averages, RF pulse shape, and offset frequency—were systematically varied to identify optimal settings.

For benchmarking, the results obtained with F-uTSI and BaSSI were compared directly to the 3D UTE bSSFP sequence [145], which is widely used in preclinical fluorine imaging due to its acquisition efficiency and practical robustness.

The remainder of this chapter provides a detailed account of the experimental methodology, including phantom construction, imaging setup, data acquisition, post-processing workflow, and quantitative analysis procedures used for performance benchmarking.

6.1 Methods

6.1.1 Contrast Media and Phantom Materials

This study primarily utilized contrast agents based on PFOB, one of the earliest PFCs introduced for medical use. Initially developed as a blood substitute [165], PFOB was later evaluated as a contrast agent in X-ray imaging [50, 51, 166]. It is among the few PFCs that have undergone multiple phases of human use evaluation [49], [167–169].

In addition to PFOB, perfluoro-15-crown-5 ether (PFCE) was used in several experiments. Although not biocompatible, PFCE offers a single-resonance ^{19}F spectrum and was employed as a reference agent during sequence development.

PFOB and PFCE were purchased from Fluorochem Ltd. (Hadfield, UK) at purities of 99.5% and 99%, respectively. PFOB underwent further purification and sterilization to eliminate cytotoxic impurities observed during cellular uptake studies [170]. Their molecular structures and NMR spectra of PFOB and PFCE are shown in Figure 6.1, whereas their respective physical properties are given in Table 6.1.

Perfluoro-tert-butyl cyclohexane (PTBCH), also known as ABL-101 or Oxycyte, was also considered due to its favorable spectral properties and demonstrated biocompatibility [171]. Although the compound is patented as a contrast agent for ^{19}F imaging [7], [10], its experimental use in this work was not feasible. Access to clinical-grade material was restricted due to its exclusive allocation to ongoing clinical trials investigating therapeutic applications in traumatic brain injury [168], [169].

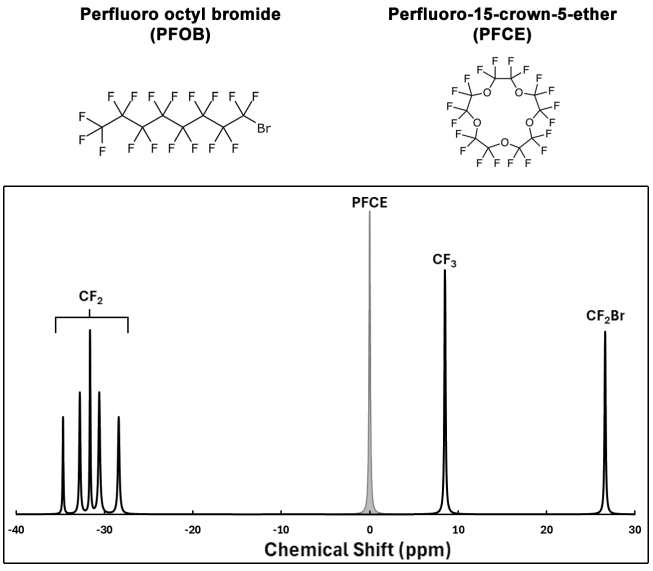

Figure 6.1 Molecular structures and NMR spectra of PFOB and PFCE.

Table 6.1
Molecular formula, molecular weight, density, and boiling point of PFOB and PFCE.

Compound	Formula	Mol. Weight (g/mol)	Density (g/mL)	Boiling Point (°C)
PFOB	C_8BrF_{17}	498.96	1.93–1.98	142–144
PFCE	$C_{10}F_{20}O_5$	580.07	1.30–1.78	145

PFOB was used in its bulk liquid form for sequence optimization and benchmarking, as presented in this chapter, and in polymer microspheres for anatomic localization and gastrointestinal tract imaging described in the applications chapter. Emulsified nanoparticles of both PFOB and PFCE were used *in vivo* for imaging with orally administered contrast media. Targeted PFOB emulsions, functionalized for integrin binding, were used for imaging angiogenesis induced by tumor growth and menstrual cycling in small animal models. The preparation of these contrast materials is detailed in the following sections.

6.1.1.1 Bulk Material-Based Phantoms. Bulk phantoms were prepared by dispensing undiluted PFOB into centrifuge tubes (0.1 mL capacity). In early proof-of-concept experiments, non-sterile material was used; subsequent quantitative studies utilized purified PFOB.

Each sample was weighed with a microbalance to determine volume and mass precisely (Table 6.2). Particular attention was given to the sample height to facilitate slice-selective imaging. As shown in Figure 6.2, samples with volumes less than 0.10 µL exhibited heights under 1 mm, ensuring confinement to a single imaging slice. This enabled a fair comparison between 2D spectroscopic and 3D imaging protocols.

Table 6.2
Volume and weights of undiluted bulk PFOB phantoms.

Volume (μL)	Weight (mg)
0.05	0.101
0.1	0.196
0.5	0.954
1	1.937
10	19.110

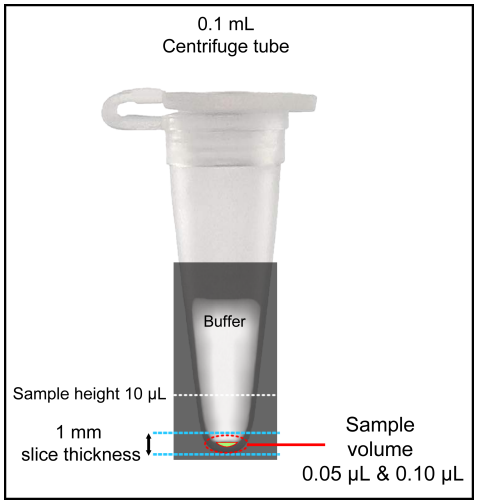

Figure 6.2 Sample height of bulk phantoms. Small phantoms fit within a thin slice.

6.1.1.2 Emulsions. Emulsified nanoparticles were synthesized with a PFC-filled core and a phospholipid shell designed to mimic the structure and behavior of biological liposomes (Figure 6.3). The lipid formulation consisted of distearoylphosphatidylcholine (DSPC), cholesterol, polyethylene glycol-conjugated distearoylphosphatidylethanolamine (PEG2000-DSPE), and a maleimide-functionalized PEG2000-DSPE, which allowed for subsequent biofunctionalization.

For formulations based on perfluoro-15-crown-5 ether (PFCE), the maleimide-functionalized lipids were substituted with DSPE-Gd-DOTA to investigate the effects of gadolinium-induced T_1 shortening on the fluorine signal. In addition, rhodamine-PE was incorporated to enable fluorescence-based detection and validation of nanoparticle uptake.

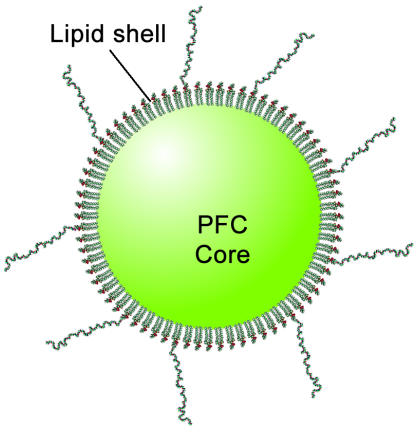

Figure 6.3 Emulsified PFC nanoparticle with a lipid shell and perfluorocarbon core. The lipid shell is made of DSPC, cholesterol, PEG2000-DSPE. maleimide-functionalized PEG2000-DSPE.

Nanoparticles were prepared using the well-established thin lipid film hydration technique [172]. All lipid components were first dissolved in a 4:1 (v/v) chloroform/ethanol mixture, ensuring uniform mixing of the hydrophobic components. The resulting solution was evaporated under rotary conditions at 50 °C to form a thin lipid film, which was dried under a gentle stream of nitrogen gas to remove residual solvent.

After solvent was fully evaporated, the dried lipid film was subsequently hydrated with 22 mL of pH 7.2 Tris(hydroxymethyl)aminomethane (THAM) buffer at 60 °C with constant agitation. Following hydration, 4.51 g of liquid PFOB was added to the aqueous suspension under ultrastirring to promote encapsulation within the forming vesicles.

To reduce droplet polydispersity and enhance encapsulation efficiency, the emulsion was passed through a high-pressure microfluidizer at 65 °C with a circulation frequency of 1 Hz for a total of 10 minutes. This step was critical for achieving uniform nanoparticle size and improving long-term stability. The same homogenization protocol was applied to PFCE-based emulsions, which incorporated the modified lipid formulation containing rhodamine and gadolinium. The final PFCE emulsions exhibited a faint red hue, visually indicating the presence of the rhodamine fluorophore.

To facilitate molecular targeting of angiogenic tissue, emulsions were biofunctionalized with cyclic RGD peptides specific to $\alpha_v\beta_3$ integrins, which are overexpressed in neovasculature. The cyclic RGD peptide was deacetylated using a buffered hydroxylamine solution (HEPES/EDTA, pH 7.0), then immediately reacted with the maleimide-functionalized lipids at pH 6.7. The mixture was gently vortexed to ensure homogeneous peptide conjugation and stored overnight at 4 °C under nitrogen atmosphere to preserve peptide integrity and nanoparticle stability.

The final nanoparticle diameter, as determined by dynamic light scattering (DLS), was approximately 220 nm with a polydispersity index below 0.2. Morphological characterization using cryogenic transmission electron microscopy (cryo-TEM) revealed a well-defined lipid shell and a uniform distribution of encapsulated PFC droplets. Approximately 75% of the vesicles contained encapsulated PFOB or PFCE, while the remaining 25% consisted of partially filled or empty lipid vesicles which are also known as liposomes (Figure 6.4).

The emulsions demonstrated high colloidal stability and retained their structural integrity for several weeks when stored at 4 °C, making them suitable for imaging and biodistribution studies.

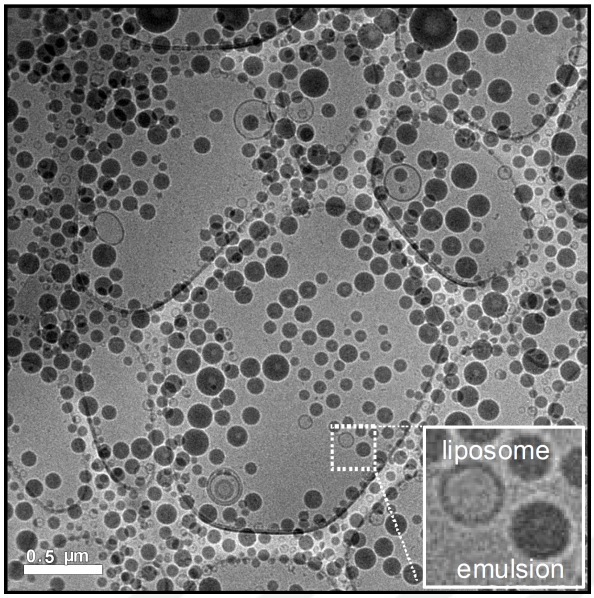

Figure 6.4 Cryo-TEM images of PFC emulsions show that about 75% of particles are filled with PFC. The rest of the particles are either partially filled, or empty vesicles also known as liposomes.

6.1.1.3 Polymer Microbubbles. Polymer-encapsulated PFOB microbubbles (Figure 6.5) were prepared using a solvent evaporation method based on the protocol by Pisani et al. [173], widely adopted for fabricating biodegradable microspheres containing hydrophobic or fluorinated cores.

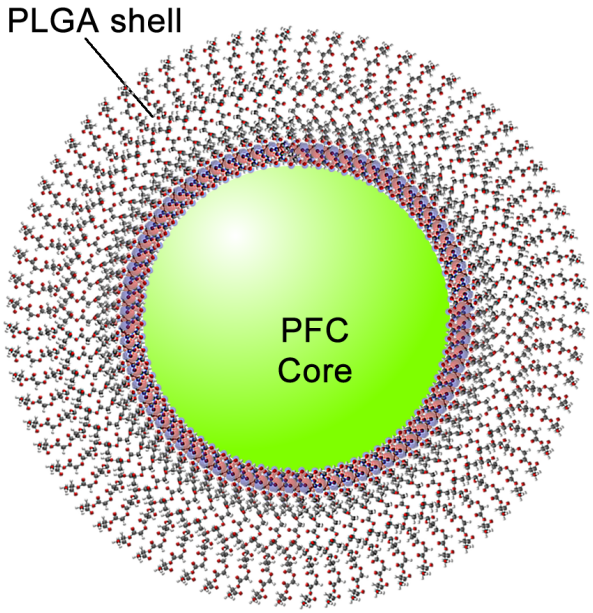

Figure 6.5 PLGA microbubbles filled with perfluorocarbon (PFC) cores.

Briefly, 100 mg of poly(lactic-co-glycolic acid) (PLGA) was dissolved in 4 mL of dichloromethane (DCM), and 60 µL of neat PFOB was added under magnetic stirring to form a uniform dispersion. This organic phase was then slowly introduced into 20 mL of an aqueous solution containing 1.5% sodium cholate, a biocompatible surfactant, to stabilize the emulsion.

Emulsification was carried out using an Ultraturrax T18 high-shear disperser at 24000 rpm for 1 minute under ice-cold conditions (0 °C) to minimize thermal degradation and early solvent evaporation. The resulting emulsion was then stirred at room temperature for 3 hours to allow complete DCM evaporation, leading to the solidification of the PLGA shell around the dispersed PFOB core.

The hardened microspheres were washed by dilution with deionized water and centrifugation at 2000 rpm for 10 minutes at 4 °C. The pellet was resuspended in 5 mL of distilled water by gentle vortexing to obtain a stable suspension of PFOB-loaded PLGA microbubbles.

Particle sizing using a Coulter counter revealed a mean diameter of 2.4 ± 1.5 µm (Figure 6.6). The relatively broad size distribution, typical of emulsification-based production, was considered suitable for post-mortem biodistribution and anatomical correlation studies, where neither long circulation times nor vascular entrapment were critical requirements.

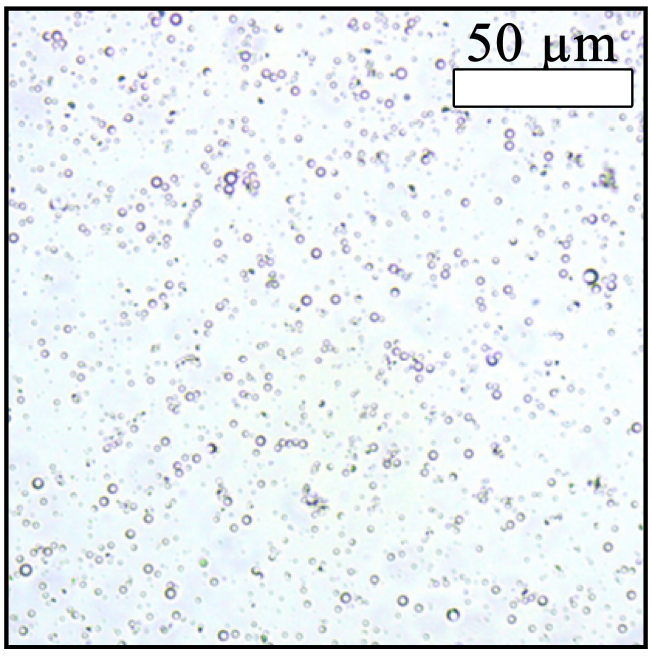

Figure 6.6 Optical microscopy images of PLGA microbubbles filled with PFOB.

6.1.2 Animal Studies

To evaluate the applicability and performance of F-uTSI and BaSSI, both live and postmortem animal experiments were conducted. Wherever feasible, live animal use was minimized in favor of phantoms and postmortem specimens. Live experiments were reserved for essential studies requiring targeted imaging or the assessment of contrast agent biodistribution.

All procedures were performed under strict regulatory oversight and were approved by the relevant medical-ethical commissions of the participating institutions. Experimental protocols were designed to minimize stress, discomfort, and procedural invasiveness.

Postmortem imaging served as the primary modality for protocol development and optimization. Small animal specimens, which were previously used in unrelated research, were repurposed to reduce the need for additional animal sacrifice. These studies provided a physiologically representative and stable tissue environment for evaluating signal detectability and spatial localization. They also allowed for systematic testing of sequence parameters, such as echo spacing, spectral integration, and reconstruction methods, without the effects of physiological motion or metabolic variation.

Live animal experiments were conducted specifically to assess targeted imaging and biodistribution, primarily using emulsified nanoparticles labeled with targeting moieties such as RGD peptides. These studies demonstrated the utility of ^{19}F spectroscopic imaging in visualizing biological processes like angiogenesis and mapping the accumulation of perfluorocarbon-based tracers.

Anesthesia was administered either via inhalation of isoflurane (1–3% in medical air at 0.4 L/min) delivered through a respiratory mask or by intraperitoneal injection of a KMA cocktail made of ketamine (75 mg/kg), medetomidine (1.0 mg/kg), and atropine (0.04 mg/kg). Vital signs, including core temperature, respiration, and ECG, were continuously monitored using a physiology monitoring system equipped with a heated bed, fiberoptic temperature probe, respiratory cushion, and surface electrodes.

Each imaging session was limited to a maximum of four hours. At the conclusion of each session, animals were euthanized humanely by cervical dislocation, in accordance with institutional guidelines. Postmortem, subjects were either preserved for additional imaging or underwent necropsy for histological analyses.

6.1.3 Measurement Setup

All experiments were conducted using a 3.0 T clinical magnetic resonance (MRI system (Achieva®, Philips Healthcare, Best, The Netherlands), equipped with a dual-tuned $^{1}H/^{19}F$ RF coil (Rapid Biomedical GmbH, Rimpar, Germany) and a high-performance gradient subsystem capable of delivering 40 mT/m maximum gradient strength and a 235 T/m/s slew rate.

To ensure accurate and reproducible sample positioning, custom holders were fabricated via additive manufacturing (3D printing) to match the internal geometry of the RF coil and accommodate specific phantom or animal models (Figure 6.7). These fixtures were designed to align the imaging volume precisely at the gradient isocenter and within the homogeneous region of the RF transmit and receive fields. This not only maximized SNR but also minimized artifacts arising from gradient non-linearity, magnetic field inhomogeneity, and RF field distortions.

Consistent sample alignment across sessions significantly improved experimental reproducibility and facilitated longitudinal studies by enabling consistent slice prescription, registration, and ROI placement. Moreover, this setup streamlined post-processing workflows by reducing the need for extensive manual alignment or normalization steps, supporting automated evaluation of image quality, signal uniformity, and quantification metrics across datasets.

Together, the integration of clinical-grade imaging hardware, dual-resonant RF coil technology, and precision positioning strategies established a robust and reproducible platform for evaluating the F-uTSI and BaSSI sequences under controlled phantom conditions as well as in preclinical imaging studies.

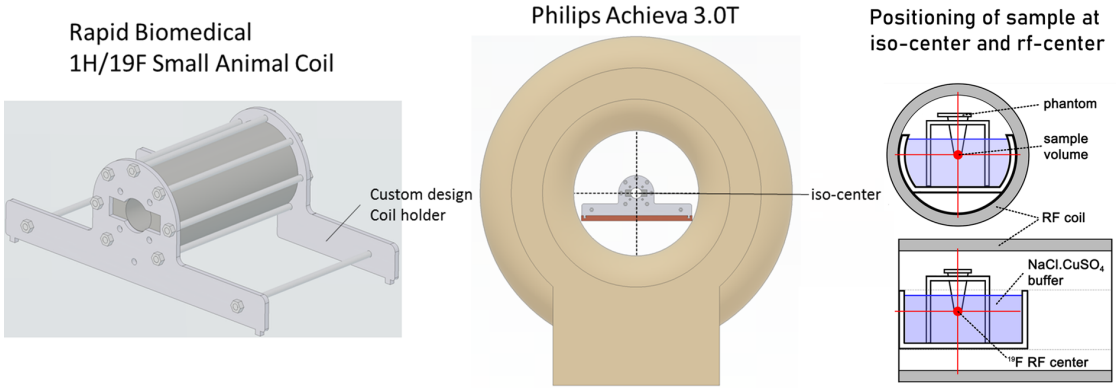

Figure 6.7 Setup for precise phantom measurements.

6.1.4 Thermal Effects on SNR and Pre-Acquisition Stabilization

Thermal buildup within the scanner bore and gradient system can introduce subtle but measurable variations in signal stability, particularly during extended scan sessions involving repeated RF excitation and gradient switching. As the system accumulates heat with each acquisition, small shifts in thermal noise characteristics and amplifier performance may occur. While typically modest, these changes can gradually reduce the observed SNR and impact the reproducibility of quantitative measurements.

To characterize the extent of thermal drift, a 12-hour experiment was conducted in which a gradient echo sequence, with moderate RF and gradient duty cycle, was continuously repeated. Each scan had a duration of approximately one minute, and the SNR of each repetition was quantified and plotted over time (Figure 6.8).

During the first hour of acquisition, a progressive SNR reduction of approximately 12% was observed, attributed primarily to thermal stabilization of the scanner components. Beyond this initial phase, slower, long-term variations in SNR were detected, likely reflecting gradual shifts in ambient room temperature. Despite these trends, the overall SNR remained stable within a range of ±2% relative to the post-stabilization baseline over the remaining 11 hours.

To mitigate these effects and ensure consistency in subsequent experiments, the system was allowed to reach thermal equilibrium prior to each quantitative measurement series. This was accomplished by executing 60 dummy scans over the course of one hour, effectively stabilizing the scanner's thermal state before data acquisition began.

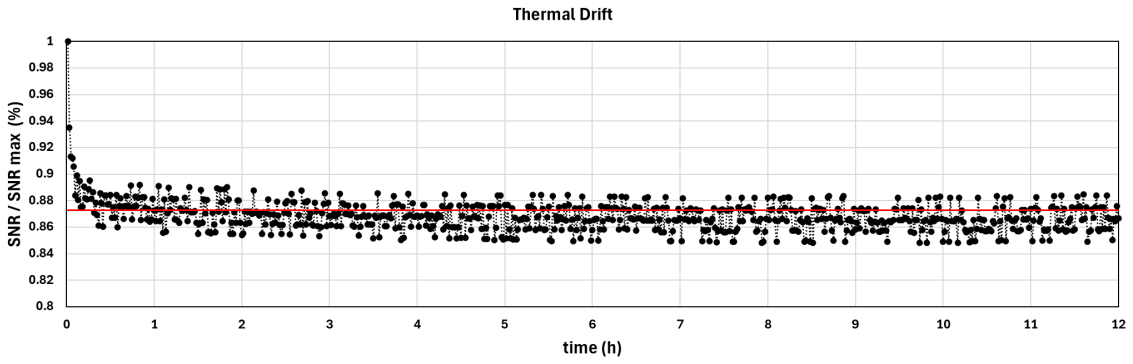

Figure 6.8 SNR measured over 12 hours of repeated scanning. The drop of 12% is observed in the first hour is due to thermal stabilization of the scanner. Long-term fluctuations remain within ±2%.

6.1.5 Experimental Methodology

All experiments adhered to a standardized acquisition and analysis pipeline designed to maximize consistency, reproducibility, and measurement accuracy across independent datasets.

Each imaging session began with manual tuning and matching of the dual-tuned RF coil to optimize energy transfer efficiency at the relevant Larmor frequency. The coil was tuned to minimize reflected RF power, targeting a reflection coefficient below 0.2% of the transmitted signal. Achieving this threshold ensured optimal excitation efficiency and minimal power loss (Figure 6.9).

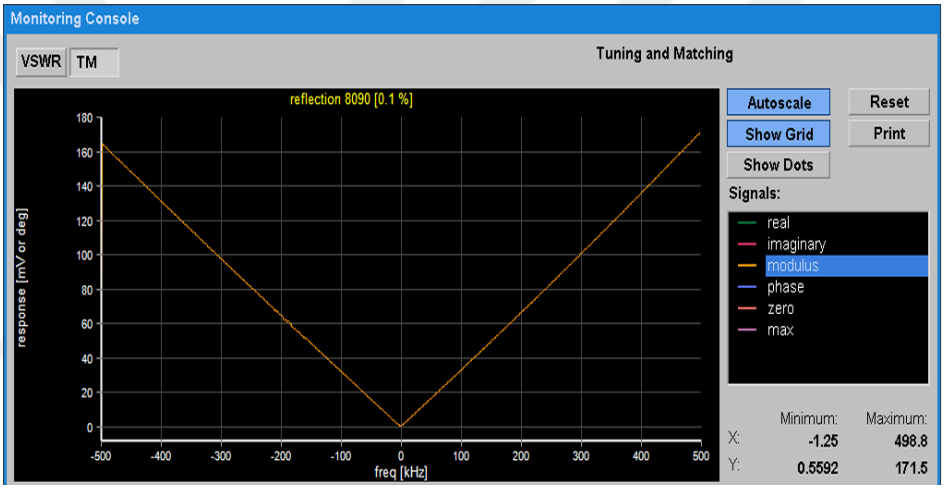

Figure 6.9 Manual tuning and matching to ensure reflected RF power remains below 0.2%.

Following coil tuning, transmit power calibration for ^{19}F was performed using a flip angle (FA) series. A series of free induction decay (FID) acquisitions were executed at nominal flip angles ranging from 10° to 210°. The resulting signal amplitudes were plotted to verify that the expected maximum occurred near 90°. If the peak was observed at a different angle, indicating either under or overdriving of the RF amplifier, the reference power scale was adjusted accordingly to match the effective flip angle with the intended excitation (Figure 6.10).

Once RF system calibration was complete, experimental measurements were acquired using either ^{1}H or ^{19}F imaging sequences. Dual-nucleus imaging was routinely employed to combine high-resolution anatomical information (from ^{1}H imaging) with molecular specificity from ^{19}F acquisitions. This enabled both co-registration and anatomical validation of fluorinated signal distributions.

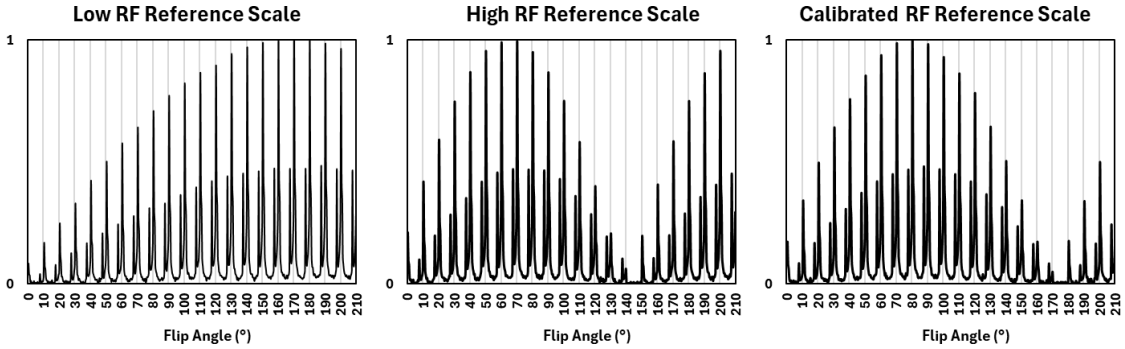

Figure 6.10 Transmit RF power is calibrated using flip angle series and monitoring signal at 90°. Low reference scale results in under-excitation, while high scale values overdrive the excitation pulse.

Image data were exported in Philips PAR/REC format, while ^{19}F spectroscopic imaging datasets were saved in XML/XSDATA format. All datasets were subsequently imported into a custom MATLAB^{TM} processing pipeline for reconstruction, visualization, and quantitative analysis [161].

SNR was computed using a rectangular region of interest (ROI) placed over the fluorinated object, and noise was estimated from multiple background ROIs in artifact-free areas of the image (Figure 6.11). In addition to SNR, object detectability was quantified using the Rose criterion (See Section 4 for details).

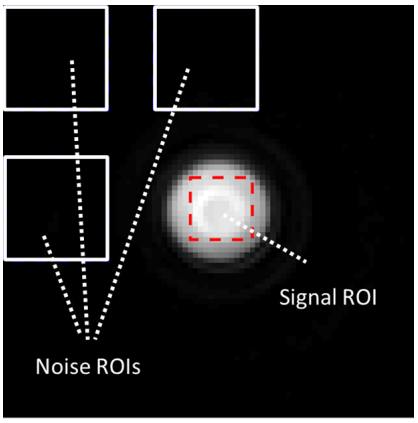

Figure 6.11 Region of interests used for quantitative analysis of signal and noise. Central ROI captures the average signal, whereas the peripheral ROIs are used for background noise estimation.

To facilitate traceability and reproducibility, final analysis results—including SNR values, Rose scores, and relevant acquisition parameters were automatically saved in comma-separated value (CSV) format. These outputs were used for batch visualization, comparative benchmarking, and statistical analysis throughout the experimental validation chapter.

6.2 Optimization of F-uTSI and BaSSI

The development of F-uTSI and BaSSI required fine-tuning of both sequence and hardware parameters to achieve high signal fidelity, efficient acquisition, and compliance with safety constraints. Optimization efforts focused on maximizing SNR while ensuring robustness to relaxation effects and hardware limitations.

For F-uTSI, the primary parameters under investigation were TR and NSA, both influencing the imaging efficiency of the sequence. In contrast, BaSSI optimization focused on the timing parameters, including the acquisition window (T_{acq}) and TR, as well as flip angle, all of which critically impact the spectral resolution and temporal efficiency of the sequence.

6.2.1 Optimized Hardware Settings

Prior to sequence optimization, key hardware parameters were swept to establish baseline settings for RF and gradient performance. Maximum RF transmit field (B_1), gradient strength, and slew rate were varied systematically, with all safety routines active to ensure compliance with IEC 60601-2-33 (edition 3.1) [174].

Gradient strength was tested from 31–35 mT/m, slew rate from 200–230 T/m/s, and B_1 from 48–55 μT. Measurements were performed on a phantom filled with bulk-phase PFOB to ensure stable signal conditions.

The optimal configuration of $B_1 = 52$ μT, gradient strength = 33 mT/m, and slew rate = 225 T/m/s offered the best trade-off between excitation efficiency, timing stability, and image quality. These values were used in all subsequent sequence optimization experiments (Figure 6.12).

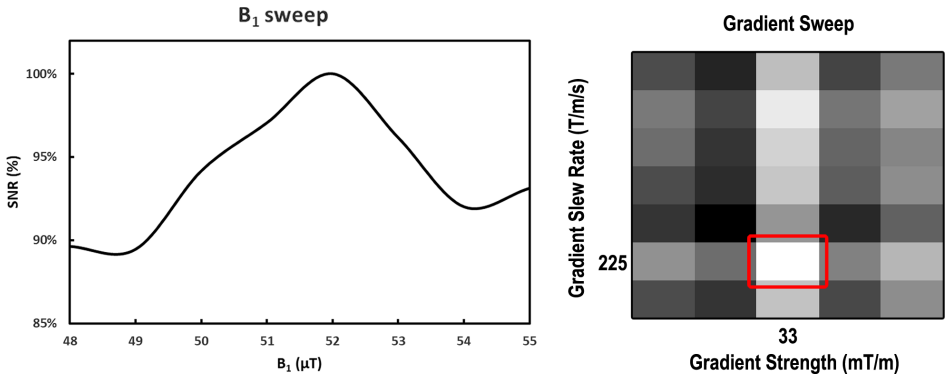

Figure 6.12 Optimal hardware settings are found experimentally using parameter sweeps.

6.2.2 Sampling Bandwidth and Spectral Resolution

As described in Section 5.1.3, both F-uTSI and BaSSI sequences support acquisition bandwidths of 32 kHz and 64 kHz. With 64 spectral points, these correspond to spectral resolutions of 0.5 kHz and 1 kHz, respectively. Alternatively, 32 samples over 32 kHz yield a 1 kHz resolution as well. These parameter combinations allow for flexible spectral encoding strategies depending on trade-offs between resolution, scan time, and signal stability.

To assess the impact of acquisition bandwidth and spectral resolution on spectral quality, randomly selected spectra from comparable acquisitions were analyzed. Figure 6.13 illustrates representative spectra targeting the CF_2 group. All spectra are aligned to the CF_2 resonance maximum for visual comparison. As seen in the figure, the high-resolution spectrum (32 kHz bandwidth with 64 points; 0.5 kHz resolution) exhibits sharper and more distinct peaks. In contrast, both lower-resolution acquisitions (1 kHz resolution) show broader peaks and some degradation in spectral definition.

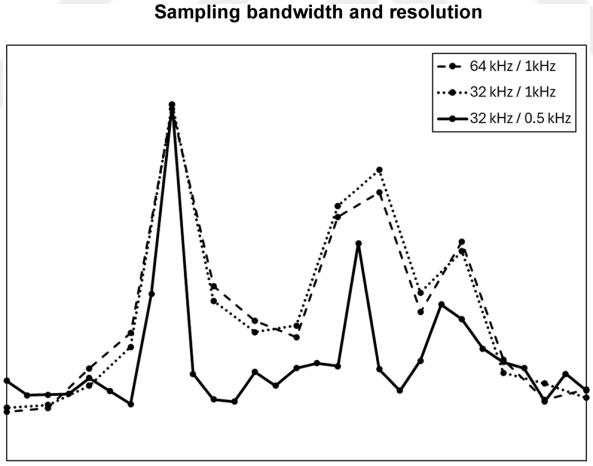

Figure 6.13 Spectra obtained with different acquisition settings. All spectra are aligned to the CF_2 peak position for direct comparison.

Despite the differences in spectral appearance, the SNR across the three acquisition schemes remained relatively similar. Based on the empirically determined optimal integration bandwidth of approximately 1.4 times the FWHM, and using non-interpolated data, the integration window spanned at most three spectral points centered around the peak. Within this window, SNR was computed for each acquisition condition (Table 6.3). This narrow but consistent window ensured that the integration captured the majority of the signal energy while minimizing the contribution of surrounding noise, enabling a fair comparison across encoding schemes.

While this may suggest that SNR is relatively robust against changes in acquisition bandwidth and resolution, such a conclusion should be drawn with caution. The effective SNR depends not only on acquisition parameters but also on experimental factors such as baseline noise, susceptibility-induced field inhomogeneities, and variations in the effective Larmor frequency and peak linewidths. These can differentially affect spectral resolution and signal integration accuracy, particularly *in vivo* or in systems with complex susceptibility distributions.

Table 6.3
SNR values for different acquisition settings.

Bandwidth / Resolution	**SNR**
64 kHz / 1 kHz	27.1
32 kHz / 1 kHz	29.3
32 kHz / 0.5 kHz	29.5

6.2.3 Optimization of F-uTSI

F-uTSI is a CPMG-based multi-spin echo sequence that generates echo trains using a 90° excitation pulse and 180° refocusing pulses. The refocusing pulse is applied with phase alternation, alternating between +90° and -90° every other echo, as prescribed by the CPMG conditions (See Appendix A.2.4 for a description of the CPMG echo train).

With the flip angles of the RF pulses fixed, the optimization experiments were performed by varying the timing parameters—particularly the TR—to assess the benefit of extended longitudinal relaxation. These variations were compared against the effect of increasing the NSA, using the imaging efficiency metric defined as $\mathrm{SNR}/\sqrt{T_{\mathrm{scan}}}$.

Data with varying NSA and TR was obtained using a 64 × 64 F-uTSI scan of a small PFOB sample, acquired with 1 mm × 1 mm in-plane resolution. The echo time and echo spacing were both set to 4 ms. Spectral sampling was performed with a 32 kHz acquisition bandwidth and 0.5 kHz spectral resolution.

The resulting SNR values, shown in Figure 6.14, demonstrated that SNR increased with TR, consistent with the exponential signal recovery described in Section 5.3.4, while increases in NSA scaled approximately with the square root of the number of averages.

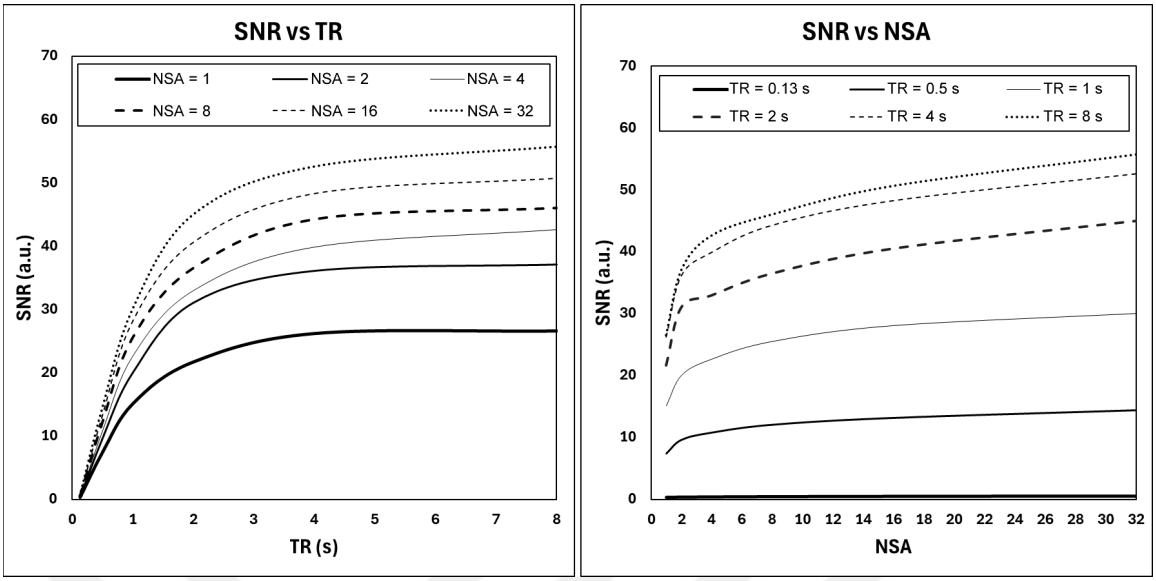

Figure 6.14 SNR as a function of repetition time (left) and number of signal averages (right).

Although higher TR or NSA improved SNR, they also increased the total scan time. Imaging efficiency values calculated from the measured scan durations are shown in Figure 6.15. As seen, four combinations, which are encircled in red, yielded similar imaging efficiencies. Among these, configurations with NSA = 2 were preferable, as even-numbered NSA enabled the reversed acquisition strategy to be applied for suppression of the strike artifact, as discussed in Section 5.3.7.

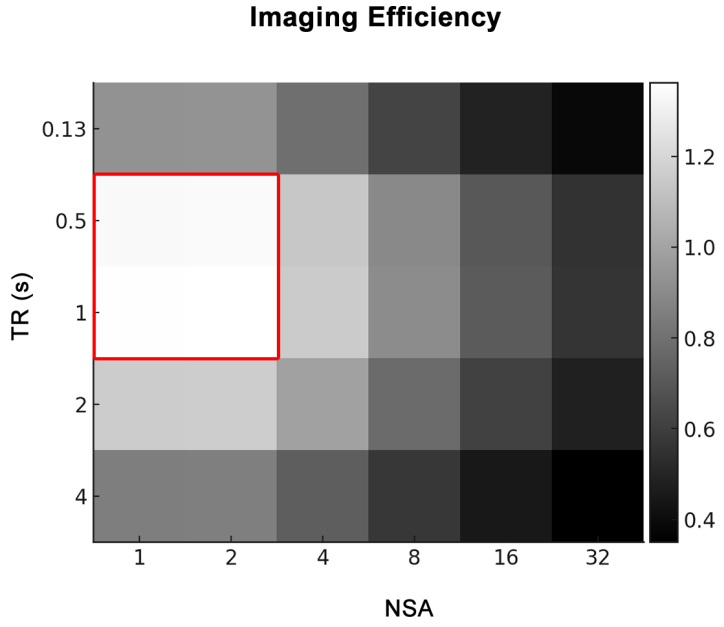

Figure 6.15 Imaging efficiency measurements for different TR and NSA combinations.

6.2.4 Optimization of BaSSI

The optimization of BaSSI was guided by the *in silico* parameter space analysis presented in Section 5.4. While simulations offered valuable insight into the sequence's theoretical behavior, experimental validation was essential to confirm these predictions under real-world conditions involving system imperfections, relaxation effects, and hardware limitations. To this end, phantom experiments were conducted using a sample containing 10 μL of undiluted, bulk-phase PFOB, prepared as described in Section 6.1.1.1. All measurements were acquired on a 64 $\times$ 64 Cartesian k-space grid with 1 mm $\times$ 1 mm in-plane resolution.

The first step in the experimental workflow was a frequency sweep to empirically identify the offset frequencies of PFOB's resonance lines and evaluate their relative signal strengths. Although the chemical shifts of PFOB's peaks are well established, their actual visibility in the BaSSI readout depends on factors such as the excitation bandwidth and sequence timing. Direct measurement was thus necessary to assess the realized spectral profile and select the optimal target resonance.

As shown in Figure 6.16, the CF_2 resonance, originating from the central chain fluorines, produced the dominant and most stable signal. This finding was in excellent agreement with *in silico* predictions and established the CF_2 group as the preferred excitation target. All subsequent experiments were conducted with the BaSSI sequence tuned to this resonance.

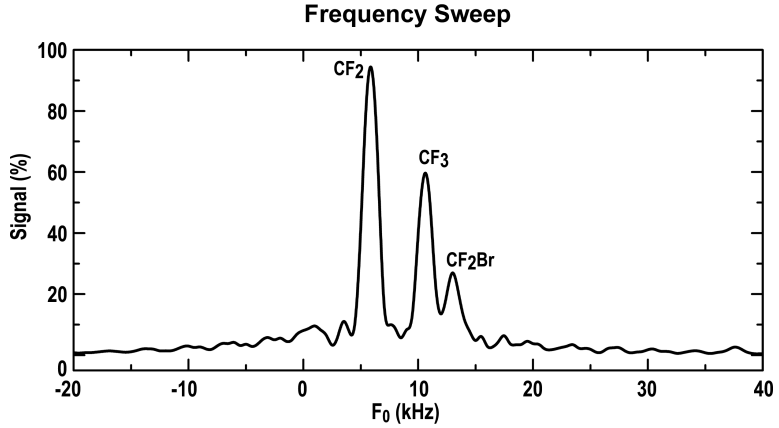

Figure 6.16 Frequency sweep showing the CF_2 resonance line as the dominant peak in PFOB.

Following peak identification, T_{acq} was optimized. T_{acq} was swept from its minimum allowable value of 0.615 ms up to 0.8 ms in 1 μs increments. For each value, data were acquired across flip angles ranging from 5° to 55°.

The resulting measurements revealed that SNR varied smoothly with T_{acq}, showing a broad optimum centered at 0.675 ms. Notably, this trend held consistently across the entire flip angle range, confirming that the behavior was primarily governed by echo timing rather than excitation energy. A fifth-degree polynomial fit confirmed the presence and location of the optimum (Figure 6.17).

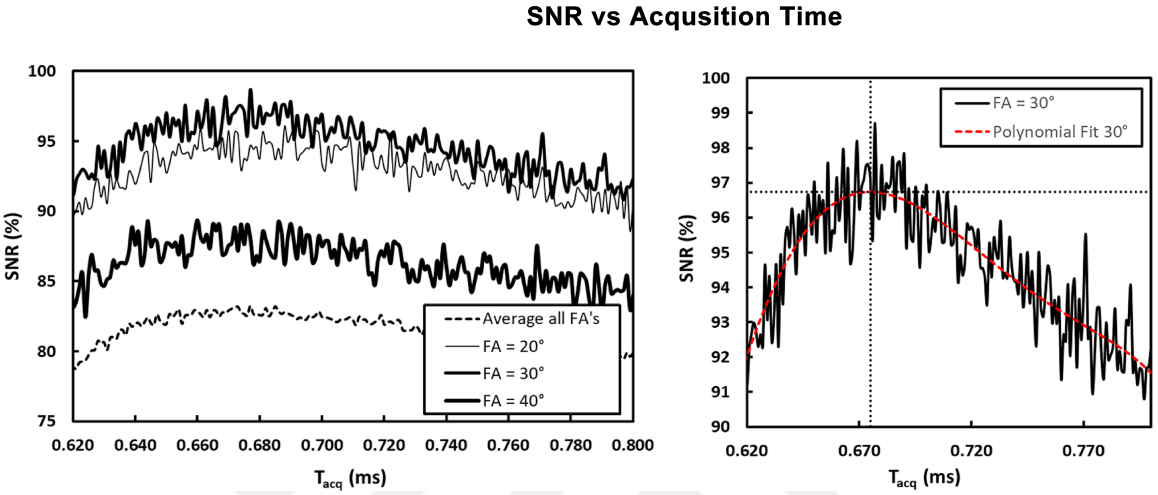

Figure 6.17 SNR as a function of T_{acq}, with a broad optimum centered at 0.675 ms.

With T_{acq} fixed at 0.675 ms, a joint sweep of TR and flip angle was performed to evaluate how these parameters jointly influence steady-state signal behavior. TR was varied from 2.5 to 5.0 ms in 0.1 ms steps, and further extended up to 1 s using larger intervals to probe the regime of full relaxation. Flip angle was incremented from 5° to 55° in 5° steps. This design allowed investigation of both under- and fully relaxed signal conditions. All experiments used the optimized hardware settings identified earlier.

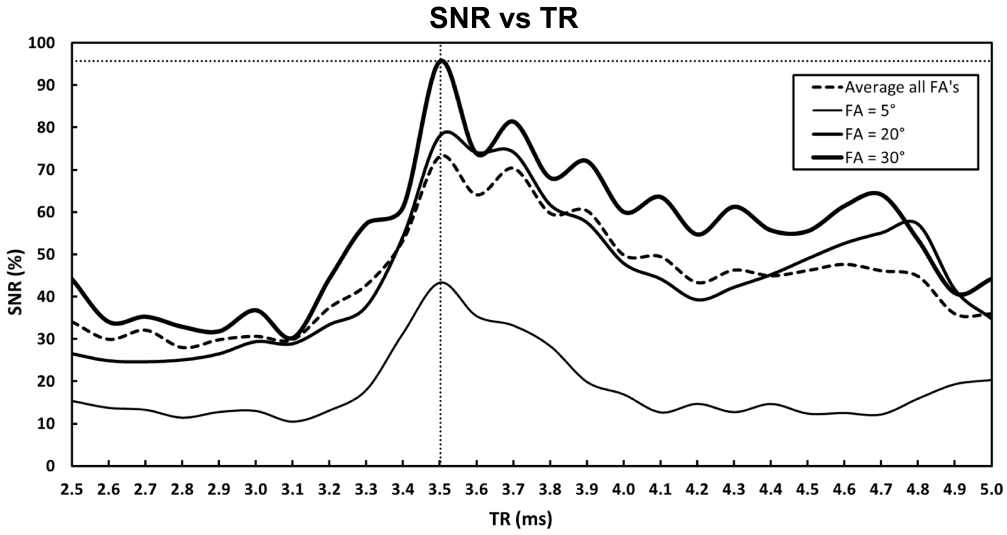

Figure 6.18 SNR variation as a function of TR for $T_{\text{acq}} = 0.675$ ms. The optimal TR was 3.5 ms.

When SNR was plotted as a function of TR, a periodic modulation emerged, reflecting the interplay between excitation timing and transverse magnetization recovery. A local maximum was observed at TR = 3.5 ms, which offered the best trade-off between signal amplitude and scan duration (Figure 6.18). This TR was used as the baseline for further joint TR/FA analysis.

To evaluate the combined influence of TR and flip angle on signal performance, a two-dimensional SNR map was constructed. Several regions exhibited high signal intensity, but one in particular stood out for its consistency, reproducibility, and compliance with physiological safety standards. Optimal performance was achieved for flip angles in the range of 20° to 35°, and TR values between 3.3 and 4.0 ms. Within this window, a clear global maximum was identified at FA = 30° and TR = 3.5 ms (Figure 6.19), closely matching predictions from *in silico* simulations. This combination also remained well within SAR constraints defined by IEC 60601-2-33 [174].

Based on these results, the optimal configuration for BaSSI was defined as $T_{\text{acq}} = 0.675$ ms, TR = 3.5 ms, and FA = 30°, in line with the results obtained in *in silico* assesments. At these settings, a 64 × 64 2D BaSSI scan with 1 mm × 1 mm voxel size completed in 14 s for NSA = 1. As expected, scan time scaled linearly with the number of signal averages. These experimentally derived settings confirmed the theoretical predictions and provided a robust foundation for subsequent *in vivo* studies.

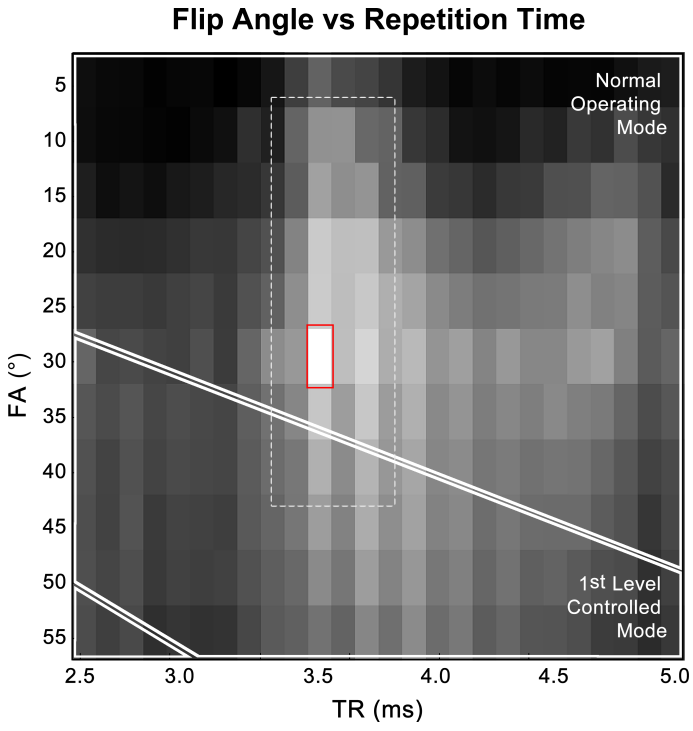

Figure 6.19 TR/FA optimization map showing peak SNR at TR = 3.5 ms and FA = 30°.

6.3 Summary

This chapter gave an overview of the methods, materials, and experimental setup and procedure used for experimental validation of F-uTSI and BaSSI, as well as for performance benchmarking and applications of ^{19}F spectroscopic imaging presented in subsequent chapters.

The validation experiments were designed to evaluate signal detectability, spectral fidelity, and imaging performance of the newly developed sequences. Optimization of F-uTSI and BaSSI was carried out using a comprehensive parametric sweep approach under carefully controlled phantom conditions.

Initial hardware sweeps established an optimal baseline configuration of B_1 = 52 μT, gradient strength = 33 mT/m, and slew rate = 225 T/m/s. These settings balanced safety constraints with gradient timing and excitation performance and were adopted for all subsequent experiments.

Spectral resolution and bandwidth combinations were compared using spectra acquired from PFOB samples. While high-resolution spectra displayed better-defined peaks, measured SNR remained similar across conditions, underscoring the need to consider additional experimental factors when interpreting resolution-dependent SNR.

For F-uTSI, sequence timing parameters, such as TR and NSA, were systematically varied to optimize SNR and imaging efficiency. Among several comparable configurations, those with NSA = 2 were preferred due to their compatibility with strike artifact suppression. The optimal balance was reached by jointly maximizing SNR and minimizing scan duration under fixed resolution and spectral settings.

For BaSSI, optimization began with a frequency sweep that confirmed the CF_2 group as the most stable and dominant resonance. Subsequently, a broader parameter space was explored by varying the T_{acq}, TR, and flip angle. These experiments confirmed simulation predictions, revealing a robust signal optimum at T_{acq} = 0.675 ms, TR = 3.5 ms, and flip angle = 30°, which defined the default acquisition parameters for BaSSI in all subsequent studies.

This configuration yielded high sensitivity and scan efficiency while ensuring compliance with SAR limits and hardware constraints. Collectively, the experimental findings validated both sequences and provided the foundation for the comparative benchmarking and application studies detailed in the following chapters.

7. BENCHMARKING OF F-uTSI AND BaSSI

The performance evaluation of F-uTSI and BaSSI follows the historical progression of their development and application in ^{19}F MRI.

As the earlier of the two sequences, F-uTSI was initially benchmarked against conventional imaging methods available at the time, specifically 2D multi-gradient echo (2D GRE) and 2D Turbo Spin Echo (2D TSE), both of which were spectrally selective sequences commonly used for detecting fluorinated agents at clinical field strengths [3]. These comparative experiments were performed on a 3.0 T Philips Achieva scanner equipped with dedicated ^{19}F surface coils. The sequence was implemented with pseudo-radial k-space sampling scheme, acquiring data on a 48 × 48 grid using echo trains of 24 echoes and a spectral resolution of 0.5 kHz. A bulk PFC phantom was imaged across varying voxel volumes to assess sensitivity under varying geometry and scan time conditions.

As shown in Figure 7.1, all three sequences demonstrated linear increases in SNR with increasing voxel—and therefore PFOB—volume. However, F-uTSI consistently outperformed both GRE and TSE across the full range. When normalized to scan time using the imaging efficiency metric, F-uTSI showed a 1.5 to 2.8-fold improvement in efficiency compared to the conventional sequences.

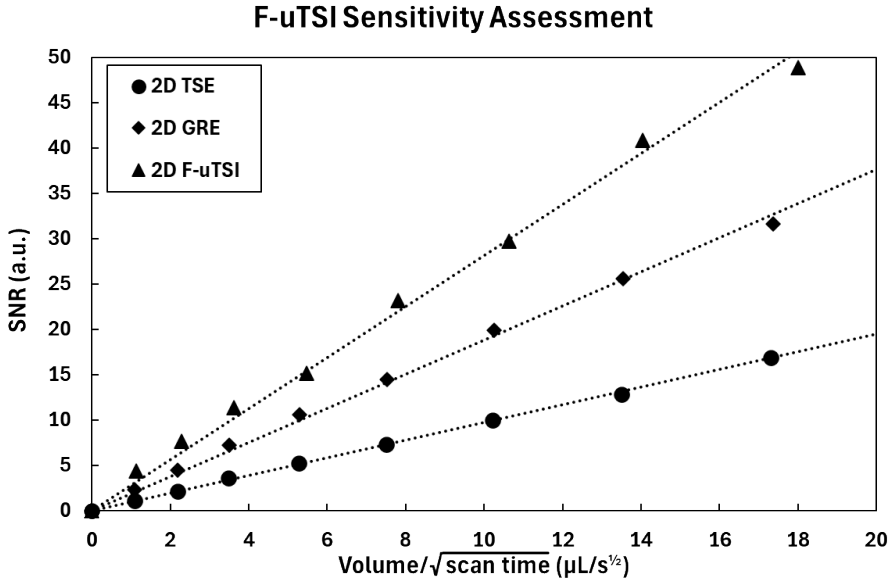

Figure 7.1 Sensitivity comparison between 2D F-uTSI, 2D TSE and 2D GRE sequences.

These early findings confirmed the feasibility of fast clinical MR spectroscopic protocols with F-uTSI, even at standard field strengths and without requiring extended scan durations. They also validated F-uTSI's potential for sparse fluorine imaging applications, helping establish a foundation for the subsequent development of BaSSI.

In a subsequent preclinical study conducted on a 6.0 T small-animal MRI system, F-uTSI was compared with Multi-Chemical Shift Selective RARE (MCSS-RARE) [15]. Both sequences were tested on phantoms containing emulsions of PFOB and PFCE. In these experiments, F-uTSI used a pseudo-radial trajectory with echo trains consisting of 16 echoes, while MCSS-RARE used a 64 × 64 matrix and a RARE factor of 64.

In vivo studies were performed in ApoE$^{-/-}$ mice, 24 hours after intravenous injection of PFOB emulsion. Both sequences successfully detected ^{19}F signal in liver and spleen, consistent with the known biodistribution of PFCs. Signal from vascular plaques remained below the detection threshold *in vivo*. However, *ex vivo* imaging with MCSS-RARE, using long scan times, revealed localized signal in the aortic arch and carotid bifurcations, confirming passive uptake of PFOB by atherosclerotic lesions.

Quantitative analysis revealed that MCSS-RARE outperformed F-uTSI in both acquisition speed and sensitivity. In phantom studies, MCSS-RARE acquired data more than 50 times faster and achieved a 3.7-fold higher SNR (31.9 vs. 8.7). In vivo, MCSS-RARE achieved a 2.8-fold SNR gain (15 vs. 5.4) while using only one-third of the scan time and providing higher spatial resolution (Figure 7.2).

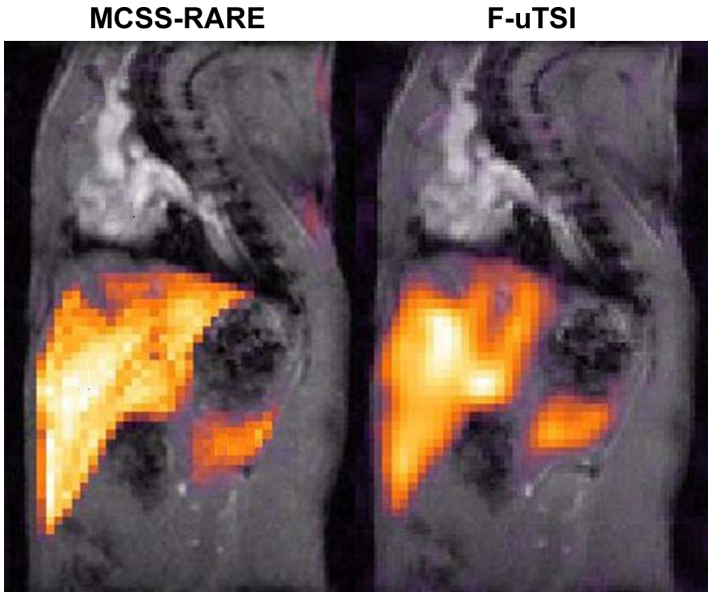

Figure 7.2 MCSS-RARE (left) showed better SNR and spatial resolution than 2D F-uTSI (right).

More recently, as part of the present dissertation work, F-uTSI was evaluated against 3D UTE bSSFP, a later-generation imaging sequence that has gained significant traction in the ^{19}F MRI community [145], [175]. This comparison was performed using bulk PFOB phantom of 19.6 μL. While F-uTSI generally performed well, 3D UTE bSSFP demonstrated superior sensitivity. The sequence successfully imaged the sample even at the shortest scan time of 22 s, with high fidelity.

F-uTSI, by contrast, failed to detect the same sample under the 22 s scan configuration. However, as scan time was increased by adjusting NSA and TR to match those of the 3D UTE bSSFP protocol, the phantom signal began to emerge and became visibly detectable at a scan time of 42 s (Figure 7.3).

Despite displaying lower sensitivity, F-uTSI yielded better image quality in terms of spatial fidelity, preserving the circular shape of the phantom more accurately than 3D UTE bSSFP. This advantage was primarily due to F-uTSI's higher spatial resolution: 1 mm $\times$ 1 mm in-plane voxels on a 64 $\times$ 64 grid. In comparison, the 3D bFFE UTE images were acquired with a coarser resolution of 1.6 mm $\times$ 1.6 mm.

While the difference in voxel size partially accounts for the performance disparity, the results underscored the need for a more sensitive spectroscopic imaging approach—ultimately motivating the development of BaSSI.

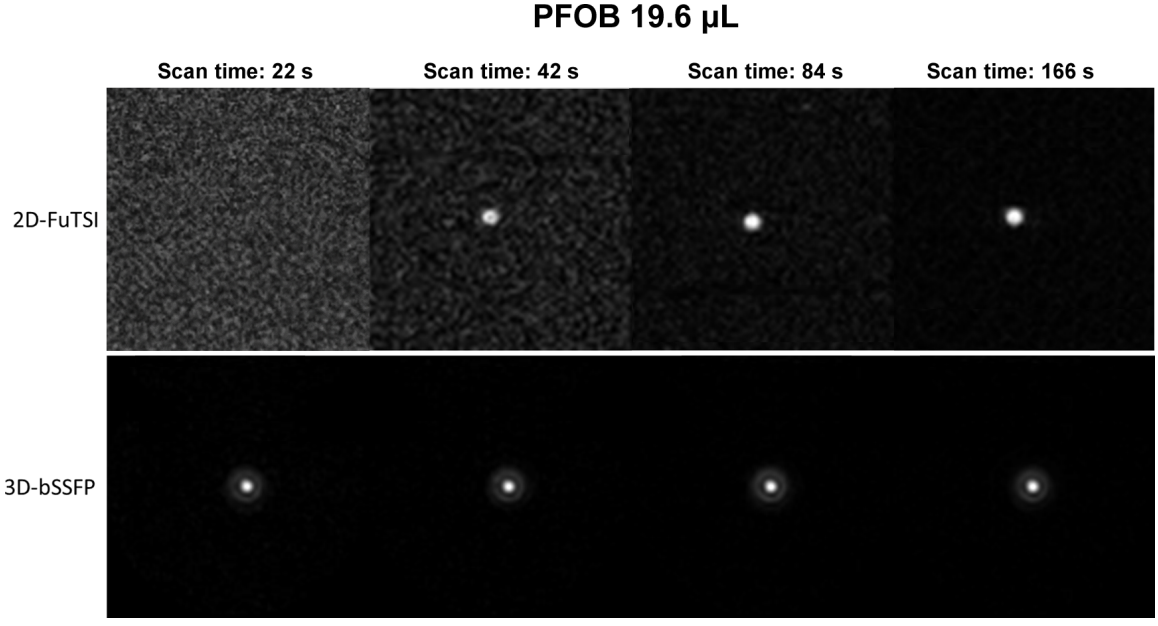

Figure 7.3 3D UTE bSSFP outperformed F-uTSI in imaging a phantom of 19.6 μL PFOB.

7.1 Benchmarking BaSSI against 3D UTE bSSFP

Following its conception, BaSSI underwent extensive implementation and optimization, as detailed in the preceding sections. It was then benchmarked against 3D UTE bSSFP using a similar protocol to that used with F-uTSI. However, due to the encouraging preliminary results from BaSSI, the benchmarking study was extended to include even smaller sample volumes, down to 0.10 μL.

This section presents the outcomes of these benchmarking studies. To provide context, the section begins with an overview of 3D UTE bSSFP, outlining its implementation and performance characteristics. The section concludes with a quantitative comparison of F-uTSI and BaSSI, highlighting the progression and practical advantages introduced by the latter.

7.1.1 Benchmark Sequence: 3D UTE bSSFP

The 3D UTE-bSSFP sequence, shown in Figure 7.4, is a radial steady-state free precession (SSFP) technique specifically optimized for ^{19}F MRI of compounds exhibiting complex spectra, such as PFOB [145]. These agents often contain multiple chemically distinct fluorine environments, resulting in a multipeak spectrum with chemical shifts that span several kilohertz. Imaging such compounds with conventional gradient-echo sequences is problematic due to chemical shift-induced dephasing, which leads to destructive interference between peaks, signal loss, and spatial misregistration.

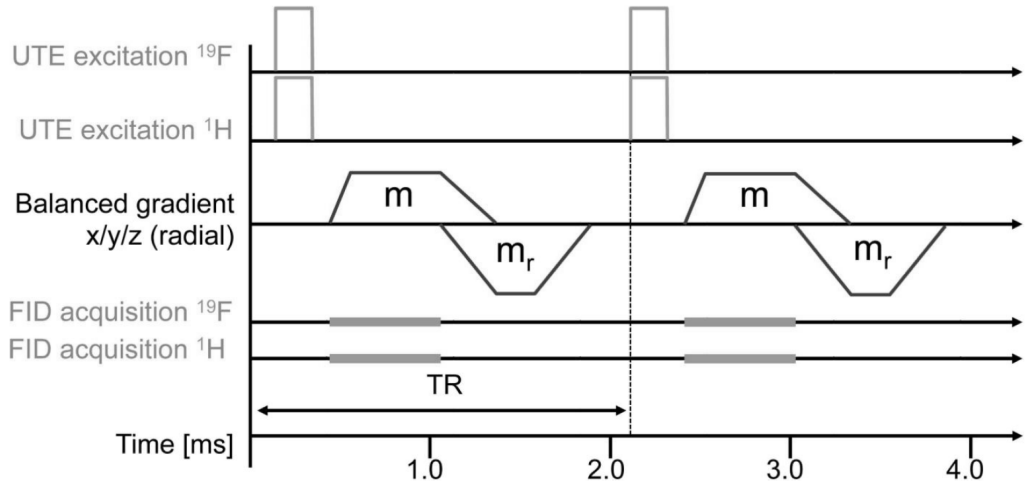

Figure 7.4 The 3D balanced UTE-SSFP pulse sequence by Goette et al. [145], consists of RF excitation followed by FID acquisition accompanied with Wong-type [176] radial readout trajectory.

The UTE-bSSFP sequence addresses these limitations by combining a center-out radial k-space trajectory, known as the Wong type radial spokes [176] with balanced gradient refocusing and ultrashort TEs. The radial trajectory ensures that each spoke samples the center of k-space early, preserving signal from fast-decaying components. Balanced gradients maintain steady-state coherence across phase cycles, while the ultrashort TEs minimize dephasing from chemical shift differences. Together, these features promote coherent summation of signals across all spectral components and suppress spatial artifacts, enabling robust imaging even in the presence of broad or overlapping resonances.

In addition to its robustness against spectral complexity, UTE-bSSFP offers excellent imaging efficiency due to its continuous signal replenishment in the steady-state and its compatibility with low flip-angle excitations. These properties make it particularly well-suited for applications, where scan time, sensitivity, and artifact suppression must be carefully balanced. Consequently, UTE-bSSFP has emerged as one of the most widely adopted sequences for ^{19}F imaging in preclinical and translational research.

7.1.1.1 Sequence Design and Key Features. The pulse sequence, consists of the following elements:

- **Balanced gradient refocusing:** Gradients are fully balanced in all three spatial directions during each TR interval, thereby preserving phase coherence and reducing intravoxel dephasing.
- **3D radial center-out acquisition:** The k-space is sampled using a spherical stack of radial spokes originating at the center, enabling rapid acquisition of central k-space data where most signal energy resides.
- **Half-pulse slab excitation:** The use of asymmetric half-sinc RF pulses and zero gradient prephasing allows for slab-selective excitation and extremely short echo times.
- **Ultrashort echo time:** The sequence achieves an effective TE of 90 µs, capturing signal from fast-decaying resonances and reducing signal loss due to T_2* relaxation and chemical shift evolution.

7.1.1.2 Acquisition Parameters. The 3D UTE bSSFP sequence was implemented on a 3.0 T Philips clinical MRI scanner equipped with a dual-tuned $^{1}H/^{19}F$ quadrature birdcage coil. Representative acquisition parameters used in phantom studies comprised a spatial resolution of 1 mm isotropic over a 128 mm FOV. The excitation bandwidth and the pixel bandwidth were set to 5 kHz and 900 Hz, respectively, to cover the CF_2 group. With a TR of 2.1 ms and a TE of 90 µs, the total scan time of phantom experiments was 71 s for NSA = 1. For the *in vivo* experiments, the authors increased FOV to 140 mm and reduced spatial resolution to 2.19 mm. The TR was set to 1.75 ms, resulting into a scan time of 30 minutes with presumably high NSA. While the authors did not report an optimal flip angle they employed an excitation RF pulse with 30° for both *in vitro* and *in vivo* experiments.

7.1.1.3 Performance and Conclusions. Phantom studies carried out by authors have shown that 3D UTE bSSFP maintains high signal intensity across all resonance peaks of PFOB, while preserving geometric fidelity without ghosting or blurring. *in vivo* imaging further demonstrated its ability to visualize targeted ^{19}F agents with high contrast and minimal artifacts, without requiring frequency-selective excitation or spectroscopic post-processing.

The authors concluded that 3D UTE bSSFP is a robust and clinically compatible method for ^{19}F MRI of spectrally complex agents. Its rapid acquisition, resistance to off-resonance effects, and compatibility with clinical hardware make it a promising candidate for translational applications in molecular imaging and targeted drug delivery.

7.1.2 In-House Implementation and Optimization of 3D UTE-bSSFP

The 3D UTE-bSSFP sequence was not readily available on the test platform and was therefore implemented in-house based on the design by Goette et al. [145]. Although the scanner used here matched the original in field strength (3.0 T) and hardware configuration—including a dual-tuned $^{1}H/^{19}F$ quadrature birdcage coil—exact replication of timing parameters was not feasible due to system-specific constraints. In particular, SAR limits, peak B_1 restrictions, and limitations in gradient performance affected RF pulse shaping and ramp timing, preventing achievement of the originally reported TE of 90 µs. Despite best efforts, the shortest achievable TE on the current system was 115 µs.

Optimization was carried out using a 1 mL sample of pharmaceutical-grade PFOB. All measurements were repeated in sets of five with NSA = 1 to ensure statistical consistency. Prior to each scan, the RF system was tuned and matched to maintain reflected power below 0.1%, and transmit power was optimized to ensure accurate flip angle calibration. These steps ensured that observed variations in signal and contrast were attributable to sequence parameters rather than system instability.

The parameter space was explored as follows:

- **Long TR Assessment:** To establish a baseline for relative SNR comparisons, TR was extended from 10 ms to 1000 ms to measure the maximum achievable SNR under fully relaxed conditions (Figure 7.5).

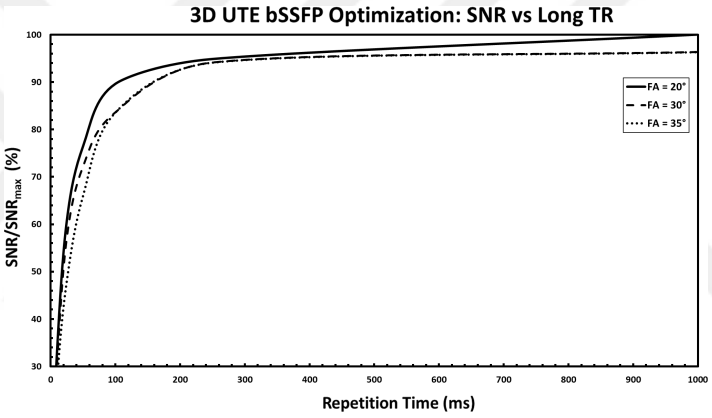

Figure 7.5 SNR obtained with full relaxation for three different flip angles.

- **TE optimization:** TE was swept between 0.115 ms and 0.200 ms. A value of 0.145 ms delivered approximately 90% of the peak SNR obtained with full relaxation and was adopted as a robust compromise (Figure 7.6).

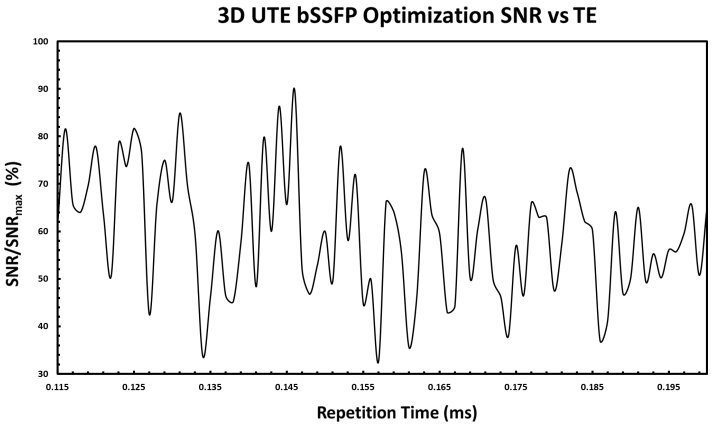

Figure 7.6 Optimization of 3D UTE-bSSFP for echo time.

- **TR and flip angle:** TR was varied from 1.67 ms to 5 ms (step size: 0.1 ms), with flip angles from 5° to 55°. The optimal combination—TR = 2.5 ms and FA = 20°—provided the highest SNR (Figure 7.7).

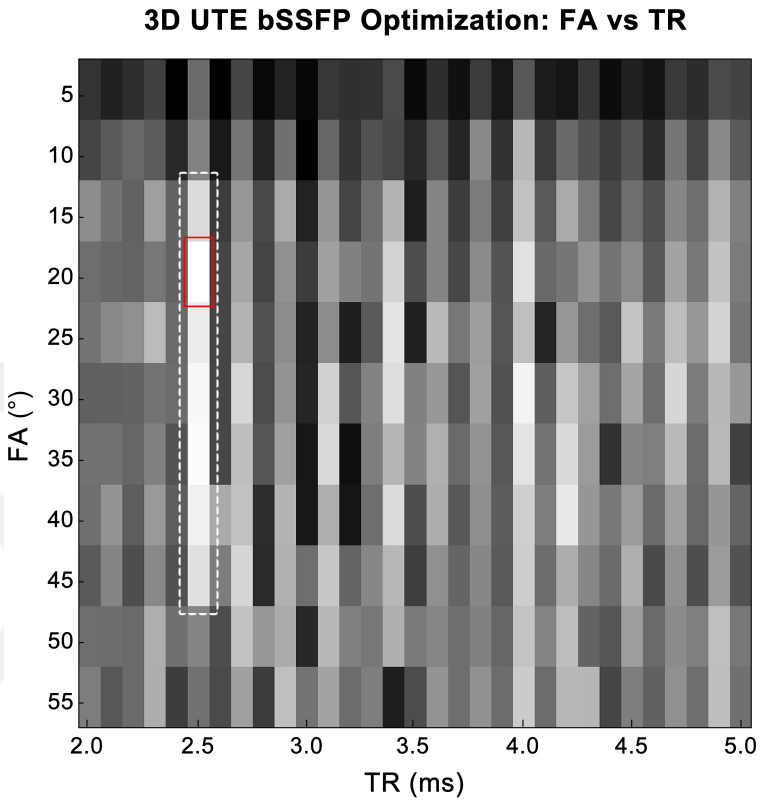

Figure 7.7 Optimization of 3D UTE-bSSFP for a combined range of flip angles and repetition times. The combination of TR = 2.5 ms and FA = 20° demonstrated the best SNR performance.

- **Spatial and spectral resolution:** The excitation frequency was centered on the CF_2 resonance of PFOB. A 1 kHz pixel bandwidth was used to maintain spectral fidelity. Acquisition was performed on a 64 × 64 × 64 isotropic grid (1 mm voxels), and data were regridded to 80 × 80 × 80 during reconstruction.

The final configuration required 25 seconds per 3D acquisition at NSA = 1. Scan time scaled linearly with NSA up to 8, after which gradient duty-cycle limits caused nonlinear increases in acquisition time.

In their original implementation, Goette et al. [145] used an ultrashort TE of 90 µs and TR of 2.4 ms, achieving 2 mm isotropic resolution over a 160 mm FOV in 4 minutes. Although they did not conduct a formal optimization of TR and FA, they proposed a flip angle of 30° as a suitable choice for *in vivo* imaging of nanoparticle-encapsulated PFOB, where faster T_2 decay is expected.

In contrast, the in-house implementation focused on optimizing SNR and spatial resolution under more conservative hardware constraints. A finer voxel size (1 mm) and lower bandwidth (1 kHz) were prioritized, at the expense of a slightly longer TE and acquisition time. These adjustments enabled artifact-resistant imaging and provided a suitable benchmark for evaluating the performance of BaSSI and F-uTSI sequences under realistic imaging conditions.

7.1.3 Benchmarking Results

The development of BaSSI was motivated by the limitations encountered during a direct performance comparison between F-uTSI and an optimized 3D UTE bSSFP sequence [145].

The ultrashort echo-based sequence delivered superior SNR per unit time by combining efficient volumetric encoding with a very short TE, rapid 3D acquisition, and advantageous averaging properties. Although F-uTSI retained inherent strengths in spectral resolution, this advantage alone was insufficient to compensate for the speed and coverage gains of 3D imaging.

In response, BaSSI was conceived as a next-generation spectroscopic imaging method designed to address the shortcomings of F-uTSI while preserving its unique benefits. BaSSI integrates balanced excitation with spiral k-space sampling in a steady-state acquisition framework, enabling both high temporal efficiency and reliable spectral discrimination.

The sequence architecture of BaSSI was carefully optimized to improve sensitivity per unit scan time, making it suitable for detecting microliter- and sub-microliter quantities of PFC agents within clinically acceptable scan durations. Additionally, its balanced nature minimizes banding artifacts, which are common in bSSFP-based methods when off-resonance effects are present.

To rigorously evaluate its performance, BaSSI was benchmarked against 3D UTE bSSFP using standardized phantoms containing bulk PFOB in volumes of 1.0 μL, 0.5 μL, and 0.1 μL. As described in Section 6.1.1.1, these phantoms were fabricated with maximum dimensions of 1 mm in both diameter and height, ensuring that the signal originated entirely from within a single 2 mm imaging slice. This design effectively eliminated partial volume effects, signal leakage, and interpolation errors, isolating acquisition strategy as the primary variable under comparison.

To quantify imaging efficiency, a linear regression through the origin was performed for each dataset under the assumption that zero material corresponds to zero signal. The slope of each fit, expressed in units of SNR per $\sqrt{\text{s}}$, was taken as a robust, time-normalized figure of merit that reflects the intrinsic sensitivity of each acquisition strategy.

Utilization of imaging efficiency enabled direct comparison between BaSSI and 3D UTE bSSFP across all phantom volumes, independent of scan duration or NSA, as shown in Figure 7.8.

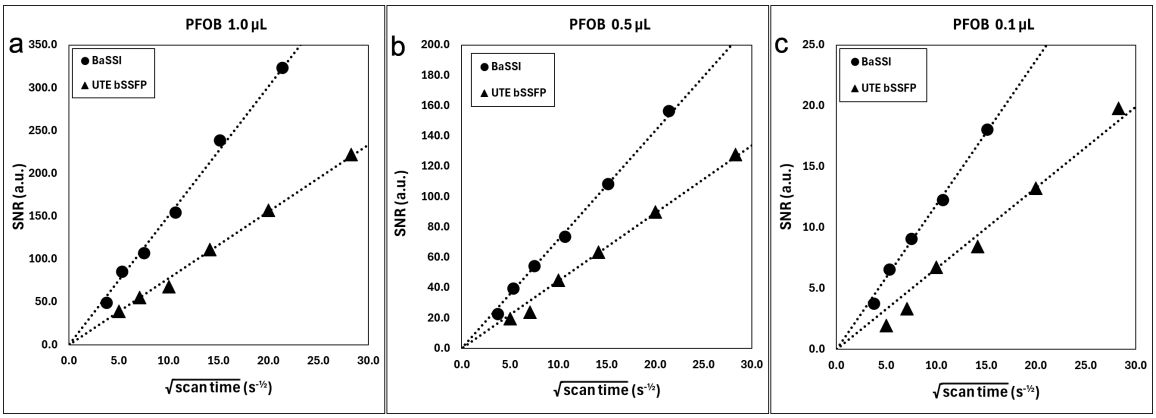

Figure 7.8 Benchmarking data obtained for the three samples by varying NSA.

As summarized in Table 7.1, BaSSI consistently outperformed 3D UTE bSSFP at all tested volumes. At 1.0 µL, BaSSI achieved an imaging efficiency of 15.09 ± 0.25 compared to 7.79 ± 0.12 for UTE bSSFP—a near twofold improvement. At 0.1 µL, BaSSI maintained an efficiency of 1.19 ± 0.01 while UTE bSSFP yielded 0.61 ± 0.02, corresponding to a relative gain of approximately 1.95-fold.

Table 7.1
Imaging efficiency for BaSSI and 3D UTE bSSFP across different sample volumes.

	Imaging Efficiency (SNR/$\sqrt{\text{s}}$)	
Sample	**BaSSI**	**3D UTE bSSFP**
1.0 µL	15.09 ± 0.25	7.79 ± 0.12
0.5 µL	7.18 ± 0.10	4.47 ± 0.09
0.1 µL	1.19 ± 0.01	0.61 ± 0.02

Further evaluation used the Rose criterion (R_c), a well-establishewd metric for object detectability, which is given by:

$$R_c = \frac{\langle I_{\text{obj}} \rangle - \langle \text{noise} \rangle}{0.8 \cdot \langle \text{noise} \rangle} > 3, \tag{7.1}$$

where $\langle I_{\text{obj}} \rangle$ and $\langle \text{noise} \rangle$ denote mean intensities within object and background ROIs, respectively. As discussed in Section 4.1 $R_c \geq 3$ is required for confident detection.

Figure 7.9 shows that BaSSI consistently outperformed UTE bSSFP in terms of R_c scores at comparable scan durations. For example, in a 2-minute scan with a 0.10 μL sample, BaSSI achieved $R_c = 11.0$ (NSA = 8), while UTE bSSFP yielded $R_c = 4.5$ (NSA = 4). BaSSI reached $R_c = 5.3$ in just 28 seconds (NSA = 2), while UTE bSSFP required over 50 seconds to reach a sub-threshold $R_c = 2.0$. At 8 minutes, BaSSI achieved $R_c = 24.4$ versus $R_c = 11.9$ for UTE bSSFP, demonstrating both superior detectability and faster convergence.

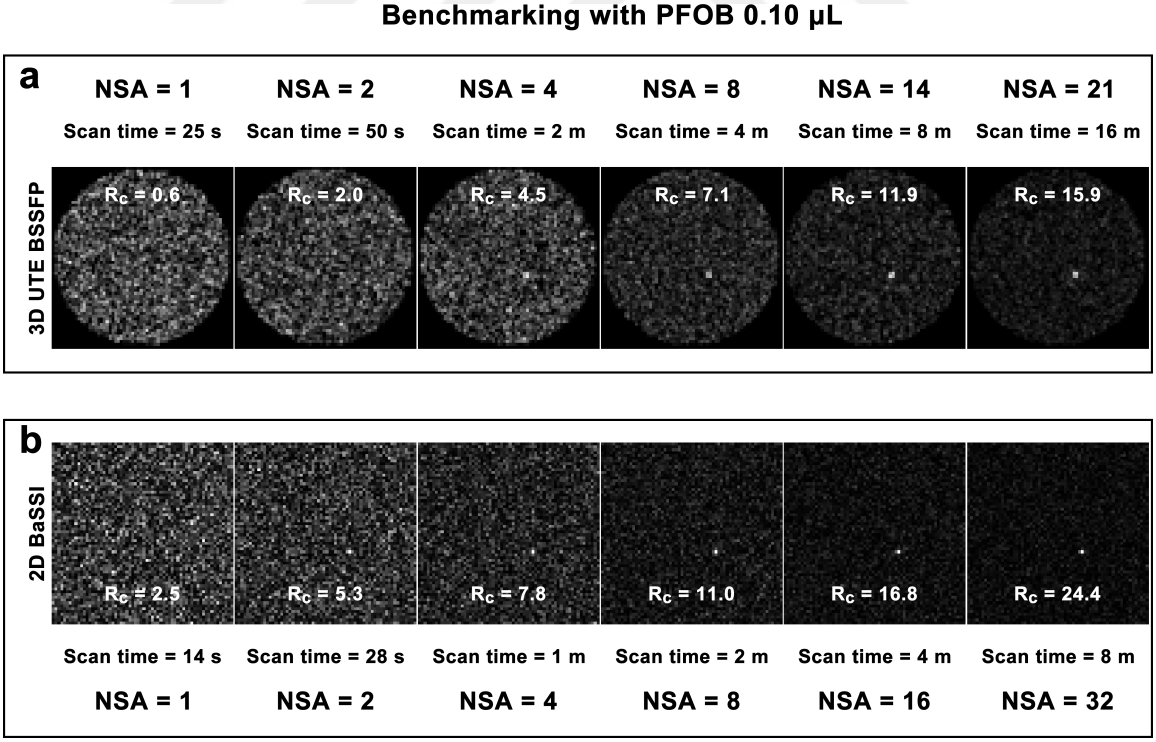

Figure 7.9 Benchmarking results for 3D UTE bSSFP (**a**) and 2D BaSSI (**b**) with a 0.10 µL PFOB sample. Each image shows the Rose criterion score (R_c), scan time, and NSA. For all scan times BaSSI consistently outperformed 3D UTE bSSFP in imaging sensitivity and detection performance.

To investigate the detection threshold of BaSSI, a final benchmark was conducted using a 0.05 μL PFOB sample—smaller than any volume previously tested. Measurement at this level was expected to approach the noise floor; therefore, an analytical approach was used to assess the feasibility of detection.

Imaging efficiency was first estimated by fitting a zero-intercept linear regression to the values obtained at 1.0 μL, 0.5 μL, and 0.1 μL, under the assumption of linear proportionality between SNR and sample volume. The resulting slope, 14.92 $\pm$ 0.28 SNR per $\sqrt{\text{s}}$ per μL, provided a time-normalized, concentration-scaled model of expected sensitivity (Figure 8.13a).

Using this model, the projected imaging efficiency for a 0.05 μL sample was estimated as 0.75 SNR / $\sqrt{\text{s}}$. The expected signal levels were then modeled as a function of scan time assuming ideal acquisition conditions and Gaussian noise propagation:

$$\text{SNR} = 0.75 \times \sqrt{\text{scan time}}. \tag{7.2}$$

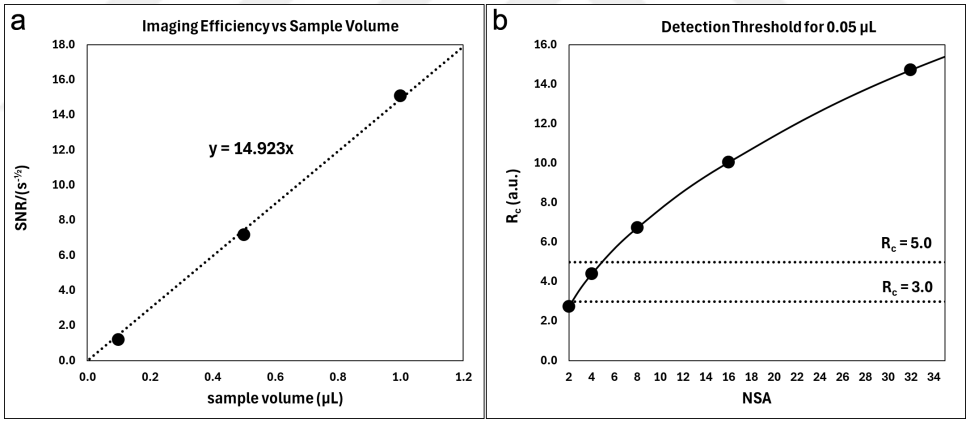

Figure 7.10 Estimated R_c values for a 0.05 μL PFOB sample, extrapolated from data obtained in prior benchmark experiments. Detection thresholds ($R_c = 3$ and $R_c = 5$) are marked for reference.

To convert SNR predictions into a visibility metric, modeled values were transformed into Rose criterion scores using $R_c = \text{SNR} - 1.25$, where the offset accounts for the Rayleigh distribution of noise in magnitude-reconstructed images (See Appendix A.10 for additional details).

As seen in Figure 8.13b, this model predicted that the 0.05 μL sample would surpass the conventional detection threshold of $R_c = 3$ between NSA values of 3 and 4, corresponding to scan durations of 45–60 seconds.

Experimental validation was then performed using BaSSI under identical acquisition settings. As shown in Figure 7.11, BaSSI achieved $R_c = 2.7$ at NSA = 4 (1-minute scan), closely aligning with the model's lower-bound prediction. Visibility improved progressively with increased averaging. The result obtained with the 2-minute scan (NSA = 8) marked the first instance in which the sample became visually identifiable. At NSA = 16 (4 minutes), R_c reached 8.0; at NSA = 32 (8 minutes), R_c rose to 13.7, yielding a clearly resolved signal with minimal background interference.

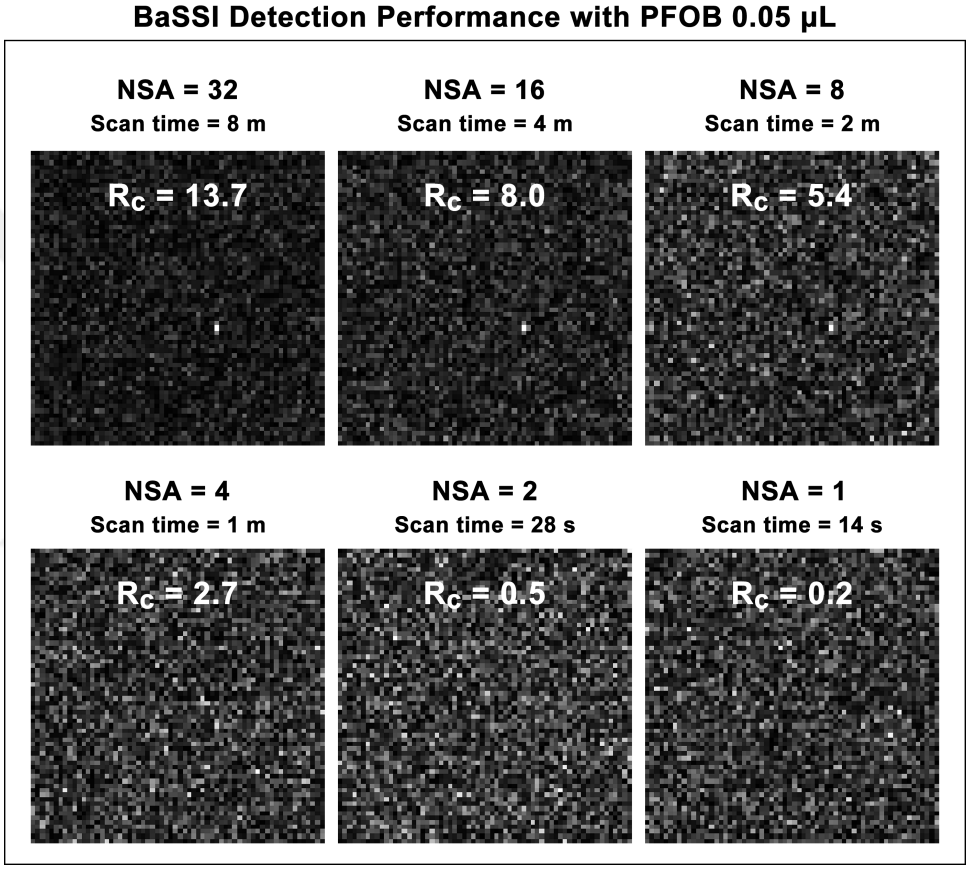

Figure 7.11 Detection performance of BaSSI using the 0.05 µL PFOB sample.

3D UTE bSSFP was unable to complete the scan under equivalent protocol conditions due to repeated gradient amplifier shutdowns. These failures were attributed to excessive gradient duty cycle demands imposed by the sequence's volumetric readout settings, and high number of NSA needed to cope with BaSSI.

In the original study by Goette et al. [145], 3D UTE bSSFP was implemented with an isotropic field of view (FOV) of 160 mm × 160 mm × 160 mm and a voxel size of 2 mm × 2 mm × 2 mm—parameters that helped maintain the gradient load within safe operational limits. The benchmarking experiments in this work imposed more demanding acquisition constraints, including a higher spatial resolution of 1 mm × 1 mm × 1 mm

and a reduced FOV of 80 mm × 80 mm × 80 mm. Combined with a short TR of 2.5 ms and the high NSA required to match BaSSI's sensitivity, this configuration resulted in sustained gradient activity that exceeded the system's duty cycle limits and triggered repeated hardware failures.

Spectral validation offered an independent confirmation of signal integrity at low sample volumes. As shown in Figure 6.12, the characteristic CF_2 resonance peak remained detectable in both the 0.10 μL and 0.05 μL samples even at NSA = 4, supporting the imaging-based detection results. At higher NSA values (16 and 32), spectral profiles increased in SNR and exhibited strong convergence in amplitude and shape across both volumes.

This consistency between spectral and image-based assessments reinforces the reproducibility of the acquisition and highlights the chemical specificity of BaSSI, even under near-threshold conditions. The preservation of peak structure and relative intensities at minimal volumes affirmed BaSSI's suitability for frequency-resolved ^{19}F applications, where both spatial localization and molecular identification are essential.

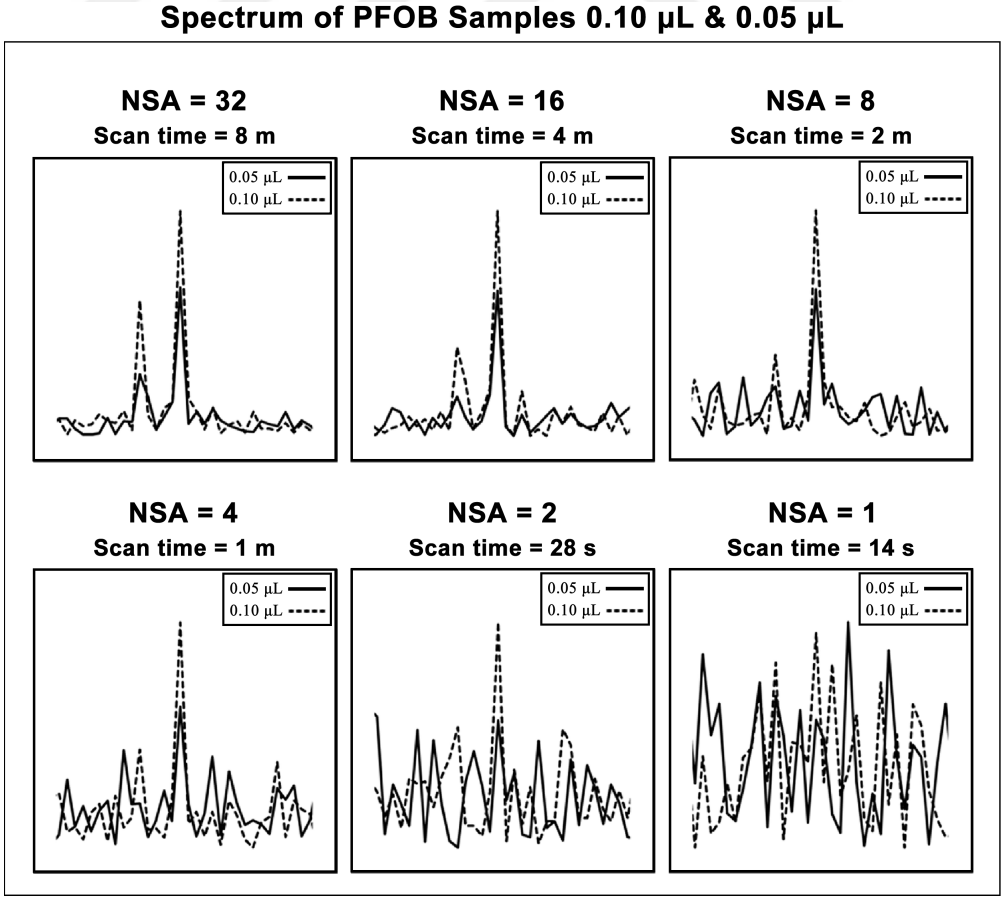

Figure 7.12 BaSSI demonstrated reliable spectral detection for low-volume samples. The CF_2 peak and nearby resonances were visible at NSA = 4, with improved quality at higher NSA levels.

7.2 Summary

This chapter presented a comprehensive evaluation of the spectroscopic imaging sequences F-uTSI and BaSSI, focusing on their ability to detect and characterize small quantities of ^{19}F-labeled agents with high sensitivity and spectral fidelity. While F-uTSI had previously demonstrated strong performance against conventional 2D spin echo and gradient echo methods, it fell short of matching the speed, volumetric coverage, and time-normalized sensitivity of modern sequences such as 3D UTE bSSFP. Despite its robustness to off-resonance effects and favorable spectral properties, F-uTSI was ultimately constrained by scan-time inefficiency in low-SNR regimes.

BaSSI was developed to overcome these limitations while preserving F-uTSI's spectroscopic strengths. By combining balanced excitation and a spiral k-space trajectory within an FID architecture approaching steady-state, BaSSI was designed to maximize imaging efficiency and retain spectral precision. The sequence circumvents the chemical shift artifact and supports short, efficient acquisitions that are well-suited to imaging spectrally complex tracers such as PFOB.

Benchmarking experiments using standardized phantoms demonstrated that BaSSI consistently outperformed 3D UTE bSSFP across all tested volumes, with up to a 1.95-fold improvement in imaging efficiency at 0.1 μL. Even at the lowest tested volume of 0.05 μL, BaSSI achieved reliable detection in 2 minutes, while 3D UTE bSSFP failed due to hardware limitations. These findings highlight BaSSI's scalability to low-volume applications and its robustness under system-level constraints such as gradient duty cycle and RF load.

Beyond spatial detection, BaSSI preserved spectral integrity at low signal levels. The CF_2 resonance peak remained detectable even at NSA = 4 in 0.05 μL samples, and spectral profiles converged across volumes at higher NSA values. This dual capability—robust localization with accurate chemical identification—positions BaSSI as a highly effective fluorine imaging sequence.

Taken together, these results demonstrated that BaSSI advanced the detection frontier of ^{19}F MRI. It offered reliable performance across a wide dynamic range, compatibility with clinical hardware, and the methodological rigor needed for high-value molecular imaging applications. As a successor to F-uTSI, BaSSI provided both enhanced sensitivity and retained spectral discrimination, making it a versatile and scalable solution for preclinical and translational imaging.

8. APPLICATIONS OF ^{19}F SPECTROSCOPIC IMAGING

8.1 *Post-Mortem* Imaging of PFOB Microcapsules Using BaSSI

This section is adapted from [16] and [17].

The BaSSI sequence is a free induction decay (FID) method that acquires the MR signal using an all-phase encoded sampling scheme. The core sequence is a spoiler-free, non-spatially and spectrally selective derivative of the CE-FAST sequence [164], consisting of a broadband excitation pulse, a set of phase-encoding and rewinding gradients, and a data acquisition window (As depicted in (Figure 8.1). Spatial encoding is achieved using a two-dimensional pseudo-spiral k-space trajectory, which can be extended to a three-dimensional stack of spirals for volumetric imaging.

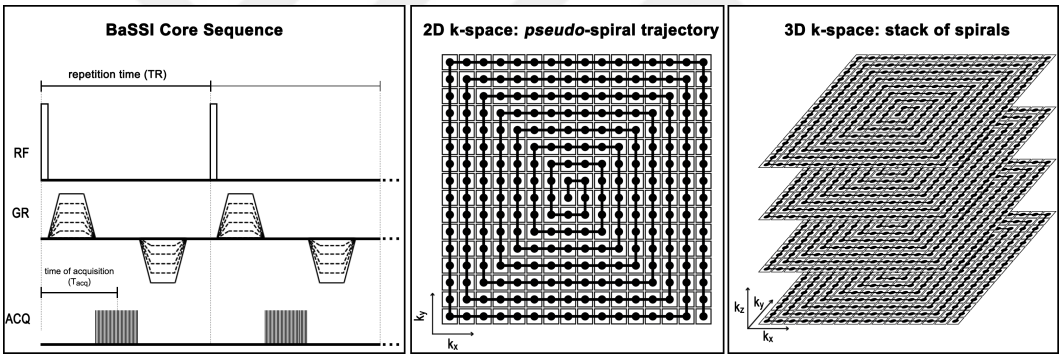

Figure 8.1 BaSSI uses a *pseudo*-spiral k-space trajectory suitable for both 2D and 3D acquisitions.

PLGA microspheres with a mean diameter of 2.4 µm, filled with PFOB, were injected into post-mortem BALB/c mice and imaged using the 3D BaSSI sequence. The aim was to achieve accurate anatomic localization of ^{19}F hot-spots. Imaging was conducted using 200 µL of microbubble solution, containing PFOB at a concentration of 10 mM, which corresponds to 0.5 μL of pure PFOB.

Anatomical images were acquired with 1 mm slice thickness and 0.5 mm × 0.5 mm in-plane resolution. The ^{19}F hot-spot images were obtained with 3D BaSSI using a stack-of-spirals scheme, employing isotropic voxels of 1 mm^3 over a 48 × 48 × 48 grid.

To ensure sufficient signal-to-noise ratio (SNR), the number of signal averages (NSA) was set to 16. This resulted in a scan time of approximately 2.15 minutes per slice, with a total acquisition time of about 1 hour and 45 minutes.

Post-processing involved denoising the ^{19}F data using a Rose criterion (R_c)-based filter, which eliminated voxels that did not meet a threshold of object visibility. The value of R_c was varied between 0.1 and 10.0 to identify the optimal setting that produced clean hot-spot images free of false positives, which typically manifested as signal outside of the target region.

The optimal R_c was found to be 5.7. This setting yielded the cleanest results, effectively eliminating non-specific signals while preserving relevant voxels. Figure 8.2a shows color-inverted raw ^{19}F images of PFOB-loaded microspheres accumulated in the peritoneal cavity. Figure 8.2d displays the denoised results obtained with $R_c = 5.7$.

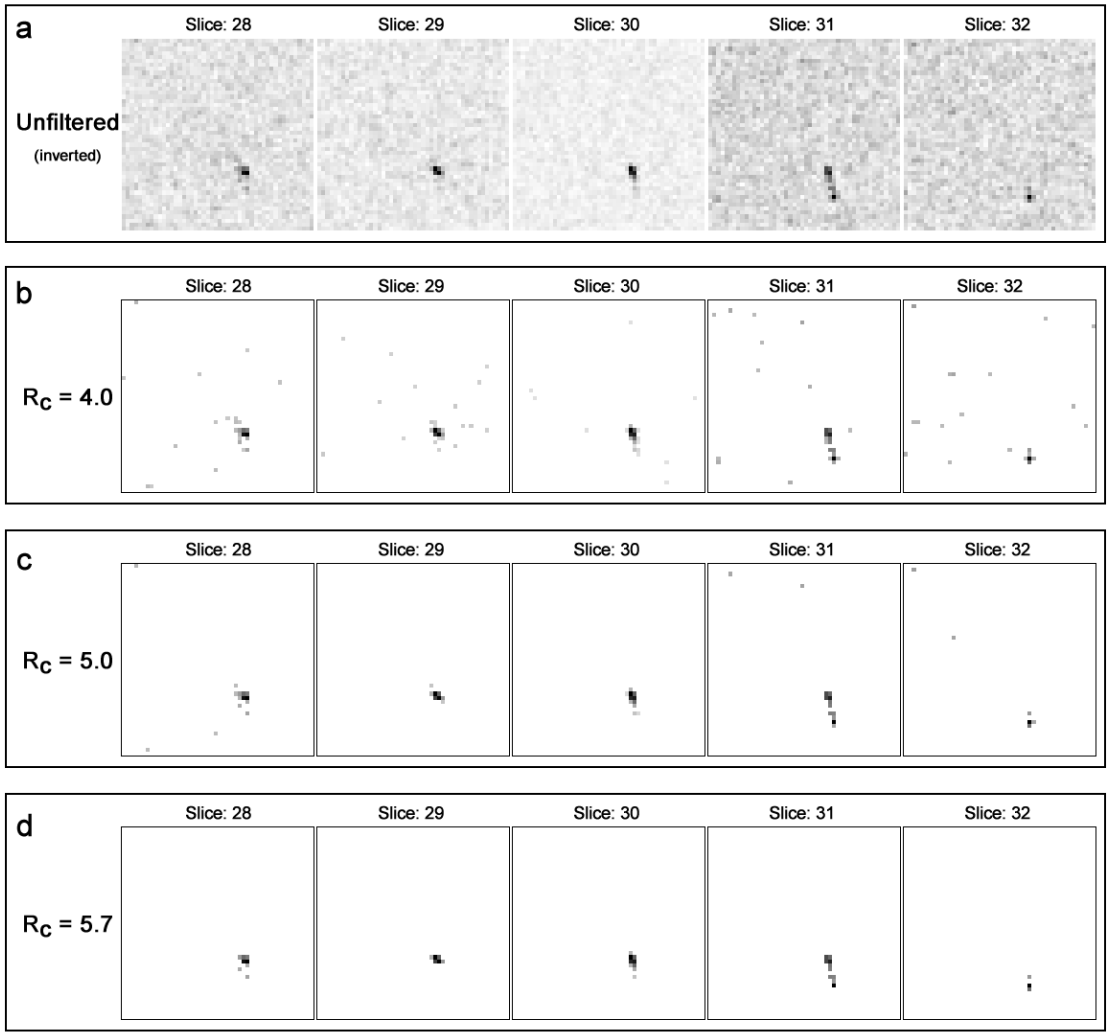

Figure 8.2 Rose criterion based filtering of hot-spots produce clean images. Original image with substantial noise is filtered with different R_c settings.$R_c = 5.7$ produces images free of false negatives.

For anatomical localization, ^{19}F images were registered to corresponding ^{1}H images using the acquisition geometry parameters (Figure 8.3).

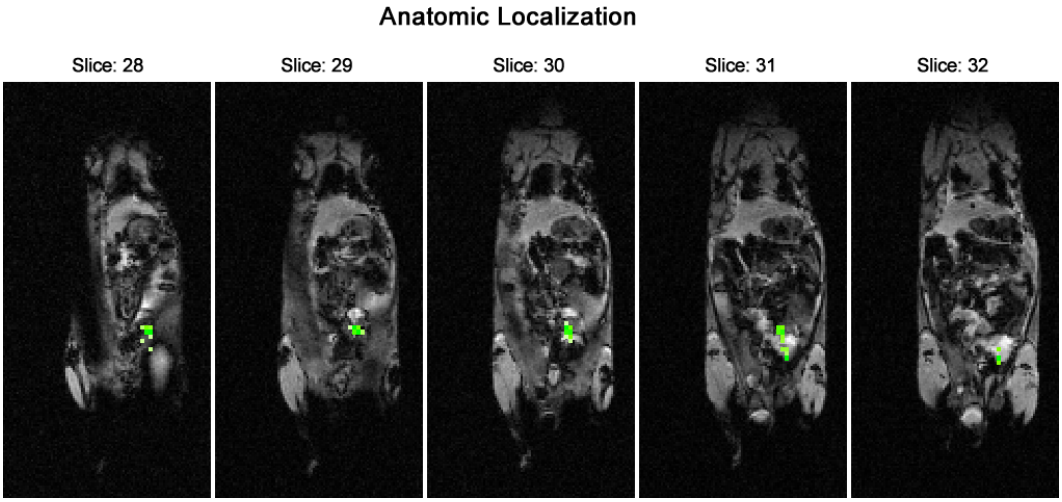

Figure 8.3 Anatomic localization of ^{19}F accumulation sites is achieved by co-registering R_c-filtered hot-spot images with high-resolution ^{1}H anatomic images, based on the respective scan geometries.

The study demonstrates that BaSSI reliably detects trace amounts of ^{19}F contrast agents under clinically viable conditions. Its denoising capability, based on the Rose criterion, effectively removes false positives and enhances specificity. However, overly strict thresholds can exclude true-positive voxels with low signal, so the R_c value must be balanced based on prior anatomical knowledge.

In the postmortem experiments, using $R_c = 5.7$ successfully suppressed off-target signals and enabled accurate anatomical localization of PFOB-filled microcapsules. These results confirm BaSSI's ability to generate artifact-free hot-spot images co-registered with anatomical structures.

For clinical translation, BaSSI must be evaluated under regulatory constraints, notably limited agent dosage and scan duration—two inherently competing requirements. Although faster than conventional CSI, BaSSI's full 3D scans remain time-intensive. A 48^3 acquisition with NSA = 16 required 1.5 hours, which aligns with durations reported at higher field strengths [146], [177–179]. This limitation stems from BaSSI's discrete k-space sampling using a stacked-spirals trajectory—an approach that offers robustness and spectral fidelity at the cost of acquisition speed.

In conclusion, BaSSI is a robust and sensitive spectroscopic imaging sequence capable of producing artifact-free ^{19}F images using an all-phase-encoded k-space strategy. Its effectiveness has been demonstrated *in vitro* and postmortem using PFOB-loaded polymer microcapsules, supporting its translational potential for preclinical and future clinical ^{19}F MRI applications.

8.2 *In Vivo* 3D Backprojection ^{19}F Spectroscopic Imaging

This section is adapted from [14].

Backprojection was one of the earliest MRI techniques for generating volumetric images [180]. Although largely replaced by Fourier-based methods, it remains relevant for reducing scan time in 3D imaging. This section evaluates the use of 3D backprojection with the F-uTSI sequence to image orally administered ^{19}F agents in mice.

All procedures followed Dutch animal welfare regulations under approval from the Maastricht University ethics committee. Imaging was performed on a 3 T scanner (Achieva, Philips Healthcare) with dual-tuned ^{1}H/^{19}F capability, using a thermally regulated animal cradle and physiological monitoring.

Mice received 300 μL of a 10% w/v suspension of PLGA encapsulated PFOB, corresponding to 0.3 μL of pure PFOB, orally, two hours before scanning. Anesthesia was induced and maintained by continuous infusion of KMA mixture.

Backprojection data were acquired as 2D F-uTSI projections at angular steps of 5°–30°. Each projection sampled a 32 × 32 k-space grid using 16 radial echoes at 1 mm × 1 mm resolution. For comparison, a fully phase-encoded 3D F-uTSI scan used a stack-of-radials acquisition (32 × 32 × 32 voxels, 1 mm^3, NSA = 2). Sequence parameters were consistent across acquisitions: echo time (TE) and echo spacing (ES) were set to 5.6 ms, repetition time (TR) to 1.0 s, and spectral resolution to 500 Hz, with an acquisition bandwidth of 32 kHz. Backprojection scan time varied according to angular resolution: 77 min (5°), 38.5 min (10°), 25.5 min (15°), 19 min (20°), and 13 min (30°), whereas the full 3D scan required 68 min.

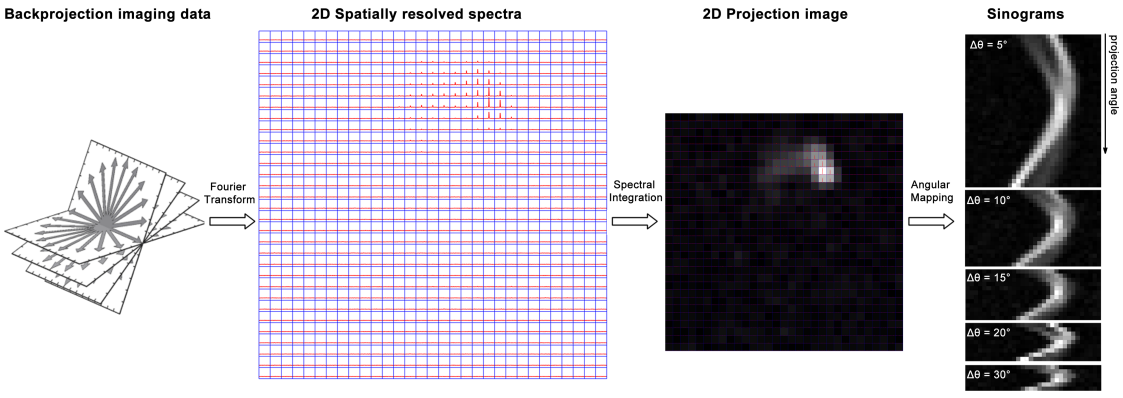

Figure 8.4 Projection set obtained with different angular resolutions are converted into sinograms.

As shown in Figure 8.4, spatially resolved spectra were obtained by applying a Fourier transform to the 2D F-uTSI data along both spatial dimensions and the spectral axis. Spectral integration was then performed to generate projection images for each acquisition angle. These projection images were subsequently assembled into sinograms by aligning them according to the angular sampling pattern.

Filtered backprojection images were reconstructed by applying the inverse Radon transform to the sinograms (Please see Section 3.1.4 for a detailed description of filtered backprojection). This step used MATLAB^{TM}'s `iradon` [161] function with a "Hann" filter and nearest-neighbor interpolation. Figure 8.5 presents a subset of resulting reconstructions at varying angular resolutions used in the acquisition.

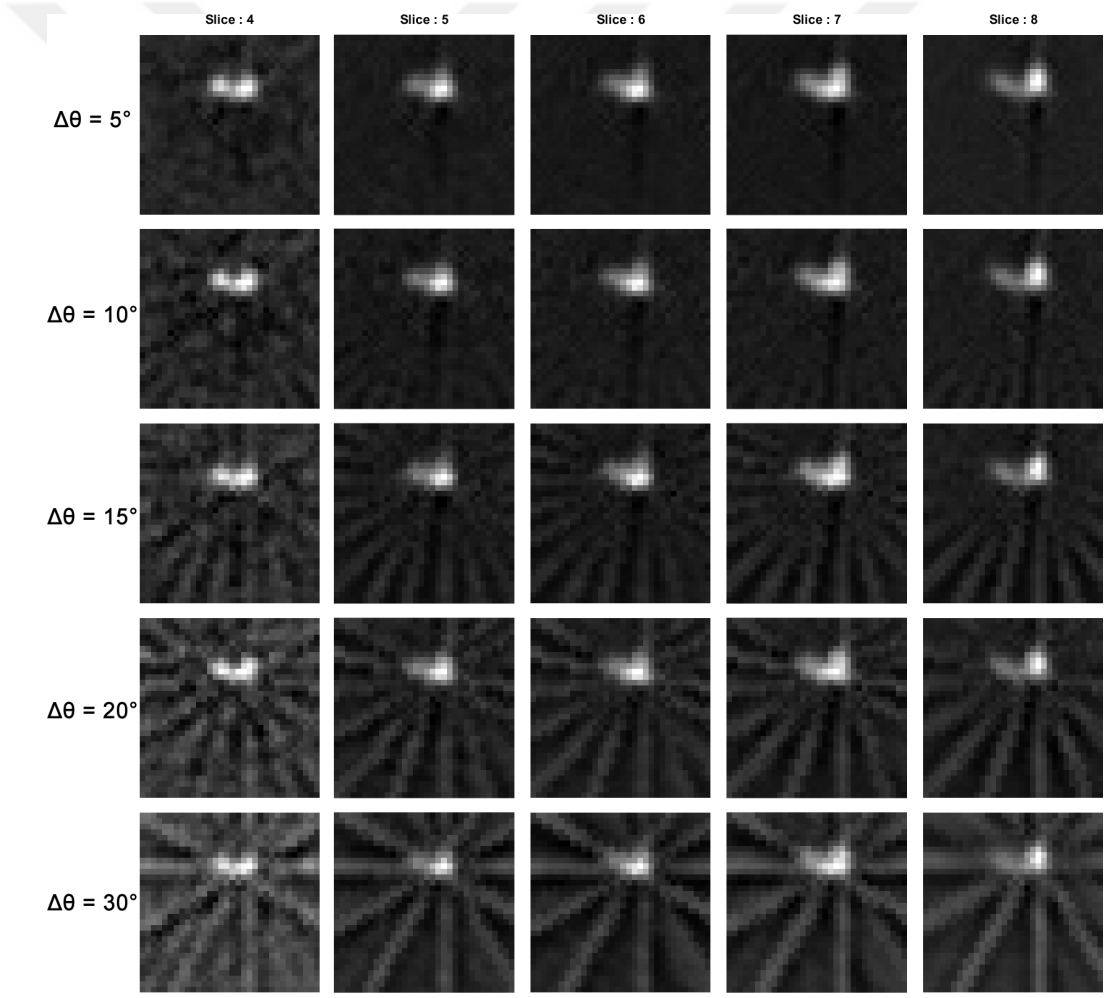

Figure 8.5 Slices reconstructed by means of filtered backprojection with Hann filter. Reconstruction artifacts become more pronounced as the angular resolution reduces.

For anatomical reference, T_1-weighted ^{1}H images were acquired in three orthogonal planes with 0.25 mm × 0.25 mm in-plane resolution using a fast gradient echo sequence. Geometric co-registration was used to overlay ^{1}H and ^{19}F data (Figure 8.6).

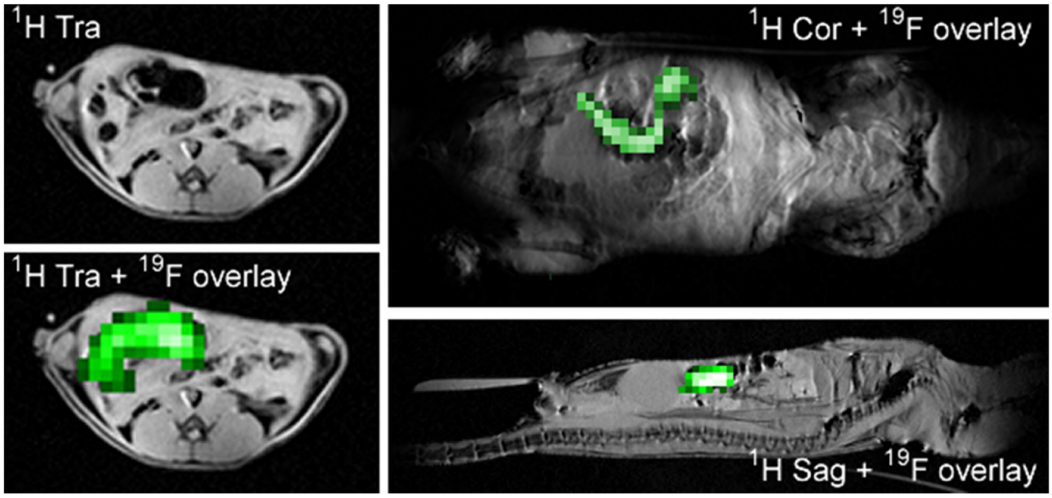

Figure 8.6 Anatomical localization of ^{19}F backprojection images.

Image quality was found to degrade with increasing angular step size. Larger increments resulted in undersampling artifacts and reduced signal-to-noise ratio (SNR), whereas fine angular resolutions (5° and 10°) yielded reconstructions with higher fidelity and fewer artifacts (Figure 8.7). Notably, the 10° dataset achieved superior image quality compared to the full 3D F-uTSI acquisition in approximately 45% less time (38.5 min vs. 68 min). The 5° acquisition provided the best reconstruction but required 13% more scan time.

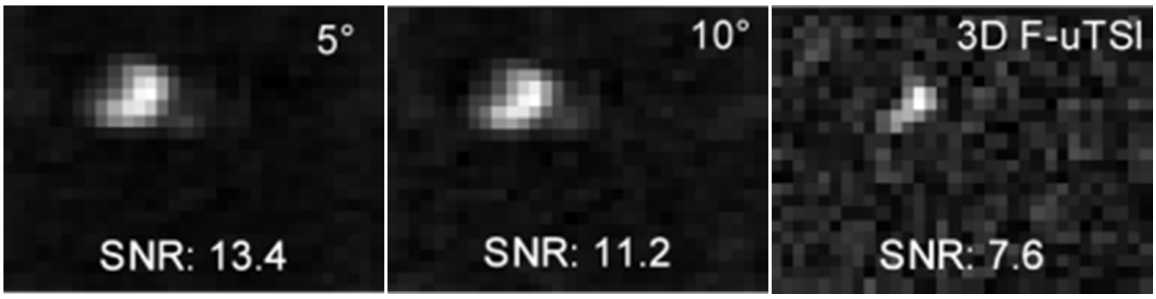

Figure 8.7 SNR of high angular resolution backprojection outperforms 3D cartesian acquisition.

These results demonstrate that backprojection imaging with F-uTSI provides a viable, time-efficient alternative to conventional 3D encoding for targeted applications in ^{19}F imaging. High-resolution datasets allowed precise anatomical localization of perfluorocarbon microparticles, suggesting potential use in preclinical imaging pipelines where throughput is critical.

8.3 *In Vivo* Multicolor Imaging of PFC Emulsions

This section is adapted from [5].

Spectroscopic imaging offers a powerful approach for detecting multiple contrast agents simultaneously by leveraging the chemical shift specificity of the perfluorocarbons. In contrast to conventional MRI contrast agents that rely on T_1 or T_2^* relaxation mechanisms [145, 146], PFCs can be uniquely identified via their resonance signatures in the ^{19}F NMR spectrum. This enables the spatially resolved mapping of different compounds without requiring separate scans or pre-contrast baselines.

Following data acquisition, ^{19}F MRSI allows individual resonance peaks to be integrated selectively, generating separate spatial maps for each agent. Assigning a distinct color to each map and overlaying them yields a composite *multi-color* image that visualizes the spatial distribution of multiple PFC agents within the imaging volume. An illustrative example is shown in Figure 8.8, where a phantom containing PFCE and PFOB is imaged. Integrating the full spectrum provides a combined image, whereas peak-specific integration produces chemically selective maps that are color-coded and fused into a multicolor representation.

This technique is particularly advantageous in molecular imaging studies that involve co-administered agents targeting distinct biological processes. By assigning distinct colors to chemically separable probes, multicolor imaging enables simultaneous visualization of phenomena such as inflammation and angiogenesis.

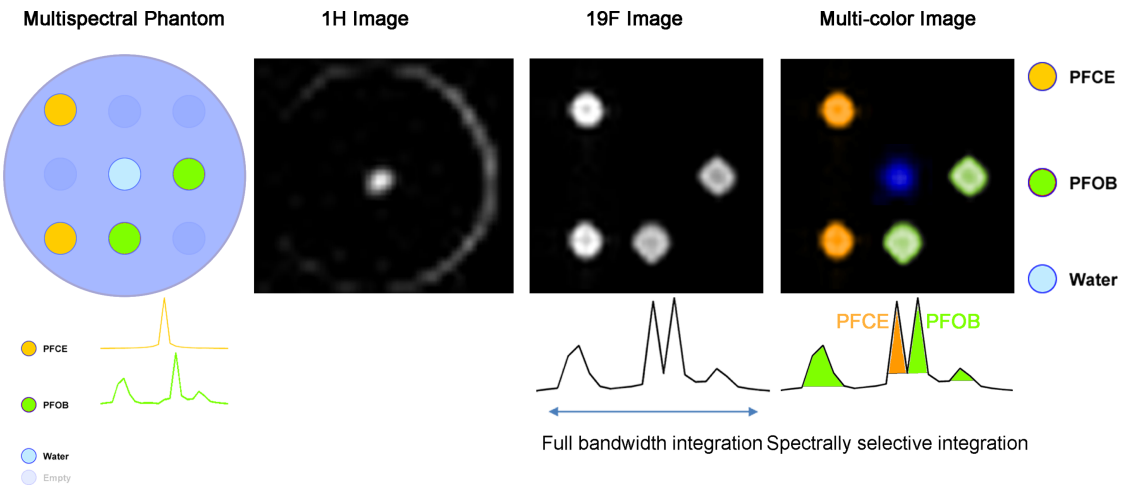

Figure 8.8 Spectroscopic imaging can be used to generate multi-color images by assigning colors to peaks in acquired spectra. Peak images are produced separately and combined into one image.

To demonstrate *in vivo* feasibility, F-uTSI was used to image rectally administered PFCE and PFOB in C57BL/6 mice. All procedures complied with Dutch legislation and were approved by the Maastricht University animal ethics committee. Mice received intraperitoneal KMA anesthesia (Ketamine 75 mg/kg, Medetomidine 1.0 mg/kg, Atropine 0.04 mg/kg), followed by continuous infusion. The contrast agents, comprised of 25% (v/v) PFOB and 16% (v/v) PFCE emulsions, were administered rectally approximately one hour before scanning. The amounts of contrast media used in the experiments corresponded to 50 μL of PFOB and 48 μL of PFCE.

Data were acquired on a 3 T scanner (Achieva, Philips Healthcare) using a dual-tuned ^{1}H/^{19}F spectrometer and a 7 × 12 cm surface coil. F-uTSI was used to sample a 48 × 48 × 14 k-space grid with 2 × 2 × 3 mm voxels. Acquisition parameters included 24 echoes per excitation, 437.5 Hz spectral resolution, 28 kHz bandwidth, TE = ES = 5 ms, TR = 285 ms, and NSA = 1 (total scan time: 6:23). The RF frequency was centered on the PFCE resonance. Spectral integration was performed over the CF_2 peaks of PFCE and PFOB. Anatomical reference was provided by T_1-weighted images (flip angle 35°, TE = 6.5 ms, TR = 24 ms) acquired with 0.55 mm × 0.55 mm × 4.0 mm resolution and geometrically co-registered to the ^{19}F dataset.

The resulting images were color-coded and fused into a multicolor composite. As shown in Figure 8.9, PFCE and PFOB are distinctly localized in the mouse colon.

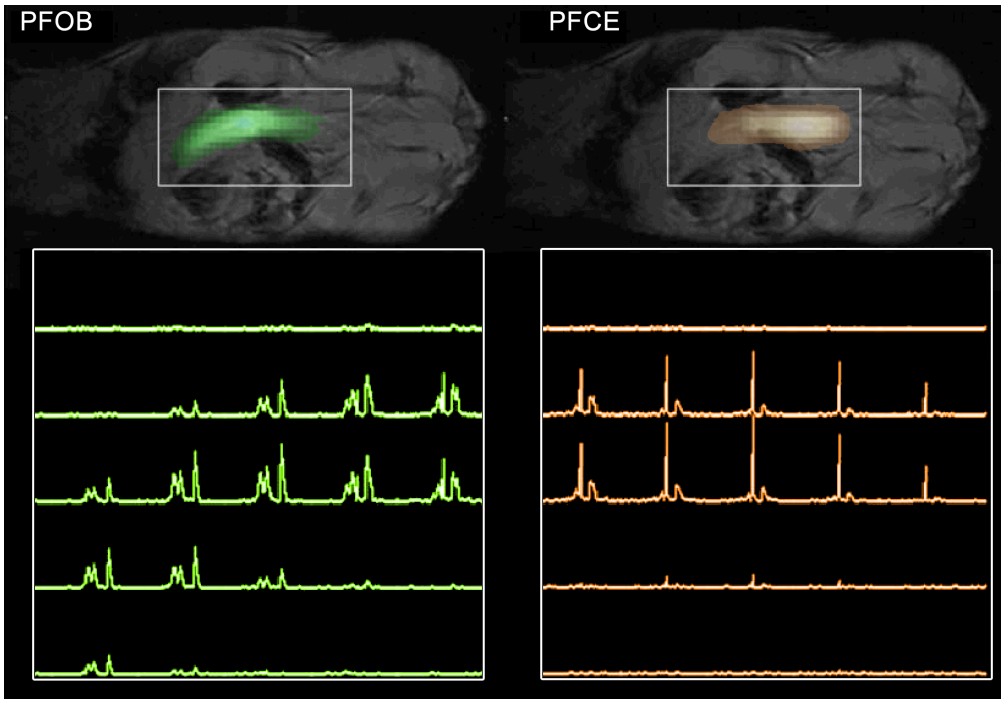

Figure 8.9 Multicolor imaging of rectally administered PFCE and PFOB in vivo.

8.4 *In Vivo* Imaging of Vx-2 tumors in Rabbit Models

This section is adapted from [13].

Quantitative molecular MR imaging of angiogenesis addresses a critical clinical need by improving prediction of response to anti-angiogenic therapies. Perfluorocarbons (PFCs) targeted to $\alpha_v\beta_3$-integrin have been widely investigated for this purpose, using both paramagnetic labeling and direct ^{19}F MR detection [87–89], [181], [182]. Fluorine-based imaging offers high specificity due to the absence of endogenous ^{19}F signal and removes the need for pre-contrast scans.

A major challenge in imaging clinically relevant PFCs is their broad chemical shift dispersion, which results in multiple resonances. When imaged with conventional gradient-echo or spin-echo sequences, these features generate severe chemical shift artifacts in both the readout and slice-selection directions. To address this limitation, a fast spectroscopic imaging method was developed to encode both spectral and spatial information simultaneously while minimizing distortions [1], [3]. This section demonstrates the use of this approach to detect angiogenesis in tumor-bearing rabbits using targeted PFC nanoparticles.

Vx-2 carcinoma cells (National Cancer Institute, USA) were implanted in the hind limb of male New Zealand White rabbits (2 kg). Tumors grew from 2–3 mm to 15 mm over two weeks. Imaging was performed three hours after intravenous administration of 1.0 mL/kg of $\alpha_v\beta_3$-targeted nanoparticles (20% v/v), corresponding to 400 μL PFOB. The emulsions were further enhanced by including Gd-DTPA-bis-oleate in the lipid shell for dual T_1 and ^{19}F contrast.

Anesthesia was induced with intramuscular xylazine/ketamine and maintained via intravenous ketamine infusion (20 mL/h). All procedures were approved by the Washington University animal ethics committee.

Imaging was conducted on a 3 T whole-body scanner (Achieva, Philips Healthcare) using a dual-tuned ^{1}H/^{19}F spectrometer and a 7 $\times$ 12 cm surface coil, with thermal regulation and physiological monitoring.

^{19}F data were acquired using the F-uTSI sequence, which samples a 32 $\times$ 32 $\times$ 32 k-space grid using pseudo-radial spin-echo trains. A stack-of-stars configuration was applied by phase-encoding each echo along the slice direction (Figure 8.10).

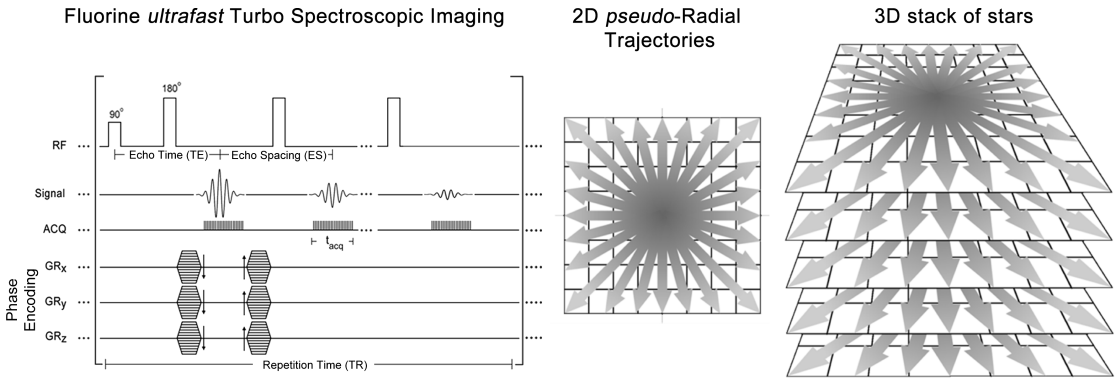

Figure 8.10 3D F-uTSI Imaging sequence with stack of stars k-space acquisition.

Sequence parameters were TE = ES = 5 ms and TR = 192 ms. For NSA = 1, the total scan time was 6.5 minutes for 1 NSA. Scans with NSA = 4–6 provided sufficient SNR, yielding acquisition times between 26 and 40 minutes.

The RF pulse was centered on the CF_2 resonance. Reconstruction was performed on the scanner, and ^{19}F images were generated by integrating over the CF_2 spectral band. Anatomical reference images were acquired using a T_1-weighted fast gradient echo sequence with flip angle 35°, TE = 6.5 ms, TR = 24 ms and a voxel size of 0.55 mm × 0.55 mm × 4.0 mm. Co-registration aligned the anatomical and ^{19}F datasets.

As shown in Figure 8.11, ^{19}F signal localized specifically to the tumor region, confirming selective binding of the targeted nanoparticles to $\alpha_v\beta_3$-integrins on angiogenic vasculature. These results demonstrate that F-uTSI enables artifact-free, chemically specific imaging of targeted agents with high sensitivity and clinically feasible scan times, supporting its utility in preclinical and translational angiogenesis imaging.

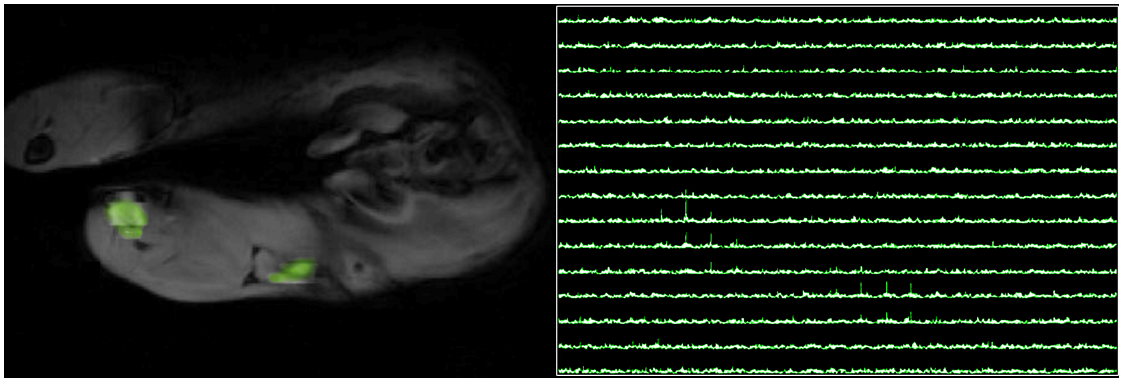

Figure 8.11 In vivo ^{19}F spectroscopic imaging of Vx2 tumors in rabbits.

8.5 *In Vivo* Imaging of Angiogenesis in Murine Models

This section is adapted from [6].

Angiogenesis is essential to endometrial physiology and implicated in disorders such as endometriosis and endometrial cancer [183]. Experimental models show that vascular remodeling peaks during the proliferative and secretory phases of the menstrual cycle, yet its regulation in mammals remains incompletely understood [184]. To visualize angiogenic activity *in situ*, we used ^{19}F MRI with F-uTSI and PFC nanoparticles functionalized with Arg-Gly-Asp (RGD) peptides targeting integrin receptors on newly formed endothelial cells.

Experiments were conducted on a 3 T scanner (Achieva, Philips Healthcare) with a dual-tuned ^{1}H/^{19}F system and a small-animal surface coil. Mice were scanned under anesthesia with full physiological monitoring. All procedures complied with Dutch animal welfare regulations and were ethically approved.

Male and female Swiss nu/nu mice received two intravenous doses of 150 μL of PFOB-based nanoparticles (2% lipid, 20% w/v PFOB, corresponding to 15.5 μL of pure PFOB) at 20 and 4 hours before imaging. The lipid shell contained DSPC, DSPE-PEG-2000, cholesterol, Rhodamine-PE, and DSPE-PEG2000-maleimide for RGD conjugation. Male mice served as controls.

F-uTSI was configured with 32-echo spin-echo trains and 3D pseudo-radial encoding across a $64 \times 64 \times 7$ k-space grid. The field of view of the volumetric acquistion was set to 64 mm $\times$ 64 mm $\times$ 21 mm, resulting in a voxel size of 1 mm $\times$ 1 mm $\times$ 3 mm. The RF carrier was centered on the CF_2 resonance of PFOB. Imaging was performed with 8 signal averages, TE = ES = 4 ms, and TR = 375 ms, for a total scan time of 45 minutes.

Spectral data were integrated over a 2 kHz window centered on the CF_2 resonance to generate spatial maps of tracer distribution. For anatomical localization, T_1-weighted ^{1}H images were acquired using a multi-gradient echo sequence with a voxel size of 0.5 mm $\times$ 0.5 mm $\times$ 1.0 mm.

As shown in Figure 8.12, ^{19}F signals in female mice localized prominently to the liver and spleen, consistent with known PFC clearance pathways [49], [185], [186]. In three of five female subjects, an additional focal signal was observed in the urogenital region. This signal was not present in male controls.

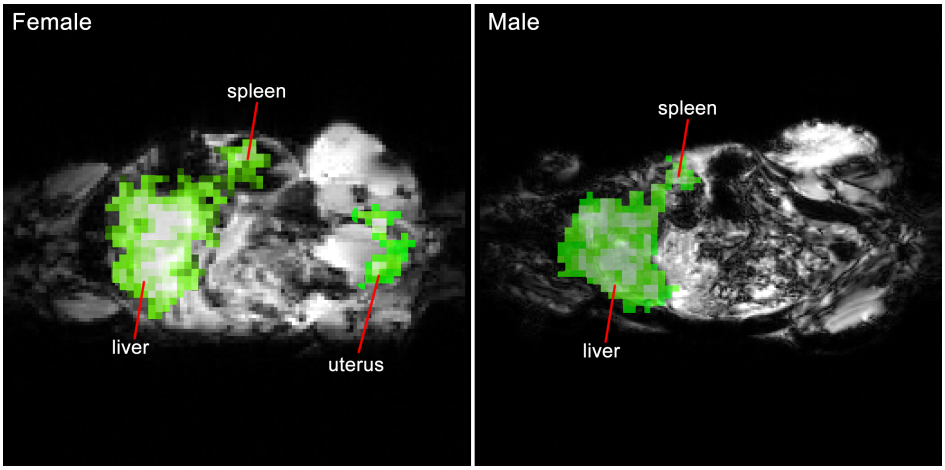

Figure 8.12 In vivo ^{19}F spectroscopic imaging shows signal in the urogenital region of females (left), indicating angiogenic activity during the menstrual cycle, with no uptake in males references(right).

Imaging results suggested selective accumulation via RGD-mediated targeting of integrin receptors associated with angiogenic activity in the reproductive tract.Post-mortem analysis supported these findings. Mice were euthanized by cervical dislocation, and major organs, including liver, spleen, and uterus, were excised for spectroscopy. Single-voxel ^{19}F MR spectroscopy was performed using a perfluoro-15-crown-5-ether (PFCE) reference standard to enable quantitative comparison. As shown in Figure 8.13, PFOB signal intensity in the uterus reached approximately 10–20% of liver and spleen levels when normalized to the PFCE reference, confirming selective accumulation in the reproductive tract.

This study demonstrates that ^{19}F MRSI using RGD-functionalized PFC nanoparticles enables non-invasive, chemically selective imaging of angiogenesis in the female reproductive system. The method provides spatially resolved maps of molecular targets without requiring baseline subtraction, and holds potential for investigating endometrial physiology as well as for future clinical translation in gynecologic pathologies involving aberrant vascularization.

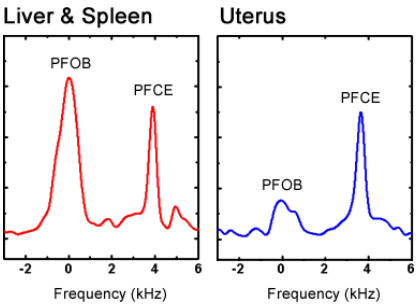

Figure 8.13 ^{19}F spectroscopy with PFCE reference confirms PFC accumulation in the uterus.

8.6 Summary

This chapter explored a range of preclinical applications of ^{19}F MRSI, with emphasis on the BaSSI and F-uTSI sequences in both post-mortem and *in vivo* studies. The experiments highlight the versatility, sensitivity, and translational potential of these methods for molecular and cellular imaging with fluorinated contrast agents.

BaSSI was validated through *post-mortem* imaging of PLGA microcapsules filled with PFOB in euthanized mice [16], [17]. These experiments confirmed that BaSSI can detect trace amounts of ^{19}F contrast agent with high specificity and without ghosting artifacts. A Rose criterion–based denoising filter with $R_c = 5.7$ proved effective in removing false positives, producing clean, artifact-free images under clinically viable conditions.

In vivo applications included high-resolution 3D backprojection imaging of orally administered PFOB-labeled PLGA microbubbles in small mice [14]. Angularly spaced projections reconstructed via filtered backprojection achieved high spatial fidelity and reduced scan times relative to conventional phase-encoded MRSI. An angular resolution of 10° outperformed a full 3D F-uTSI scan in both image quality and efficiency.

Multicolor imaging was demonstrated by simultaneous detection of PFCE and PFOB in rectally dosed mice [5]. Distinct spectral signatures enabled chemical differentiation, and peak-specific integration produced spatial maps that were fused into a composite image—offering a powerful strategy for visualizing multiple biological targets in a single scan.

Targeted angiogenesis imaging was shown in a Vx-2 tumor model in rabbits using $\alpha_v\beta_3$-integrin-targeted PFC nanoparticles, which localized ^{19}F signal specifically to the tumor [13]. A related study in mice focused on endometrial angiogenesis, where RGD-functionalized PFOB nanoparticles accumulated in the reproductive tract [6]. Post-mortem spectroscopy confirmed these findings, illustrating potential applications in gynecologic imaging.

Together, these studies demonstrate that ^{19}F MRSI with BaSSI and F-uTSI is sensitive, robust, and adaptable across diverse experimental models. These techniques enable artifact-resistant imaging with submillimolar detection sensitivity, supporting their translational promise for both preclinical and future clinical ^{19}F MRI.

9. SUMMARY OF INNOVATIONS AND CONTRIBUTIONS

This thesis advances ^{19}F magnetic resonance spectroscopic imaging (MRSI) through the development of **BaSSI** (Balanced Spiral Spectroscopic Imaging), a broadband, fully phase-encoded sequence optimized for sparse-agent detection under realistic scan-time and hardware constraints. Designed as a successor to Fluorine ultrafast Turbo Spectroscopic Imaging (F-uTSI), BaSSI integrates short-TR broadband excitation, spiral k-space sampling, and voxelwise denoising based on the Rose criterion. Together, these features enable chemically specific hot-spot imaging of fluorinated agents in both preclinical and translational settings.

The contributions of this work are summarized as follows:

- **Reimplementation of F-uTSI:**

  F-uTSI, a turbo spin echo–based broadband MRSI sequence, was re-implemented and re-evaluated as a technical foundation for further innovation. This step enabled performance benchmarking on modern hardware and affirmed the feasibility of broadband ^{19}F spectroscopic imaging.

- **Invention of BaSSI:**

  BaSSI was designed as a broadband, FID-based, fully phase-encoded spectroscopic sequence using a pseudo-spiral k-space trajectory. Free from steady-state constraints, it operates at short repetition times and supports robust imaging of chemically complex agents in formats ranging from neat liquids to emulsions and polymer-encapsulated microbubbles.

- **Rose Criterion as Performance Metric and Denoising Method:**

  The Rose criterion (R_c) was applied voxelwise as both a visibility metric and a denoising tool, enabling principled background suppression and false-positive rejection in sparse-signal regimes. Unlike conventional thresholding or smoothing techniques, this approach preserved spatial fidelity while providing a statistically grounded basis for signal detectability.

- **Experimental Validation of MRSI Sequences:**

  Both F-uTSI and BaSSI were implemented on a clinical 3.0 T MRI scanner with a dual-tuned ^{1}H/^{19}F coil, and validated through Bloch simulations and phantom experiments using sub-microliter PFOB volumes. These studies enabled parameter optimization and confirmed the sequences' stability, reproducibility, and resistance to artifacts under realistic imaging conditions.

- **Performance Benchmarking:**

  BaSSI was benchmarked against 3D UTE bSSFP using standardized phantom models. It demonstrated superior imaging efficiency, lower detection thresholds, and improved hardware compatibility, successfully detecting 0.05 μL PFOB in 2-minute scans—conditions under which UTE bSSFP failed.

- **Demonstrated Applications in Preclinical Imaging:**

  ^{19}F MRSI was applied across a range of preclinical experiments. BaSSI enabled co-registered hot-spot imaging of PFOB-labeled microbubbles in postmortem mouse models, angiogenesis imaging in rabbit and murine models using targeted nanoparticles, multicolor imaging of co-administered PFCs, and fast 3D reconstructions via filtered backprojection.

- **Scientific Output:**

  Results from this thesis were disseminated through peer-reviewed venues, including the 15$^{\text{th}}$ ISMRM Annual Meeting [16] and *NMR in Biomedicine* [17]:

  1. Fast Fluorine Spectroscopic Imaging with pseudo-spiral k-space sampling, M. Yildirim, P. Scholtz, M. Schütz, X. Kovalyk, E. Heijman, R. Lamerichs, H. Grüll, E. O. Isik, *Proceedings of the 15th Annual Meeting of the International Society for Magnetic Resonance in Medicine (ISMRM)*, Abstract 1249, Berlin, Germany, 2007.
  2. Fast ^{19}F spectroscopic imaging with pseudo-spiral k-space sampling, M. Yildirim, X. Kovalyk, P. Scholtz, M. Schütz, J. Lindemeyer, R. Lamerichs, H. Grüll, E. O. Isik, *NMR in Biomedicine*, Vol. 37, No. 4, e5086, 2024. DOI: `https://doi.org/10.1002/nbm.5086`

Taken together, these contributions establish BaSSI as a versatile, time-efficient spectroscopic imaging platform with high sensitivity to low-concentration fluorinated agents. Through the invention of a new acquisition strategy, the integration of statistical visibility metrics, and translational validation across preclinical models, this thesis advances the state of ^{19}F MRSI and lays the groundwork for future clinical applications.

10. DISCUSSION AND CONCLUDING REMARKS

This thesis presents the development, implementation, and validation of **BaSSI**, the Balanced Spiral Spectroscopic Imaging sequence, which is a broadband, fully phase-encoded ^{19}F MR spectroscopic imaging (MRSI) sequence tailored for the detection and localization of low-concentration fluorinated agents under clinically realistic conditions. Conceived as a successor to the F-uTSI sequence developed by the author in earlier work, BaSSI directly addresses critical limitations in ^{19}F MRI, including poor spectral flexibility, long acquisition times, and unreliable detection in sparse-signal settings.

The design of BaSSI centers on three core engineering strategies: broadband excitation, FID-based acquisition, and fully phase-encoded pseudo-spiral k-space traversal. A short rectangular RF pulse (6.7–73.5 µs) uniformly excites spectral bandwidths exceeding 20 kHz, enabling simultaneous excitation of multiple resonance groups, such as CF_3, CF_2, and CF_2Br in PFOB, without the need for frequency-selective excitation or spectral preconditioning.

Spatial encoding is performed via a center-out pseudo-spiral trajectory implemented using blipped phase-encoding gradients over a discretized Cartesian grid. This trajectory, which mimics a single-arm Archimedean spiral, was carefully selected based on numerical simulations showing minimal point spread function (PSF) broadening under T_2^*-dominated signal decay.

BaSSI initiates FID sampling within 0.62–0.68 ms of excitation, ensuring the recovery of fast-decaying components like the CF_2 group. These early acquisition windows were optimized through Bloch simulations and confirmed experimentally to maximize signal retention in low-SNR environments.

The sequence operates at short repetition times (TR = 2.5–3.5 ms) and moderate flip angles (30°), balancing signal efficiency with RF and SAR constraints. Flip angle sweeps performed during optimization confirmed that 30° provided the highest SNR per unit scan time while maintaining hardware stability. Importantly, these design parameters were validated in practice using calibrated phantoms and a clinical 3.0 T MRI scanner equipped with a dual-tuned ^{1}H/^{19}F coil, demonstrating the method's feasibility under clinically relevant conditions.

Performance validation was conducted across sub-microliter samples of PFOB in a systematic benchmarking study against 3D UTE bSSFP, a widely adopted sequence in the ^{19}F MRI community. BaSSI consistently outperformed 3D UTE bSSFP across

multiple metrics. It achieved a 1.8× improvement in imaging efficiency and successfully detected 0.05 µL volumes within 2-minute scans, whereas 3D UTE bSSFP failed under identical conditions due to gradient amplifier overload. These findings highlight BaSSI's robustness, resilience to hardware limitations, and sensitivity under realistic operational constraints.

Spectral fidelity, which is a key requirement for chemically specific imaging, was preserved across all acquisition settings. BaSSI reliably resolved the resonance structure of PFOB, and CF_2Br peaks, even at low NSA values. This fidelity generalizes BaSSI's utility to other spectrally complex agents such as PFCE, PTBCH, and fluorinated emulsions or polymer-encapsulated nanoparticles. Its ability to generate spatially resolved, chemically specific maps without the use of spectral preselection establishes BaSSI as a uniquely versatile platform for multicolor molecular imaging.

A key methodological contribution of this thesis is the integration of the Rose criterion as both a voxelwise detection metric and a denoising tool. Unlike traditional metrics such as SNR or CNR, which offer limited interpretability in sparse-signal regimes, the Rose criterion provides a statistically grounded visibility threshold. When applied voxelwise, it enables robust background suppression and false-positive rejection without relying on smoothing filters or regularization, which often compromise resolution or introduce spatial ambiguity. In postmortem imaging of PFOB-labeled microbubbles, thresholding at $R_c = 5.7$ yielded anatomically accurate hot-spot maps that retained chemically specific signal while eliminating non-specific background—underscoring the power of principled statistical inference in image post-processing. Although computationally tractable, voxelwise denoising and spectral-domain reconstruction may require optimization or hardware acceleration for integration into real-time clinical workflows.

BaSSI's architecture also eliminates the dependencies that often plague spectroscopic methods: it requires no echo train stability, no steady-state buildup, and no spectral filtering. This design simplifies implementation and improves robustness against hardware inconsistencies, all while supporting broadband, short-TR imaging with high spatial fidelity. The successful deployment of BaSSI on an aging 3.0 T clinical system further emphasizes its low reliance on custom hardware or proprietary sequences.

BaSSI emerges from this work as a coherent synthesis of engineering innovation, signal modeling, and practical implementation. It builds upon the foundational principles introduced by F-uTSI, extending them with modern encoding strategies and detection frameworks. The resulting sequence demonstrates reliable, spectrally rich

imaging under realistic hardware and scan-time constraints, offering a robust platform for chemically specific ^{19}F molecular imaging. Its successful implementation on clinical-grade systems, paired with statistically grounded performance metrics, affirms its readiness for broader application across both preclinical and translational domains.

However, the pathway from methodological innovation to clinical adoption is not without obstacles. Several limitations observed during experimental validation must be addressed before BaSSI can fulfill its translational potential.

All experimental validations in this thesis were performed using a 5 cm quadrature animal coil. For clinical deployment, these methods must be adapted and verified on larger, human-scale hardware. Coil diameter directly affects sensitivity and noise characteristics, and clinical systems typically suffer from lower SNR and greater B_1 inhomogeneity across the field of view. Consequently, BaSSI must be tested under the electromagnetic and geometric constraints of clinical coils to assess scalability. Comprehensive validation on full-scale, clinically approved coils and scanners is therefore a necessary step toward translational readiness. In parallel, the integration of BaSSI into routine imaging workflows will require robust calibration pipelines, minimal operator intervention, and streamlined reconstruction compatible with clinical timelines.

Another main challenge is the issue of scan duration. While BaSSI demonstrated excellent performance in 2D hot-spot detection, successfully imaging sub-microliter PFOB samples within 2-minute scans, full 3D acquisitions remain time-intensive. As shown in postmortem anatomical localization experiments, a typical 48×48×48 acquisition with NSA = 16 required approximately 105 minutes to complete. Such scan times are not uncommon in ^{19}F MRI, even at high magnetic fields. Mastropietro et al. [146] reported a 2-hour acquisition for a 32×32 RARE scan of potassium hexafluorophosphate (KPF_6) phantoms at 7.0 T, while Zhong et al. [178] acquired a 64^3 dataset in just over an hour using a PFPE-based agent at 11.7 T.

BaSSI, by comparison, operates at 3.0 T and uses a discrete, fully phase-encoded encoding scheme. Its stacked-spiral trajectory samples one k-space grid point per TR, inherently lengthening total acquisition time. Comparable work by Kampf et al. [177] using fully phase-encoded CSI required 37 minutes at 7.0 T to acquire a 48×48×70 dataset with NSA = 1, which is an acquisition that would require well over an hour when projected to 3.0 T based on linear scaling. These observations confirm that long scan durations, while acceptable for preclinical research, are impractical for routine clinical workflows.

To mitigate this constraint, scan acceleration techniques must be pursued. Compressed sensing presents a promising solution, exploiting the inherent sparsity of ^{19}F datasets. Kampf et al. [177], [179] demonstrated significant scan time reduction in fully phase-encoded CSI through compressed sensing reconstruction, while Darçot et al. [171] and Schoormans et al. [138] explored variable-density undersampling schemes specifically tailored to the low-SNR conditions of ^{19}F MRI. These strategies emphasize dense sampling in the central k-space region, where signal energy is highest, while sparsely sampling the periphery.

However, most of these studies were conducted at field strengths of 7.0 T or higher, where intrinsic SNR is markedly greater. At 3.0 T, the risk of undersampling artifacts, signal loss, or false-positive hot-spots becomes more pronounced particularly in settings where small-volume signals are to be detected reliably. Thus, while compressed sensing remains a critical direction for future development, its application in BaSSI must be approached with careful validation, conservative undersampling strategies, and possibly field-specific adaptation.

Another promising avenue involves contrast agent engineering. Enhancing the relaxometric properties of perfluorocarbons, such as by doping the emulsifying lipid shell with Gd^{3+}, could shorten T_1, increase per-TR signal yield, and reduce the number of averages required for detectability [125]. However, this approach carries significant caveats: toxicity, limited biological clearance, contrast quenching at high agent concentrations, and regulatory complexity may all limit its widespread applicability. Initial work using Gd-DOTA-modified nanoparticles has demonstrated improved signal performance, but also revealed issues with cell viability and quantification accuracy that will need to be addressed through refined formulation strategies. In parallel, the development of clinically approved fluorinated contrast agents with favorable pharmacokinetics will be essential to support translation of ^{19}F imaging platforms such as BaSSI into diagnostic practice.

Quantification presents perhaps the most fundamental challenge for the future of ^{19}F MRI. Unlike ^{1}H imaging, ^{19}F MRI lacks an endogenous signal for referencing, and inter-scan variability in coil sensitivity and system calibration complicates absolute measurements. Embedded referencing, such as integrating stable signal sources into the imaging chain (e.g., within the RF coil) and applying spectral separation through multi-color imaging, offers one possible solution. However, this approach is prone to spatial B_1 inhomogeneity, ADC saturation effects, and calibration drift, which limit its reliability across imaging sessions, coil loadings and platforms.

Alternatively, and in a decidedly Don Quixotian spirit, a more radical solution may lie in the development of standardized, scanner-independent quantification protocols based on external referencing schemes derived from population-level datasets. This approach would require the acquisition of a large data set of ^{19}F measurements obtained under systematically varied conditions, including differences in coil geometry, thermal loading, magnetic field inhomogeneity, and both physical and physiological variability across subjects. These data could then be used to train predictive quantification models capable of mapping voxelwise signal amplitudes to absolute concentrations of contrast agent. If successful, this strategy would provide a statistically grounded framework for reproducible, system-independent interpretation of spectroscopic imaging datasets, enabling quantitative readouts that are resilient to hardware configuration and operational variability.

In closing, BaSSI is both the product of two decades of spectroscopic imaging development and a foundation for future innovation. While its current implementation is constrained by hardware limitations and quantification challenges, its conceptual framework—built on efficient broadband encoding, statistical visibility metrics, and spectral richness—remains sound and extensible. Future work focused on acceleration, agent engineering, and standardized quantification will be essential to fully realize BaSSI's promise in both preclinical and clinical imaging. The groundwork laid in this thesis provides a robust platform from which such advances can be launched.

APPENDIX A. PRINCIPLES OF NMR AND MRI

This chapter provides a brief introduction to the principles of NMR and MRI, which are based on the seminal works of Nobel laureates Richard R. Ernst (NMR), Peter Mansfield (MRI), and Paul C. Lauterbur (MRI), and their co-authors, as well as the textbooks of Anatol Abragam, E. Mark Haacke et al., and Matt A. Bernstein et al. [187–192]. The chapter also references Oppenheim et al.'s textbook on signal theory [193] when elaboration on fundamental concepts governing signals, sampling, and Fourier transforms is deemed necessary.

A.1 Nuclear Magnetic Resonance

Nuclear Magnetic Resonance (NMR) is a technique that involves the study of how energy is transferred between nuclei and magnetic fields, and it is the key mechanism behind Magnetic Resonance Imaging (MRI). To fully understand NMR, one must begin at the nuclear level, examining subatomic properties, and then consider how groups of atoms interact with magnetic fields on a macroscopic scale.

In MR practice, the focus is typically on ensembles of nuclei rather than individual spins. These ensembles can be described from both a microscopic view, considering each nucleus individually, and a macroscopic perspective, treating the group as a whole. Statistical mechanics bridges these views by relating individual spin behavior to the collective magnetization of the system.

At the microscopic level, NMR principles are rooted in nuclear structure. Nuclei consist of protons and neutrons, with protons contributing to magnetic behavior due to their charge and spin. The angular momentum or spin of the nucleus gives rise to a magnetic moment:

$$\vec{\mu} = \gamma \vec{J} \tag{A.1}$$

Here, γ is the gyromagnetic ratio specific to the nucleus, and $\vec{J}$ is its angular momentum.

Quantum mechanics dictates that $\vec{J}$ is quantized:

$$J = \hbar \sqrt{I(I+1)} \tag{A.2}$$

where I is the spin quantum number and $\hbar = h/2\pi$ is the reduced Planck constant.

The magnetic moment magnitude becomes:

$$\mu = \gamma\hbar\sqrt{I(I+1)} \tag{A.3}$$

Most elements possess isotopes with nonzero spin, making them candidates for NMR. Spin quantum numbers determine magnetic behavior:

- $I = 0$: No magnetic moment
- $I = 1$: Integral spin (odd atomic number, even mass)
- $I = \frac{1}{2}$: Half-integer spin (odd mass number)

Hydrogen-1 (^{1}H), with $I = \frac{1}{2}$, is the most commonly imaged nucleus in MRI due to its abundance in biological tissues. Other NMR-active nuclei include ^{31}P, ^{23}Na, ^{13}C, and ^{19}F.

In the absence of an external magnetic field, magnetic moment orientations are random. Under a static field $\vec{B}_0$, quantum mechanics restricts $\vec{\mu}$ to discrete orientations:

$$\mu_z = \gamma\hbar m_I \quad \text{where} \quad m_I = -I, -I+1, \ldots, I \tag{A.4}$$

The angle θ between $\vec{\mu}$ and B_0 satisfies:

$$\cos\theta = \frac{m_I}{\sqrt{I(I+1)}} \tag{A.5}$$

For spin-1/2 nuclei:

$$\cos\theta = \pm\frac{1}{\sqrt{3}} \quad \Rightarrow \quad \theta = \pm 54.73^\circ \tag{A.6}$$

In an external field $\vec{B}_0 = B_0\hat{k}$, the magnetic moment precesses at the Larmor frequency ω_0:

$$\frac{d\vec{\mu}}{dt} = \gamma\vec{\mu} \times \vec{B}_0 \quad \Rightarrow \quad \vec{\omega} = -\gamma\vec{B}_0 \tag{A.7}$$

$$\mu_z(t) = \mu_z(0), \quad \mu_{xy}(t) = \mu_{xy}(0)e^{-i\gamma B_0 t} \tag{A.8}$$

The energy difference between spin states in a field B_0 is:

$$\Delta E = \gamma \hbar B_0 \tag{A.9}$$

Spin populations follow the Boltzmann distribution:

$$\frac{N_\uparrow}{N_\downarrow} = e^{-\Delta E/kT}, \quad N_\uparrow - N_\downarrow = N_s \frac{\gamma \hbar B_0}{2kT} \tag{A.10}$$

The net magnetization $\vec{M}$ in thermal equilibrium is:

$$\vec{M} = N_s \frac{\gamma^2 \hbar^2 B_0}{4kT} \vec{k} \tag{A.11}$$

and its magnitude is proportional to the field strength B_0 and inversely to temperature T.

This basic framework establishes how an ensemble of spins in an external magnetic field gives rise to a measurable net magnetization, forming the basis for signal generation and manipulation in MRI.

A.2 RF Excitation and Signal Generation

Once a net magnetization $\vec{M}$ has formed along the direction of the static magnetic field $\vec{B}_0$, it can be perturbed by applying a time-varying magnetic field $\vec{B}_1(t)$ perpendicular to $\vec{B}_0$. This field is typically delivered as a short burst of radiofrequency (RF) energy oscillating at the Larmor frequency ω_0. The interaction between $\vec{B}_1$ and the spin system induces transitions between energy states, altering the distribution of spin populations and thereby the orientation of the net magnetization vector.

The flip angle α induced by the RF pulse is given by:

$$\alpha = \gamma B_1 \tau \tag{A.12}$$

where B_1 is the amplitude of the RF field and τ is its duration. A 90° pulse rotates $\vec{M}$ entirely into the transverse (xy) plane, while a 180° pulse inverts its direction along the z-axis.

Following RF excitation, the transverse component of magnetization M_{xy} begins to precess in the xy-plane at the Larmor frequency. This precessing magnetic moment

induces an electromotive force (EMF) in receiver coils according to Faraday's law of electromagnetic induction. The resulting time-domain signal is known as the free induction decay (FID).

After excitation, the net magnetization vector $\vec{M}$ begins to return to its equilibrium state through two independent processes:

- **Longitudinal relaxation** (T_1): Also known as spin-lattice relaxation, this process describes the recovery of the M_z component of magnetization along the direction of the main magnetic field. It results from energy exchange between the spin system and its surrounding lattice.
- **Transverse relaxation** (T_2): Also known as spin-spin relaxation, this process describes the decay of the M_{xy} component due to loss of phase coherence among spins without energy exchange with the environment.

These processes are modeled by exponential functions:

$$M_z(t) = M_0 \left(1 - e^{-t/T_1}\right) \tag{A.13}$$

$$M_{xy}(t) = M_{xy}(0)\, e^{-t/T_2} \tag{A.14}$$

The combined effect of T_1 and T_2 relaxation governs signal intensity and contrast in MR imaging, with different tissues exhibiting unique relaxation time constants. Accurate timing of data acquisition relative to these time constants enables selective contrast weighting in MRI protocols.

A.2.1 Free Induction Decay (FID)

Free Induction Decay (FID) represents the most fundamental NMR response, generated when the magnetization vector is perturbed from its equilibrium orientation and observed during its relaxation phase. Characterized as a sinusoidal waveform, the FID oscillates in accordance with the Larmor frequency intrinsic to the spin system, while its amplitude undergoes an exponential decay influenced by the transverse relaxation time, T_2.

The FID signal is expressed as the sum of sinusoidal induction signals from spins

across the entire spectral range of the spin system:

$$S(t) = \int_{-\infty}^{\infty} \sin\alpha(\omega)\,\rho(\omega)\,e^{-t/T_{2,\omega}}\,e^{-i\omega t}\,d\omega \tag{A.15}$$

Here, $\rho(\omega)$ indicates the spectral density function that specifies the signal strength of an iso-chromat resonating at Larmor frequency ω, $\alpha(\omega)$ is the flip angle achieved by the iso-chromat during excitation, and $T_{2,\omega}$ denotes the transverse relaxation time specific to the iso-chromat.

For a spin system containing only one iso-chromat, the equation for the signal simplifies to:

$$S(t) = M_{xy,0}\,e^{-t/T_2}\,e^{-i\omega_0 t} \tag{A.16}$$

Here, $M_{xy,0}$ denotes the transverse magnetization immediately after excitation, determined by the equilibrium magnetization M_z^0 and the flip angle of the RF pulse:

$$M_{xy,0} = M_z^0 \sin\alpha \tag{A.17}$$

The FID signal is characterized by two fundamental attributes: its initial amplitude and its rate of decay. The signal's peak amplitude is observed immediately after the excitation phase, influenced by both the flip angle and the thermal equilibrium magnetization of the spin system.

The decay rate of a Free Induction Decay (FID) signal crucially depends on the spin system's spectral distribution. In the case of a single spectral component within a uniformly homogeneous sample and magnetic field environment, the FID signal decays in accordance with the transverse relaxation time, T_2.

Contrastingly, inhomogeneities within the magnetic field, such as those caused by variations in susceptibility across the imaging volume, result in an expedited decay rate for the FID signal. This accelerated decay is attributed to the disparate magnetic field strengths encountered by spins during excitation, leading to a range of transverse phases. The resultant phase diversity among spins induces destructive interference, precipitating a net magnetization that decays faster than would be observed in a homogeneous field setting. This field inhomogeneity effect is often modeled using a three-parameter Lorentzian distribution shown in Figure A.1, which modifies

the spectral density function as follows:

$$\rho(\omega) = M_z^0 \frac{(\gamma \Delta B_0)^2}{(\gamma \Delta B_0)^2 + (\omega - \omega_0)^2} \tag{A.18}$$

Here, ΔB_0 represents the degree of field inhomogeneity, and ω_0 is the spin-system's primary Larmor frequency.

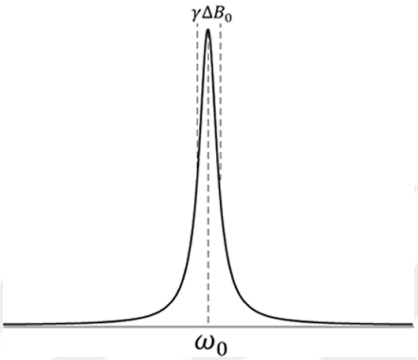

Figure A.1 The three-parameter Lorentzian function used to model the distribution of Larmor frequencies within a spin system, illustrating line broadening effects caused by field inhomogeneities.

Applying the adjusted spectral density given by the Lorentzian to the FID signal equation yields:

$$S(t) = \int_{-\infty}^{\infty} M_z^0 \sin\alpha(\omega) \frac{(\gamma \Delta B_0)^2}{(\gamma \Delta B_0)^2 + (\omega - \omega_0)^2} e^{-t/T_{2,\omega}} e^{-i\omega t}\, d\omega \tag{A.19}$$

Under the assumption that variations in flip angle and intrinsic T_2 across the spectral range are minimal, the signal expression simplifies to:

$$S(t) = \pi \sin\alpha\, \gamma \Delta B_0 M_z^0\, e^{-t/T_2}\, e^{-i\omega_0 t}\, e^{-i\gamma \Delta B_0 t} \tag{A.20}$$

This formulation presents the signal observed under conditions of magnetic field inhomogeneity as:

$$S(t) = \pi \sin\alpha\, \gamma \Delta B_0 M_z^0\, e^{-t/T_2^*}\, e^{-i\omega_0 t} \tag{A.21}$$

where T_2^* stands for the composite decay rate integrating the intrinsic transverse relaxation time T_2 and the extent of magnetic field inhomogeneity ΔB_0, formulated as:

$$\frac{1}{T_2^*} = \frac{1}{T_2} + \gamma \Delta B_0 \tag{A.22}$$

Thus, a free induction decay emerges as a spin-system's immediate response to an RF pulse. The signal's strength relies on the total spin count, the flip angle initiated by the pulse, and the magnetic field's strength. The duration for which an FID signal remains detectable is governed by the intrinsic transverse relaxation rate, T_2, and the magnitude of magnetic field inhomogeneity within the system. These factors collectively contribute to the T_2^* relaxation constant, which serves as a comprehensive indicator of both the inherent relaxation properties of the spin system and the homogeneity of the magnetic field, thereby influencing the FID signal's decay rate, as depicted in Figure A.2.

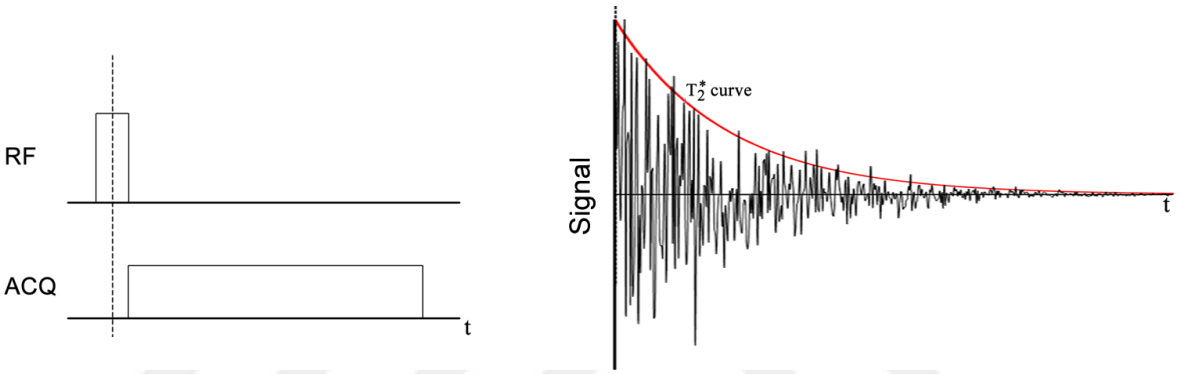

Figure A.2 MR sequence consisting of a single pulse generates a free induction decay signal (left). The FID signal is subject to the effective T_2^* relaxation rate dictated by field inhomogeneities (right).

A.2.2 The RF Echo

The RF echo signal, commonly referred to as the *spin echo*, is produced by a sequence of at least two RF pulses. In a typical two-pulse sequence, an initial excitation pulse with a 90° flip angle is applied along the x' axis of the rotating frame. This is followed by a 180° refocusing pulse aligned along the y' axis, separated from the first by a predetermined time interval τ.

In such a scheme, initially, RF excitation flips the spin-system's net magnetization towards the y' axis and causes the magnetization vector to precess around the z' axis through the time interval τ, acquiring a phase angle $\phi = \omega\tau$ in the $x'y'$ plane, with respect to the y' axis. Here, ω is defined by the effective magnetic field the spins experience, which, due to field inhomogeneities, varies widely, leading to phase dispersion and a decay governed by T_2^*, as discussed in the generation of an FID.

Following the application of the 180° pulse along the y' axis at $t = \tau$, the magnetization vector undergoes a rotation around the y' axis, reversing its phase to a negative angle $-\phi$ with respect to the y' axis. Following this inversion, the overall magnetization vector of the system resumes its precession around the z' axis. In this stage, the previously incurred dephasing reverses, aligning all magnetization vectors in phase coherence at $t = 2\tau$, resulting in a peak of the induction signal. As precession continues past the peak at $t = 2\tau$, magnetization experiences dephasing again, governed by the decay rate T_2^*.

The induction signal detected following the application of a 180° pulse—during the period in which phase coherence is first regained and then subsequently lost due to dephasing—is referred to as the *RF echo*. It is in a way an "echo" of the original FID generated by the excitation pulse, that is induced by 180°, which is also called the *RF echo pulse* (Figure A.3).

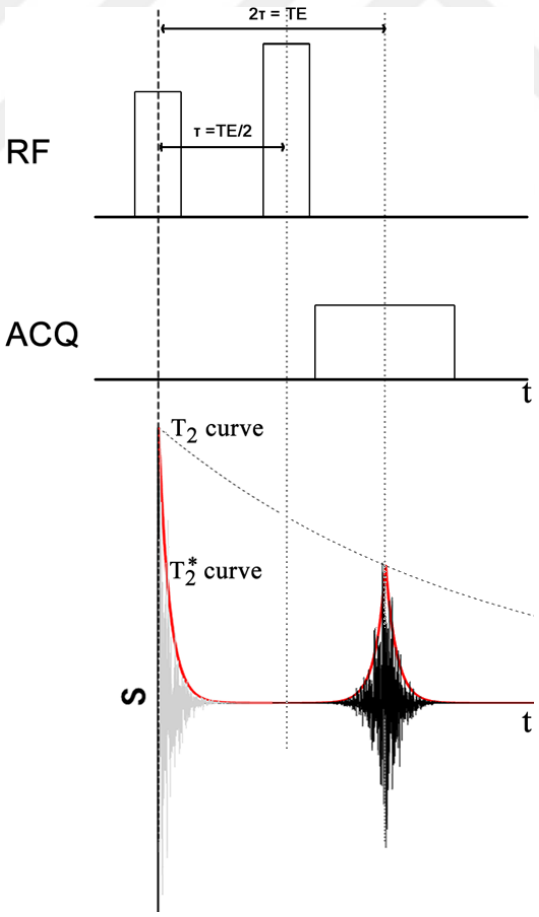

Figure A.3 An MR sequence with an excitation pulse and a refocusing pulse is used to generate a spin-echo signal (top). In response to the sequence, the spin-system undergoes dephasing, rephasing and relaxation. The sequence generates a spin-echo at $t = TE$ with a peak set by T_2 curve (bottom).

The underlying process that leads to dephasing, or the loss of phase coherence, is identical to the mechanism that facilitates rephasing, or the restoration of phase coherence. As a result, the magnetization vector exhibits a mirror symmetry around the moment the RF echo pulse is applied. As illustrated in Figure A.3, the induction signal adheres to the T_2^* relaxation time both during dephasing and rephasing, presenting a symmetric signal with its peak at time $t = 2\tau$. The signal emerges as a result of RF-induced rephasing and dephasing with its peak at TE and is called the *RF echo*. As seen, T_2^* determines the span of both phasing and rephasing, effectively outlining the width of the echo signal.

The 90°–180° RF pulse pair can be generalized in the form of a pair of pulses with arbitrary flip angles α_1 and α_2, that are applied consecutively with a time interval τ. The flips caused by the pulses are then defined by rotation operators. Initially, the magnetization vector is flipped by the angle α_1, creating a non-zero component in the $x'y'$ plane. This component precesses until $t = \tau$, experiencing a rotation by the angle $\phi = \omega\tau$. At $t = \tau$, a second flip by angle α_2 inverts the magnetization, which then precesses for an additional interval of τ, effectively undergoing a total rotation by angle $\phi = 2\omega\tau$. At $t = 2\tau$, the process leads to a coherent alignment of the magnetization vectors, producing a peak in the signal amplitude before it disperses into a fully dephased state, influenced by the transverse relaxation constant T_2^*.

The resulting echo signal of a spin-system characterized by a spin-density function $\rho(\omega)$ can be expressed as:

$$S(t) = \sin\alpha_1 \, \sin^2\left(\frac{\alpha_2}{2}\right) \int_{-\infty}^{\infty} \rho(\omega)\, e^{-t/T_2}\, e^{-i\omega(t-T_E)}\, d\omega \tag{A.23}$$

Here, T_E, the echo time, is defined as $T_E = 2\tau$. The echo signal reaches its peak at $t = T_E$, with the peak value given by:

$$S_E = \sin\alpha_1 \, \sin^2\left(\frac{\alpha_2}{2}\right) \int_{-\infty}^{\infty} \rho(\omega)\, e^{-T_E/T_2}\, d\omega \tag{A.24}$$

This expression can be simplified to:

$$S_E = A_E \, \sin\alpha_1 \, \sin^2\left(\frac{\alpha_2}{2}\right) e^{-T_E/T_2} \tag{A.25}$$

where A_E is directly proportional to the net equilibrium magnetization of the spin-system. This indicates that the formation and extent of an RF echo signal are influenced by T_2^*, whereas its amplitude is defined by the flip angles of the RF pulses

used to generate the echo, the intrinsic T_2 relaxation time of the spin-system, and the echo timing given by T_E.

A.2.3 The Gradient Echo

Gradient echoes are generated through the manipulation of spin-system magnetization via time-varying gradient magnetic fields. These fields allow for the controlled dephasing and rephasing of signals, enabling the creation of one or multiple echo signals. A gradient field, characterized by its linear variation along a specified direction, alters the magnetic field linearly along an axis—for example, a gradient G_x along the x-axis leads to a magnetic field variation represented by

$$B_{G,z} = G_x x \tag{A.26}$$

Similar linear variations can be achieved along the y and z axes with gradients G_y and G_z, respectively.

To initiate a gradient echo, an RF excitation pulse disturbs the spin system, inducing a free induction decay (FID). Following excitation, a negative gradient applied along an axis, such as the x-axis, causes spins at different positions to acquire distinct phases. This phase shift, within the rotating frame for a position x, is given by:

$$\phi(x,t) = \gamma \int_0^\tau -G_x(t) x \, dt' \tag{A.27}$$

where τ represents the gradient application duration. If the gradient has a constant strength, the phase shift at the end of the gradient application is:

$$\phi(x) = -\gamma G_x x \tau \tag{A.28}$$

The application of a gradient field accelerates the dephasing of transverse magnetization, leading to a more rapid signal decay than what is observed in a typical FID. This accelerated decay is characterized by an effective decay constant denoted as T_2^{**}, which is significantly shorter than T_2^*. A complete signal loss occurs if the gradient is applied for a duration significantly exceeding T_2^{**}, such as when $\tau > 3T_2^{**}$.

To generate a gradient echo, the process of dephasing is reversed by applying an inverse gradient with the same magnitude but opposite direction for the same duration. This inversion of the gradient counteracts the earlier phase dispersion, leading to signal regeneration and the creation of a gradient echo at $t = 2\tau$, as shown in Figure A.4.

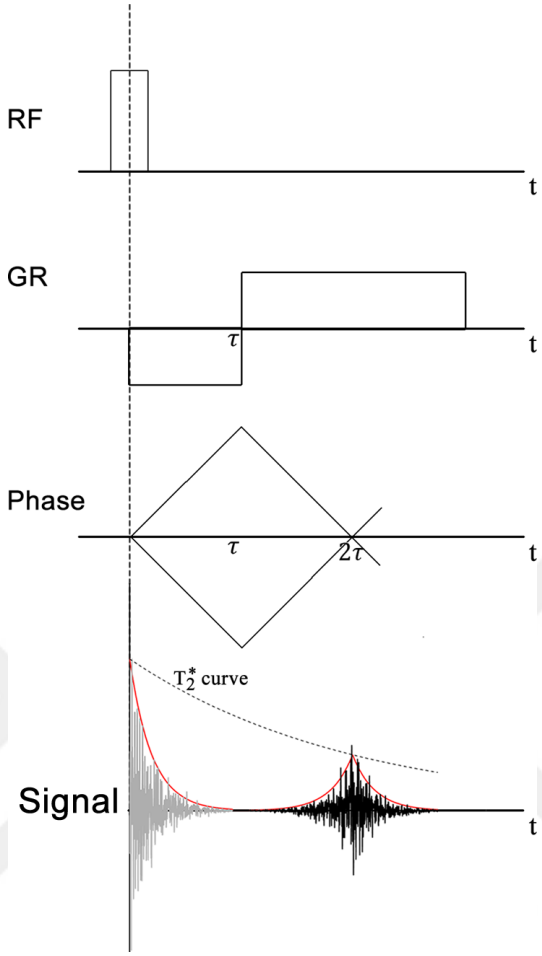

Figure A.4 A gradient echo is generated by reversing the polarity of the gradient field. This reverses dephasing and generates a field-echo signal with a peak that follows the T_2^* relaxation curve.

In the presence of B_0 inhomogeneities, however, the complete rephasing of spins through gradient reversal becomes unattainable. This is because the phase dispersion caused by static field inhomogeneities is not reversed by gradient polarity inversion. As a result, the amplitude of a gradient echo is influenced by T_2^* weighting, in contrast with the T_2 weighting that characterizes the amplitude of spin echoes. This distinction arises because B_0 inhomogeneities introduce additional phase variation among spins that cannot be reversed by gradient-based rephasing, leading to an accelerated signal decay.

Thus, while gradient echo sequences enable rapid acquisition and are widely used in techniques such as functional MRI (fMRI), susceptibility-weighted imaging (SWI), and time-of-flight angiography, they are inherently more susceptible to artifacts and signal loss due to their sensitivity to T_2^* effects.

A.2.4 The RF Echo Train

An RF echo train is a sequence of spin echoes generated by applying more than two RF pulses at specific intervals. Each combination of excitation and refocusing pulses leads to the generation of an echo, and depending on the pulse sequence, multiple types of echoes can be observed—including conventional spin echoes, secondary echoes, and stimulated echoes.

Consider a sequence with three RF pulses of arbitrary flip angles α_1, α_2, and α_3, applied at times separated by intervals τ_1 and τ_2 (Figure A.5).

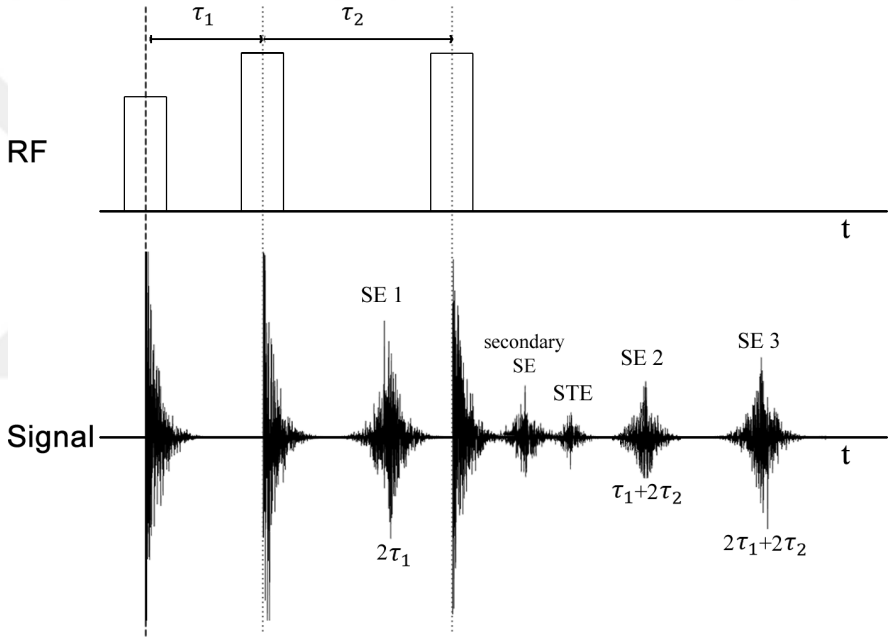

Figure A.5 A three-pulse sequence generates five echoes.

This configuration can generate up to five distinct echoes:

- **Echo 1 (Primary):** Generated by α_1 and α_2 at $t = 2\tau_1$
- **Echo 2 (Primary):** Generated by α_2 and α_3 at $t = \tau_1 + 2\tau_2$
- **Echo 3 (Primary):** Generated by α_1 and α_3 at $t = 2(\tau_1 + \tau_2)$
- **Echo 4 (Secondary):** Refocusing of the first spin echo by α_3, at $t = 2\tau_2$
- **Echo 5 (Stimulated):** Arises from interference among spins excited by all three pulses, peaking near τ_1 after the third pulse.

The stimulated echo (STE) is a unique phenomenon that arises from partial storage and subsequent rephasing of longitudinal magnetization. It occurs when a portion of the transverse magnetization is rotated into the longitudinal axis by the second pulse and later returned to the transverse plane by the third pulse. This echo typically appears at a time τ_1 after the third pulse, assuming $\tau_2 > 2\tau_1$.

A special and widely used form of spin echo train begins with a 90° excitation pulse followed by a sequence of equidistant 180° refocusing pulses (Figure A.6). If the first 180° refocusing pulse is applied at $t = \tau$, and subsequent pulses follow at regular intervals of 2τ, then the echo signals will appear at $t = 2\tau, 4\tau, 6\tau, \ldots$, forming a periodic train. The amplitude of the n-th echo (E_n) follows exponential decay governed by the transverse relaxation constant T_2: $E_n = e^{-2n\tau/T_2}$

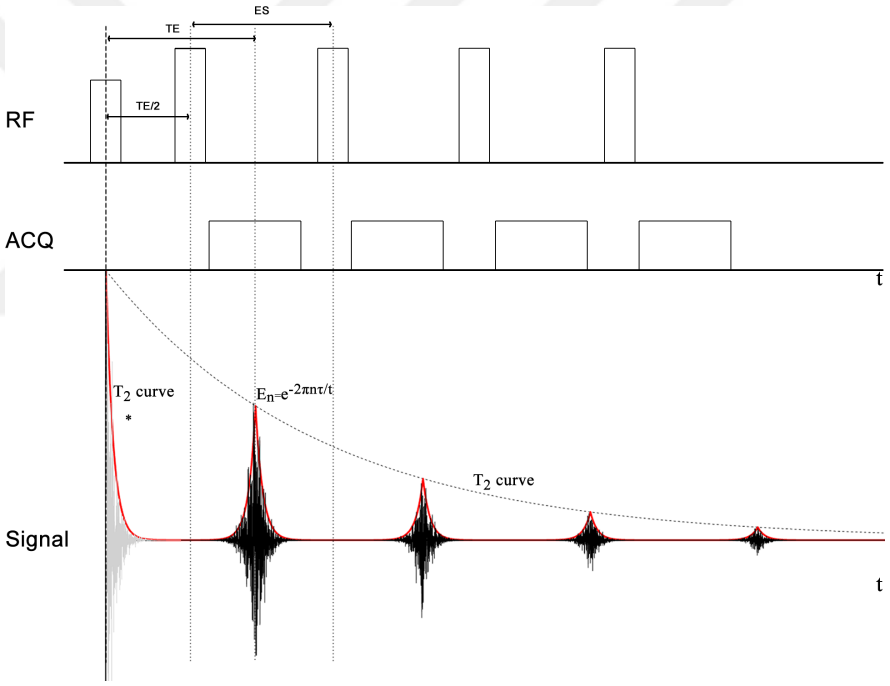

Figure A.6 A spin-echo train generated by equidistant refocusing pulses.

If all the refocusing pulses in the train are applied along the same axis, small imperfections in pulse angles and magnetic field inhomogeneities can lead to cumulative phase errors, causing signal loss. To mitigate these effects, the Carr-Purcell-Meiboom-Gill (CPMG) sequence was introduced.

In a CPMG sequence, the initial 90° excitation pulse is applied along the x' axis in the rotating frame, while subsequent 180° refocusing pulses alternate between the y' and $-y'$ axes. This alternation helps to maintain coherence among iso-chromats and corrects for systematic phase errors, preserving echo amplitude over longer echo trains.

A.2.5 The Gradient Echo Train

A gradient echo train is a series of echo signals generated from a single Free Induction Decay (FID) event through repeated alternation of gradient magnetic field polarity. Each reversal of the gradient field rephases the dephased spins, producing an echo, and this process can be repeated multiple times within the same acquisition window (Figure A.7).

The number of observable gradient echoes is limited by two main factors: the switching speed of gradient coils and the transverse relaxation constant T_2^*. Because gradient echoes are governed by T_2^* rather than T_2, they are highly sensitive to magnetic field inhomogeneities. As a result, echo amplitudes decay more rapidly than in RF echo trains, and only a few echoes can be acquired before the signal drops below the noise floor.

Gradient echo trains are essential to rapid imaging protocols, especially in applications requiring short acquisition times. Advances in MRI hardware, particularly high-performance gradient systems, now enable polarity switching on the order of microseconds. This allows acquisition of multiple gradient echoes within a short window following a single RF excitation.

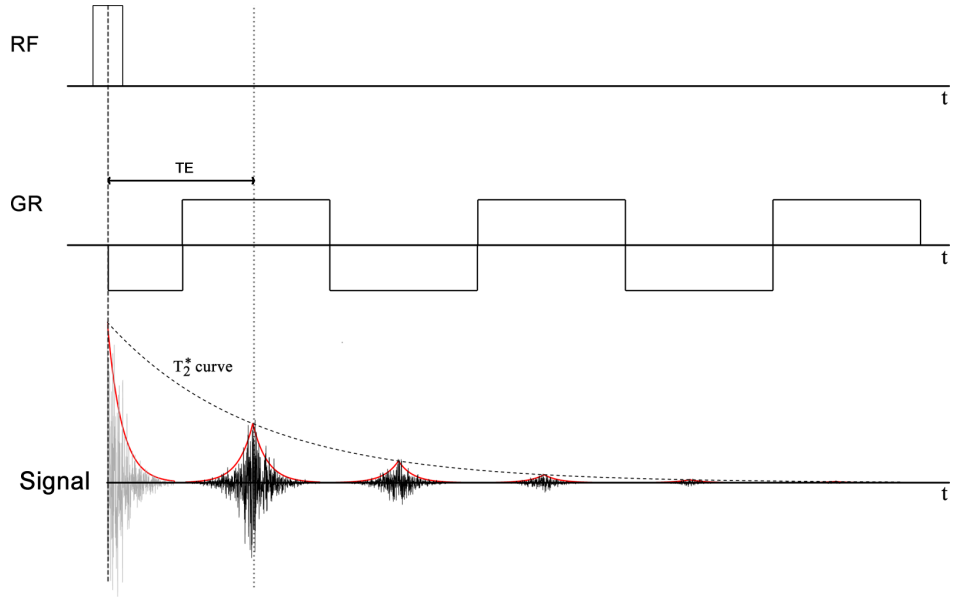

Figure A.7 A gradient echo train is generated by repeatedly alternating gradient polarity, producing a sequence of echoes whose peak amplitudes decay in accordance with T_2^* relaxation.

A.3 The Bloch Equation

The behavior of nuclear magnetization under the influence of magnetic fields and relaxation processes is governed by the *Bloch equation*, named after Felix Bloch, who first formulated it in 1946 [194]. This classical equation provides a comprehensive model for the temporal evolution of the macroscopic magnetization vector $\vec{M}(t)$ in the presence of a static magnetic field, time-varying RF fields, and intrinsic relaxation mechanisms.

A.3.1 Magnetization Dynamics

The Bloch equation is given by:

$$\frac{d\vec{M}(t)}{dt} = \gamma\vec{M}(t) \times \vec{B}(t) - \frac{M_x(t)}{T_2}\,\hat{i} - \frac{M_y(t)}{T_2}\,\hat{j} - \frac{M_z(t) - M_0}{T_1}\,\hat{k} \tag{A.29}$$

Here,

- $\vec{M}(t)$ is the time-dependent magnetization vector, composed of components $M_x(t)$, $M_y(t)$, and $M_z(t)$ along the x, y, and z axes, respectively.
- $\vec{B}(t)$ is the total magnetic field experienced by the spins, including the static field $\vec{B}_0$ and any time-varying components such as $\vec{B}_1(t)$ from RF pulses or magnetic field gradients.
- γ is the gyromagnetic ratio of the spin species.
- T_1 is the longitudinal relaxation time constant, governing the return of $M_z(t)$ to its equilibrium value M_0.
- T_2 is the transverse relaxation time constant, governing the decay of $M_x(t)$ and $M_y(t)$.
- M_0 is the equilibrium magnetization aligned with the static field $\vec{B}_0$.

The first term describes precession of the magnetization vector around the magnetic field, while the second term describes the exponential decay and recovery behavior due to relaxation processes.

A.3.2 Simplified Cases and Analytical Solutions

For a static magnetic field $\vec{B}(t) = B_0\hat{z}$ and in the absence of any RF excitation, the Bloch equation simplifies to:

$$\vec{B}(t) = \begin{bmatrix} 0 \\ 0 \\ B_0 \end{bmatrix} \tag{A.30}$$

In this regime, the analytical solution to the Bloch equation is given by:

$$M_x(t) = M_{xy}(0)\cos(\omega_0 t)\, e^{-t/T_2} \tag{A.31}$$

$$M_y(t) = M_{xy}(0)\sin(\omega_0 t)\, e^{-t/T_2} \tag{A.32}$$

$$M_z(t) = M_0\left(1 - e^{-t/T_1}\right) \tag{A.33}$$

where $\omega_0 = \gamma B_0$ is the Larmor frequency of precession. This solution describes:

- Transverse magnetization precessing at ω_0, with exponential decay governed by the time constant T_2.
- Longitudinal magnetization recovering toward its equilibrium value M_0, with exponential growth governed by T_1.

A.4 Rotating Frame of Reference

In the laboratory frame, the net magnetization vector $\vec{M}(t)$ undergoes continuous precession around the z-axis under the influence of the static magnetic field $\vec{B}_0$. This precession occurs at the Larmor frequency $\omega_0 = \gamma B_0$ and manifests as a rapidly oscillating transverse component in the MHz range. While this representation is physically accurate, the high-frequency nature of the transverse magnetization complicates both the mathematical treatment of spin dynamics and the physical interpretation of MR signals—particularly when evaluating the effects of time-varying fields or RF excitation.

To facilitate both analytical modeling and conceptual understanding, a transformation into a rotating reference frame is often employed. In the *rotating frame*, the coordinate system itself rotates about the z-axis at an angular frequency ω_{RF}, which is typically chosen to match the Larmor frequency ω_0. In this frame, the static field $\vec{B}_0$

appears effectively canceled, and the magnetization vector $\vec{M}_{\text{rot}}$ remains stationary unless perturbed by additional magnetic fields, such as RF excitation or gradient-induced offsets. This frame shift thus allows a simplified description of the spin system in which the effects of the static field are effectively removed.

The rotating frame effectively demodulates the signal by removing the carrier frequency ω_0, isolating the envelope of the magnetization behavior. As a result, spin dynamics—which appear as rapid, sinusoidal oscillations in the laboratory frame—become smooth, low-frequency rotations in the rotating frame, typically on the order of kilohertz. This simplification is not only conceptually useful but also crucial in the development and analysis of RF pulse sequences, where the rotating frame offers a clearer view of how RF fields influence the orientation and evolution of $\vec{M}$.

Mathematically, the transformation from the laboratory frame $\vec{M}(t)$ to the rotating frame $\vec{M}_{\text{rot}}(t)$ introduces a fictitious angular velocity $\vec{\omega}$ that corresponds to the angular rotation of the coordinate system. The total time derivative of the magnetization in the laboratory frame is expressed as:

$$\frac{d\vec{M}}{dt} = \vec{\omega} \times \vec{M}_{\text{rot}} + \frac{\partial \vec{M}_{\text{rot}}}{\partial t} \tag{A.34}$$

The first term accounts for the apparent rotation of $\vec{M}_{\text{rot}}$ due to the motion of the reference frame itself, while the second term describes the true physical evolution of the magnetization in that frame. By setting the angular velocity of the rotating frame equal to the Larmor frequency, we define:

$$\vec{\omega} = -\gamma \vec{B}_0 \tag{A.35}$$

Substituting this into the Bloch equation and recognizing that $\vec{B} = \vec{B}_0 = B_0 \hat{k}'$, where $\hat{k}'$ denotes the z-axis in both coordinate systems, leads to:

$$\frac{\partial \vec{M}_{\text{rot}}}{\partial t} = \gamma \vec{M}_{\text{rot}} \times \left(\vec{B}_0 + \frac{1}{\gamma} \vec{\omega} \right) \tag{A.36}$$

With $\vec{\omega} = -\gamma B_0 \hat{k}'$, this simplifies to:

$$\frac{\partial \vec{M}_{\text{rot}}}{\partial t} = \gamma \vec{M}_{\text{rot}} \times \left(B_0 \hat{k}' - B_0 \hat{k}' \right) = 0 \tag{A.37}$$

Thus, in the absence of RF excitation and other perturbations, the magnetiza-

tion vector is stationary in the rotating frame:

$$\vec{M}_{\text{rot}} = M_z \hat{k}' + \vec{M}_{xy} \tag{A.38}$$

This apparent stillness provides a powerful tool for conceptualizing RF interactions. Whereas RF pulses produce complex precessional responses in the laboratory frame, they appear as simple rotations about the effective field axis in the rotating frame. Accordingly, the rotating frame forms the basis for most of the pulse sequence design and theoretical modeling in MRI, enabling intuitive descriptions of nutation, tipping angles, and spin refocusing mechanisms.

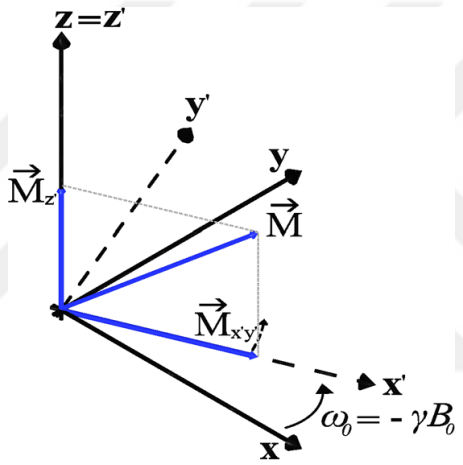

Figure A.8 Magnetization in rotating frame of reference: M_z aligns with z' and remains identical to M_z in the laboratory frame. $M_{x'y'}$ rotates in sync with the rotating frame and appears stationary.

A.5 RF Pulses and Rotating Frame Dynamics

When an RF pulse is applied to a spin system, the total magnetic field experienced by the nuclei becomes the sum of the static external field and the RF field:

$$\vec{B}(t) = \vec{B}_0 + \vec{B}_1(t) \tag{A.39}$$

Here, $\vec{B}_0 = B_0 \hat{k}$ is the constant main magnetic field aligned along the z-axis, and $\vec{B}_1(t)$ is a time-varying RF field oscillating in the transverse (xy) plane. In the laboratory frame, the RF field can be represented as a linearly polarized wave:

$$\vec{B}_1(t) = 2B_1^e(t)\cos(\omega_{\text{RF}} t + \phi)\hat{i} \tag{A.40}$$

or, alternatively, as the sum of two circularly polarized fields rotating in opposite directions:

$$\begin{aligned}\vec{B}_1(t) = B_1^e(t)\left[\cos(\omega_{\mathrm{RF}}t+\phi)\hat{i} - \sin(\omega_{\mathrm{RF}}t+\phi)\hat{j}\right] + \\ B_1^e(t)\left[\cos(\omega_{\mathrm{RF}}t+\phi)\hat{i} + \sin(\omega_{\mathrm{RF}}t+\phi)\hat{j}\right]\end{aligned} \tag{A.41}$$

The circularly polarized form matches the nature of fields produced by quadrature RF coils used in modern MR systems.

A.5.1 On-Resonance Excitation

Transforming into a rotating frame aligned with the Larmor frequency ω_0 (i.e., setting $\omega_{\mathrm{RF}} = \omega_0$), the oscillatory component of the RF field vanishes, yielding a static field in the transverse plane:

$$\vec{B}_{1,\mathrm{rot}}(t) = B_1^e(t)\hat{i}' \tag{A.42}$$

Thus, the effective field experienced in the rotating frame becomes:

$$\vec{B}_{\mathrm{rot}}(t) = B_0\hat{k}' + B_1^e(t)\hat{i}' \tag{A.43}$$

Using this in the Bloch equation in the rotating frame and substituting the angular velocity $\vec{\omega} = -\gamma B_0\hat{k}'$ results in:

$$\frac{\partial \vec{M}_{\mathrm{rot}}}{\partial t} = \gamma\vec{M}_{\mathrm{rot}} \times B_1^e(t)\hat{i}' \tag{A.44}$$

This yields the system:

$$\begin{aligned}\frac{dM_{x'}}{dt} &= 0 \\ \frac{dM_{y'}}{dt} &= \gamma B_1^e(t)M_{z'} \\ \frac{dM_{z'}}{dt} &= -\gamma B_1^e(t)M_{y'}\end{aligned} \tag{A.45}$$

Assuming an initial condition where $\vec{M}$ is aligned along z', the solution becomes:

$$\begin{aligned}M_{x'}(t) &= 0 \\ M_{y'}(t) &= M_z^0 \sin\left(\gamma\int_0^t B_1^e(t')dt'\right) \\ M_{z'}(t) &= M_z^0 \cos\left(\gamma\int_0^t B_1^e(t')dt'\right)\end{aligned} \tag{A.46}$$

For a rectangular pulse of duration τ_P and amplitude B_1^e, the solution at $t = \tau_P$ is:

$$\begin{aligned} M_{y'}(\tau_P) &= M_z^0 \sin(\alpha) \\ M_{z'}(\tau_P) &= M_z^0 \cos(\alpha) \end{aligned} \tag{A.47}$$

where the flip angle α is defined as:

$$\alpha = \gamma B_1^e \tau_P \tag{A.48}$$

If the RF pulse has a non-zero phase ϕ, the transverse magnetization becomes:

$$M_{x'y'} = M_{x'} + iM_{y'} = M_z^0 \sin(\alpha) e^{i\phi} \tag{A.49}$$

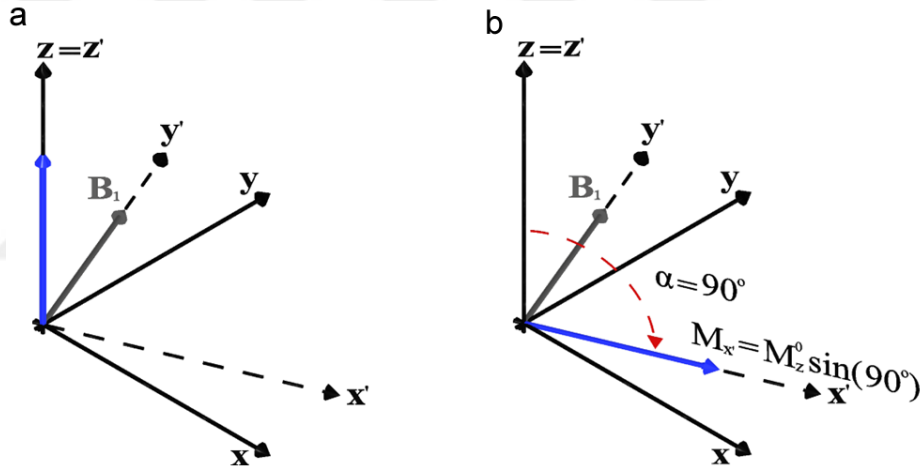

Figure A.9 **a)** Magnetization vector under equilibrium conditions and in absence of the B_1 field. **b)** On resonance excitation flipping magnetization into the $x'y'$ plane by a 90° RF pulse along y'.

A.5.2 Off-Resonance Excitation

When the RF pulse frequency ω_{RF} deviates from the Larmor frequency ω_0, the excitation becomes off-resonance. The effective magnetic field in the rotating frame becomes:

$$\vec{B}_{\text{eff}} = \frac{\Delta\omega_0}{\gamma}\hat{k}' + B_1^e(t)\hat{i}' \tag{A.50}$$

with the frequency offset defined as:

$$\Delta\omega_0 = \gamma B_0 - \omega_{\text{RF}} \tag{A.51}$$

In this case, the Bloch equations yield:

$$\begin{aligned}\frac{dM_{x'}}{dt} &= \Delta\omega_0 M_{y'} \\ \frac{dM_{y'}}{dt} &= -\Delta\omega_0 M_{x'} + \gamma B_1^e(t) M_{z'} \\ \frac{dM_{z'}}{dt} &= -\gamma B_1^e(t) M_{y'}\end{aligned} \tag{A.52}$$

For a rectangular pulse of duration τ_P and amplitude B_1, the analytical solution becomes:

$$\begin{aligned}M_{x'}(t) &= M_z^0 \sin\theta\cos\theta\,[1-\cos(\omega_{\text{eff}}t)] \\ M_{y'}(t) &= M_z^0 \sin\theta\sin(\omega_{\text{eff}}t) \\ M_{z'}(t) &= M_z^0\left[\cos^2\theta + \sin^2\theta\cos(\omega_{\text{eff}}t)\right]\end{aligned} \tag{A.53}$$

where

$$\omega_{\text{eff}} = \sqrt{\Delta\omega_0^2 + \omega_{\text{RF}}^2}, \quad \theta = \tan^{-1}\left(\frac{\omega_{\text{RF}}}{\Delta\omega_0}\right) \tag{A.54}$$

At $t = \tau_P$, the flip angle is $\alpha = \omega_{\text{eff}}\tau_P$, and the transverse phase is:

$$\phi = \tan^{-1}\left(\frac{\alpha}{2}\cdot\frac{\Delta\omega_0}{\omega_{\text{eff}}}\right) \tag{A.55}$$

The resulting transverse component of the magnetization vector is:

$$M_{x'y'} = M_z^0 \sin\theta\sqrt{\sin^2\alpha + (1-\cos\alpha)^2\cos^2\theta} \tag{A.56}$$

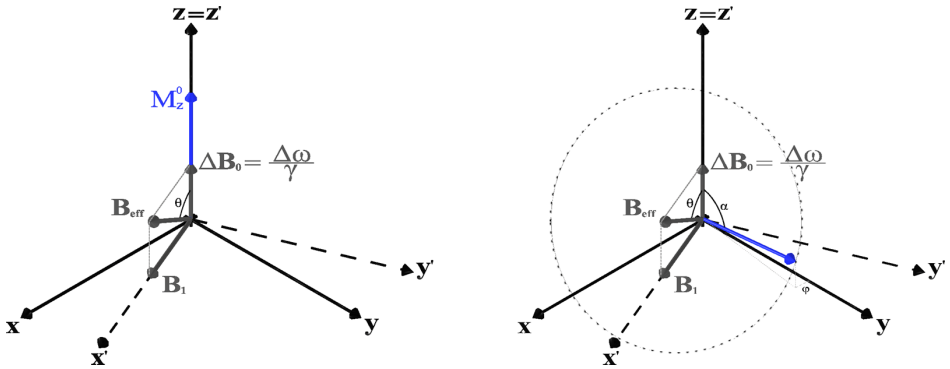

Figure A.10 **a)** Magnetization vector under equilibrium conditions and in absence of the B_1 field. **b)** Off-resonance excitation causing an oblique flip with an angle smaller than the desired flip angle.

This analysis shows that the rotating frame of reference simplifies the description of spin dynamics under both on-resonance and off-resonance conditions, providing analytical access to the influence of RF pulses on nuclear magnetization and the resulting induction signals.

A.6 Spatial Localization

Spatial localization in MRI is achieved by manipulating the magnetic field experienced by nuclear spins so that their resonance frequencies vary with spatial position. This allows spatial information to be encoded into the MR signal and later reconstructed into an image. The two primary mechanisms of localization are *selective excitation* and *spatial encoding*.

A.6.1 Selective Excitation (Slice Selection)

Selective excitation in MRI is the process of exciting spins confined to a specific spatial region—typically a thin slab—by simultaneously applying a magnetic field gradient and a radiofrequency (RF) pulse. When selection is applied along one axis (e.g., z-axis), the resulting excited volume is called a *slice*. Slices can be selected along any orthogonal direction by choosing the appropriate gradient (Figure A.11).

Slice selection is achieved by applying an RF pulse in the presence of a magnetic field gradient $\vec{G}_s$, oriented along the desired selection axis. The gradient causes the Larmor frequency to vary linearly with spatial position. Only spins whose local Larmor frequencies fall within the bandwidth of the RF pulse are excited, thereby localizing excitation to the desired slice.

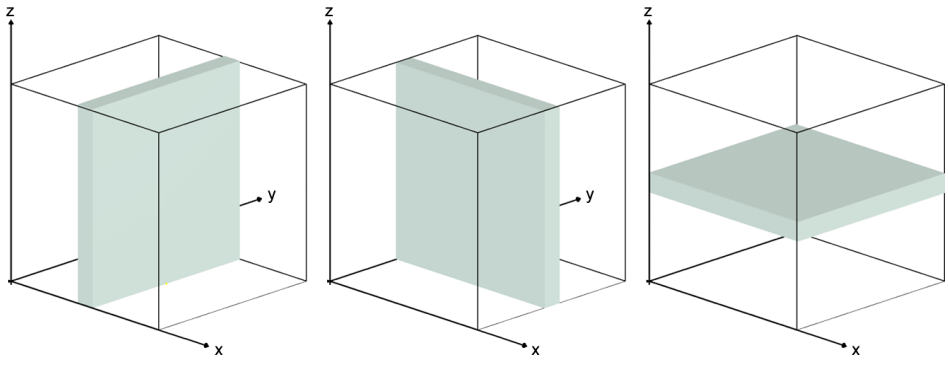

Figure A.11 Gradients enable slice selection along their direction when applied individually.

The thickness of the selected slice is determined by both the strength of the gradient and the bandwidth of the RF pulse. A broader RF bandwidth or a weaker gradient results in a thicker slice, while a narrower bandwidth or a stronger gradient yields a thinner slice. This interplay between RF pulse design and gradient amplitude is central to spatial localization in MRI, and it underpins many advanced imaging protocols such as multi-slice, interleaved, or oblique slice acquisitions.

A.6.1.1 Mathematical Formulation. The process of slice selection in MRI can be rigorously described using the Bloch equations in the rotating frame of reference. During selective excitation, a magnetic field gradient $\vec{G}_s$ is applied along the desired slice-selection axis, in conjunction with a radiofrequency (RF) pulse. This gradient linearly modulates the local Larmor frequency with spatial position, enabling spatial localization of excitation. In the rotating frame, the slice-selection gradient is defined as:

$$\vec{G}_s = (G_{s,x} + G_{s,y} + G_{s,z})\hat{k}' \tag{A.57}$$

Assuming the gradient is aligned with the z-axis, the local magnetic field experienced at position z becomes:

$$B_z = B_0 + G_{s,z}z \tag{A.58}$$

During excitation, an RF field is applied in the transverse plane. In the rotating frame, the effective magnetic field experienced by the spins is then:

$$\vec{B}_{\text{eff}}(t) = B_1^e(t)\hat{i}' + \left(B_0 + G_{s,z}z - \frac{\omega_{\text{RF}}}{\gamma}\right)\hat{k}' \tag{A.59}$$

Here, $B_1^e(t)$ denotes the envelope of the RF field, ω_{RF} is the carrier frequency of the RF pulse, and γ is the gyromagnetic ratio.

The time evolution of magnetization components under the influence of $\vec{B}_{\text{eff}}(t)$ is governed by the Bloch equations in the rotating frame:

$$\begin{aligned}
\frac{dM_{x'}(z,t)}{dt} &= \gamma\left(B_0 + G_{s,z}z - \frac{\omega_{\text{RF}}}{\gamma}\right)M_{y'}(z,t) \\
\frac{dM_{y'}(z,t)}{dt} &= -\gamma\left(B_0 + G_{s,z}z - \frac{\omega_{\text{RF}}}{\gamma}\right)M_{x'}(z,t) + \gamma B_1^e(t)M_{z'}(z,t) \\
\frac{dM_{z'}(z,t)}{dt} &= -\gamma B_1^e(t)M_{y'}(z,t)
\end{aligned} \tag{A.60}$$

To localize excitation around a central slice at position z_0, the RF carrier frequency is set to match the local Larmor frequency at that position:

$$\omega_{\mathrm{RF}} = \omega_0 + \gamma G_{s,z} z_0 \tag{A.61}$$

Substituting this into the equations simplifies the frequency offset term, yielding:

$$\begin{aligned}
\frac{dM_{x'}(z,t)}{dt} &= \gamma G_{s,z}(z - z_0) M_{y'}(z,t) \\
\frac{dM_{y'}(z,t)}{dt} &= -\gamma G_{s,z}(z - z_0) M_{x'}(z,t) + \gamma B_1^e(t) M_{z'}(z,t) \\
\frac{dM_{z'}(z,t)}{dt} &= -\gamma B_1^e(t) M_{y'}(z,t)
\end{aligned} \tag{A.62}$$

This formulation reveals that each location z behaves like a spin system with a unique resonance offset, proportional to its distance from the center of the selected slice, z_0. Spins located far from z_0 experience a large off-resonance condition and are not effectively excited, while spins near z_0 undergo coherent tipping into the transverse plane. The spatial profile of excitation is thus determined by the convolution of the RF pulse envelope and the frequency distribution introduced by the gradient.

A.6.1.2 Simplified Solution for Hard Pulses. To gain insight into the spatial excitation profile without resorting to full numerical integration of the Bloch equations, a useful simplification is to model the RF pulse as a 'hard' pulse. This idealized pulse is assumed to have infinitesimal duration and constant amplitude, delivering all its energy instantaneously. Under this assumption, the longitudinal magnetization is considered unchanged during the pulse, allowing the excitation process to be treated as an instantaneous rotation. This greatly simplifies the analysis and permits an analytical expression for the resulting transverse magnetization, facilitating an intuitive understanding of slice excitation.

Assuming: the center of the selected slice is at $z_0 = 0$ and the longitudinal magnetization remains constant during excitation, $M_{z'}(z,t) \approx M_{z'}^0$, the Bloch equations in the rotating frame simplify to:

$$\begin{aligned}
\frac{dM_{x'}(z,t)}{dt} &= \gamma G_{s,z} z M_{y'}(z,t) \\
\frac{dM_{y'}(z,t)}{dt} &= -\gamma G_{s,z} z M_{x'}(z,t) + \gamma B_1^e(t) M_{z'}^0 \\
\frac{dM_{z'}(z,t)}{dt} &= 0
\end{aligned} \tag{A.63}$$

Combining the transverse components into a single complex variable $M_{x'y'} = M_{x'} + iM_{y'}$, the system reduces to a first-order inhomogeneous differential equation:

$$\frac{dM_{x'y'}(z,t)}{dt} = -i\gamma G_{s,z} z M_{x'y'}(z,t) + i\gamma B_1^e(t) M_{z'}^0 \tag{A.64}$$

This equation describes a driven precession of transverse magnetization in the rotating frame. For a rectangular RF pulse of duration τ_p and constant amplitude $B_1^e(t) = B_1^e$, the solution at the end of the pulse is:

$$M_{x'y'}(z,\tau_p) = i\gamma M_{z'}^0 e^{-i\gamma G_{s,z} z \tau_p/2} \int_{-\tau_p/2}^{\tau_p/2} B_1^e(\tau + \tau_p/2) e^{i\gamma G_{s,z} z \tau}\, d\tau \tag{A.65}$$

This expression demonstrates that the spatial profile of excited transverse magnetization is proportional to the inverse Fourier transform of the RF pulse envelope. Defining:

$$f = \frac{\gamma}{2\pi} G_{s,z} z \tag{A.66}$$

the relationship becomes:

$$\frac{-ie^{i\gamma G_{s,z} z \tau_p/2}}{\gamma M_{z'}^0} M_{x'y'}(z,\tau_p) = \mathcal{F}^{-1}\left\{ B_1^e\left(\tau + \frac{\tau_p}{2}\right)\right\} \tag{A.67}$$

A.6.1.3 RF Pulse Design and Slice Profile. The spatial selectivity of an RF excitation in MRI is determined not only by the strength of the slice-selection gradient but also by the shape of the RF pulse envelope. As derived in the previous section, the transverse magnetization excited by a hard pulse under a linear gradient field can be expressed as:

$$M_{x'y'}(z,\tau_p) = i\gamma M_{z'}^0 e^{-i\gamma G_{s,z} z \tau_p/2} \int_{-\tau_p/2}^{\tau_p/2} B_1^e(\tau + \tau_p/2) e^{i\gamma G_{s,z} z \tau}\, d\tau \tag{A.68}$$

This expression shows that the spatial slice profile is proportional to the inverse Fourier transform of the RF pulse envelope $B_1^e(t)$. In other words, the spatial selectivity of excitation is governed by the spectral properties of the applied RF pulse in the presence of a gradient.

For example, a rectangular RF pulse corresponds to a sinc-shaped slice profile in space due to the Fourier transform pair between a rectangular time-domain function and a sinc function in frequency (and thus, spatial) domain. While such sinc profiles

provide reasonably good spatial localization, they exhibit sidelobes (Gibbs ringing), which can lead to partial excitation of spins outside the intended slice.

Conversely, a sinc-shaped RF pulse—truncated in time for practical implementation—yields a more uniform (rectangular) slice profile. However, due to the truncation, this approach introduces Gibbs oscillations at the slice boundaries, as seen in Figure A.12.

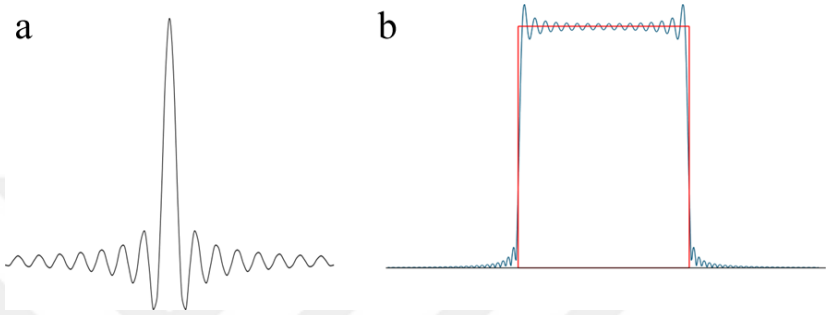

Figure A.12 **a)** A truncated sinc pulse used for RF excitation with a finite number of side-lobes. **b)** The resulting slice profile exhibits Gibbs oscillations due to time-domain truncation of the pulse.

To mitigate these artifacts, RF pulses are typically windowed using functions such as Hamming, Hann, or Kaiser windows. These smooth the transition at the time-domain edges of the pulse, reducing the amplitude of sidelobes and thereby improving slice fidelity. These design strategies are crucial for precise spatial localization and to avoid cross-talk between adjacent slices, especially in multi-slice imaging protocols.

A.7 Spatial Encoding

Spatial encoding enables the localization of the signal origin within the body. It transforms the MR signal from a single, undifferentiated response into a spatially resolved dataset, allowing image reconstruction. This is accomplished by imposing controlled variations in the local magnetic field through the use of gradient fields. Spatial encoding typically includes three components: *slice selection*, *frequency encoding*, and *phase encoding*, each acting along orthogonal axes of the imaging volume.

The combined use of slice selection, frequency encoding, and phase encoding provides the foundation for spatially resolved image acquisition in MRI. Each encoding mechanism targets one spatial axis, and together, they enable comprehensive localization within a three-dimensional imaging volume.

A.7.1 Frequency Encoding

Frequency encoding is the process by which positional information is embedded into the frequency of the MR signal. After slice selection has isolated a planar region within the imaging volume, a gradient field, which is commonly called the *readout gradient*, is applied along one spatial direction (e.g., the x-axis) during signal acquisition. This gradient causes the Larmor frequency of spins to vary linearly with position along its direction, resulting in location-specific precession frequencies. As the signal is recorded over time, the resulting frequency spectrum directly reflects the spatial distribution of transverse magnetization along the gradient axis. This principle allows the one-dimensional Fourier transform of the acquired signal to reconstruct the spatial variation of spin density, forming the basis of spatial encoding along the readout direction.

In the rotating frame, the influence of this gradient modifies the transverse magnetization according to:

$$\frac{dM_{x'y'}(x,t)}{dt} = -i\gamma G_x x M_{x'y'}(x,t) \tag{A.69}$$

Solving this differential equation yields:

$$M_{x'y'}(x,t) = M^0_{x'y'} e^{-i\gamma G_x x t} \tag{A.70}$$

Here, $M^0_{x'y'}$ is the transverse magnetization at $t = 0$, and the exponential term represents a position-dependent phase evolution that translates directly into frequency modulation. This phase modulation accumulates linearly over time and is proportional to both the local position x and the gradient strength G_x.

The total MR signal from the imaging object is the superposition of signals from all locations:

$$S(t) = \int_{-\infty}^{\infty} \rho(x) M^0_{x'y'} e^{-i\gamma G_x x t}\, dx \tag{A.71}$$

This integral is a one-dimensional Fourier transform of the spin density $\rho(x)$, with time t acting as the reciprocal of spatial frequency. Therefore, frequency encoding maps spatial location into spectral components, where each frequency corresponds to a unique position along the gradient. This mapping forms the basis of spatial decoding in the readout direction, complementing phase encoding steps applied along

the orthogonal dimensions.

This concept can be generalized to multiple dimensions. Using a gradient vector $\vec{G} = G_x\hat{i} + G_y\hat{j} + G_z\hat{k}$ and position vector $\vec{r}$, the signal becomes:

$$S(t) = \int \rho(\vec{r}) e^{-i\gamma(\vec{G}\cdot\vec{r})t}\, d\vec{r} \tag{A.72}$$

The exponential phase factor represents a spatially varying frequency, where the instantaneous frequency at point $\vec{r}$ is:

$$f(\vec{r}) = \gamma\vec{G}\cdot\vec{r} \tag{A.73}$$

This means that each point in space contributes to the signal at a unique frequency, but only along the axis of the gradient. Consequently, points that lie on the same iso-frequency line or plane (perpendicular to $\vec{G}$) are indistinguishable by frequency encoding alone. For full spatial localization, frequency encoding must therefore be complemented by additional encoding dimensions—typically achieved through phase encoding gradients orthogonal to the readout direction.

A.7.2 Phase Encoding

To resolve ambiguities along iso-frequency contours, a second gradient is applied *before* signal acquisition, in a direction orthogonal to the frequency encoding axis. This *phase encoding* gradient is typically applied for a brief period T_{PE} and then turned off before readout begins. During its application, the phase encoding gradient alters the precession frequency of spins according to their position, temporarily causing them to precess at different rates. Once the gradient is turned off, all spins return to the same Larmor frequency, but the relative phase shifts they have acquired persist.

The phase shift at location x is given by:

$$\phi(x) = -\gamma G_x x T_{\mathrm{PE}} \tag{A.74}$$

Thus, the signal from a spin at x becomes:

$$dS(x) = \rho(x)dx\, e^{i\phi(x)} = \rho(x)dx\, e^{-i\gamma G_x x T_{\mathrm{PE}}} \tag{A.75}$$

The total signal is again a Fourier transform:

$$S = \int \rho(x) e^{-i\gamma G_x x T_{\mathrm{PE}}} dx \tag{A.76}$$

Because the phase encoding gradient is varied from acquisition to acquisition—typically in discrete steps across multiple acquisitions —each line in k-space (the frequency domain representation of the image) corresponds to a specific phase encoding step. When combined with frequency encoding along a second axis during readout, the full two-dimensional spatial distribution can be reconstructed.

In 3D, a phase shift at position $\vec{r}$ due to a phase encoding gradient $\vec{G}_{\mathrm{PE}}$ is:

$$\phi(\vec{r}) = -\gamma T_{\mathrm{PE}} \vec{G}_{\mathrm{PE}} \cdot \vec{r} \tag{A.77}$$

And the MR signal becomes:

$$S = \int \rho(\vec{r}) e^{-i\gamma T_{\mathrm{PE}} \vec{G}_{\mathrm{PE}} \cdot \vec{r}} d\vec{r} \tag{A.78}$$

This is again a Fourier transform, where $\vec{G}_{\mathrm{PE}}$ defines a point in k-space.

A.7.3 Multi-slice 2D Acquisition

A commonly employed approach in clinical and research MRI is to acquire the three-dimensional imaging volume in a slice-by-slice manner. This method partitions the imaging task into multiple two-dimensional planes, each independently excited and encoded. In this scheme:

- **Slice selection** is performed using a frequency-selective RF pulse in the presence of a slice-selection gradient field, thereby localizing excitation to a specific slab along the slice-selection axis (commonly the z-axis).
- **Phase encoding** is applied within each slice to differentiate spatial locations along one in-plane axis (e.g., the y-axis).
- **Frequency encoding** occurs during signal acquisition to resolve the orthogonal in-plane axis (e.g., the x-axis).

To avoid cross-talk between adjacent slices, gaps are often introduced between them, or interleaved slice acquisition strategies are employed. After each slice is excited and read out using these spatial encoding gradients, the two-dimensional k-space matrix is filled line by line. The full image is reconstructed by performing a two-dimensional inverse Fourier transform on the collected data. Repeating this process across a series of slices yields a stack of 2D images that together represent the full volume (Figure A.13). This approach benefits from relatively short repetition times (TR) and flexible slice selection, making it widely applicable for both anatomical and functional imaging.

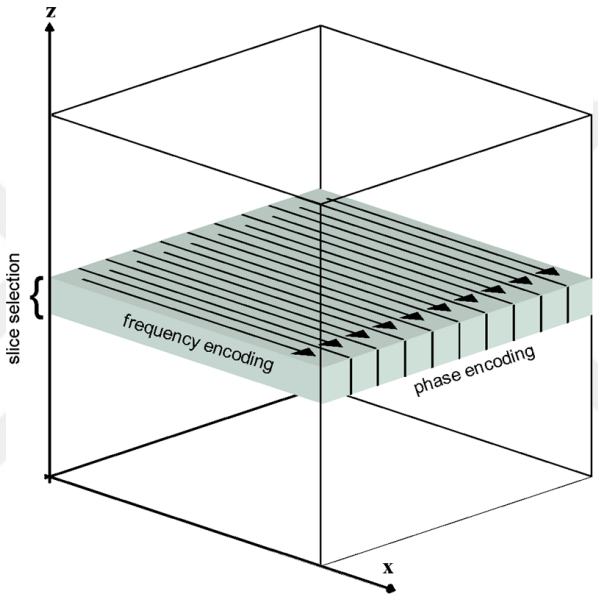

Figure A.13 A 3D space can be addressed by means of slice-by-slice acquisition.

A.7.4 Volumetric 3D Acquisition

An alternative to the multi-slice technique is volumetric 3D imaging, which acquires the entire imaging volume in a single excitation. Rather than isolating individual slices during acquisition, the entire excited slab is spatially encoded using a combination of gradient fields:

- **Phase encoding** is applied in two orthogonal directions (e.g., y and z) to differentiate spatial locations throughout the volume.
- **Frequency encoding** is performed along the remaining direction (e.g., x) during signal readout.

The resulting dataset represents a fully sampled three-dimensional k-space, where each line is assigned two phase encoding values and one frequency encoding dimension. After acquisition, the volumetric data is reconstructed using a three-dimensional inverse Fourier transform, yielding a high-resolution image of the entire volume. Arbitrary slices or projections can then be retrospectively extracted in any orientation (Figure A.14).

While 3D acquisition typically requires longer scan times due to the additional phase encoding dimension, it offers higher signal-to-noise ratio (SNR) per unit volume and inherently avoids slice gaps or inter-slice interference. These advantages make it particularly suitable for applications requiring isotropic resolution, seamless volumetric coverage, or retrospective reformatting.

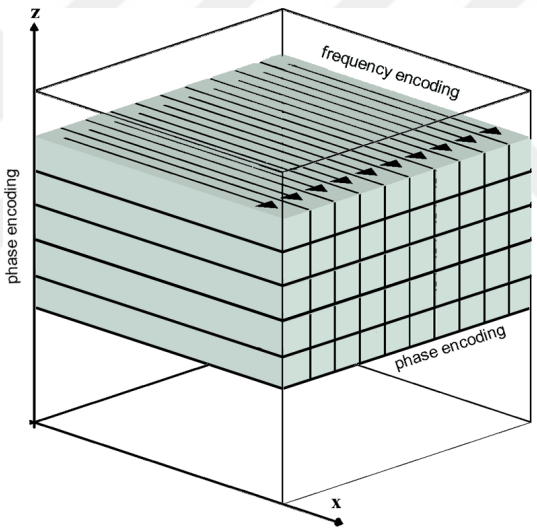

Figure A.14 A 3D volume can be encoded using 2D phase encoding and 1D frequency-encoding.

A.8 The k-space and Fourier Imaging

The concept of *k-space* provides a powerful mathematical framework that links spatial encoding in MRI to Fourier analysis. It serves as the domain in which MR signals are stored and manipulated during acquisition, allowing for systematic image reconstruction. Each point in k-space contains a spatial frequency component of the imaged object, and the entire dataset collectively represents the spatial structure of the image.

A.8.1 k-Space as the Domain of Fourier Encoding

The idea of k-space is rooted in the Fourier transform representation of the MR signal. Consider the previously derived relationship for frequency-encoded signal acquisition:

$$S(k_x) = \int_{-\infty}^{\infty} \rho(x)\, e^{-i2\pi k_x x}\, dx \tag{A.79}$$

where $\rho(x)$ is the spin density, and k_x is a time-dependent spatial frequency defined as:

$$k_x(t) = \frac{\gamma}{2\pi} \int_0^t G_x(\tau)\, d\tau \tag{A.80}$$

For a constant gradient G_x, this simplifies to $k_x = \frac{\gamma}{2\pi} G_x t$, establishing a direct correspondence between acquisition time and position in k-space.

In the multi-dimensional case, the general Fourier transform relationship between the spatial spin density $\rho(\vec{r})$ and its k-space representation $S(\vec{k})$ is given by:

$$S(\vec{k}) = \int \rho(\vec{r})\, e^{-i2\pi \vec{k}\cdot\vec{r}}\, d\vec{r} \tag{A.81}$$

with:

$$\vec{k}(t) = \frac{\gamma}{2\pi} \int_0^t \vec{G}(\tau)\, d\tau \tag{A.82}$$

Here, $\vec{G}(t)$ is the applied gradient vector, and $\vec{k}(t)$ defines the trajectory through k-space determined by gradient timing and amplitude.

A.8.2 Trajectories and Sampling in k-Space

The character of a k-space trajectory depends on the configuration of the gradient waveforms. Constant gradients produce linear trajectories, while time-varying gradients allow for spiral, radial, or other non-Cartesian paths.

Because MRI hardware cannot change gradient strengths instantaneously, practical waveforms ramp up and down over finite time intervals. Despite these transients, the integral of the gradient—its area—determines the final k-space location. Therefore, smooth gradient shapes can be used without changing the encoded spatial frequency, as long as the total area under the curve remains the same (Figure A.15).

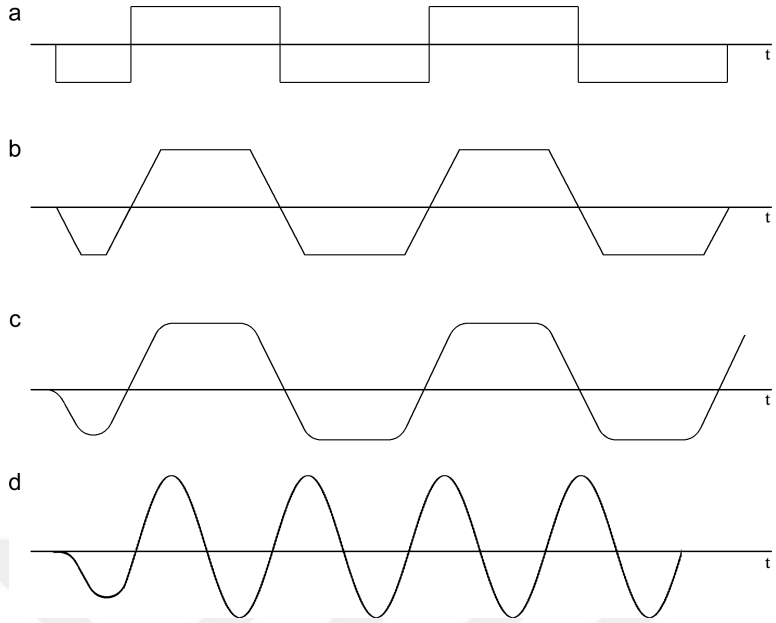

Figure A.15 Gradient waveforms define the k-space sampling trajectory, and can take different shapes: **a)** Rectangular. **b)** Trapezoidal. **c)** Trapezoidal with rounded corners. **d)** Sinusoidal.

A.8.3 k-Space and Phase Encoding

Phase encoding defines discrete points in k-space. If a phase encoding gradient $\vec{G}_{\mathrm{PE}}$ is applied for a time T_{PE}, it sets the k-space location:

$$\vec{k}_{\mathrm{PE}} = \frac{\gamma}{2\pi}\vec{G}_{\mathrm{PE}}T_{\mathrm{PE}} \tag{A.83}$$

By incrementing the amplitude of $\vec{G}_{\mathrm{PE}}$ across successive acquisitions, one populates a grid in k-space. This grid is typically sampled uniformly in Cartesian acquisitions, facilitating the use of fast Fourier transform (FFT) algorithms during reconstruction.

A.8.4 2D and 3D k-Space Sampling

In 2D multi-slice imaging, each slice is excited separately and encoded with:

$$S_{\mathrm{slice}}(k_x, k_y) = \iint \rho_{\mathrm{slice}}(x, y)\, e^{-i2\pi(k_x x + k_y y)}\, dx\, dy \tag{A.84}$$

Here, frequency encoding occurs along x, and phase encoding along y. The values of k_x and k_y are determined by:

$$\begin{aligned} k_x &= \frac{\gamma}{2\pi} G_x t \\ k_y &= \frac{\gamma}{2\pi} m G_{\mathrm{PE}_y} T_{\mathrm{PE}_y} \end{aligned} \tag{A.85}$$

where (m) denotes the integer phase encoding step index.

For 3D imaging, a second phase encoding direction is added:

$$S(k_x, k_y, k_z) = \iiint \rho(x, y, z)\, e^{-i2\pi(k_x x + k_y y + k_z z)}\, dx\, dy\, dz \tag{A.86}$$

$$k_z = \frac{\gamma}{2\pi} n G_{\mathrm{PE}_z} T_{\mathrm{PE}_z} \tag{A.87}$$

A.8.5 Sampling Theorem and Resolution Limits

Since the MR signal is acquired in discrete time steps, it must be sampled according to the Nyquist-Shannon sampling theorem to prevent aliasing [195], [196]. For a bandlimited spatial signal, the sampling interval Δk must satisfy:

$$\Delta k \leq \frac{1}{FOV} \tag{A.88}$$

where FOV is the field of view along the corresponding axis.

This implies that the spacing of phase encoding gradients must be:

$$\Delta G_{\mathrm{PE}} \leq \frac{2\pi}{\gamma T_{\mathrm{PE}} W} \tag{A.89}$$

and the readout gradient must be chosen such that the acquisition bandwidth $f_s = \frac{1}{\Delta t}$ satisfies:

$$f_s \geq 2 \cdot f_{\max} = \frac{\gamma}{\pi} G_x W_x \tag{A.90}$$

A.8.6 Implications for Reconstruction

Once the k-space is fully sampled, image reconstruction becomes a matter of applying the inverse Fourier transform:

$$\rho(\vec{r}) = \int S(\vec{k})\, e^{i2\pi \vec{k}\cdot\vec{r}}\, d\vec{k} \tag{A.91}$$

In practice, this is implemented via the discrete Fourier transform (DFT), which assumes uniform k-space sampling and defines the resolution and extent of the reconstructed image. The next section will describe the reconstruction process in detail, covering the discrete implementation of the Fourier transform, interpolation strategies, and common pitfalls such as aliasing and Gibbs ringing.

A.9 Image Reconstruction

Magnetic Resonance Imaging (MRI) encodes spatial information into the phase and frequency of the received signal using gradient fields. The time-domain signal collected during acquisition corresponds to samples in a domain known as *k-space*. Image reconstruction involves converting these k-space samples into a spatial distribution of spin density, $I(\vec{r})$, using the Discrete Fourier Transform (DFT), which approximates the continuous Fourier transform under the assumption of uniform sampling.

A.9.1 From k-Space to Image Space

The basic imaging equation expresses the MR signal in k-space as the Fourier transform of the spin density:

$$S(\vec{k}) = \int I(\vec{r}) e^{-i2\pi \vec{k}\cdot\vec{r}}\, d\vec{r} \tag{A.92}$$

When k-space is sampled at discrete points $\vec{k}_{l,m,n}$, the sampled signal becomes:

$$S(\vec{k}_{l,m,n}) = \int I(\vec{r}) e^{-i2\pi \vec{k}_{l,m,n}\cdot\vec{r}}\, d\vec{r} \tag{A.93}$$

Assuming uniform sampling and a rectilinear trajectory, the coordinates in k-space are:

$$k_l = \frac{l}{\mathrm{FOV}_x}, \quad k_m = \frac{m}{\mathrm{FOV}_y}, \quad k_n = \frac{n}{\mathrm{FOV}_z} \tag{A.94}$$

The reconstruction aims to estimate $I(\vec{r})$ from its sampled k-space representa-

tion using the inverse DFT:

$$\hat{I}[m] = \sum_{n=-N/2}^{N/2-1} S[n] e^{i2\pi nm/N} \tag{A.95}$$

This digital form is implemented efficiently using the Fast Fourier Transform (FFT), which assumes the signal is periodic and bandlimited. The reconstructed voxel resolution Δx is related to the sampling interval Δk_x by:

$$\Delta x = \frac{1}{N \Delta k_x} \tag{A.96}$$

A.9.2 Practical Considerations in DFT Reconstruction

A.9.2.1 DFT Definitions. The Discrete Fourier Transform (DFT) and its inverse are formally defined as:

$$\begin{aligned} D_m &= \sum_{n=0}^{N-1} d_n \, e^{-i2\pi mn/N} \\ d_n &= \frac{1}{N} \sum_{m=0}^{N-1} D_m \, e^{i2\pi mn/N} \end{aligned} \tag{A.97}$$

In MRI, the DFT is used to transform between k-space (frequency domain) and image space. However, the standard DFT assumes k-space is ordered with the zero-frequency component at the beginning of the array. In MR imaging, k-space is typically acquired with its center at the midpoint of the array. To correct for this, a phase shift is introduced prior to reconstruction:

$$\hat{I}[m] = (-1)^m \sum_{\hat{n}=0}^{N-1} (-1)^{\hat{n}} \, S[\hat{n} - N/2] \, e^{i2\pi \hat{n} m/N} \tag{A.98}$$

This operation is equivalent to centering the k-space data and applying an appropriate spatial phase correction. In practical terms, it is implemented using the `fftshift` function before and after performing the Fast Fourier Transform (FFT), ensuring that the reconstructed image is spatially aligned and free of wrap-around phase artifacts.

A.9.2.2 Interpolation and Zero Filling. Interpolation in k-space, commonly performed via zero-filling, increases the number of points in the Fourier grid by appending zeros beyond the acquired k-space extent. This results in a denser output grid upon inverse transformation, yielding smoother images with reduced pixelation. However, zero-filling does not increase true spatial resolution, as no additional high-frequency information is introduced.

Mathematically, zero-filling in k-space corresponds to sinc interpolation in image space, effectively refining the sampling grid without altering the underlying point spread function. It is a post-processing technique used to enhance image appearance and aid visualization, but it does not improve the ability to resolve smaller structures or sharp transitions.

A.9.2.3 Aliasing. When the field of view (FOV) is insufficient to encompass the entire object, signals from outside the FOV are aliased, or "folded over," into the image domain. This occurs due to periodicity in the discrete Fourier transform:

$$\hat{I}(x) = \sum_{n=-\infty}^{\infty} I\left(x - \frac{n}{\Delta k_x}\right) \tag{A.99}$$

Here, Δk_x is the k-space sampling interval, and aliasing arises when it is too large to satisfy the Nyquist criterion. In practical terms, structures outside the FOV reappear at incorrect spatial locations, often causing confusing or misleading image artifacts. Aliasing can be avoided by ensuring:

$$\Delta k_x \leq \frac{1}{\mathrm{FOV}_x} \tag{A.100}$$

or equivalently, by increasing the FOV, decreasing the spacing between k-space samples, or applying spatial suppression techniques (e.g., presaturation bands or outer-volume suppression) before acquisition.

A.9.2.4 Gibbs Ringing. Truncation of high-frequency components in k-space leads to oscillatory artifacts near sharp edges, known as Gibbs ringing. These artifacts arise from the limited bandwidth of the acquired data and reflect the sinc-like response

of a finite Fourier series:

$$\hat{I}(x) = \sum_{n=-N/2}^{N/2-1} w_k(n) S[n] e^{i2\pi n \Delta k_x x} \tag{A.101}$$

Here, $S[n]$ denotes the sampled k-space signal and $w_k(n)$ is an optional windowing function—such as a Hamming, Hann, or Gaussian window—used to smooth the spectral edges. Windowing reduces the amplitude of ringing by tapering the abrupt k-space cutoff, but it also broadens the main lobe of the point spread function, leading to a modest reduction in spatial resolution. Gibbs artifacts are particularly prominent at sharp intensity transitions, such as tissue boundaries or object edges.

A.9.2.5 Reconstruction from Non-Cartesian Trajectories. Non-Cartesian k-space trajectories—such as radial or spiral—are often used to improve acquisition efficiency or robustness to motion. However, as these data are not sampled on a uniform Cartesian grid, direct application of the FFT is not feasible. Instead, a reconstruction technique known as *regridding* is employed to interpolate the non-uniform samples onto a Cartesian grid prior to Fourier transformation.

The regridding process involves three key steps:

1. **Density compensation:** Each k-space sample is weighted to correct for variable sampling density.
2. **Convolutional interpolation:** Data are interpolated onto a Cartesian grid using a kernel (e.g., Kaiser-Bessel).
3. **FFT and deapodization:** An FFT is applied, followed by division by the Fourier transform of the kernel to correct for apodization.

While regridding enables efficient image reconstruction, it introduces interpolation errors, particularly in undersampled regimes. Nevertheless, it remains the standard approach for non-Cartesian data when computational speed is prioritized.

A.10 Noise and SNR

In MRI, noise is an unavoidable component of measurements, stemming from random fluctuations due to thermal movements within the imaging volume or the electronic components of the MRI system. It is crucial to comprehend how the imaging process influences noise—whether amplifying or mitigating it—to enhance signal detectability and image quality.

Noise, inherently random, lacks a consistent value across measurements, rendering it a random variable defined across the imaging volume. For any single measurement, this variable assumes arbitrary complex values, yet exhibits distinct statistical characteristics over multiple measurements, encapsulated by a probability density function (PDF). This PDF delineates the likelihood of observing specific values within a measurement range, ensuring that the sum of probabilities across all possible outcomes equals one:

$$\int_{-\infty}^{\infty} p_\xi(x)\,dx = 1 \tag{A.102}$$

where p_ξ symbolizes the PDF of the complex random variable ξ. Essential statistical descriptors of a random variable include its mean and variance. The mean $\bar{\xi}$ calculates the probability-weighted average value across the spectrum:

$$\bar{\xi} = E\{\xi\} = \int_{-\infty}^{\infty} x\, p_\xi(x)\,dx \tag{A.103}$$

where $E\{\xi\}$ is the mathematical expectation operator.

The variance σ_ξ^2 quantifies the spread of the variable from its mean, computed as:

$$\sigma_\xi^2 = E\left\{(x-\bar{\xi})(x-\bar{\xi})^*\right\} = \int_{-\infty}^{\infty}(x-\bar{\xi})p_\xi(x)\,dx \cdot \int_{-\infty}^{\infty}(x-\bar{\xi})^* p_\xi(x)\,dx \tag{A.104}$$

with $*$ denoting the complex conjugate of $(x-\bar{\xi})$. Here, σ_ξ is called the standard deviation and measures the average deviation from the mean, which is always positive.

Noise in MR experiments, generally assumed Gaussian, is defined by its mean μ and standard deviation σ, or variance σ^2:

$$p_\xi(x) = \frac{1}{\sigma\sqrt{2\pi}} e^{-\frac{(x-\mu)^2}{2\sigma^2}} \tag{A.105}$$

In MRI, when noise originates from entirely random sources, it is characterized as ergodic, stationary, and uncorrelated, commonly referred to as white noise. This type of noise typically exhibits a zero mean and is primarily defined by its standard deviation. Such assumptions about noise are generally valid in MRI due to the thermal movements within the imaging volume, subject, and the MRI system, which follow the zero-mean characteristics of Brownian motion. Consequently, this feature of noise allows it to be considered as an additive component, thereby rendering the noise-corrupted k-space signal as:

$$\hat{S}(k) = S(k) + \xi_s(k) \tag{A.106}$$

with $\xi_s(k)$ denoting random noise at k, and $S(k)$ the measured signal.

Post-reconstruction, the noise-impacted image appears as:

$$\hat{I}(x) = I(x) + \xi_I(x) \tag{A.107}$$

with $\xi_I(x)$ being the noise measured at point x, which is a transformation of $\xi_s(k)$ defined by the image reconstruction process, which typically relies on direct FFT reconstruction.

The Fourier transform-based reconstruction method also alters the noise from k-space data into the image domain, resulting in the following noise representation:

$$\xi_I[m] = \frac{1}{N} \sum_{n=-N/2}^{N/2-1} \xi_s[n] e^{i2\pi mn/N} \tag{A.108}$$

If the noise in k-space $\xi_s[n]$ follows a Gaussian distribution with zero mean, then the noise in the image domain ξ_I also exhibits a Gaussian distribution with zero mean, and its variance is expressed as:

$$\sigma^2_{\xi_I} = \frac{1}{N} \sigma^2_{\xi_s} \tag{A.109}$$

The above expression of variance in the image domain implies that the signal-to-noise ratio per pixel of an FFT image is inversely proportional to $\sqrt{N}$ as:

$$\mathrm{SNR}_{\mathrm{voxel}} = \frac{I_{\mathrm{average}}}{\sigma_{\xi_I}} = \frac{\left(\sum_{n=-N/2}^{N/2-1} |S[n]|^2 \right)^{1/2}}{\sigma_{\xi_s} \sqrt{N}} \propto \frac{1}{\sqrt{N}} \tag{A.110}$$

This relationship can further be extended to two or three dimensions:

$$\mathrm{SNR}_{\mathrm{voxel}} \propto \frac{1}{\sqrt{N_x N_y}} \tag{A.111}$$

for 2D, and,

$$\mathrm{SNR}_{\mathrm{voxel}} \propto \frac{1}{\sqrt{N_x N_y N_z}} \tag{A.112}$$

for 3D.

Consequently, the SNR per voxel diminishes as the quantity of sampled k-space data increases, highlighting a crucial aspect of MR image reconstruction that balances resolution enhancement against the inherent increase in noise.

In practice, repeating an MRI experiment multiple times and averaging the acquired signals enhances the SNR due to the random nature of noise. For N_{acq} repetitions, the average signal at a k-space point is:

$$\hat{S}(k) = \frac{1}{N_{\mathrm{acq}}} \sum_{n=1}^{N_{\mathrm{acq}}} \hat{s}_n(k) \tag{A.113}$$

Here, $\hat{s}_n(k)$ represents the acquired k-space data from the n-th repetition, composed of a signal and a noise component:

$$\hat{s}_n(k) = s(k) + \xi_{s,n}(k) \tag{A.114}$$

Assuming the signal remains invariant across repetitions and the noise is independent with zero mean, the average signal equals the signal from a single acquisition:

$$\hat{S}(k) = s(k) + \frac{1}{N_{\mathrm{acq}}} \sum_{n=1}^{N_{\mathrm{acq}}} \xi_{s,n}(k) = s(k) \tag{A.115}$$

The variance of noise in the average image is reduced proportionally to the number of acquisitions:

$$\sigma^2_{N_{\mathrm{acq}}}(k) = \frac{\sigma^2(k)}{N_{\mathrm{acq}}} \tag{A.116}$$

Thus, the standard deviation becomes:

$$\sigma_{N_{\text{acq}}}(k) = \frac{\sigma(k)}{\sqrt{N_{\text{acq}}}} \tag{A.117}$$

This reduction implies that the SNR improves with the square root of the number of acquisitions, which can be expressed as

$$\text{SNR}_{N_{\text{acq}}}(k) = \sqrt{N_{\text{acq}}}\frac{s(k)}{\sigma(k)} = \sqrt{N_{\text{acq}}} \cdot \text{SNR} \tag{A.118}$$

in k-space, and as

$$\text{SNR}_{N_{\text{acq}}}(x) = \sqrt{N_{\text{acq}}}\frac{s(x)}{\sigma(x)} = \sqrt{N_{\text{acq}}} \cdot \text{SNR} \tag{A.119}$$

in space domain.

These expressions indicate that the SNR improves proportionally to the square root of the number of acquisitions if the noise is uncorrelated across experiments.

Thus far, both signal and image have been treated as complex quantities, with the noise in real and imaginary parts modeled as Gaussian white noise. The variance of complex noise is given by:

$$\sigma^2 = \sigma_R^2 + \sigma_I^2 \tag{A.120}$$

Accordingly, the signal-to-noise ratio (SNR) is defined as:

$$\text{SNR} = \frac{\langle s_{\text{abs}} \rangle}{\sqrt{\sigma_R^2 + \sigma_I^2}} \tag{A.121}$$

When analyzing SNR in MR images, it is common to evaluate the magnitude of the complex image. Therefore, the pixel value is computed as:

$$\hat{I}(x) = \sqrt{(I_R(x) + \xi_R)^2 + (I_I(x) + \xi_I)^2} \tag{A.122}$$

Here, I_R and I_I are the real and imaginary parts of the signal, and ξ_R, ξ_I are the corresponding noise components, modeled as white noise with zero mean and standard deviation σ.

Upon transitioning to a magnitude image, the noise probability distribution

transitions from Gaussian to a Rician distribution, which is approximated by the Rayleigh distribution. This results in a PDF with non-zero mean and strictly non-negative values for the noise, as shown in Figure A.16).

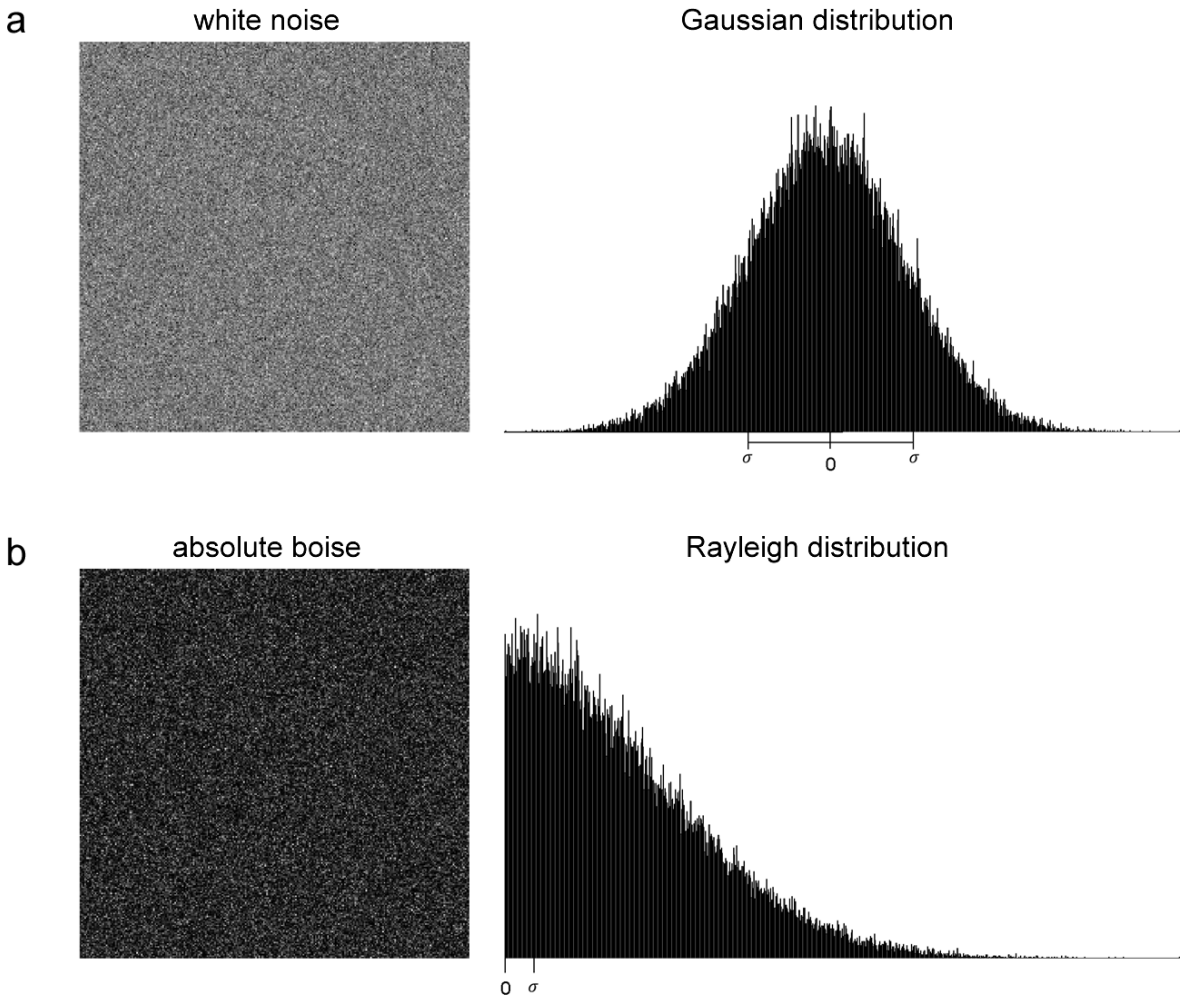

Figure A.16 **a)** The noise distribution of a complex image shows the characteristics of white noise represented by a zero-mean Gaussian. **b)** The noise of a magnitude image exhibits the characteristics of a Rician distribution, which is approximated by the Rayleigh distribution with a non-zero mean.

If it is assumed that the real and imaginary noise components are statistically independent, identically distributed, and share the same standard deviation σ, then the expected value of the magnitude noise over a signal-free region can be estimated using the following integral expression:

$$\mu_{\text{abs}} = \int_{\text{ROI}} I(x)\, p_{\xi_{\text{r}}}(x)\, p_{\xi_{\text{i}}}(x)\, dx \tag{A.123}$$

where $p_{\xi_{\text{r}}}(x)$ and $p_{\xi_{\text{i}}}(x)$ denote the probability density functions of the real and imagi-

nary noise components, respectively, and $I(x)$ is the magnitude of the complex signal. This formulation assumes a Rayleigh distribution in the absence of signal, which arises from the quadrature combination of two zero-mean Gaussian noise sources.

Implementing the Gaussian distributions for p_{ξ_r} and p_{ξ_i} and converting the noise to polar coordinates yields the mean absolute noise as:

$$\mu_{\mathrm{abs}} = \sigma \frac{\sqrt{\pi}}{\sqrt{2}} \approx 1.25\sigma \tag{A.124}$$

Continuing with this analytical approach, the variance of the absolute signal is determined to be:

$$\sigma^2_{\mathrm{abs}} = \left(2 - \frac{\pi}{2}\right) \sigma^2 \tag{A.125}$$

Leading to a standard deviation for the absolute noise of:

$$\sigma_{\mathrm{abs}} = \sigma \sqrt{2 - \frac{\pi}{2}} \approx 0.655\sigma \tag{A.126}$$

The SNR for a given MRI acquisition is traditionally calculated as the ratio of the signal's magnitude to the standard deviation of the complex noise. However, with magnitude-based assessments, the SNR is adjusted to account for the altered noise characteristics, and expressed as:

$$\mathrm{SNR} = \frac{\langle \hat{I} \rangle}{\sigma} = \frac{1.25 \langle \hat{I} \rangle}{\mu_{\mathrm{abs}}} = \frac{0.655 \langle \hat{I} \rangle}{\sigma_{\mathrm{abs}}} \tag{A.127}$$

APPENDIX B. THE GENERALIZED BLOCH EQUATION

B.1 Overview

This appendix presents a detailed derivation of the Bloch equation in the rotating frame, including relaxation, off-resonance, gradient fields, and RF excitation. The derivation is expressed in scalar form and establishes the foundation for modeling signal dynamics in broadband spectroscopic imaging experiments.

B.2 Bloch Equation in the Rotating Frame

The Bloch equation in the rotating frame of reference, including relaxation terms, is given by:

$$\frac{d\vec{M}_{\text{rot}}}{dt} = \gamma_s \vec{M}_{\text{rot}} \times \vec{B}_{\text{eff}} - \frac{M_{x,\text{rot}}\hat{i} + M_{y,\text{rot}}\hat{j}}{T_2} - \frac{(M_{z,\text{rot}} - M_z^0)\hat{k}}{T_1}, \tag{B.1}$$

where γ_s is the gyromagnetic ratio of the spin species, and $\vec{B}_{\text{eff}}$ is the effective magnetic field experienced by the iso-chromat in the rotating frame.

B.3 Effective Field Components

In the rotating frame, the effective field is given by:

$$\vec{B}_{\text{eff}} = \vec{B}_{\text{rot}} + \frac{\vec{\omega}_{\text{rot}}}{\gamma_s}, \tag{B.2}$$

with the angular velocity vector of the rotating frame defined as:

$$\vec{\omega}_{\text{rot}} = -\omega_{\text{rot}}\hat{k}. \tag{B.3}$$

The RF field in the laboratory frame is:

$$\vec{B}_1(t) = B_1^e(t)\cos(\omega_{\text{RF}}t + \phi_{\text{RF}})\hat{i} - B_1^e(t)\sin(\omega_{\text{RF}}t + \phi_{\text{RF}})\hat{j}. \tag{B.4}$$

Translating this into the frame rotating at frequency ω_{rot}, we obtain:

$$\vec{B}_{1,\text{rot}}(t) = B_1^e(t)\cos(\omega_{\text{RF}}t + \phi_{\text{RF}} - \omega_{\text{rot}}t)\hat{i} - B_1^e(t)\sin(\omega_{\text{RF}}t + \phi_{\text{RF}} - \omega_{\text{rot}}t)\hat{j}. \tag{B.5}$$

Assuming $\omega_{\mathrm{RF}} = \omega_{\mathrm{rot}}$, this simplifies to:

$$\vec{B}_{1,\mathrm{rot}}(t) = B_1^e(t)\cos(\phi_{\mathrm{RF}})\hat{i} - B_1^e(t)\sin(\phi_{\mathrm{RF}})\hat{j}, \tag{B.6}$$

which is time-independent.

B.4 Effective Field with Gradients and Off-Resonance

In the presence of gradient fields $\vec{G}(t)$, main field B_0, and spatial position $\vec{r}$, the total field in the rotating frame becomes:

$$\vec{B}_{\mathrm{rot}}(t) = \left(B_0 + \vec{G}(t)\cdot\vec{r}\right)\hat{k} + \vec{B}_{1,\mathrm{rot}}(t), \tag{B.7}$$

and therefore,

$$\vec{B}_{\mathrm{eff}}(t) = \left(B_0 + \vec{G}(t)\cdot\vec{r} - \frac{\omega_{\mathrm{rot}}}{\gamma_s}\right)\hat{k} + \vec{B}_{1,\mathrm{rot}}(t). \tag{B.8}$$

B.5 Scalar Form of the Bloch Equation

Substituting into the Bloch equation and resolving into components yields:

$$\begin{aligned}
\frac{dM_{x,\mathrm{rot}}}{dt} &= \gamma_s M_{y,\mathrm{rot}}\left(B_0 + \vec{G}(t)\cdot\vec{r} - \frac{\omega_{\mathrm{rot}}}{\gamma_s}\right) + \gamma_s M_{z,\mathrm{rot}} B_1^e(t)\sin(\omega_{\mathrm{RF}}t + \phi_{\mathrm{RF}} - \omega_{\mathrm{rot}}t) - \frac{M_{x,\mathrm{rot}}}{T_2},\\
\frac{dM_{y,\mathrm{rot}}}{dt} &= -\gamma_s M_{x,\mathrm{rot}}\left(B_0 + \vec{G}(t)\cdot\vec{r} - \frac{\omega_{\mathrm{rot}}}{\gamma_s}\right) + \gamma_s M_{z,\mathrm{rot}} B_1^e(t)\cos(\omega_{\mathrm{RF}}t + \phi_{\mathrm{RF}} - \omega_{\mathrm{rot}}t) - \frac{M_{y,\mathrm{rot}}}{T_2},\\
\frac{dM_{z,\mathrm{rot}}}{dt} &= -\gamma_s M_{x,\mathrm{rot}} B_1^e(t)\sin(\omega_{\mathrm{RF}}t + \phi_{\mathrm{RF}} - \omega_{\mathrm{rot}}t)\\
&\quad - \gamma_s M_{y,\mathrm{rot}} B_1^e(t)\cos(\omega_{\mathrm{RF}}t + \phi_{\mathrm{RF}} - \omega_{\mathrm{rot}}t) - \frac{M_{z,\mathrm{rot}} - M_z^0}{T_1}.
\end{aligned} \tag{B.9}$$

B.6 Generalized Form with Gradient and Detuning Terms

Grouping terms by physical origin, the generalized Bloch equation becomes:

$$\begin{aligned}
\frac{dM_{x,\mathrm{rot}}}{dt} &= \gamma_s M_{y,\mathrm{rot}}(\vec{G}(t)\cdot\vec{r}) + (\gamma_s B_0 - \omega_{\mathrm{rot}})M_{y,\mathrm{rot}} \\
&\quad + \gamma_s M_{z,\mathrm{rot}} B_1^e(t)\sin(\omega_{\mathrm{RF}}t + \phi_{\mathrm{RF}} - \omega_{\mathrm{rot}}t) - \frac{M_{x,\mathrm{rot}}}{T_2}, \\
\frac{dM_{y,\mathrm{rot}}}{dt} &= -\gamma_s M_{x,\mathrm{rot}}(\vec{G}(t)\cdot\vec{r}) - (\gamma_s B_0 - \omega_{\mathrm{rot}})M_{x,\mathrm{rot}} \\
&\quad + \gamma_s M_{z,\mathrm{rot}} B_1^e(t)\cos(\omega_{\mathrm{RF}}t + \phi_{\mathrm{RF}} - \omega_{\mathrm{rot}}t) - \frac{M_{y,\mathrm{rot}}}{T_2}, \\
\frac{dM_{z,\mathrm{rot}}}{dt} &= -\gamma_s M_{x,\mathrm{rot}} B_1^e(t)\sin(\omega_{\mathrm{RF}}t + \phi_{\mathrm{RF}} - \omega_{\mathrm{rot}}t) \\
&\quad - \gamma_s M_{y,\mathrm{rot}} B_1^e(t)\cos(\omega_{\mathrm{RF}}t + \phi_{\mathrm{RF}} - \omega_{\mathrm{rot}}t) - \frac{M_{z,\mathrm{rot}} - M_z^0}{T_1}.
\end{aligned} \tag{B.10}$$

B.7 Conclusion

This scalar form of the generalized Bloch equation in the rotating frame incorporates broadband RF excitation, off-resonance precession, gradient encoding, and relaxation. It supports numerical integration for spin dynamics simulations, such as those used in this thesis for modeling the behavior of spin-systems under the influence of varying RF field and gradients.

REFERENCES

1. Yildirim, M., Keupp, J., Nicolay, K., and Lamerichs, R., "Chemical shift independent imaging of ^{19}F contrast agents using ultrafast MRSI (F-uTSI)," in *Proceedings of the 15th Annual Meeting of the International Society for Magnetic Resonance in Medicine (ISMRM)*, Vol. 16, (Berlin, Germany), p. 1249, 2007.

2. Yildirim, M., Lamerichs, R., and Keupp, J., "Multifrequency magnetic resonance device and method." WO2008135878A1, World Intellectual Property Organization Patent Application, 2008.

3. Yildirim, M., "Assessment of SNR and detection sensitivity of F-uTSI," in *Proceedings of the 16th Annual Meeting of the International Society for Magnetic Resonance in Medicine (ISMRM)*, Vol. 16, (Toronto, ON, Canada), p. 3257, 2008.

4. Lamerichs, R., and Yildirim, M., "Magnetic resonance device and method: Fast magnetic resonance spectroscopic imaging." EP2130058, European Patent, 2009.

5. Yildirim, M., Caruthers, S. D., Nederveen, A. J., Stoker, J., and Lamerichs, R., "*In vivo* multicolor imaging of perfluorocarbon emulsions using ultrafast spectroscopic imaging (F-uTSI)," in *Proceedings of the 18th Annual Meeting of the International Society for Magnetic Resonance in Medicine (ISMRM)*, (Stockholm, Sweden), p. 999, 2010.

6. Yildirim, M., Vries, A. D., Berben, M., van Cammen, C., Nicolay, K., Gruell, H., and Lamerichs, R., "*In vivo* molecular imaging of angiogenesis in murine urogenital organs with targeted perfluorocarbon nanoparticles and ^{19}F ultrafast turbo spectroscopic imaging (F-uTSI)," in *Proceedings of the 18th Annual Meeting of the International Society for Magnetic Resonance in Medicine (ISMRM)*, Vol. 18, (Stockholm, Sweden), p. 996, 2010.

7. Yildirim, M., Gruell, H., and Lamerichs, R., "Perfluoro compounds (PERFLUORO-T-BUTYL CYCLOHEXANE) for use in imaging," 2012. EP2459235B1, European Patent, 2012.

8. Yildirim, M., Gruell, H., and Lamerichs, R., "Perfluoro compounds (PERFLUORO-T-BUTYL CYCLOHEXANE) for use in imaging," 2012. US20120128589A1, U.S. Patent Application, 2012.

9. Yildirim, M., Gruell, H., and Lamerichs, R., "Perfluoro compounds (PERFLUORO-T-BUTYL CYCLOHEXANE) for use in imaging," 2015. CN102497888B, Chinese Patent, 2015.

10. Yildirim, M., Gruell, H., and Lamerichs, R., "Perfluoro compounds (PERFLUORO-T-BUTYL CYCLOHEXANE) for use in imaging," 2016. JP2016029098A, Japanese Patent Application, 2016.

11. Lamerichs, R., Kammen, C., Yildirim, M., and Nicolay, K., "*In vivo* ultra-fast spectroscopic imaging of ^{19}F containing contrast agents," in *Proceedings of the 17th Annual Meeting of the International Society for Magnetic Resonance in Medicine (ISMRM)*, (Honolulu, Hawaii, USA), p. 616, 2009.

12. Lamerichs, R., and Yildirim, M., "Magnetic resonance device and method: Fast magnetic resonance spectroscopic imaging," 2013. US8498688B2, U.S. Patent, 2013.

13. Lamerichs, R., Yildirim, M., Nederveen, A. J., Stoker, J., Lanza, G. M., Wickline, S. A., and Caruthers, S. D., "*In vivo* 3D ^{19}F fast spectroscopic imaging (F-uTSI) of angiogenesis on Vx-2 tumors in rabbits using targeted perfluorocarbon emulsions," in *Proceedings of the 18th Annual Meeting of the International Society for Magnetic Resonance in Medicine (ISMRM)*, (Stockholm, Sweden), p. 457, 2010.

14. Yildirim, M., Díaz López, R., Nicolay, K., and Lamerichs, R., "*In Vivo* 3D spectroscopic imaging of ^{19}F compounds using backprojection," in *Proceedings of the 21st Annual Meeting of the International Society for Magnetic Resonance in Medicine (ISMRM)*, Vol. 21, (Salt Lake City, Utah, USA), p. 4009, 2013.

15. Moonen, R., Strijkers, G., Motaal, A., Lamerichs, R., Yildirim, M., Aussems-Custers, E., Gruell, H., Wolters, M., Kooi, E., Jacoby, C., Flügel, U., and Nicolay, K., "A comparison of two sequences for spectral imaging of ^{19}F resonances of perfluorocarbon emulsions," in *Proceedings of the Joint Annual Meeting ISMRM-ESMRMB*, Vol. 22, (Milan, Italy), p. 2552, 2014.

16. Yildirim, M., Scholtz, P., Schütz, M., Kovalyk, X., Heijman, E., Lamerichs, R., Grüll, H., and Isik, E. O., "Fast fluorine spectroscopic imaging with pseudo-spiral k-space sampling," in *Proceedings of the 29th Annual Meeting of the International Society for Magnetic Resonance in Medicine (ISMRM)*, Vol. 29, (Online), p. 1810, 2021.

17. Yildirim, M., Kovalyk, X., Scholtz, P., Schütz, M., Lindemeyer, J., Lamerichs, R., Grüll, H., and Isik, E. O., "Fast ^{19}F spectroscopic imaging with pseudo-spiral k-space sampling," *NMR in Biomedicine*, Vol. 37, no. 4, p. e5086, 2024.

18. Klos, D., Risko, J., Lovecek, M., Neoral, C., Havluj, L., Ferko, A., Rozkoš, T., Stasek, J., Skrovina, M., and Penka, I., "Trends in peritoneal surface malignancies: evidence from a czech nationwide population-based study," *World Journal of Surgical Oncology*, Vol. 17, p. 182, 2019.

19. Cortés-Guiral, D., *et al.*, "Primary and metastatic peritoneal surface malignancies," *Nature Reviews Disease Primers*, Vol. 7, no. 1, p. 91, 2021.

20. Rijken, A., van Erning, F. N., Rovers, K. P., Lemmens, V. E. P. P., and de Hingh, I. H. J. T., "On the origin of peritoneal metastases," *European Journal of Cancer*, Vol. 181, pp. 1–2, 2023.

21. Foster, J. M., Zhang, C., Rehman, S., Sharma, P., and Alexander, H. R., "The contemporary management of peritoneal metastasis: A journey from the cold past of treatment futility to a warm present and a bright future," *CA: A Cancer Journal for Clinicians*, Vol. 73, no. 1, pp. 49–71, 2023.

22. Lifante, J.-C., Glehen, O., Cotte, E., Beaujard, A.-C., and Gilly, F. N., "Natural history of peritoneal carcinomatosis from digestive origin," in *Peritoneal Carcinomatosis: A Multidisciplinary Approach* (Passot, G., Elias, D., and Glehen, O., eds.), Vol. 134 of *Cancer Treatment and Research*, pp. 119–129, Springer, 2007.

23. Ketcham, A. S., Hoye, R. C., Pilch, Y. H., and Morton, D. L., "Delayed intestinal obstruction following treatment for cancer," *Cancer*, Vol. 25, no. 2, pp. 406–410, 1970.

24. Koppe, M. J., Boerman, O. C., Oyen, W. J., and Bleichrodt, R. P., "Peritoneal carcinomatosis of colorectal origin: incidence and current treatment strategies," *Ann Surg*, Vol. 243, no. 2, pp. 212–222, 2006.

25. Sugarbaker, P. H., "Treatment of peritoneal carcinomatosis from colon or appendiceal cancer with induction intraperitoneal chemotherapy," *Cancer Treatment and Research*, Vol. 82, pp. 317–325, 1996.

26. Aarts, F., Hendriks, T., Boerman, O. C., Koppe, M. J., Oyen, W. J. G., and Bleichrodt, R. P., "A comparison between radioimmunotherapy and hyperthermic intraperitoneal chemotherapy for the treatment of peritoneal carcinomatosis of colonic origin in rats," *Annals of Surgical Oncology*, Vol. 14, no. 11, pp. 3274–3282, 2007.

27. Los, G., van Vugt, M. J., and Pinedo, H. M., "Response of peritoneal solid tumours after intraperitoneal chemohyperthermia treatment with cisplatin or carboplatin," *British Journal of Cancer*, Vol. 69, no. 2, pp. 235–241, 1994.

28. Bajaj, G., and Yeo, Y., "Drug delivery systems for intraperitoneal therapy," *Pharmaceutical Research*, Vol. 27, pp. 735–738, May 2010. Epub 2010 Mar 3.

29. van der Ven, R. G. F. M., van den Heuvel, T. B. M., Rovers, K. P. B., Nienhuijs, S. W., Boerma, D., van Grevenstein, W. M. U., Hemmer, P. H. J., Kok, N. F. M., Madsen, E. V. E., de Reuver, P., Tuynman, J. B., van Erning, F. N., and de Hingh, I. H. J. T., "Towards equal access to cytoreductive surgery with hyperthermic intraperitoneal chemotherapy and survival in patients with isolated colorectal peritoneal metastases: A nationwide population-based study," *Ann Surg Oncol*, Vol. 31, pp. 3758–3768, Jun 2024.

30. van Oudheusden, T., Grüll, H., Dankers, P. Y. W., and de Hingh, I. H. J. T., "Targeting the peritoneum with novel drug delivery systems in peritoneal carcinomatosis," *Anticancer Research*, Vol. 35, no. 2, pp. 627–634, 2015.

31. Vassileva, V., Moriyama, E. H., De Souza, R., Grant, J., Allen, C. J., Wilson, B. C., and Piquette-Miller, M., "Efficacy assessment of sustained intraperitoneal paclitaxel therapy in a murine model of ovarian cancer using bioluminescent imaging," *Br J Cancer*, Vol. 99, pp. 2037–2043, Dec 2008.

32. Gunji, S., Obama, K., Matsui, M., Tabata, Y., and Sakai, Y., "A novel drug delivery system of intraperitoneal chemotherapy for peritoneal carcinomatosis using gelatin microspheres incorporating cisplatin," *Surgery*, Vol. 154, no. 5, pp. 991–999, 2013.

33. Emoto, S., Yamaguchi, H., Kishikawa, J., Yamashita, H., Ishigami, H., and Kitayama, J., "Antitumor effect and pharmacokinetics of intraperitoneal NK105, a nanomicellar paclitaxel formulation for peritoneal dissemination," *Cancer Science*, Vol. 103, no. 7, pp. 1304–1310, 2012.

34. Tsai, M., Lu, Z., Wientjes, M. G., and Au, J. L.-S., "Paclitaxel-loaded polymeric microparticles: Quantitative relationships between in vitro drug release rate and in vivo pharmacodynamics," *Journal of Controlled Release*, Vol. 172, no. 3, pp. 737–744, 2013.

35. Fan, R., Wang, Y., Han, B., Luo, Y., Zhou, L., Peng, X., Wu, M., Zheng, Y., and Guo, G., "Docetaxel-loaded biodegradable porous microspheres for the treatment of colorectal peritoneal carcinomatosis," *International Journal of Biological Macromolecules*, Vol. 69, pp. 100–107, 2014.

36. Gong, C., Wang, C., Wang, Y., Wu, Q., Zhang, D., Luo, F., and Shi, H., "Efficient inhibition of colorectal peritoneal carcinomatosis by drug-loaded micelles in thermosensitive hydrogel composites," *Nanoscale*, Vol. 4, no. 10, pp. 3095–3104, 2012.

37. Future Tech Taiwan, "Drug delivery system for peritoneal metastasis." `https://www.futuretech.org.tw`, 2025. Accessed: 2025-06-26.

38. Judd, R. M., Rottman, G. A., Forder, J. R., Yin, F. C., and Blackband, S. J., "Feasibility of ^{19}f imaging of perfluorochemical emulsions to measure myocardial vascular volume," *Magnetic Resonance in Medicine*, Vol. 28, no. 1, pp. 129–136, 1992.

39. Chen, J., Lanza, G. M., and Wickline, S. A., "Quantitative magnetic resonance fluorine imaging: Today and tomorrow," *Wiley Interdisciplinary Reviews: Nanomedicine and Nanobiotechnology*, Vol. 2, no. 4, pp. 431–440, 2010.

40. Knight, J. C., Edwards, P. G., and Paisey, S. J., "Fluorinated contrast agents for magnetic resonance imaging: A review of recent developments," *RSC Advances*, Vol. 1, no. 8, pp. 1415–1425, 2011.

41. Ruiz-Cabello, J., Barnett, B. P., Bottomley, P. A., and Bulte, J. W., "Fluorine (^{19}F) MRS and MRI in biomedicine," *NMR Biomed*, Vol. 24, pp. 114–129, Feb 2011.

42. Li, Y., Cui, J., Li, C., Zhou, H., Chang, J., Aras, O., and An, F., "^{19}F MRI nanotheranostics for cancer management: Progress and prospects," *ChemMedChem*, Vol. 17, no. 4, p. e202100701, 2022.

43. Holland, G. N., Bottomley, P. A., and Hinshaw, W. S., "^{19}f Magnetic Resonance Imaging," *Journal of Magnetic Resonance (1969)*, Vol. 28, no. 1, pp. 133–136, 1977.

44. Clark, Jr., L. C., and Gollan, F., "Survival of mammals breathing organic liquids equilibrated with oxygen at atmospheric pressure," *Science*, Vol. 152, no. 3730, pp. 1755–1756, 1966.

45. Heidelberger, C., Chaudhuri, N. K., Danneberg, P., Mooren, D., Griesbach, L., Duschinsky, R., Schnitzer, R. J., Pleven, E., and Scheiner, J., "Fluorinated pyrimidines: A new class of tumor inhibitory compounds," *Nature*, Vol. 179, pp. 663–666, 1957.

46. Clark, Jr., L. C., Ackerman, J. L., Thomas, S. R., Millard, R. W., Hoffman, R. E., Pratt, R. G., Ragle-Cole, H., Kinsey, R. A., and Janakiraman, R., "Perfluorinated organic liquids and emulsions as biocompatible NMR imaging agents for ^{19}F and dissolved oxygen," *Adv Exp Med Biol*, Vol. 180, pp. 835–845, 1984.

47. Mattrey, R. F., and Long, D. C., "Potential role of PFOB in diagnostic imaging," *Investigative Radiology*, Vol. 23, no. Suppl 1, pp. S298–S301, 1988.

48. Mattrey, R. F., "Perfluorooctylbromide: A new contrast agent for CT, sonography, and MR imaging," *American Journal of Roentgenology*, Vol. 152, no. 2, pp. 247–252, 1989.

49. Bruneton, J. N., Falewée, M. N., François, E., Cambon, P., Philip, C., Riess, J. G., Balu-Maestro, C., and Rogopoulos, A., "Liver, spleen, and vessels: preliminary clinical results of ct with perfluorooctylbromide," *Radiology*, Vol. 170, no. 1 Pt 1, pp. 179–183, 1989.

50. Riess, J. G., "Overview of progress in the fluorocarbon approach to in vivo oxygen delivery," *Biomater Artif Cells Immobilization Biotechnol*, Vol. 20, no. 2–4, pp. 183–202, 1992.

51. Riess, J.-P. G., Dalfors, J. L., Hanna, G. K., Klein, D. H., Krafft, M.-P., Pelura, T. J., and Schutt, E. G., "Development of highly fluid, concentrated and stable fluorocarbon emulsions for diagnosis and therapy," *Biomaterials, Artificial Cells and Immobilization Biotechnology*, Vol. 20, no. 2–4, pp. 1029–1040, 1992.

52. Riess, J. G., "The design and development of improved fluorocarbon-based products for use in medicine and biology," *Artif Cells Blood Substit Immobil Biotechnol*, Vol. 22, no. 2, pp. 215–234, 1994.

53. Lanza, G. M., Wallace, K. D., Scott, M. J., Cacheris, W. P., Abendschein, D. R., Christy, D. H., Sharkey, A. M., Miller, J. G., Gaffney, P. J., and Wickline, S. A., "A novel site-targeted ultrasonic contrast agent with broad biomedical application," *Circulation*, Vol. 94, no. 12, pp. 3334–3340, 1996. Erratum in: Circulation 1997 May 20;95(10):2458.

54. Lanza, G. M., Trousil, R. L., Wallace, K. D., *et al.*, "In vitro characterization of a novel, tissue-targeted ultrasonic contrast system with acoustic microscopy," *J Acoust Soc Am*, Vol. 104, no. 6, pp. 3665–3672, 1998.

55. Riess, J. G., "Oxygen carriers ("blood substitutes")—raison d'etre, chemistry, and some physiology," *Chem Rev*, Vol. 101, no. 9, pp. 2797–2920, 2001.

56. Riess, J. G., "Highly fluorinated amphiphilic molecules and self-assemblies with biomedical potential," *Current Opinion in Colloid & Interface Science*, Vol. 14, no. 5, pp. 294–304, 2009.

57. Riess, J. G., "Understanding the fundamentals of perfluorocarbons and perfluorocarbon emulsions relevant to in vivo oxygen delivery," *Artif Cells Blood Substit Immobil Biotechnol*, Vol. 33, no. 1, pp. 47–63, 2005.

58. Riess, J. G., "Perfluorocarbon-based oxygen delivery," *Artif Cells Blood Substit Immobil Biotechnol*, Vol. 34, no. 6, pp. 567–580, 2006.

59. Tirotta, I., Dichiarante, V., Pigliacelli, C., Cavallo, G., Terraneo, G., Bombelli, F. B., Metrangolo, P., and Resnati, G., "^{19}f magnetic resonance imaging (MRI): From design of materials to clinical applications," *Chemical Reviews*, Vol. 115, no. 2, pp. 1106–1129, 2015.

60. Tirotta, I., Dichiarante, V., Pigliacelli, C., Cavallo, G., Terraneo, G., Bombelli, F. B., Metrangolo, P., and Resnati, G., "Hydrophilic fluorinated molecules for spectral ^{19}F MRI," *Scientific Reports*, Vol. 8, no. 1, p. 2889, 2018.

61. Bulte, J. W. M., "Hot spot MRI emerges from the background," *Nature Biotechnology*, Vol. 23, no. 8, pp. 945–946, 2005.

62. Mason, R., Antich, P., Babcock, E., Gerberich, J., and Nunnally, R., "Perfluorocarbon imaging *in vivo*: a ^{19}F MRI study in tumor-bearing mice," *Magn Reson Imaging*, Vol. 7, pp. 475–85, Sep-Oct 1989.

63. Mason, R., Shukla, H., and Antich, P., "In vivo oxygen tension and temperature: simultaneous determination using ^{19}F NMR spectroscopy of perfluorocarbon," *Magn Reson Med*, Vol. 29, no. 3, pp. 296–302, 1993.

64. Mason, R., Antich, P., Babcock, E., Constantinescu, A., Peschke, P., and Hahn, E., "Non-invasive determination of tumor oxygen tension and local variation with growth," *Int J Radiat Oncol Biol Phys*, Vol. 29, no. 1, pp. 95–103, 1994.

65. Kaufman, R. J., "Clinical development of perfluorocarbon-based emulsions as red blood cell substitutes," in *Blood Substitutes and Related Products: Advances in Development, Trial Design and Clinical Development* (Winslow, R. M., Vandegriff, K. D., and Intaglietta, M., eds.), pp. 125–137, Springer, 1994.

66. Mason, R. P., Constantinescu, A., Hunjan, S., Le, D., Hahn, E. W., Antich, P. P., Blum, C., and Peschke, P., "Regional tumor oxygenation and measurement of dynamic changes," *Radiation Research*, Vol. 152, pp. 239–249, Sep 1999.

67. Mason, R., Ran, S., and Thorpe, P., "Quantitative assessment of tumor oxygen dynamics: molecular imaging for prognostic radiology," *J Cell Biochem Suppl*, Vol. 39, pp. 45–53, 2002.

68. McIntyre, D. J. O., McCoy, C. L., and Griffiths, J. R., "Tumour oxygenation measurements by ^{19}F magnetic resonance imaging of perfluorocarbons," *Current Science*, Vol. 76, no. 6, pp. 753–762, 1999.

69. McNab, J. A., Yung, A. C., and Kozlowski, P., "Tissue oxygen tension measurements in the Shionogi model of prostate cancer using ^{19}F MRS and MRI," *MAGMA*, Vol. 17, pp. 288–295, Dec 2004.

70. Yu, J. X., Kodibagkar, V. D., Cui, W., and Mason, R. P., "^{19}f: A versatile reporter for non-invasive physiology and pharmacology using magnetic resonance," *Current Medicinal Chemistry*, Vol. 12, no. 7, pp. 819–848, 2005.

71. Yu, J., Cui, W., Zhao, D., and Mason, R. P., "Chapter 5 - non-invasive physiology and pharmacology using ^{19}f magnetic resonance," in *Fluorine and Health* (Tressaud, A., ed.), pp. 197–276, Amsterdam: Elsevier, 2008.

72. Yu, J. X., Hallac, R. R., Chiguru, S., and Mason, R. P., "New frontiers and developing applications in ^{19}F NMR," *Progress in Nuclear Magnetic Resonance Spectroscopy*, Vol. 70, pp. 25–49, 2013. Epub 2012 Nov 2.

73. Spiess, B. D., "Perfluorocarbon emulsions as a promising technology: A review of tissue and vascular gas dynamics," *Journal of Applied Physiology*, Vol. 106, no. 4, pp. 1444–1452, 2009. Epub 2009 Jan 29.

74. Parhami, P., and Fung, B. M., "Fluorine-19 relaxation study of perfluorochemicals as oxygen carriers," *The Journal of Physical Chemistry*, Vol. 87, no. 11, pp. 1928–1931, 1983.

75. Zhao, D., Constantinescu, A., Hahn, E. W., and Mason, R. P., "Tumor oxygen dynamics with respect to growth and respiratory challenge: investigation of the dunning prostate r3327-hi tumor," *Radiat Res*, Vol. 156, no. 5 Pt 1, pp. 510–520, 2001.

76. Zhao, D., Constantinescu, A., Jiang, L., Hahn, E. W., and Mason, R. P., "Prognostic radiology: quantitative assessment of tumor oxygen dynamics by MRI," *Am J Clin Oncol*, Vol. 24, no. 5, pp. 462–466, 2001.

77. Song, Y., Constantinescu, A., and Mason, R., "Dynamic breast tumor oximetry: the development of prognostic radiology," *Technology in Cancer Research & Treatment*, Vol. 1, no. 6, pp. 471–478, 2002.

78. Xie, D., Kim, S., Kohli, V., Banerjee, A., Yu, M., Enriquez, J. S., Luci, J. J., and Que, E. L., "Hypoxia-responsive ^{19}F MRI probes with improved redox properties and biocompatibility," *Inorganic Chemistry*, Vol. 56, no. 11, pp. 6429–6437, 2017.

79. Shimizu, M., Kobayashi, T., Morimoto, H., Matsuura, N., Shimano, T., Nomura, N., Itoh, S., Yamazaki, M., Iriguchi, N., Yamamoto, T., *et al.*, "Tumor imaging with anti-cea antibody labeled ^{19}F emulsion," *Magnetic Resonance in Medicine*, Vol. 5, no. 3, pp. 290–295, 1987.

80. Lanza, G. M., Lorenz, C. H., Fischer, S. E., Scott, M. J., Cacheris, W. P., Kaufmann, R. J., Gaffney, P. J., and Wickline, S. A., "Enhanced detection of thrombi with a novel fibrin-targeted magnetic resonance imaging agent," *Acad Radiol*, Vol. 5, pp. S173–S176, Apr 1998. Discussion S183–S184.

81. Caruthers, S. D., Neubauer, A. M., Hockett, F. D., Lamerichs, R., Winter, P. M., Scott, M. J., Gaffney, P. J., Wickline, S. A., and Lanza, G. M., "In vitro demonstration using ^{19}F magnetic resonance to augment molecular imaging with paramagnetic perfluorocarbon nanoparticles at 1.5 Tesla," *Invest Radiol*, Vol. 41, no. 3, pp. 305–312, 2006.

82. Caruthers, S. D., Cyrus, T., Winter, P. M., Wickline, S. A., and Lanza, G. M., "Anti-angiogenic perfluorocarbon nanoparticles for diagnosis and treatment of atherosclerosis," *Wiley Interdiscip Rev Nanomed Nanobiotechnol*, Vol. 1, pp. 311–323, 2009.

83. Southworth, R., Kaneda, M., Chen, J., Zhang, L., Zhang, H., Yang, X., Razavi, R., Lanza, G., and Wickline, S., "Renal vascular inflammation induced by western diet in apoe-null mice quantified by ^{19}F NMR of VCAM-1 targeted nanobeacons," *Nanomedicine: Nanotechnology, Biology and Medicine*, Vol. 5, no. 3, pp. 359–367, 2009.

84. Yu, X., Song, S.-K., Chen, J., Scott, M. J., Fuhrhop, R. J., Hall, C. S., Gaffney, P. J., Wickline, S. A., and Lanza, G. M., "High-resolution MRI characterization of human thrombus using a novel fibrin-targeted paramagnetic nanoparticle contrast agent," *Magn Reson Med*, Vol. 44, no. 6, pp. 867–872, 2000.

85. Flacke, S., Fischer, S., Scott, M. J., Fuhrhop, R. J., Allen, J. S., McLean, M., Winter, P., Sicard, G. A., Gaffney, P. J., Wickline, S. A., and Lanza, G. M., "Novel MRI contrast agent for molecular imaging of fibrin: implications for detecting vulnerable plaques," *Circulation*, Vol. 104, pp. 1280–1285, 2001.

86. Winter, P. M., Caruthers, S. D., Yu, X., Song, S.-K., Chen, J., Miller, B., Bulte, J. W., Robertson, J. D., Gaffney, P. J., Wickline, S. A., and Lanza, G. M., "Improved molecular imaging contrast agent for detection of human thrombus," *Magn Reson Med*, Vol. 50, no. 2, pp. 411–416, 2003.

87. Winter, P. M., Morawski, A. M., Caruthers, S. D., Fuhrhop, R. W., Zhang, H., Williams, T. A., Allen, J. S., Lacy, E. K., Robertson, J. D., Lanza, G. M., and Wickline, S. A., "Molecular imaging of angiogenesis in early-stage atherosclerosis with $\alpha_v\beta_3$-integrin–targeted nanoparticles," *Circulation*, Vol. 108, no. 18, pp. 2270–2274, 2003. Epub 2003 Oct 13.

88. Winter, P. M., Neubauer, A. M., Caruthers, S. D., Harris, T. D., Robertson, J. D., Williams, T. A., Schmieder, A. H., Hu, G., Allen, J. S., Lacy, E. K., Zhang, H., Wickline, S. A., and Lanza, G. M., "Endothelial $\alpha_v\beta_3$ integrin–targeted fumagillin nanoparticles inhibit angiogenesis in atherosclerosis," *Arterioscler Thromb Vasc Biol*, Vol. 26, no. 9, pp. 2103–2109, 2006. Epub 2006 Jul 6.

89. Winter, P. M., Schmieder, A. H., Caruthers, S. D., Keene, J. L., Zhang, H., Wickline, S. A., and Lanza, G. M., "Minute dosages of $\alpha_v\beta_3$-targeted fumagillin nanoparticles impair Vx-2 tumor angiogenesis and development in rabbits," *FASEB J*, Vol. 22, no. 8, pp. 2758–2767, 2008. Epub 2008 Mar 24.

90. Lanza, G. M., Yu, X., Winter, P. M., Abendschein, D. R., Karukstis, K. K., Scott, M. J., Chinen, L. K., Fuhrhop, R. W., Scherrer, D. E., and Wickline, S. A., "Targeted antiproliferative drug delivery to vascular smooth muscle cells with a magnetic resonance

imaging nanoparticle contrast agent: implications for rational therapy of restenosis," *Circulation*, Vol. 106, no. 22, pp. 2842–2847, 2002.

91. Morawski, A. M., Winter, P. M., Yu, X., Fuhrhop, R. W., Scott, M. J., Hockett, F., Robertson, J. D., Gaffney, P. J., Lanza, G. M., and Wickline, S. A., "Quantitative "magnetic resonance immunohistochemistry" with ligand-targeted ^{19}F nanoparticles," *Magnetic Resonance in Medicine*, Vol. 52, pp. 1255–1262, Dec 2004.

92. Ahrens, E., Flores, R., Xu, H., and Morel, P., "In vivo imaging platform for tracking immunotherapeutic cells," *Nature Biotechnology*, Vol. 23, pp. 983–987, 2005.

93. Srinivas, M., Morel, P., Ernst, L., Laidlaw, D., and Ahrens, E., "Fluorine-19 MRI for visualization and quantification of cell migration in a diabetes model," *Magnetic Resonance in Medicine*, Vol. 58, no. 4, pp. 725–734, 2007.

94. Ye, Y. X., Basse-Lüsebrink, T. C., Arias-Loza, P. A., Kocoski, V., Kampf, T., Gan, Q., Bauer, E., Sparka, S., Helluy, X., Hu, K., Hiller, K. H., Boivin-Jahns, V., Jakob, P. M., Jahns, R., and Bauer, W. R., "Monitoring of monocyte recruitment in reperfused myocardial infarction with intramyocardial hemorrhage and microvascular obstruction by combined Fluorine 19 and proton cardiac magnetic resonance imaging," *Circulation*, Vol. 128, no. 17, pp. 1878–1888, 2013. Epub 2013 Sep 11.

95. van Heeswijk, R. B., Pellegrin, M., Flögel, U., Gonzales, C., Aubert, J.-F., Mazzolai, L., Schwitter, J., and Stuber, M., "Fluorine MR imaging of inflammation in atherosclerotic plaque in vivo," *Radiology*, Vol. 275, pp. 421–429, 2015.

96. Ebner, B., Behm, P., Jacoby, C., Burghoff, S., French, B. A., Schrader, J., and Flögel, U., "Early assessment of pulmonary inflammation by ^{19}F MRI *in vivo*," *Circ Cardiovasc Imaging*, Vol. 3, pp. 202–210, 2010.

97. Flögel, U., Burghoff, S., van Lent, P. L. E. M., Temme, S., Galbarz, L., Ding, Z., El-Tayeb, A., Huels, S., Bönner, F., Borg, N., Jacoby, C., Müller, C. E., van den Berg, W. B., and Schrader, J., "Selective activation of adenosine A2A receptors on immune cells by a CD73-dependent prodrug suppresses joint inflammation in experimental rheumatoid arthritis," *Science Translational Medicine*, Vol. 4, no. 146, p. 146ra108, 2012.

98. Balducci, A., Wen, Y., Zhang, Y., Helfer, B. M., Hitchens, T. K., Meng, W. S., Wesa, A. K., and Janjic, J. M., "A novel probe for the non-invasive detection of tumor-associated inflammation," *OncoImmunology*, Vol. 2, no. 2, p. e23034, 2013.

99. Constantinides, C., Basnett, P., Lukasiewicz, B., Carnicer, R., Swider, E., Majid, Q. A., Srinivas, M., Carr, C. A., and Roy, I., "*in Vivo* tracking and ^{1}H/^{19}F Magnetic Resonance Imaging of biodegradable polyhydroxyalkanoate/polycaprolactone blend scaffolds seeded with labeled cardiac stem cells," *ACS Appl Mater Interfaces*, Vol. 10, no. 30, pp. 25056–25068, 2018.

100. Fink, C., Gaudet, J. M., Fox, M. S., Bhatt, S., Viswanathan, S., Smith, M., Chin, J., Foster, P. J., and Dekaban, G. A., "^{19}F-perfluorocarbon-labeled human peripheral blood mononuclear cells can be detected in vivo using clinical MRI parameters in a therapeutic cell setting," *Scientific Reports*, Vol. 8, no. 1, p. 590, 2018.

101. Gaudet, J. M., Hamilton, A. M., Chen, Y., Fox, M. S., and Foster, P. J., "Application of dual ^{19}F and iron cellular MRI agents to track the infiltration of immune cells to the site of a rejected stem cell transplant," *Magnetic Resonance in Medicine*, Vol. 78, no. 2, pp. 713–720, 2017. Epub 2016 Sep 9.

102. Rapoport, N., Pitt, W. G., Sun, H., and Nelson, J. L., "Drug delivery in polymeric micelles: From *in Vitro* to *in Vivo*," *J Control Release*, Vol. 91, pp. 85–95, Aug 2003.

103. Rapoport, N., Gao, Z., and Kennedy, A., "Multifunctional nanoparticles for combining ultrasonic tumor imaging and targeted chemotherapy," *J Natl Cancer Inst*, Vol. 99, pp. 1095–1106, Jul 2007. Epub 2007 Jul 10.

104. Rapoport, N., Gupta, R., Kim, Y. S., and O'Neill, B. E., "Polymeric micelles and nanoemulsions as tumor-targeted drug carriers: Insight through intravital imaging," *J Control Release*, Vol. 206, pp. 153–160, May 2015. Epub 2015 Mar 14.

105. Kuethe, D. O., Caprihan, A., Fukushima, E., and Waggoner, R. A., "Imaging lungs using inert fluorinated gases," *Magn Reson Med*, Vol. 39, no. 1, pp. 85–88, 1998. PMID: 9438441.

106. Schreiber, W. G., Eberle, B., Laukemper-Ostendorf, S., Markstaller, K., Weiler, N., Scholz, A., Bürger, K., Heussel, C. P., Thelen, M., and Kauczor, H. U., "Dynamic ^{19}F-MRI of pulmonary ventilation using sulfur hexafluoride (SF_6) gas," *Magn Reson Med*, Vol. 45, no. 4, pp. 605–613, 2001.

107. Pérez-Sánchez, J., Pérez de Alejo, R., Rodríguez, I., Cortijo, M., Peces-Barba, G., and Ruiz-Cabello, J., "In vivo diffusion weighted ^{19}F MRI using sf_6," *Magn Reson Med*, Vol. 54, no. 2, pp. 460–463, 2005.

108. Wolf, U., Scholz, A., Heussel, C. P., Markstaller, K., and Schreiber, W. G., "Subsecond Fluorine-19 MRI of the lung," *Magn Reson Med*, Vol. 55, no. 4, pp. 948–951, 2006.

109. Scholz, A. W., Wolf, U., Fabel, M., Weiler, N., Heussel, C. P., Eberle, B., David, M., and Schreiber, W. G., "Comparison of magnetic resonance imaging of inhaled SF_6 with respiratory gas analysis," *Magn Reson Imaging*, Vol. 27, no. 4, pp. 549–556, 2009.

110. Halaweish, A. F., Moon, R. E., Foster, W. M., Soher, B. J., McAdams, H. P., MacFall, J. R., Ainslie, M. D., MacIntyre, N. R., and Charles, H. C., "Perfluoropropane gas as a magnetic resonance lung imaging contrast agent in humans," *Chest*, Vol. 144, pp. 1300–1310, Oct 2013.

111. Couch, M. J., Ball, I. K., Li, T., Fox, M. S., Littlefield, S. L., Biman, B., and Albert, M. S., "Pulmonary ultrashort echo time ^{19}F MR imaging with inhaled fluorinated gas mixtures in healthy volunteers: Feasibility," *Radiology*, Vol. 269, no. 3, pp. 903–909, 2013.

112. Higuchi, M., Iwata, N., Matsuba, Y., Sato, K., Sasamoto, K., and Saido, T. C., "^{19}F and ^{1}H MRI detection of amyloid beta plaques in vivo," *Nature Neuroscience*, Vol. 8, no. 4, pp. 527–533, 2005.

113. Porcari, P., Capuani, S., Campanella, R., La Bella, A., Migneco, L. M., and Maraviglia, B., "Multi-nuclear MRS and ^{19}F MRI of ^{19}F-labelled and ^{10}B-enriched p-boronophenylalanine-fructose complex to optimize boron neutron capture therapy: phantom studies at high magnetic fields," *Phys Med Biol*, Vol. 51, no. 12, pp. 3141–3154, 2006. Epub 2006 Jun 6.

114. Porcari, P., Capuani, S., D'Amore, E., Lecce, M., La Bella, A., Fasano, F., Campanella, R., Migneco, L. M., Pastore, F. S., and Maraviglia, B., "In vivo ^{19}F MRI and ^{19}F MRS of ^{19}F-labelled boronophenylalanine-fructose complex on a C6 rat glioma model to optimize boron neutron capture therapy (BNCT)," *Phys Med Biol*, Vol. 53, no. 23, pp. 6979–6989, 2008. Epub 2008 Nov 12.

115. Porcari, P., Capuani, S., D'Amore, E., Lecce, M., La Bella, A., Fasano, F., Migneco, L. M., Campanella, R., Maraviglia, B., and Pastore, F. S., "In vivo ^{19}F MR imaging and spectroscopy for the BNCT optimization," *Appl Radiat Isot*, Vol. 67, pp. S365–S368, Jul 2009. Epub 2009 Mar 27.

116. Shani, J., and Wolf, W., "A model for prediction of chemotherapy response to 5-fluorouracil based on the differential distribution of 5-[^{18}F]fluorouracil in sensitive versus resistant lymphocytic leukemia in mice," *Cancer Research*, Vol. 37, no. 7 Pt 1, pp. 2306–2308, 1977.

117. Presant, C. A., Wolf, W., Waluch, V., Wiseman, C., Kennedy, P., Blayney, D., and Brechner, R. R., "Association of intratumoral pharmacokinetics of fluorouracil with clinical response," *Lancet*, Vol. 343, no. 8907, pp. 1184–1187, 1994.

118. Wolf, W., Albright, M. J., Silver, M. S., Weber, H., Reichardt, U., and Sauer, R., "Fluorine-19 NMR spectroscopic studies of the metabolism of 5-fluorouracil in the liver of patients undergoing chemotherapy," *Magn Reson Imaging*, Vol. 5, no. 3, pp. 165–169, 1987.

119. Wolf, W., Waluch, V., and Presant, C. A., "Non-invasive ^{19}F-NMRS of 5-fluorouracil in pharmacokinetics and pharmacodynamic studies," *NMR Biomed*, Vol. 11, no. 7, pp. 380–387, 1998.

120. Wolf, W., Presant, C. A., and Waluch, V., "^{19}F-MRS studies of fluorinated drugs in humans," *Adv Drug Deliv Rev*, Vol. 41, no. 1, pp. 55–74, 2000.

121. Li, X., Li, H., Liu, G., Deng, Z., Wu, S., Li, P., Xu, Z., Xu, H., and Chu, P. K., "Magnetite-loaded fluorine-containing polymeric micelles for magnetic resonance imaging and drug delivery," *Biomaterials*, Vol. 33, no. 10, pp. 3013–3024, 2012.

122. Börnert, P., Norris, D. G., Koch, H., Dreher, W., Reichelt, H., and Leibfritz, D., "Fast perfluorocarbon imaging using ^{19}F U-FLARE," *Magn Reson Med*, Vol. 29, no. 2, pp. 226–234, 1993.

123. Knight-Scott, J., Brennan, P., Palasis, S., and Zhong, X., "Effect of repetition time on metabolite quantification in the human brain in ^{1}H MR spectroscopy at 3 Tesla," *Journal of Magnetic Resonance Imaging*, Vol. 45, pp. 710–721, Mar. 2017. Epub 2016 Jul 30.

124. Maxouri, O., van der Veen, E., de Vries, I. J. M., Figdor, C. G., Heskamp, S., and Aarntzen, E. H. J. G., "How to ^{19}F MRI: applications, technique, and getting started," *BJR Open*, Vol. 5, no. 1, p. 20230019, 2023.

125. de Vries, A., Moonen, R., Yildirim, M., Langereis, S., Lamerichs, R., Pikkemaat, J. A., Baroni, S., Terreno, E., Nicolay, K., Strijkers, G. J., and Grüll, H., "Relaxometric studies of gadolinium-functionalized perfluorocarbon nanoparticles for MR imaging," *Contrast Media & Molecular Imaging*, Vol. 9, no. 1, pp. 83–91, 2014.

126. Hequet, E., Henoumont, C., Djouana Kenfack, V., Lemaur, V., Lazzaroni, R., Boutry, S., Vander Elst, L., Muller, R., and Laurent, S., "Design, characterization and molecular modeling of new fluorinated paramagnetic contrast agents for dual ^{1}h/^{19}f mri," *Magnetochemistry*, Vol. 6, no. 1, p. 8, 2020.

127. Şologan, M., Padelli, F., Giachetti, I., Aquino, D., Boccalon, M., Adami, G., Pengo, P., and Pasquato, L., "Functionalized gold nanoparticles as contrast agents for proton and dual proton/fluorine mri," *Nanomaterials*, Vol. 9, no. 6, p. 879, 2019.

128. Darçot, E., Yerly, J., Hilbert, T., Colotti, R., Najdenovska, E., Kober, T., Stuber, M., and van Heeswijk, R. B., "Compressed sensing with signal averaging for improved sensitivity and motion artifact reduction in Fluorine-19 MRI," *arXiv preprint arXiv:1909.04442*, 2019. No page number assigned.

129. Sehl, O. C., and Foster, P. J., "The sensitivity of magnetic particle imaging and Fluorine-19 magnetic resonance imaging for cell tracking," *Scientific Reports*, Vol. 11, no. 1, p. 22198, 2021.

130. Sotak, C., Hees, P., Huang, H., Hung, M., Krespan, C., and Raynolds, S., "A new perfluorocarbon for use in Fluorine-19 magnetic resonance imaging and spectroscopy," *Magnetic Resonance in Medicine*, Vol. 29, no. 2, pp. 188–195, 1993.

131. Ratner, A. V., Quay, S., Muller, H. H., Simpson, B. B., Hurd, R., and Young, S. W., "^{19}F relaxation rate enhancement and frequency shift with Gd-DTPA," *Invest Radiol*, Vol. 24, pp. 224–227, Mar 1989.

132. Chan, K. W.-Y., and Wong, W.-T., "Small molecular Gadolinium(III) complexes as MRI contrast agents for diagnostic imaging," *Coordination Chemistry Reviews*, Vol. 251, no. 17, pp. 2428–2451, 2007. Inorganic Chemistry in Hong Kong.

133. Jacoby, C., Temme, S., Mayenfels, F., Benoit, N., Krafft, M., Schubert, R., Schrader, J., and Flögel, U., "Probing different perfluorocarbons for in vivo inflammation imaging by ^{19}F MRI: Image reconstruction, biological half-lives and sensitivity," *NMR Biomed*, Vol. 27, no. 3, pp. 261–271, 2014.

134. Lee, H. K., Nalcioglu, O., and Buxton, R. B., "Correction of chemical-shift artifacts in ^{19}F imaging of PFOB: A robust signed magnitude method," *Magn Reson Med*, Vol. 23, no. 2, pp. 254–263, 1992.

135. Lee, H. K., Nalcioglu, O., and Buxton, R. B., "Correction for chemical-shift artifacts in ^{19}F imaging of PFOB: Simultaneous multislice imaging," *Magn Reson Med*, Vol. 21, no. 1, pp. 21–29, 1991.

136. Lee, H. K., and Nalcioglu, O., "Reblurred deconvolution method for chemical shift removal in ^{19}F PFOB MR imaging," *J Magn Reson Imaging*, Vol. 2, no. 1, pp. 53–61, 1992.

137. Meissner, M., Reisert, M., Hugger, T., Hennig, J., von Elverfeldt, D., and Leupold, J., "Revealing signal from noisy ^{19}F MR images by chemical shift artifact correction," *Magnetic Resonance in Medicine*, Vol. 73, no. 6, pp. 2225–2233, 2015.

138. Schoormans, J., Calcagno, C., Daal, M. R. R., Wüst, R. C. I., Faries, C., Maier, A., Teunissen, A. J. P., Naidu, S., Sanchez-Gaytan, B. L., Nederveen, A. J., Fayad, Z. A., Mulder, W. J. M., Coolen, B. F., and Strijkers, G. J., "An iterative sparse deconvolution method for simultaneous multicolor ^{19}F-MRI of multiple contrast agents," *Magn Reson Med*, Vol. 83, no. 1, pp. 228–239, 2020.

139. Staal, A. H. J., Veltien, A., Srinivas, M., and Scheenen, T. W. J., "^{19}F MRI imaging strategies to reduce isoflurane artifacts in *In Vivo* images," *Molecular Imaging and Biology*, Vol. 24, pp. 71–81, 2022.

140. Jirak, D., Galisova, A., Kolouchova, K., Babuka, D., and Hruby, M., "Fluorine polymer probes for magnetic resonance imaging: Quo vadis?," *MAGMA*, Vol. 32, no. 1, pp. 173–185, 2019.

141. Jägers, J., Wrobeln, A., and Ferenz, K. B., "Perfluorocarbon-based oxygen carriers: from physics to physiology," *Pflügers Archiv-European Journal of Physiology*, Vol. 472, no. 1, pp. 111–125, 2020.

142. Wu, L., Liu, F., Liu, S., Xu, X., Liu, Z., and Sun, X., "Perfluorocarbons-based 19F magnetic resonance imaging in biomedicine," *International Journal of Nanomedicine*, Vol. 15, pp. 7377–7395, 2020.

143. Kakaei, N., Amirian, R., Azadi, M., Mohammadi, G., and Izadi, Z., "Perfluorocarbons: A perspective of theranostic applications and challenges," *Frontiers in Bioengineering and Biotechnology*, Vol. 11, p. 1115254, 2023.

144. Nocentini, G., MacLaren, G., Bartlett, R., De Luca, D., Perdichizzi, S., Stoppa, F., Marano, M., Cecchetti, C., Biasucci, D. G., Polito, A., AlGhobaishi, A., Guner, Y., Gowda, S. H., Hirschl, R. B., and Di Nardo, M., "Perfluorocarbons in research and clinical practice: A narrative review," *ASAIO Journal*, Vol. 69, no. 12, pp. 1039–1048, 2023.

145. Goette, M. J., Keupp, J., Rahmer, J., and et al., "Balanced UTE-SSFP for ^{19}F MR imaging of complex spectra," *Magnetic Resonance in Medicine*, Vol. 74, no. 2, pp. 537–543, 2015.

146. Mastropietro, A., De Bernardi, E., Breschi, G. L., Zucca, I., Cametti, M., Soffientini, C. D. L., de Curtis, M., Terraneo, G., Metrangolo, P., Spreafico, R., Resnati, G., and Baselli, G., "Optimization of rapid acquisition with relaxation enhancement (RARE) pulse sequence parameters for ^{19}F-MRI studies," *Journal of Magnetic Resonance Imaging*, Vol. 40, no. 1, pp. 162–170, 2014.

147. van Heeswijk, R. B., Colotti, R., Darçot, E., Delacoste, J., Pellegrin, M., Piccini, D., and Hernando, D., "Chemical shift encoding (CSE) for sensitive Fluorine-19 MRI of perfluorocarbons with complex spectra," *Magn Reson Med*, Vol. 79, pp. 2724–2730, 2018.

148. Busse, L. J., Thomas, S. R., Pratt, R. G., Clark, L. C. J., Ackerman, J. L., Samaratunga, R. C., and Hoffmann, R. E., "Deconvolution techniques for removing the effects of chemical shift in ^{19}F Nuclear Magnetic Resonance Imaging of perfluorocarbon compounds," *Med Phys*, Vol. 13, no. 4, pp. 518–524, 1986.

149. Brown, T. R., Kincaid, B. M., and Ugurbil, K., "NMR chemical shift imaging in three dimensions," *Proc Natl Acad Sci U S A*, Vol. 79, no. 11, pp. 3523–3526, 1982.

150. Santos-Díaz, A., and Noseworthy, M. D., "Phosphorus magnetic resonance spectroscopy and imaging (^{31}P-MRS/MRSI) as a window to brain and muscle metabolism: A review of the methods," *Biomedical Signal Processing and Control*, Vol. 60, p. 101967, 2020.

151. Deans, S. R., *The Radon Transform and Some of Its Applications*, Mineola, NY: Dover Publications, 2007.

152. Herman, G. T., *Fundamentals of Computerized Tomography: Image Reconstruction from Projections*, London: Springer, 2nd ed., 2009.

153. Rose, A., *Vision: Human and Electronic*, New York: Academic Press, 1975.

154. Morris, G. A., and Freeman, R., "Selective excitation in fourier transform nuclear magnetic resonance," *Journal of Magnetic Resonance*, Vol. 29, pp. 433–462, 1978.

155. Shinnar, M., Bolinger, L., and Leigh, J. S., "Use of finite impulse response filters in pulse design," in *Proceedings of the 7th Annual Meeting of the SMRM*, p. 695, 1988.

156. Shinnar, M., Bolinger, L., and Leigh, J. S., "Synthesis of soft pulses with specified frequency responses," in *Proceedings of the 7th Annual Meeting of the SMRM*, p. 1040, 1988.

157. Le Roux, P., "Exact synthesis of radio frequency waveforms," in *Proceedings of the 7th Annual Meeting of the SMRM*, p. 1049, 1988.

158. Shinnar, M., Bolinger, L., and Leigh, J. S., "The use of finite impulse response filters in pulse design," *Magnetic Resonance in Medicine*, Vol. 12, pp. 81–87, October 1989.

159. Runge, C. D. T., "Über die numerische auflösung von differentialgleichungen," *Mathematische Annalen*, Vol. 46, no. 2, pp. 167–178, 1895.

160. Kutta, W., "Beitrag zur näherungsweisen integration totaler differentialgleichungen," *Zeitschrift für Mathematik und Physik*, Vol. 46, pp. 435–453, 1901.

161. "MATLAB Version: R2023b," Natick, Massachusetts, United States: The MathWorks Inc., 2023.

162. Duyn, J. H., Gillen, J., Sobering, G., van Zijl, P. C. M., and Moonen, C. T. W., "Multisection proton mr spectroscopic imaging of the brain," *Radiology*, Vol. 188, pp. 277–282, July 1993.

163. Duyn, J., and Moonen, C., "Fast proton spectroscopic imaging of human brain using multiple spin-echoes," *Magn Reson Med.*, Vol. 30, pp. 409–414, 1993.

164. Dreher, W., Geppert, C., Althaus, M., and Leibfritz, D., "Fast proton spectroscopic imaging using steady-state free precession methods," *Magnetic Resonance in Medicine*, Vol. 50, no. 3, pp. 453–460, 2003.

165. Chen, H. S., and Yang, Z. H., "Perfluorocarbon as blood substitute in clinical applications and in war casualties," *Biomaterials, Artificial Cells and Artificial Organs*, Vol. 16, no. 1-3, pp. 403–409, 1988.

166. Follana, R., Klein, D., Krafft, M. P., Long, D. M., Long, C. D., Ni, Y., Riess, J. G., and Valla, A., "Prolonged shelf stability and biocompatibility of a concentrated injectable fluorocarbon emulsion," *Biomaterials, Artificial Cells and Immobilization Biotechnology*, Vol. 20, no. 2-4, pp. 1059–1061, 1992.

167. "Fluid filled lung oxygenation assistance trial (FFLOAT)." https://clinicaltrials.gov/ct2/show/NCT03041740, 2017. Clinical Drug Experience Knowledgebase, ClinicalTrials.gov Identifier: NCT03041740.

168. "Effects of oxygen delivery with oxycyte in patients with severe traumatic head injury." `https://cdek.pharmacy.purdue.edu/trial/NCT00174980`, n.d. Clinical Drug Experience Knowledgebase, ClinicalTrials.gov Identifier: NCT00174980.

169. "Perfluorooctyl bromide which empowers the liquid to flat the detached retina and displace the underneath fluids anteriorly." https://clinicaltrials.gov/ct2/show/NCT05699096, 2024. Clinical Drug Experience Knowledgebase, ClinicalTrials.gov Identifier: NCT05699096.

170. Kok, M. B., de Vries, A., Abdurrachim, D., Prompers, J. J., Grüll, H., Nicolay, K., and Strijkers, G. J., "Quantitative ^{1}H MRI, ^{19}F MRI, and ^{19}F MRS of cell-internalized perfluorocarbon paramagnetic nanoparticles," *Contrast Media Mol Imaging*, Vol. 6, no. 1, pp. 19–27, 2011. PMID: 20648660.

171. Darçot, E., Colotti, R., Brennan, D., Deuchar, G. A., Santosh, C., and van Heeswijk, R. B., "A characterization of ABL-101 as a potential tracer for clinical fluorine-19 MRI," *NMR in Biomedicine*, Vol. 33, no. 1, p. e4212, 2020. Epub 2019 Nov 13.

172. Vorob'ev, S. I., "First- and second-generation perfluorocarbon emulsions," *Pharmaceutical Chemistry Journal*, Vol. 43, no. 4, pp. 209–218, 2009.

173. Pisani, E., Tsapis, N., Paris, J., Nicolas, V., Cattel, L., and Fattal, E., "Polymeric nano/microcapsules of liquid perfluorocarbons for ultrasonic imaging: Physical characterization," *Langmuir*, Vol. 22, no. 9, pp. 4397–4402, 2006.

174. International Electrotechnical Commission (IEC), "International Standard IEC 60601 Medical Electrical Equipment. Part 2–33: Particular Requirements for the Basic Safety and Essential Performance of Magnetic Resonance Equipment for Medical Diagnosis," 2015. Edition 3.1.

175. Ahrens, E., and Flögel, U., eds., *Fluorine Magnetic Resonance Imaging*, Pan Stanford Publishing, 2017.

176. Wong, S. T., and Roos, M. S., "A strategy for sampling on a sphere applied to 3d selective rf pulse design," *Magnetic Resonance in Medicine*, Vol. 32, no. 6, pp. 778–784, 1994.

177. Kampf, T., Fischer, A., Basse-Lüsebrink, T. C., Ladewig, G., Breuer, F., Stoll, G., Jakob, P. M., and Bauer, W. R., "Application of compressed sensing to in vivo 3d ^{19}f csi," *Journal of Magnetic Resonance*, Vol. 207, no. 2, pp. 262–273, 2010.

178. Zhong, J., Mills, P. H., Hitchens, T. K., and Ahrens, E. T., "Accelerated fluorine-19 MRI cell tracking using compressed sensing," *Magn Reson Med.*, Vol. 69, no. 6, pp. 1683–1690, 2013.

179. Kampf, T., Sturm, V. J. F., Basse-Lüsebrink, T. C., Fischer, A., Buschle, L. R., Kurz, F. T., Schlemmer, H. P., Ziener, C. H., Heiland, S., Bendszus, M., Pham, M., Stoll, G., and Jakob, P. M., "Improved compressed sensing reconstruction for ^{19}f magnetic resonance imaging," *MAGMA*, Vol. 32, no. 1, pp. 63–77, 2019.

180. Lauterbur, P. C., "Progress in n.m.r. zeugmatography imaging," *Philosophical Transactions of the Royal Society of London. Series B, Biological Sciences*, Vol. 289, pp. 483–487, June 1980.

181. Waters, E., Chen, J., Yang, X., Zhang, H., Neumann, R., Santeford, A., Arbeit, J., Lanza, G., and Wickline, S., "Detection of targeted perfluorocarbon nanoparticle binding using ^{19}F diffusion weighted MR spectroscopy," *Magn Reson Med*, Vol. 60, no. 5, pp. 1232–6, 2008.

182. Waters, E., Chen, J., Allen, J., Zhang, H., Lanza, G., and Wickline, S., "Detection and quantification of angiogenesis in experimental valve disease with integrin-targeted nanoparticles and 19-fluorine MRI/MRS," *J Cardiovasc Magn Reson*, Vol. 10, no. 1, p. 43, 2008.

183. Maas, J. W. M., Groothuis, P. G., Dunselman, G. A. J., de Goeij, A. F. P. M., Boudier, H. A. J. S., and Evers, J. L. H., "Endometrial angiogenesis throughout the human menstrual cycle," *Human Reproduction*, Vol. 16, no. 8, pp. 1557–1561, 2001.

184. Robinson, R. S., Woad, K. J., Hammond, A. J., Laird, M., Hunter, M. G., and Mann, G. E., "Angiogenesis and vascular function in the ovary," *Reproduction*, Vol. 138, no. 6, pp. 869–881, 2009.

185. Giraudeau, C., Flament, J., Marty, B., Boumezbeur, F., Mériaux, S., Robic, C., Port, M., Tsapis, N., Fattal, E., Giacomini, E., Lethimonnier, F., Le Bihan, D., and Valette, J., "A new paradigm for high-sensitivity ^{19}F magnetic resonance imaging of perfluorooctylbromide," *Magn Reson Med*, Vol. 63, no. 4, pp. 1119–1124, 2010.

186. Giraudeau, C., Djemaï, B., Ghaly, M. A., Boumezbeur, F., Mériaux, S., Robert, P., Port, M., Robic, C., Le Bihan, D., Lethimonnier, F., and Valette, J., "High sensitivity ^{19}f MRI of a perfluorooctyl bromide emulsion: application to a dynamic biodistribution study and oxygen tension mapping in the mouse liver and spleen," *NMR in Biomedicine*, Vol. 25, no. 4, pp. 654–660, 2012. Epub 2011 Sep 26.

187. Abragam, A., *The Principles of Nuclear Magnetism*, Oxford University Press, 1961.

188. Ernst, R. R., Bodenhausen, G., and Wokaun, A., *Principles of Nuclear Magnetic Resonance in One and Two Dimensions*, Oxford University Press, 1987.

189. Mansfield, P., and Morris, P. G., *NMR Imaging in Biomedicine*, Academic Press, 1982.

190. Haacke, E. M., Brown, R. W., Thompson, M. R., and Venkatesan, R., *Magnetic Resonance Imaging: Physical Principles and Sequence Design*, Wiley-Liss, 1999.

191. Liang, Z.-P., and Lauterbur, P. C., *Principles of Magnetic Resonance Imaging: A Signal Processing Perspective*, IEEE Press, 2000.

192. Bernstein, M. A., King, K. F., and Zhou, X. J., *Handbook of MRI Pulse Sequences*, Elsevier Academic Press, 2004.

193. Oppenheim, A. V., Willsky, A. S., and Nawab, S. H., *Signals and Systems*, Prentice Hall, 2nd ed., 1997.

194. Bloch, F., "Nuclear induction," *Physical Review*, Vol. 70, no. 7-8, pp. 460–474, 1946.

195. Nyquist, H., "Certain topics in telegraph transmission theory," *Transactions of the American Institute of Electrical Engineers*, Vol. 47, pp. 617–644, April 1928.

196. Shannon, C., "Communication in the presence of noise," *Proceedings of the IRE*, Vol. 37, no. 1, pp. 10–21, 1949.